NUREG/CR-3427
BMI-2113
Vol. 4

Long-Term Performance of Materials Used for High-Level Waste Packaging

Annual Report, Year Two
April 1983 - April 1984

Compiled by D. Stahl, N. E. Miller

Battelle Columbus Laboratories

Prepared for
U.S. Nuclear Regulatory Commission

NOTICE

This report was prepared as an account of work sponsored by an agency of the United States Government. Neither the United States Government nor any agency thereof, or any of their employees, makes any warranty, expressed or implied, or assumes any legal liability or responsibility for any third party's use, or the results of such use, of any information, apparatus, product or process disclosed in this report, or represents that its use by such third party would not infringe privately owned rights.

NOTICE

Availability of Reference Materials Cited in NRC Publications

Most documents cited in NRC publications will be available from one of the following sources:

1. The NRC Public Document Room, 1717 H Street, N.W.
   Washington, DC 20555
2. The NRC/GPO Sales Program, U.S. Nuclear Regulatory Commission,
   Washington, DC 20555
3. The National Technical Information Service, Springfield, VA 22161

Although the listing that follows represents the majority of documents cited in NRC publications, it is not intended to be exhaustive.

Referenced documents available for inspection and copying for a fee from the NRC Public Document Room include NRC correspondence and internal NRC memoranda; NRC Office of Inspection and Enforcement bulletins, circulars, information notices, inspection and investigation notices; Licensee Event Reports; vendor reports and correspondence; Commission papers; and applicant and licensee documents and correspondence.

The following documents in the NUREG series are available for purchase from the NRC/GPO Sales Program: formal NRC staff and contractor reports, NRC-sponsored conference proceedings, and NRC booklets and brochures. Also available are Regulatory Guides, NRC regulations in the *Code of Federal Regulations*, and *Nuclear Regulatory Commission Issuances*.

Documents available from the National Technical Information Service include NUREG series reports and technical reports prepared by other federal agencies and reports prepared by the Atomic Energy Commission, forerunner agency to the Nuclear Regulatory Commission.

Documents available from public and special technical libraries include all open literature items, such as books, journal and periodical articles, and transactions. *Federal Register* notices, federal and state legislation, and congressional reports can usually be obtained from these libraries.

Documents such as theses, dissertations, foreign reports and translations, and non-NRC conference proceedings are available for purchase from the organization sponsoring the publication cited.

Single copies of NRC draft reports are available free, to the extent of supply, upon written request to the Division of Technical Information and Document Control, U.S. Nuclear Regulatory Commission, Washington, DC 20555.

Copies of industry codes and standards used in a substantive manner in the NRC regulatory process are maintained at the NRC Library, 7920 Norfolk Avenue, Bethesda, Maryland, and are available there for reference use by the public. Codes and standards are usually copyrighted and may be purchased from the originating organization or, if they are American National Standards, from the American National Standards Institute, 1430 Broadway, New York, NY 10018.

*GPO Printed copy price: $7.00

NUREG/CR-3427
BMI-2113
Vol. 4

Long-Term Performance of Materials Used for High-Level Waste Packaging

Annual Report, Year Two
April 1983 - April 1984

Manuscript Completed: May 1984
Date Published: June 1984

Compiled by
D. Stahl, N. E. Miller

Battelle Columbus Laboratories
505 King Avenue
Columbus, OH 43201

Prepared for
Division of Radiation Programs and Earth Sciences
Office of Nuclear Regulatory Research
U.S. Nuclear Regulatory Commission
Washington, D.C. 20555
NRC FIN B6764
Under Contract No. NRC-04-82-015

CONTRIBUTORS

H. I. Avci
J. A. Beavers
H. J. Cialone
P. I. Feder
J. H. Holbrook
R. A. Holman
H. H. Krause
A. J. Markworth
J. K. McCoy
S. L. Nicolosi
M. R. Pascucci
S. W. Rust
E. D. Spinosa
N. G. Thompson

ABSTRACT

As part of the Nuclear Regulatory Commission's requirement to assess the Department of Energy's application to construct geologic repositories for high-level radioactive waste, Battelle's Columbus Laboratories is investigating the long-term performance of materials used for high-level waste packages. The effects on glass waste-form dissolution of temperature, pressure, solution chemistry, and ratio of glass surface area to solution volume have been studied. The glass-dissolution correlation is ready to be evaluated by comparison with experiments. The devitrification correlation has been completed. In canister-corrosion studies, CF8 alloy was found less susceptible to glass attack than Type 304L stainless steel. Limited experiments revealed no corrosion mechanism which would indicate that cast steel could not be used as a corrosion-allowance container material; additional tests with cracking agents are planned. In hydrogen-uptake studies, cast steel was found to absorb more hydrogen than wrought steel. Parts of the general-corrosion correlation have been tested, and work continues on obtaining realistic experimental data as input for it. Gamma fluxes and dose rates in and near the waste package were calculated for CHLW and spent-fuel waste forms. The current water-radiolysis model was found adequate when tested against existing data, and preliminary calculations were performed with the current water-chemistry model; in both cases, additional chemical species are being incorporated.

This report documents investigations performed during the period Apr 1, 1983 to April, 1984.

TABLE OF CONTENTS

Page

EXECUTIVE SUMMARY.. xxiii

1. INTRODUCTION: PROJECT OBJECTIVES AND APPROACH........... 1-1

1.1 Individual Program Tasks............................ 1-2

1.1.1 Waste Forms.................................... 1-2

1.1.1.1 Glass-Dissolution Experiments........ 1-3
1.1.1.2 Glass-Dissolution Model.............. 1-3
1.1.1.3 Spent Fuel........................... 1-4

1.1.2 Container Materials............................ 1-4

1.1.2.1 External-Canister Corrosion.......... 1-5
1.1.2.2 Hydrogen Embrittlement............... 1-6
1.1.2.3 Modeling of General Corrosion and Pitting.......................... 1-7

1.1.3 Integrated System Performance.................. 1-8

1.2 Overall Program Objectives.......................... 1-9

2. WASTE FORMS.. 2-1

2.1 Leaching/Corrosion Experiments for Glass Waste Forms.. 2-1

2.1.1 Experimental Procedure......................... 2-1

2.1.1.1 Equipment............................ 2-1
2.1.1.2 Sample Preparation................... 2-2
2.1.1.3 Data Collection and Analysis......... 2-5

2.1.2 Preliminary Leaching Experiments 2-5
2.1.3 Leaching Pilot Experiment...................... 2-7

2.1.3.1 Variables and Responses.............. 2-7
2.1.3.2 Experimental Design 2-8
2.1.3.3 Results.............................. 2-8
2.1.3.4 Statistical Analysis of Data......... 2-15
2.1.3.5 Conclusions.......................... 2-34

2.1.4 Future Work.................................... 2-36

TABLE OF CONTENTS
(Continued)

Page

2.2 Devitrification Evaluation for Glass Waste Forms..... 2-37

- 2.2.1 Methods.................................... 2-37
- 2.2.2 Data Sources............................... 2-38
  - 2.2.2.1 TRUMP Data........................... 2-40
  - 2.2.2.2 Crystallization Data................. 2-42
- 2.2.3 Results.................................... 2-45
- 2.2.4 Conclusions................................ 2-51

2.3 Transmutation Effects in Glass Waste Forms........... 2-51
2.4 Implications for Waste Form Performance.............. 2-51
2.5 Glass-Dissolution Kinetics........................... 2-53

- 2.5.1 Dissolution Plus Convective Flow............. 2-53
- 2.5.2 Dissolution Plus Reprecipitation............. 2-58
  - 2.5.2.1 Thermodynamic Basis.................. 2-58
  - 2.5.2.2 Dissolution/Reprecipitation Model.... 2-60
  - 2.5.2.3 Results.............................. 2-65

2.6 Spent Fuel as a Waste Form........................... 2-69

- 2.6.1 Cladding..................................... 2-69
- 2.6.2 Characteristics.............................. 2-70
- 2.6.3 Testing Conditions........................... 2-72
- 2.6.4 Leaching Mechanism........................... 2-73
- 2.6.5 Conclusions and Recommendations.............. 2-74

2.7 References for Section 2............................. 2-75

3. CONTAINER MATERIALS..................................... 3-1

3.1 Internal Corrosion................................... 3-1

- 3.1.1 Materials.................................... 3-2
- 3.1.2 Accelerated Test Planning/Statistics......... 3-3
- 3.1.3 Experimental Procedure....................... 3-3
- 3.1.4 Pit-Depth Measurements....................... 3-5
- 3.1.5 Corrosion-Product Analysis................... 3-11
- 3.1.6 CF8 Alloy Exposure........................... 3-25
- 3.1.7 Conclusions.................................. 3-30

TABLE OF CONTENTS
(Continued)

Page

3.2 External Corrosion.................................. 3-30

3.2.1 Titanium Grade 12-Salt System................. 3-31
3.2.2 Steel-Basalt System........................... 3-43

3.2.2.1 Autoclave Exposures.................. 3-43
3.2.2.2 Electrochemical Measurements......... 3-57
3.2.2.3 Potentiodynamic Polarization Experiments.......................... 3-67
3.2.2.4 Slow Strain Rate Tests............... 3-75
3.2.2.5 Literature Survey of Stress-Corrosion Cracking.................. 3-75

3.3 Hydrogen Embrittlement of Cast-Steel Overpacks....... 3-84

3.3.1 Materials..................................... 3-85
3.3.2 Tension Tests................................. 3-89

3.3.2.1 Effect of Hydrogen on Tensile Properties........................... 3-90
3.3.2.2 Fractography of Tensile Specimens.... 3-94

3.3.3 Fracture-Toughness Tests...................... 3-94

3.3.3.1 Effects of Hydrogen on Fracture Toughness............................ 3-97
3.3.3.2 Fractography of Fracture-Tougnness Specimens.................. 3-101

3.3.4 Hydrogen Absorption During Corrosion Reactions..................................... 3-102
3.3.5 Future Work................................... 3-106

3.4. Corrosion Correlations............................... 3-106

3.4.1 General-Corrosion Correlation................. 3-106

3.4.1.1 Mathematical Formalism............... 3-106
3.4.1.2 Refinements of the General-Corrosion Correlation................ 3-108
3.4.1.3 Possible Experimental Verification of the Correlation.................. 3-110
3.4.1.4 Numerical Methods.................... 3-110
3.4.1.5 Results of Sample Calculations....... 3-113

TABLE OF CONTENTS
(Continued)

Page

3.4.2 Pitting-Corrosion Correlation................ 3-121

3.4.2.1 Pit-Generation Kinetics.............. 3-121
3.4.2.2 Pit-Growth Kinetics.................. 3-124

3.5 References for Section 3............................ 3-134

4. INTEGRATED SYSTEM PERFORMANCE........................... 4-1

4.1 Considerations in Developing a General Description of Groundwater Radiolysis Near Waste Packages....... 4-1

4.1.1 Phenomenological Description of Water Radiolysis.................................. 4-1
4.1.2 Kinetic Description of Water Radiolysis...... 4-2

4.2 Method for Developing a General Description of Groundwater Radiolysis Near Waste Packages.......... 4-3

4.2.1 Gamma-Energy Deposition Calculations......... 4-4
4.2.2 Development of a Description for the Radiolysis of Groundwaters.................. 4-10
4.2.3 Comparisons of Experimental Data with Computed Predictions Using Water-Radiolysis Descriptions................................. 4-10

4.2.3.1 Calculations........................ 4-10
4.2.3.2 Results and Conclusions............. 4-16

4.2.4 Water-Chemistry Description Used in Correlation Calculations......................... 4-16

4.2.4.1 Testing of the Water-Chemistry Description......................... 4-20
4.2.4.2 Software Maintenance................ 4-21

4.3 Future Work... 4-21

4.3.1 Groundwater Radiolysis Studies............... 4-21
4.3.2 Homogeneous Kinetics Studies................. 4-22
4.3.3 Water Chemistry Studies...................... 4-22
4.3.4 Uncertainty Analysis......................... 4-22
4.3.5 High-Level Waste Package Integral Experiments.................................. 4-23

4.4 References for Section 4............................ 4-23

5. QUALITY ASSURANCE....................................... 5-2

LIST OF FIGURES

Page

Figure 2.1 Schematic Representation of Autoclave and TEFLON Sample Holders 2-3

Figure 2.2 Specimen Geometries Used in Leaching/Corrosion Experiments 2-4

Figure 2.3 Tree Diagram of Percentage Weight Increase Averages at 90 C 2-18

Figure 2.4 Tree Diagram of Percentage Weight Increase Averages at 225 C 2-20

Figure 2.5 Tree Diagram of pH Increase Averages for Reagent Water 2-22

Figure 2.6 Tree Diagram of pH Increase Averages for Basalt Water 2-25

Figure 2.7 Tree Diagram Showing Effect of Experimental Factors on Boron 2-32

Figure 2.8 Tree Diagram Showing Effect of Experimental Factors on Molybdenum 2-33

Figure 2.9 Nonlinear Temperature Relationship for Boron and Molybdenum 2-35

Figure 2.10 Simplified Logic Flow Chart for Devitrification Analysis 2-39

Figure 2.11 TRUMP Result for Center Cell 2-41

Figure 2.12 Spline Fit to the Viscosity Curve for Crystal Growth Calculations 2-43

Figure 2.13 Comparison of Crystallization Data Used in Devitrification Calculation 2-46

Figure 2.14 Cooling Rate Curve for Top Cells of Defense Waste Form 2-48

Figure 2.15 Cooling Rate Curve for Middle Cells of Defense Waste Form 2-49

Figure 2.16 Cooling Rate Curve for Bottom Cells of Defense Waste Form 2-50

LIST OF FIGURES
(Continued)

Page

Figure 2.17 Logarithmic Plot of ρ vs. ν (after Equation 2.8)... 2-56

Figure 2.18 Illustration of Equlibria Associated with Dissolution/Reprecipitation........................ 2-59

Figure 2.19 Variation of S with τ for Two Different Cases: Glass Dissolution Only (Broken Curve) and Dissolution Plus Reprecipitation (Solid Curve)..... 2-65

Figure 2.20 Variation of q with τ for the Cases Illustrated in Figure 2.23....................................... 2-66

Figure 2.21 Variation with Time of Al^{+3} in Solution, at pH = 3.1 and 60 C, During Gibbsite Reprecipitation...... 2-67

Figure 2.22 Cross-Section of an Oxide Fuel Pellet from High-Power Light-Water Reactor or Fast Breeder Reactor Fuel.. 2-70

Figure 3.1 Effect of Exposure Time on Pit Development at 900 C.. 3-6

Figure 3.2 Effect of Exposure Time on Pit Development at 700 C.. 3-7

Figure 3.3 Effect of Exposure Time on Pit Development at 500 C.. 3-8

Figure 3.4 Effect of Exposure Time on Pit Development at 300 C.. 3-9

Figure 3.5 Pitting Penetration Rates as a Function of Time... 3-10

Figure 3.6 Pitting Penetration Rates for Longest Exposure Times as a Function of Temperature................ 3-12

Figure 3.7 Energy Dispersive X-Ray Analysis of 900 C Specimen (400-Hour Exposure)...................... 3-13

Figure 3.8 Energy Dispersive X-Ray Analysis of Corrosion Products in 900 C Specimen (400-Hour Exposure).... 3-14

Figure 3.9 Energy Dispersive X-Ray Analysis of 900 C Specimen (750-Hour Exposure)..................... 3-15

Figure 3.10 Energy Dispersive X-Ray Analysis of 900 C Specimen (1330-Hour Exposure).................... 3-16

LIST OF FIGURES
(Continued)

Page

Figure 3.11 Energy Dispersive X-Ray Analysis of 900 C Specimen (1930-Hour Exposure)...................... 3-17

Figure 3.12 Energy Dispersive X-Ray Analysis of 700 C Specimen (470-Hour Exposure)...................... 3-19

Figure 3.13 Energy Dispersive X-Ray Analysis of 700 C Specimen (890-Hour Exposure)...................... 3-20

Figure 3.14 Energy Dispersive X-Ray Analysis of 700 C Specimen (2664-Hour Exposure)..................... 3-21

Figure 3.15 Energy Dispersive X-Ray Analysis of Corrosion Products on 500 C Specimen (620-Hour Exposure).... 3-22

Figure 3.16 Energy Dispersive X-Ray Analysis of 500 C Specimen (1172-Hour Exposure)..................... 3-23

Figure 3.17 Energy Dispersive X-Ray Analysis of 500 C Specimen (2065-Hour Exposure)..................... 3-24

Figure 3.18 Energy Dispersive X-Ray Analysis of Corrosion Products on 300 C Specimen (974-Hour Exposure).... 3-26

Figure 3.19 Energy Dispersive X-Ray Analysis of 300 C Specimen (1826-Hour Exposure)..................... 3-27

Figure 3.20 Energy Dispersive X-Ray Analysis of 300 C Specimen (3273-Hour Exposure)..................... 3-28

Figure 3.21 Photomicrographs of Type 304L and CF8 Stainless Steels.. 3-29

Figure 3.22 Galvanic Current Density as a Function of Exposure Time for a Heated Titanium Grade 12 Specimen Coupled to an Unheated Specimen (ΔT=20 C) Having Equal Surface Areas in Deaerated Brine A at 250 C.. 3-34

Figure 3.23 1/PR as a Function of Exposure Time for Heated and Unheated (ΔT=20 C) Titanium Grade 12 Specimens Exposed in Deaerated Brine A at 250 C............. 3-36

Figure 3.24 Low-Power Optical Photograph of Deposit Found on the Outer Diameter of the Internal Canister....... 3-38

LIST OF FIGURES
(Continued)

Page

Figure 3.25 Low-Power Optical Photograph of Canister, Specimen Rack, and Heat Transfer Specimen Following Testing.. 3-39

Figure 3.26 Higher-Power Optical Photograph of Deposit Found on Heat Transfer Specimen......................... 3-40

Figure 3.27 Low-Power Optical Photograph of Crevice Specimens Exposed to Vapor and Liquid Phases in the Final Autoclave Exposure............................... 3-42

Figure 3.28 Low-Power Optical Photograph of U-Bend Specimens Exposed to Vapor in the Final Autoclave Exposure.. 3-42

Figure 3.29 Rate of Deposit Growth, Averaged Over 3 Hours, as a Function of Solution Temperature and ΔT on a Titanium Grade 12 Specimen Exposed to Naturally Aerated Brine A.................................. 3-44

Figure 3.30 Data Shown in Figure 3.29, Reported as Rate of Weight Gain as a Function of 1/T.................. 3-45

Figure 3.31 Low-Power Optical Photograph of Titanium Grade 12 Heat Transfer Specimen Exposed for 4 Hours to Naturally Aerated Brine A at 65 C (ΔT=[illegible]C)......... 3-46

Figure 3.32 Specimen Temperature as a Function of Distance from Solution/Vapor Interface and Solution Temperature for Titanium Grade 12 in Brine A with a Fixed ΔT.................................... 3-47

Figure 3.33 Temperature of Titanium Grade 12 Specimen as a Function of Distance from Solution/Vapor Interface and ΔT in Brine A at 100 C.................. 3-48

Figure 3.34 SEM Photograph of Pit Found in the Crevice Region of a Cast Steel Specimen Exposed for 1000 Hours in 250 C Deaerated Simulated Basalt Groundwater Containing Crushed Basalt......................... 3-56

Figure 3.35 1/PR as a Function of Exposure Time for Cast Steel and Platinum Exposed in Deaerated Simulated Basalt Groundwater at 250 C Containing Crushed Basalt.. 3-64

LIST OF FIGURES
(Continued)

Page

Figure 3.36 Graphical Representation of Electrode Kinetics for a Corroding Metal Where the Oxidation and Reduction Reactions are Under Activation Control.. 3-65

Figure 3.37 Potential as a Function of Exposure Time for Cast Steel and Platinum Exposed in Deaerated Simulated Basalt Groundwater at 250 C Containing Crushed Basalt.. 3-66

Figure 3.38 Schematic of Typical Anodic Potentiodynamic Polarization Curves............................ 3-68

Figure 3.39 Potentiodynamic Polarization Curves for Wrought 1018 Steel in Deaerated 1X Basalt Groundwater at 90 C With and Without Crushed Basalt at Scan Rate of 0.6 V/hr.. 3-69

Figure 3.40 Potentiodynamic Polarization Curves for Wrought 1018 Steel in Deaerated 10X Basalt Groundwater at 90 C With and Without Crushed Basalt at Scan Rate of 0.6 V/hr.. 3-70

Figure 3.41 Potentiodynamic Polarization Curves for Clean Cast 1018 Steel in Deaerated 1X Basalt Groundwater at 90 C With and Without Crushed Basalt at Scan Rate of 0.6 V/hr.......................... 3-71

Figure 3.42 Potentiodynamic Polarization Curves for Clean Cast 1018 Steel in Deaerated 10X Basalt Groundwater at 90 C With and Without Crushed Basalt at Scan Rate of 0.6 V/hr.......................... 3-72

Figure 3.43 Measured Stress Corrosion Crack Velocities and Current Densities Passed at a Relatively Bare Surface for Ferritic Steel in a Variety of Solutions.. 3-79

Figure 3.44 Potential-pH Diagram for Iron With Cracking Domains for Some of the Potent Cracking Agents.... 3-82

Figure 3.45 Microstructure of Clean Steel Etched with Picral and Nital................................ 3-87

Figure 3.46 Microstructure of Doped Steel Etched with Picral and Nital................................ 3-88

LIST OF FIGURES
(Continued)

Page

Figure 3.47 Ductility of Clean and Doped Steels Tension Tested in 1000 psig Hydrogen or Nitrogen.......... 3-93

Figure 3.48 Fracture Surfaces of Clean, Cast Steel............ 3-95

Figure 3.49 Fracture Surfaces of Doped, As-Cast Steel......... 3-96

Figure 3.50 J-Resistance Curves for the As-Cast Clean Steel Tested in Nitrogen and Hydrogen................... 3-99

Figure 3.51 Hydrogen Absorbed During Exposure to Simulated Basaltic Groundwater by Clean and Doped Steels As Cast.. 3-105

Figure 3.52 Temperature Profiles Near Waste Package, Calculated with $\tau = 0.1$................................ 3-115

Figure 3.53 Temperature Profiles Near Waste Package, Calculated with $\tau = 1.0$................................ 3-116

Figure 3.54 Temperature Profiles Near Waste Package, Calculated with $\tau = 10$................................. 3-117

Figure 3.55 Concentration Profile for a Radiolytic Species Near Waste Package, Calculated with $g=1$ and $\varepsilon=1$... 3-119

Figure 3.56 Concentration Profiles for a Radiolytic Species Near Waste Package, Calculated with $g=10$ and $\varepsilon=1$.. 3-120

Figure 3.57 Concentration Profiles for a Radiolytic Species Near Waste Package, Calculated with $g=10$ and $\varepsilon=2$.. 3-122

Figure 3.58 Illustration of Pit Configurations Used with Binary-Electrolyte Model......................... 3-127

Figure 3.59 Variation of Pit-Depth Distribution with Time..... 3-133

Figure 4.1 Gamma Energy Deposition Rate to a Commercial High-Level Waste Glass Waste Form at 0, 50, and 100 Years After Reprocessing...................... 4-5

Figure 4.2 Gamma Energy Deposition Rates to the Packing Material and Basalt Rock Surrounding a CHLW Waste Package.. 4-6

LIST OF FIGURES
(Continued)

Page

Figure 4.3 Gamma Energy Deposition Rates to Groundwater in the Packing and Basalt Rock Surrounding a CHLW Waste Package.. 4-7

Figure 4.4 Gamma Energy Deposition Rates to Packing Material and Basalt Rock Surrounding a Spent Fuel Waste Package.. 4-8

Figure 4.5 Gamma Energy Deposition Rates to Groundwater Surrounding a Spent Fuel Waste Package............ 4-9

Figure 4.6 Simulation of Water Radiolysis for Case A Using the Mechanism of Rosinger and Dixon............... 4-12

Figure 4.7 Simulation of Water Radiolysis for Case B Using the Mechanism of Rosinger and Dixon............... 4-13

Figure 4.8 Simulation of Water Radiolysis for Case C Using the Mechanism of Rosinger and Dixon......... 4-14

LIST OF TABLES

Page

Table 2.1 Acid Digestion Procedure.......................... 2-6

Table 2.2 Leaching Pilot Experimental Conditions............. 2-8

Table 2.3 Run Order of Leaching Pilot Experiment............. 2-9

Table 2.4 Leaching Pilot Experimental Results for Both Replicates at 90 C and 0.1 MPa Nominal Conditions.. 2-10

Table 2.5 Leaching Pilot Experimental Results for Both Replicates at 90 C and 34.0 MPa Nominal Conditions.. 2-11

Table 2.6 Leaching Pilot Experimental Results for Both Replicates at 225 C and 2.6 MPa Nominal Conditions.. 2-12

Table 2.7 Leaching Pilot Experimental Results for Both Replicates at 225 C and 34.0 MPa Nominal Conditions.. 2-13

Table 2.8 Leaching Pilot Experimental Results for Both Replicates at 170 C and 17.0 MPa Nominal Conditions.. 2-14

Table 2.9 Analysis of Variance Table for Weight Change Data at 90 C....................................... 2-16

Table 2.10 Analysis of Variance Table for Weight Change Data at 225 C...................................... 2-19

Table 2.11 Analysis of Variance Table for Change in pH Data for Reagent Water................................. 2-21

Table 2.12 Analysis of Variance Table for Change in pH Data for Basalt Water.................................. 2-24

Table 2.13 Analysis of Variance Table for Silicon at 90 C..... 2-26

Table 2.14 Analysis of Variance Table for Silicon at 225 C.... 2-27

Table 2.15 Analysis of Variance Table for Boron at 90 C....... 2-28

Table 2.16 Analysis of Variance Table for Boron at 225 C...... 2-29

Table 2.17 Analysis of Variance Table for Molybdenum at 90 C.. 2-30

LIST OF TABLES
(Continued)

Page

Table 2.18 Analysis of Variance Table for Molybdenum at 225 C.. 2-31

Table 2.19 Glass Thermal Data Used for TRUMP Calculations..... 2-40

Table 2.20 Data Used for Crystal Growth Calculations.......... 2-44

Table 2.21 Time Required to Reach T_g and T for Selected Cells in the Waste Form............................ 2-47

Table 2.24 Glass Composition of AECL Nepheline Syenite Glass.. 2-58

Table 3.1. Certified Analyses of Type 304L Stainless Steel... 3-2

Table 3.2 Certified Analysis of CF8 Alloy.................. 3-3

Table 3.3 Composition of PNL 76-68 Glass.................... 3-4

Table 3.4 Nominal Composition of Brine A.................... 3-32

Table 3.5 Results of Inductively Coupled Argon Plasma Analyses of Test Solution from the Autoclave Exposure of Titanium Grade 12 in Brine A Where Effect of Heat Transfer was Studied............... 3-33

Table 3.6 Results of Gravimetric Measurements Performed on Titanium Grade 12 Specimens Exposed for 1000 Hours to Deaerated Brine A at 250 C (Final Autoclave Exposure).. 3-41

Table 3.7 Chemical Compositions in Weight Percent of Reference Steels and Steels Used in the Experimental Program.................................... 3-49

Table 3.8 Nominal Composition of 1X Simulated Basalt Groundwater.................................... 3-51

Table 3.9 Corrosion Rates Calculated from Weight Loss and Pit Depths for Cast Specimens of Clean 1018 Steel Exposed for 1000 Hours to a Deaerated Simulated Basalt Groundwater at 250 C....................... 3-52

Table 3.10 Corrosion Rates Calculated from Weight Loss and Pit Depths for Wrought Specimens of 1018 Steel Exposed for 1000 Hours to Deaerated Simulated Basalt Groundwater at 250 C....................... 3-53

LIST OF TABLES
(Continued)

Page

Table 3.11 Corrosion Rates Calculated from Weight Loss and Pit Depths for Cast Specimens of Clean 1018 Steel Exposed for 1000 Hours to Deaerated 10X Simulated Basalt Groundwater at 250 C........................ 3-54

Table 3.12 Corrosion Rates Calculated from Weight Loss and Pit Depths for Wrought Specimens of 1018 Steel Exposed for 1000 Hours to Deaerated 10X Simulated Basalt Groundwater at 250 C........................ 3-55

Table 3.13 Results of EDX and XRD Analyses of Cast Steel Specimen Exposed for 1000 Hours in 250 C Deaerated Simulated Basalt Groundwater Containing Crushed Basalt.. 3-58

Table 3.14 Corrosion Rates Calculated from Weight Loss and Pit Depths for Specimens of Clean Cast 1018 Steel Exposed for 1000 Hours to Deaerated 10X Simulated Basalt Groundwater at 250 C........................ 3-59

Table 3.15 Corrosion Rates Calculated from Weight Loss and Pit Depths for Duplicate Specimens of Clean Wrought 1018 Steel Exposed for 1000 Hours to Deaerated 10X Simulated Basalt Groundwater at 250 C. 3-60

Table 3.16 Corrosion Rates Calculated from Weight Loss and Pit Depths for Duplicate Specimens of Cast 1018 Steel Exposed for 1000 Hours to Deaerated 10X Simulated Basalt Groundwater at 250 C............. 3-61

Table 3.17 Corrosion Rates Calculated from Weight Loss and Pit Depths for Specimens of Wrought 1018 Steel Exposed for 1000 Hours to Deaerated 10X Simulated Basalt Groundwater at 250 C....................... 3-62

Table 3.18 Summary of Results of Potentiodynamic Polarization Tests on Clean Cast 1018 Steel in Deaerated Basalt Groundwater at 90 C and a Scan Rate of 0.6 V/hr... 3-73

Table 3.19 Summary of Results of Potentiodynamic Polarization Tests Run on Wrought 1018 Steel in Deaerated Basalt Groundwater at 90 C and a Scan Rate of 0.6 V/hr.. 3-74

LIST OF TABLES
(Continued)

Page

Table 3.20 Effect of Electrochemical Potential on Time to Failure and the Mechanical Properties of Cold-Rolled 1018 Carbon Steel Specimens in Slow Strain Rate Tests in 1X Basalt Groundwater at 90 C at a Strain Rate of 6×10^{-7}/sec........................ 3-76

Table 3.21 Summary of the Effects of Various Ions on the Corrosion of Iron-Base Alloys..................... 3-81

Table 3.22 Chemical Compositions of Steel Castings and Specified Compositions of ASTM Standards.......... 3-86

Table 3.23 Tensile Properties of Cast Steels................. 3-91

Table 3.24 Tensile Properties of Wrought Steels.............. 3-92

Table 3.25 Fracture-Toughness Data for Clean and Doped Steels... 3-100

Table 3.26 Hydrogen Absorbed During Exposure to Simulated Basalt Groundwater................................ 3-103

Table 4.1 Conditions for Hochanadel Data................... 4-11

Table 4.2 Calculated Values of H_2O_2 Concentrations for Hochanadel's Experiments.......................... 4-15

Table 4.3 Ion Product of Water Determined From Calculated H^+ and OH^- Concentrations......................... 4-17

Table 4.4 Calculated H_2O_2 Concentrations After One Second of Irradiation and Observed Steady-State Experimental Data....................................... 4-18

Table 4.5 G-Values Used in the Comparison Calculations...... 4-19

Table 5.1 Status of NRC Waste Packaging Program QA Procedures... 5-2

PREVIOUS REPORTS IN SERIES

NUREG/CR-3405, Volume 1: "Long-Term Performance of Materials Used for High-Level Waste Packaging: Annual Report, March 1982-April 1983."

NUREG/CR-3427, Volume 1: "Long-Term Performance of Materials Used for High-Level Waste Packaging: Quarterly Report, April-June 1983."

NUREG/CR-3427, Volume 2: "Long-Term Performance of Materials Used for High-Level Waste Packaging: Quarterly Report, July-September 1983."

NUREG/CR-3427, Volume 3: "Long-Term Performance of Materials Used for High-Level Waste Packaging: Quarterly Report, October-December 1983."

EXECUTIVE SUMMARY

The Department of Energy (DOE) is conducting a large program for the disposal of high-level radioactive wastes in deep-mined geologic repositories. The Nuclear Regulatory Commisson (NRC), being responsible for regulating high-level radioactive waste disposal, will review DOE's application for the construction and operation of the repositories. To assist in evaluating DOE's application, the NRC's Office of Nuclear Regulatory Research is developing an understanding of the long-term performance of geologic repositories. As part of this effort, Battelle's Columbus Laboratories has been awarded a five-year contract to investigate the long-term performance of materials used for high-level waste packages.

The program is being conducted in three parallel efforts: waste-form studies, container-material studies, and waste-package system studies. This report summarizes the results obtained during the second year of the program.

Waste-Form Studies

The waste-form studies are aimed at describing and modeling those mechanisms that will alter or "age" the waste form during the containment period, and identifying and describing those processes that will influence waste-form dissolution after it is exposed to groundwater. During the first two years of the program, the waste-form studies have been largely centered on borosilicate glasses.

Experiments were conducted to determine the relative effect of pressure, temperature, solution chemistry, and the ratio of glass surface area to solution volume on the dissolution of samples of borosilicate glass. Some synergistic effects were found, but they were minor in comparison to the effects of the individual experimental variables.

A study of the radiation effects on glass has not revealed any new approach to evaluating this phenomenon experimentally. We are largely dependent upon the existing literature which indicates that radiation has a small effect on glass performance.

The development of a glass-dissolution model began with some simplified assumptions about the rate of glass dissolution which are being modified by including phenomena known to affect dissolution processes. Mathematical expressions have been added to the model to describe the actual dissolution of the glass by transport of glass species across the glass/groundwater interface, the convective flow of the groundwater, and the reprecipitation of dissolved glass species as a more stable phase than the original glass; the latter point is believed to be very important in controlling the rate of glass dissolution. The glass-dissolution model studies (along with the water chemistry model) will also be used to identify the parameters of groundwater composition that may influence glass dissolution.

A model has been developed to predict the degree of devitrification that will occur during the post-fabrication cooling period and the subsequent reheating in the repository after disposal. Results of these calculations will be used with the data from experimental studies to evaluate the importance of devitrification in the long-term performance of the glass.

An information base on spent fuel as a waste form has been developed to identify available data on the interactions of spent fuel with groundwater. A plan for future experimental and analytical studies will be developed. Large quantities of spent fuel will be available for disposal when a repository is ready for operation; thus, data on its performance will be needed by the NRC.

Container-Material Studies

The container studies are focused on those processes that can cause degradation of the metallic waste-package container. During the second year, studies focused on cast low-carbon steel for use in a basalt environment. The dominant processes identified for degradation of the steel container are general corrosion, stress-corrosion cracking, pitting, crevice corrosion, hydrogen attack, and mechanical stress. A study was also completed on the corrosion of the Type 304L stainless steel canister by hot glass.

To determine the extent to which hot waste glass might attack the inner surface of the canister, coupons of Type 304L stainless steel were exposed to reference waste glass at temperatures of 300-900 C for a variety of exposure times. The results of these experiments indicate that although pits initiate rapidly at all temperatures, they grow very slowly. The observed pitting attack results in maximum penetration rates of approximately 10-20 µm/year. Analyses of corrosion products found in the pits indicated that silicon, zinc, and titanium from the waste glass play an important role in the mechanism of corrosion by glass at all temperatures. Limited experiments with CF8 alloy, the casting equivalent of Type 304L stainless steel, indicate that CF8 resists glass attack better than Type 304L does and thus may be preferable as a canister material.

In studying external-canister corrosion, we investigated general corrosion, pitting, crevice corrosion, and stress-corrosion cracking of cast low-carbon steel in anticipated repository environments. Two steel castings with compositions similar to ASTM Standard A216 were cast: one with low sulfur and phosphorus, and the other with sulfur and phosphorus comparable to normal foundry castings. One-half of each casting was hot rolled, resulting in four types of low-carbon steel for testing. These were tested for general corrosion, pitting, crevice corrosion and stress-corrosion cracking in two deaerated solutions (a simulated basalt groundwater and a simulated concentrated (10X) basalt groundwater) at 250 C. These experiments did not identify any corrosion mechanism which would indicate that steel could not be used as a container material.

A comprehensive literature review has been conducted to identify chemical species known to have caused stress-corrosion cracking in low-carbon steels in some environments. The basalt repository environment is being characterized by data from the literature and by data from our water-chemistry and radiolysis models. Chemical species which have caused stress-corrosion cracking of steel in environments similar to that of the basalt repository will be examined by laboratory experiments.

There are essentially no data in the literature on the effects of hydrogen on the properties of cast steels, although there are considerable data on its effects on wrought steels. To determine whether the abundant data for wrought steels could be applied to cast steels, the performances of cast and wrought steels were compared. Two castings were prepared as described above, and both cast and wrought samples of the clean and doped steel compositions were tested. Tests on samples of each of the four steels in their as-fabricated condition, after exposure to an outgassing procedure, and to a corrosion environment in basalt groundwater showed that cast steel was more susceptible to hydrogen uptake than wrought steel. The sensitivity of these steels to hydrogen embrittlement is being evaluated by conducting tensile and fracture-toughness tests in gaseous hydrogen and an inert environment and measuring the extent of degradation of the properties by hydrogen. These data will determine whether more data are needed to assess the performance of cast steel in repository environments.

In the corrosion-modeling effort, preliminary computations have been performed to test parts of the general-corrosion model. The computations have proven quite successful and preparations are being made to apply the model to more realistic problems. Applications of the model are very dependent upon realistic input data. To this end, the modelers and experimentalists are working together to define experiments to yield data for input to the model. Experiments are planned in a gamma radiation field to provide data on the enhancement of corrosion by radiation. Also, data will be sought on the rate and composition of surface film growth.

The pitting-corrosion model considers three different aspects of the overall pitting process: pit-initiation kinetics, pit-growth kinetics, and the evolution of the pit-depth distribution. Although much information is available on metal pitting, few data are available for the waste-package environment in the repository. We plan to conduct a series of experiments to give data specifically applicable to the pitting model.

Integrated System Performance

At the beginning of the second year, the programming of the system computer model was removed from the scope of study by the NRC, with greater emphasis being placed on providing information for a better understanding of the processes involved in waste-package system degradation.

One process under study is the production of radiolysis products in the groundwater by gamma radiation from the waste. The gamma fluxes and energy deposition rates as a function of time in and near the waste package were calculated using the ANISN code for both commercial high-level waste and spent fuel as gamma sources. These data are being used to calculate the radiolysis products in the groundwater surrounding the waste package. Using computations with the MAKSIMA-CHEMIST code, a set of 55 chemical reactions was found best to describe experimental data found in the literature on radiolysis products in groundwater. Various chemical species, beginning with iron, are being added to the reaction descriptions to be able to apply the analytical method to various groundwater compositions.

Another process under study is water chemistry, since it could affect glass dissolution and canister corrosion. A general-purpose water-chemistry code, WATEQ, was found not to be directly applicable, although the WATEQ data set is of value. The water-chemistry model under development has intentionally been kept simple. Simplifying assumptions were made that all chemical reactions among aqueous species were at equilibrium and no precipitation, colloid formation, or complex formation occurred; some of these assumptions are being modified as the model matures. A limited set of chemical species was used, and reactions among the species are assumed to equilibrate rapidly. Additional chemical species are being incorporated.

1. INTRODUCTION: PROJECT OBJECTIVES AND APPROACH

The Waste Policy Act of 1982 delegates to the Department of Energy (DOE) the authority for siting, construction, and operation of deep-mined geologic repositories for the disposal of high-level waste and spent fuel. The Nuclear Regulatory Commission (NRC) has the responsibility to regulate the activities of DOE to assure that the health and safety of the repository workers and of the public are adequately protected. Prior to construction, the DOE will submit a license application to the NRC describing in detail the proposed repository. The DOE has been directed to take a multiple barrier approach to the isolation of radioactive wastes with the waste package, the engineered facility, and the natural geohydrologic features of the site being the major barriers. Since NRC's compliance assessment requires the technical capability to understand relevant phenomena and processes relating to the long-term performance of the multiple barriers, the NRC's Office of Nuclear Regulatory Research (RES) has established this waste package performance program at Battelle's Columbus Laboratories to provide that part of the input to the assessment. As an important aid to this understanding, Battelle is evaluating total system performance which will integrate separate effects and improve our understanding of the long-term performance of waste package materials. This will also assist in identifying and evaluating research needs.

It is generally accepted that after repository closure the dominant mechanism to cause the release of radionuclides from the repository is groundwater transport. Considerable attention has been given to this phenomenon and many processes have been identified that affect groundwater transport. Simplistically, the water must first contact the waste, the radionuclides must be mobilized by the water from the waste, and finally, the radionuclides must be transported by the water from the repository to be accessible to the environment of humans.

The generally accepted approach to minimizing the release is to provide a number of different obstacles or barriers to the dissolution and transport of radionuclides by the groundwater. For a deep-mined repository, the geohydrologic features of the earth itself are expected to be a major barrier to the release of radionuclides. The repository site will be selected to have properties to optimize isolation of the wastes. Of major importance are initial groundwater chemistry that will inhibit dissolution of the radionuclides and water flow rates and pathways that will require very long times (>1000 yr) to reach the accessible environment.

In addition to the natural barrier to radionuclide release offered by the geohydrologic features of the site, engineered features of the repository and of the waste package will provide additional barriers to the release of radionuclides. The repository will be constructed in such a manner as to minimize disturbing the adjacent rock and will attempt to accommodate the thermomechanical effects of the emplaced wastes with a minimum of degration to its geohydrologic properties.

Upon closure, the underground openings and shafts to the surface will be backfilled and sealed to minimize groundwater flow paths.

From early waste-management studies, it has been recognized that the radioactive waste should be in a physically stable and chemically inert form which will resist physical degradation and dissolution by groundwater after disposal. More recently, it has been decided to add more confidence in isolating the waste by packaging the waste in a container that will provide essentially complete containment of the radionuclides through the period of time in which the repository is heated significantly above its ambient temperature by the heat from decaying fission products. After the container is eventually breached by some process, the waste form must remain sufficiently resistant to groundwater attack to provide high retention of the radionuclides and, together with the repository, to control the release of radionuclides for thousands of years.

The waste package is the center of study of this research program. The objective of the study is to provide an improved understanding of the long-term performance of the materials used for the high-level waste package. More specifically, we are identifying those processes that tend to degrade the performance of the waste-package materials, performing experiments to produce data where data are otherwise lacking on material performance, and analytically modeling the processes to utilize the data to better understand how the processes will affect the material's future performance.

1.1 Individual Program Tasks

The program is being conducted in three parallel efforts: waste-form studies, container studies, and waste-package system studies.

1.1.1 Waste Forms

The waste-form studies are aimed at first describing and modeling those mechanisms that will alter or "age" the waste form during the containment period, and second, identifying and describing those processes that will influence waste-form dissolution after it is exposed to groundwater. During the first two years of the program, the waste-form studies have been largely centered on borosilicate glasses for both defense and commercial high-level wastes. These waste forms are similar, with the defense wastes having higher concentrations of iron, aluminum, and zirconium from metallic matrices and claddings, and commercial wastes having higher concentrations of radioactive waste products. Some effort has also been directed toward evaluating spent fuel as a waste form.

The glass-forming agents added to each waste type can be expected to be tailored to optimize the waste-form properties for each type of high-level waste. After the waste forms are produced, particularly during the very long period of time after disposal while sealed in their container, they will experience processes that will change them. These changes can be detrimental or beneficial. A beneficial change is the decay of most of the fission products in the waste which will greatly reduce the heat output (and temperature) of the waste package, will reduce the radiation levels which can affect the dissolution process, and will reduce the quantity of radionuclides which must be controlled. Detrimental effects are those that will increase the dissolution rate of the glass and hence increase the release of radionuclides.

One detrimental effect is devitrification of the glass, which can lead both to new phases with increased solubility and to cracking of the glass (which is detrimental because it allows a greater surface area of the glass to be contacted by the groundwater). A model has been developed to predict the degree of devitrification that will occur from thermal effects during the post-fabrication cooling period and the subsequent reheating in the repository after disposal. Results of these calculations will be used with the data from experimental studies in the third year to evaluate the relative importance of devitrification in the long-term performance of the glass.

Cracking can also be caused by thermal stresses and by mechanical stresses. The latter may occur either because of external forces in the adjacent rock being applied to the waste form, because of the density change in the container materials as they corrode, or because of internal forces such as density change from radiation effects. A study of the radiation effects on glass has failed to reveal any new approach to evaluating this phenomenon experimentally. We are largely dependent upon the existing literature which indicates that radiation effects in glass have a small effect on its performance.

1.1.1.1 Glass-Dissolution Experiments

During the second year of the program, experiments were conducted to determine the relative effect of pressure, temperature, solution chemistry, and the ratio of glass surface area to solution volume on the dissolution of samples of borosilicate glass. These experimental efforts have also been valuable to establish many procedures necessary for glass dissolution studies and have formed a base of experience for future experiments.

Experiments planned for the near future have three distinct objectives. The first is to evaluate the most common leach-testing procedure to determine whether some types of data from those tests require unique interpretation. The second is to evaluate parameters of groundwater composition that may influence glass dissolution. (This is the beginning of a long series of experiments of this type.) Lastly, a series of experiments will be conducted to evaluate our analytical model of the glass dissolution process.

1.1.1.2 Glass-Dissolution Model

The development of a glass-dissolution model began with the premise that in high groundwater flow rate, the glass dissolution rate is the initial glass dissolution rate in unaltered groundwater; at low flow rate the glass dissolution rate is determined by the equilibrium solubility of the glass. These oversimplified assumptions are being modified by including those phenomena that are known to affect the processes. For example, if precipitation occurs, the solute concentration in the groundwater falls below that of equilibrium with the glass and the glass can continue to dissolve. More recently mathematical expressions were added to the model to describe the actual dissolution of the glass by transport of glass species across the glass/groundwater interface, the convective flow of the groundwater, and the reprecipitation of dissolved glass species as a more stable phase than the original glass. The latter point, described more fully in this report, is believed to be very important in controlling the rate of glass dissolution; as mentioned in the previous paragraph, the glass-dissolution model is being investigated by a carefully planned series of experiments.

The glass dissolution modeling effort is playing an increased role in planning the experimental studies for glass dissolution. In addition to the reprecipitation evaluation described above, the glass-dissolution model studies, along with the water chemistry model (described below), will be used to identify the parameters of groundwater composition that may influence glass dissolution. The ultimate goal in all of the above studies is to provide a base of integrated information to be used by the NRC in evaluating the long-term performance of glass waste forms after disposal.

1.1.1.3 Spent Fuel

Beginning in the second year of our program, we began to develop an information base to include spent fuel as a waste form in future studies. The immediate objective of this effort is to identify the data that are available on the interactions of spent fuel with groundwater to develop a plan for future experimental and analytical studies. Large quantities of spent fuel will be available for disposal when a repository is ready for operation, thus data on its performance will be needed by the NRC.

1.1.2 Container Materials

The container studies are focused on those processes that can cause degradation of the metallic waste package container. The objective is to collect data on the parameters that influence the degradation processes, to identify the controlling parameters, and to ultimately model the degradation processes that determine the long-term performance of the container. The scope of the studies are limited to the materials which are indicated by DOE to be their candidate container materials. During the first year of study a titanium alloy was the candidate material. During the second year studies were redirected to cast low-carbon steel for use in a basalt environment.

The dominant processes which have been identified as causing degradation of the steel container are general corrosion, stress-corrosion cracking, pitting, crevice corrosion, hydrogen attack, and mechanical stress. These processes may occur individually or in combination. The parameters that affect these processes include chemical composition and physical state of the steel, groundwater composition and flow rate, temperature, radiation intensity, availability of air, lithostatic forces, redox state, alkalinity/acidity, and availability of hydrogen. A study was also completed on the corrosion of the Type 304L stainless steel canister by hot glass.

1.1.2.1 External-Canister Corrosion

The use of low-carbon steel in a wet environment for a long-life container requires that a sufficient thickness of steel be available to sustain the loss of metal by corrosion without penetration over the period of interest. If general corrosion dominates the process, the rate of general corrosion will determine the necessary wall thickness. If localized attack such as pitting or crevice corrosion occurs, then the rate of the localized attack and the container life must be used to establish the wall thickness. However, if the steel is susceptible to cracking in the anticipated environment, the rate of cracking is so rapid relative to required container life that the corrosion-allowance approach cannot be used to achieve acceptable performance. What is important is the susceptibility of the metal to crack initiation. Cracking may result from stress-corrosion cracking or from reduction in fracture toughness from hydrogen attack.

A large amount of data is available from the literature on the general corrosion of low-carbon steel in a variety of environments. This is also true for pitting attack, and some data are available for crevice-corrosion and stress-corrosion cracking. Data are also available for hydrogen effects on wrought steel, but there are essentially none on cast steels. Much of the data on the corrosion of steel are for salt-water environments and shallow soil burial (such as pipe lines), but few data are directly applicable to the environments expected in a basalt repository. With the current interest in cast steel for a long-life waste container, corrosion studies have begun at several laboratories in simulated repository environments.

Our initial experimental approach was to investigate general corrosion, pitting, crevice corrosion, and stress-corrosion cracking in anticipated repository environments. Two steel castings with compositions similar to ASTM Standard A216 were cast: one a "clean" steel, with low sulfur and phosphorus, and the other "doped" with sulfur and phosphorus comparable to normal foundry castings. One-half of each casting was hot rolled, resulting in four types of low-carbon steel for testing, a wrought and a cast "clean" and "doped" steel. Specimens of these steels for general corrosion, pitting, crevice corrosion and stress-corrosion cracking were tested in two deaerated solutions, a simulated basalt groundwater and a simulated concentrated (10X) basalt groundwater, at 250 C. The concentrated solution was to simulate a solution that could occur from groundwater boiling during the early high temperatures in an unsealed repository. These experiments did not identify any corrosion mechanisms which would indicate that steel could not be used as a corrosion-allowance container material.

Subsequent experimental efforts are being directed at identifying parameters which may cause poor corrosion performance of low-carbon steel, with emphasis on stress-corrosion cracking. A comprehensive literature review has been conducted to identify chemical species known to have caused stress-corrosion cracking in low-carbon steels in some environments. The basalt repository environment is being characterized by data from the literature and by data from our water-chemistry and radiolysis models. Chemical species which have caused stress-corrosion cracking of steel in environments similar to that of the basalt repository will be examined by laboratory experiments. First, electrochemical experiments will be conducted with steel specimens in simulated basalt groundwater containing the chemical species suspected of causing the attack. Data from these experiments will show the steel's relative susceptibility to cracking and the electrochemical conditions under which it is most likely to occur. Those conditions under which the electrochemical tests show that cracking of steel may occur will be used for additional slow strain rate. These latter experiments will give more definitive data on the susceptibility of low carbon steel to stress-corrosion cracking and the conditions under which it may be expected to occur.

1.1.2.2 Hydrogen Embrittlement

Cracking of metals can also occur from degraded strength by hydrogen attack. There are essentially no data in the literature on the effects of hydrogen on the properties of cast steels, although there are considerable data on its effects on wrought steels. The initial efforts in our program were made to determine whether cast steels could be expected to react in a manner similar to that of wrought steels to hydrogen attack. If they would react similarly, then the abundant data for wrought steels could be applied to cast steels.

To compare the performance of cast and wrought steels, two castings were prepared as described above. The variation in the sulfur and phosparous was included because it was suspected that these two elements may play a significant role in hydrogen attack and corrosion. Both cast and wrought samples of the clean and doped steel compositions are available for testing.

The susceptibility of the steels to hydrogen uptake was evaluated by measuring the hydrogen content of samples of each of the four steels in their as-fabricated condition, after exposure to an outgassing procedure, and to a corrosion environment in basalt groundwater. The data showed that cast steel was more susceptible to hydrogen uptake than wrought steel.

The sensitivity of low-carbon steel to hydrogen embrittlement is being evaluated by conducting tensile and fracture-toughness tests in gaseous hydrogen and an inert environment and measuring the extent of degradation of the properties by hydrogen. Tests are being conducted on the four types of steels in the as-fabricated condition and some after annealing. It is expected that these data will show the relative susceptibility of cast and wrought steels to hydrogen degradation and determine whether more data are needed to assess the performance of cast steel in repository environments.

1.1.2.3 Modeling of General Corrosion and Pitting

A comprehensive mathematical model is under development for use in understanding the corrosion processes associated with the waste-container materials in a repository environment. The foundation for the model for the general-corrosion process is a set of mass transport equations which can be used to compute the fluxes of corrosion species to the container surface, taking into account the fact that certain corrosive species may be generated by radiolysis. The model accounts for diffusion and convective flow to transport the species. The boundary conditions that must be used to solve the set of equations also include an explicit function for the kinetics of the general-corrosion reaction. Solving the transport equations will require the use of numerical iterative techniques in which the iterations will be required to converge on the redox potential at the container surface.

Preliminary computations have been performed to test parts of the model. The thermal parts of the code have been used to calculate a temperature profile of the immediate region. With a given temperature profile the transport of a single element, oxygen, has been calculated. Also, the radiolytic generation of oxygen for a given radiation intensity and the recombination of oxygen with undefined species have been calculated. The computations have proven quite successful and preparations are being made to apply the model to more realistic problems. Applications of the model are very dependent upon realistic input data. To this end, the modelers and experimentalists are working together to define experiments to yield data for input to the model. Experiments are planned in a gamma radiation field to provide data on the enhancement of corrosion by radiation. Also, data will be sought on the rate and composition of surface film growth.

Battelle's modeling effort is also being applied to pitting attack, which may be an important mechanism for the ultimate loss of container integrity. The model being developed considers three different aspects of the overall pitting process: pit-initiation kinetics, pit-growth kinetics, and the evolution of the pit-depth distribution. Many investigators have studied the metal-pitting process and much information is available from the literature. However, few data are available for the waste-package environment in the repository. One series of experiments planned by our experimental and analytic staff is expected to give data specifically applicable to the pitting model.

The experimental and analytical efforts in the container materials task are well integrated and being directed to providing an understanding of the long-term performance of the container materials, with emphasis on those processes that can lead to poor performance.

1.1.3 Integrated System Performance

The waste-package system studies interact with the waste-form studies and the container-material studies to provide an improved understanding of the performance of the total waste-package system. During the first year of the program, the major objective of this task was to develop a waste-package system model incorporating all the separate- and multiple-effects models for waste-form and container performance into one computer model. Indeed, at the end of the first year the first-generation system model was developed and operable. At the beginning of the second year, the programming of the system computer model was removed from the scope of study by the NRC, with greater emphasis being placed on providing information for a better understanding of the processes involved in waste-package system degradation.

One aspect of the total system under study is the production of radiolysis products in the groundwater by gamma radiation from the waste. This is of major importance in modeling the corrosion of the container and in planning experiments to determine the effects of radiolysis. The gamma fluxes and energy deposition rates as a function of time in the materials of the waste package and very-near-field basalt environment were calculated using the ANISN code for both commercial high-level waste and spent fuel as gamma sources. These data are being used to calculate the radiolysis products in the groundwater surrounding the waste package. To simplify the calculation, it was initially assumed that the groundwater was pure water. A number of different sets of chemical reactions were tried by computations with the MAKSIMA-CHEMIST code to determine the complexity of the reaction descriptions necessary to describe the process adequately. A 55-reaction set was found best to describe experimental data found in the literature. Next, various chemical species, beginning with iron, are being added to the reaction descriptions to be able to apply the analytical method to various groundwater compositions. The output of the radiolysis model calculations provide input to the water-chemistry model, which is a fundamental part of the glass-dissolution model and the general-corrosion model.

A general purpose water-chemistry code, WATEQ, was evaluated for use as a basis for the glass-dissolution model and found not directly applicable, although the WATEQ data set is of value. The water-chemistry model which we initially developed for our use has intentionally been kept simple. Simplifying assumptions were made that all chemical reactions among aqueous species were at equilibrium and no precipitation, colloid formation, or complex formation occurred. In addition, only a limited set of chemical species was included. The set includes the basic water species, the species which dominate most natural groundwaters, and certain species which are assumed to result from the corrosion of iron-based metallic containers and from the dissolution of borosilicate glass. The six reactions among the aqueous species are assumed to equilibrate rapidly.

Any other reactions are excluded by the choice of species. However, additional species are being incorporated as the model matures.

Input to the model includes temperature, oxidation potential, volume of water, and amounts of each of the elements in solution (including those species from the radiolysis code). The water-chemistry model calculates the concentration and activity of each of the water species. The results are used for the glass-dissolution and corrosion models.

1.2 Overall Program Objectives

In all the program tasks, the ultimate objective is to develop a base of information to assist the NRC in evaluating the performance of the waste package proposed in DOE's license application. A near-term objective is to provide information to allow the NRC to prepare position papers on the information required of DOE for evaluation of their waste package. Of significance here is identifying sensitive parameters affecting the performance of materials and identifying data requirements.

To achieve the above objectives, the waste-form task is providing information to give a better understanding of the release of radionuclides from the waste form, beginning at the time it is first contacted by groundwater through the 10,000-year period defined in the draft EPA Standard. This includes an understanding of the probable physiochemical condition of the waste form when it is contacted by groundwater, as well as the parameters of waste-form composition and environment conditions which will cause changes from its state at the time of disposal. In addition, we are producing experimental data on the parameters that affect dissolution of the waste form, including composition of the groundwater and environmental conditions. The waste-form dissolution process is also being mathematically modeled to allow analysis of the performance of the waste form under specific input conditions.

The information on the performance of the container materials relates to the required containment period of 300 to 1000 years. The container performance is expected to be most affected by corrosion and hydrogen-attack processes. We are attempting to provide information on the parameters of container-material composition, groundwater composition, and environmental conditions that are most significant in these processes. Our preliminary study of the titanium alloy in brine did not reveal any conditions that would cause general corrosion, pitting, crevice corrosion, or stress-corrosion cracking to affect the good performance of the material as claimed in the literature. However, vapor-phase attack was identified; this could degrade the material and should be more thoroughly investigated if the DOE selects the material for use.

Our studies of cast low-carbon steel in a basalt environment are currently focused on the susceptibility of the metal to stress-corrosion cracking under repository conditions, because steel is known to fail by this process in some environments. We are studying the chemical species and environmental conditions that cause cracking to determine whether this mode of failure is expected under credible repository conditions. Our experimental studies on general and localized corrosion, together with our comprehensive general-corrosion model, will assist in evaluating the corrosion-allowance approach for the use of steel as a long-life container.

Although the development of an integrated waste-package system model is no longer included in the scope of this project, modeling efforts in the Integrated System Performance task are contributing significant information to studies of general corrosion and glass dissolution. These studies require the amount and kind of chemical species that may be produced by radiolysis of the groundwater near the waste package as a result of gamma radiation from the enclosed waste to be known. To obtain this information, energy deposition and radiolysis codes are used. The ANISN code is used to calculate the gamma fluxes and energy deposition rates in and near the waste package over the time of storage; these have been calculated for commercial high-level waste and for spent-fuel waste forms. The gamma fluxes and energy deposition rates as a function of time are then used in the water-radiolysis model to calculate the amount and kind of radiolysis products in the groundwater near the waste package. To determine how these radiolysis products may affect the performance of the canister and waste form, it is necessary to determine their chemical activities. These are calculated by the water-chemistry model, using as input data from experiments and from the groundwater-radiolysis model. The output from the water-chemistry model is the concentration and activity of each chemical species in the groundwater near the waste package. This information is used not only as input to the general-corrosion and glass-dissolution models but also as a point of reference in directing the experimental efforts in corrosion and dissolution.

2. WASTE FORMS

The second year's work in waste forms concentrated on degradation mechanisms for glasses and on evaluation of the literature for spent fuels as a waste form. Work on the glass waste form was divided into three separate tasks: evaluation of some variables that can influence leaching/corrosion, evaluation of the devitrification that may occur in a full-size waste form, and continued evaluation of the influence of various radiation-damage mechanisms on glass waste-form integrity. Separate-effects analyses of the kinetics of glass dissolution were also conducted. In addition, some consideration has been given to spent fuel as a waste form.

2.1 Leaching/Corrosion Experiments for Glass Waste Forms

The purpose of the leaching/corrosion experiments is to evaluate the influence of environmental variables on the radionuclides released to the repository. Some of the potentially detrimental variables include: the exposure temperature, the surface-area-of-glass to volume-of-solution (SA/V) ratio, the chemistry of the leaching solution or water, and the composition of the waste form. The literature review conducted in the first year indicated that many of these variables, particularly temperature and SA/V ratio, have been explored in single-variable experiments. However, the interactive or synergistic effects that could occur under repository conditions have not been adequately investigated. Therefore, the leaching/corrosion experiments for glass in this year's experiments were conducted in a manner that would allow assessment of these potentially interactive effects.

2.1.1 Experimental Procedure

Several standard procedures were developed for the leaching/corrosion experiments. These involved equipment assembly, leaching-solution preparation, sample preparation, and data recording.

2.1.1.1 Equipment

The equipment used for the leaching experiment consisted of autoclaves into which PFA TEFLON* containers were placed. When the glass samples and their retaining basket are in place, the PFA TEFLON containers hold approximately 53 ml of liquid. The screw-top lids of these containers were drilled with one hole to accommodate pressure changes. Before use, each container was cleaned using a standard procedure that included

---

*TEFLON is a registered trademark of the DuPont de Nemours Company. PFA TEFLON containers were purchased from SAVILEX Part No. 0102; screens were Part No. 26SC.

hydrofluoric/nitric acid rinses, a 5-day oven bake at 200 C, water rinses, autoclaving, and a boiling water bath to remove any possible contamination. This procedure is very similar to that recommended by DOE's Materials Characterization Center (MCC)(2.1), but was modified according to Macedo's(2.2) recommendations.

Each of the two autoclaves* was made of Type 316 stainless steel, had a 3.8-liter capacity, and was rated at 340 C/34 MPa. The autoclaves were modified by brazing copper cooling coils and wiring heater strips along the outer surface. For the experiments, the autoclaves were pre-pressurized with argon and heated to the experimental temperature. Final pressure adjustments were made by venting. A pressure control system ensured that the experimental pressure for each run was maintained at the predetermined value.

In assembling the equipment for a run, the leaching liquid was placed in the TEFLON container followed by the glass sample on top of the TEFLON basket. One container of each solution, but without a glass sample, was included in each autoclave run to serve as an analytical reference ("blank"). The containers were placed inside the autoclaves on a rack and the autoclave tops were secured. Figure 2.1 schematically displays autoclave loading.

2.1.1.2 Sample Preparation

The glass used in these experiments was obtained from the MCC in block form. These samples of MCC 76-68 were core drilled** to an approximate diameter of 6.35 mm. For the SA/V ratio of 0.001/mm, samples were first cut to the approximate length, then ground to 2.3-2.6 mm, and then cut in half on the diameter. The samples for an SA/V ratio of 0.01/mm were first cut to the approximate length, then ground to 10.00-10.30 mm. Figure 2.2 presents the shapes and diameters of these samples. After grinding to size, each sample was polished in a SiC 200-grit slurry, then rinsed with reagent-grade water. Samples were then dried at 100 C for 2 hours, weighed, and their dimensions recorded.

Two liquids were used in these experiments: reagent-grade water meeting ASTM D1192-77 specifications for Type I water, and a simulated basalt water prepared by a standardized procedure(2.3). For this simulated basalt water, two stock solutions were required. The first contained sodium salts of carbonate, silicate, sulfate, fluoride, and hydroxide,

---

*Autoclaves were purchased from High Pressure Equipment Company Catalog No. BC-5.

**Starlite Diamond Core Drill (9/64 in. O.D.) purchased from E. A. Kinsey Company.

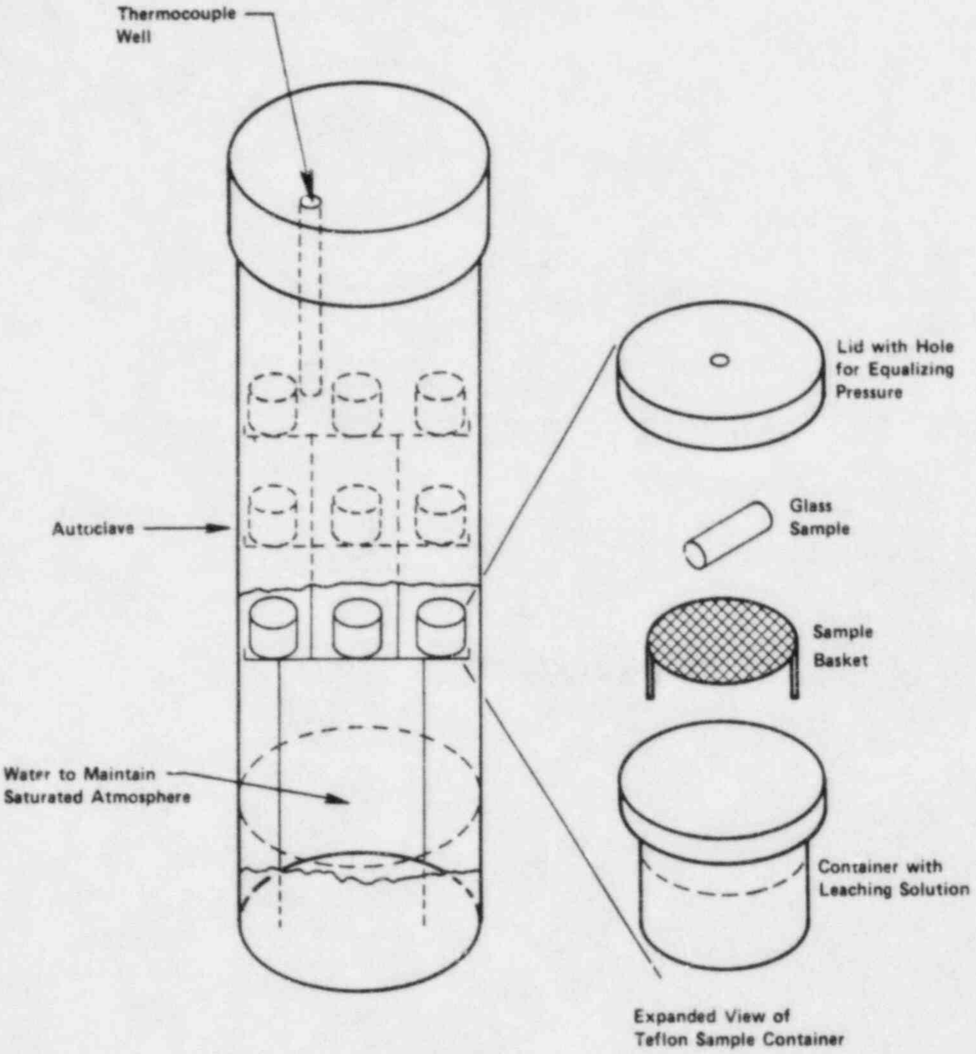

Figure 2.1. Schematic representation of autoclave and TEFLON sample holders.

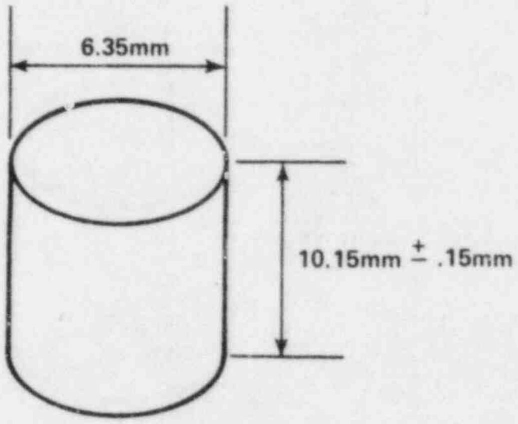

a. S/V = 0.01mm^{-1} Specimen

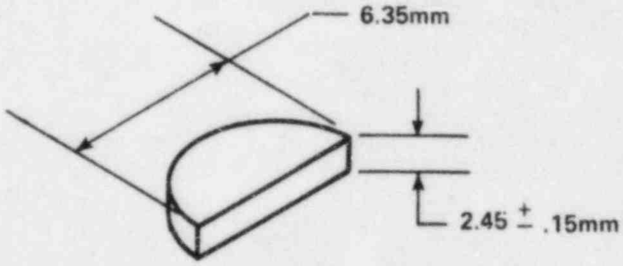

b. S/V = 0.001mm^{-1} Specimen

Figure 2.2. Specimen geometries used in leaching/corrosion experiments.

and the second contained hydrochloric acid and the chloride salts of potassium, calcium, and magnesium. These stock solutions will remain stable for a year if stored in an argon atmosphere. To make the simulated basalt solution, 25 ml of each stock solution was combined in a polyethylene jar. Reagent-grade water was added to make one liter of solution, and the pH was adjusted to 9.75 by adding 0.1 M HCl or 0.1 M NaOH.

After the glass samples were loaded into the TEFLON containers and the TEFLON containers into the autoclave, an argon purge was used to decrease the partial pressure of oxygen. The partial pressure was determined prior to leach testing by pressurizing an autoclave to 6.9 MPa using argon. After five minutes, the autoclave was vented and a sample of the vented gas was analyzed for oxygen content. Repetition of this procedure showed that after five such purges, the partial pressure of oxygen was 1.3 μPa, a sufficiently anoxic condition for the leaching/corrosion experiments. Thereafter, both autoclaves were purged 5 times before each run.

The temperature of each autoclave was monitored by a cold junction compensated, Type K thermocouple connected to a millivolt recorder. The hourly temperature deviations of each autoclave were recorded in the laboratory notebook. These values were then statistically analyzed for the mean temperature and standard deviation about that temperature.

2.1.1.3 Data Collection and Analysis

After the completion of a run, the TEFLON containers were removed from the autoclaves, and the condition of each container was recorded. The glass samples were removed and placed in a drying oven. The TEFLON containers were equilibrated to 30 C, and pH values were recorded.

To ensure that all leached material, except that clinging to the glass specimen, was analyzed, a digestion procedure was developed. This procedure is summarized in Table 2.1. After digestion, samples were submitted for ICAP analysis of boron, calcium, sodium, molybdenum, strontium, and silicon. The fraction of each element, f_i, lost was calculated by:

$$f_i = \frac{(\mu\text{g element in leachate}) - (\mu\text{g element in blank})}{\mu\text{g element in glass sample}} \quad .$$

2.1.2 Preliminary Leaching Experiments

The preliminary leaching experiments were conducted to select appropriate equipment and run duration for the primary leaching/corrosion experiments. Two types of equipment, autoclaves and ovens, were used for conducting the exposure. If both could be used simultaneously, the amount of time needed to conduct the experiments would be greatly reduced. The autoclaves were needed for the high-pressure exposures in the leaching pilot experiment. To evaluate which, if either, is suitable at low pressures, MCC 76-68 glass was exposed to 150 C reagent grade water. The ratio of surface area of the specimen to the volume of solution was 0.01 mm^{-1} in all cases. The replication of weight-loss data as a function of exposure time for 0.25 to 18 days in the oven and a similar fixed exposure in the autoclave has been used to select exposure times and type of equipment to be used in subsequent experiments.

Since two types of equipment, ovens with digestion bombs and autoclaves with TEFLON containers, could be used to conduct the low-pressure experiments, a statistical test procedure was developed to evaluate the data consistency between these two devices. These data indicate that the oven and autoclaves were not necessarily different for the solution concentration of boron, silicon, and molybdenum but were definitely different for the solution concentration of sodium, calcium, and strontium.

Table 2.1. Acid digestion procedure.

1. Evaporate original solution to just below the level of the basket.
2. Add 25 ml ULTREX* HNO_3 + 5 ml perchloric acid, each by its separate pipette.
3. Evaporate to dryness.
4. Add 1 ml H_2SO_4 (20 drops from medicine dropper).
5. Evaporate to dryness.
6. Add 40 ml 50% ULTREX HNO_3 and reagent water (1:1).
7. Evaporate until ~20 ml remains (just below basket).
8. Pour leachate into volumetric flask.
9. Rinse TEFLON container with ~2 ml of 50 volume percent nitric acid in reagent water.
10. Combine rinse with leachate in the volumetric flask.
11. Add enough reagent water to make 25 ml total.
12. Submit for analysis.

*ULTREX is a trademark of the J.T. Baker Chemical Company.

Since high pressure was required in some of the leaching pilot conditions, it was decided to conduct all the experiments in autoclaves. A 15-day, fixed exposure time was used in all cases to ensure both that sufficient time had elapsed to avoid rapidly changing effects brought about by the power-law relationship and that a measurable amount of leaching/corrosion would occur. Furthermore, the results imply that the change to a $t^{1/2}$-dependency has not occurred.

2.1.3 Leaching Pilot Experiment

The purpose of this experiment was to begin the separation and ranking of variables that affect leaching/corrosion of nuclear waste glasses. In this experiment, MCC 76-68 glass, a reference material for which a large data base exists, was used. A statistical experiment with replication was used so that the influence of the main variables and the potential interactions or synergisms between them could be evaluated.

2.1.3.1 Variables and Responses

The variables chosen for the leaching pilot experiment were temperature, pressure greater than the autogenous pressure of water at the experimental temperature, ratio of surface area of glass to volume of solution (SA/V), and solution chemistry. The temperature-pressure conditions for each autoclave exposure are listed in Table 2.2A. The lowest temperature and pressure conditions represent a reference condition. The data at this condition can be compared to many of the data that exist in the literature. The highest temperature and pressure conditions represent a testing condition derived from an extreme temperature and pressure that could develop in a repository in the early years after emplacement with exposure to lithostatic pressure.(2.4) This condition can be considered to be an accelerated test. The last condition shown in Table 2.2A is the statistical midpoint between these two values. The specimens were exposed at each autoclave condition listed in Table 2.2B. They represent SA/V ratios, differing by a factor of 10, and two different water compositions: reagent-grade water (a reference condition), and a simulated basalt water.

The responses to be evaluated at each condition were: change in pH, change in weight, and solution concentrations of silicon, boron, sodium, calcium, strontium, and molybdenum. The solution concentrations of silicon and boron should be indicators of general corrosion at the test conditions. The concentrations of strontium and molybdenum were markers for some of the radionuclides that could be present in a real waste, with strontium representing strontium-90 and molybdenum representing technetium. The analyses of sodium and calcium are a measure of leaching, or selective ion exchange, that may occur. All six of these elements were evaluated through ICAP analyses. For the purpose of this experiment, all material removed from the specimen is considered to be mobile in a repository regardless of its physical form (i.e., ionized species, colloids, or other precipitates). Therefore, the digestion procedure was used to ensure that all precipitates except those that are on the specimen itself were taken into solution to be analyzed by ICAP.

2.1.3.2 Experimental Design

The conditions presented in Table 2.2 are those of a split-plot statistical design, because each autoclave run is a specific combination of temperature and pressure which cannot be independently varied. Therefore, the temperature and pressure are whole-plot factors, and combinations of surface-area-to-volume ratio and solution chemistry that are included in each autoclave run represent a factorial design in that run and are thereby called the split-plot factors. The run order and number of replicates in each case are presented in Table 2.3, and as can be seen from reviewing that table, the experiment was a fully replicated one in which the exposure conditions were alternated between the two autoclaves used in the experiment. In this way, any statistical bias that could occur from using two different autoclaves is minimized. This particular design allows evaluation of all the main effects in temperature, pressure, surface-to-volume ratio, and solution chemistry. Also, this design allows evaluation of the interactive effects among these variables.

Table 2.2. Leaching Pilot Experimental Conditions.

A. Autoclave Conditions

Condition	Temperature, C	Pressure, MPa
A	90	0.1*
B	90	34.0
C	225	2.6*
D	225	34.0
E	170	17.0

*Autogenous Water Pressure

B. Specimens at Each Autoclave Condition.

Specimens	Glass Surface Area to Solution Volume Ratio, mm^{-1}	Water
1	0.01	Reagent
2	0.001	Reagent
3	0.01	Basalt
4	0.001	Basalt

Table 2.3. Run order of leaching pilot experiment.

Run	Autoclave 1*	Autoclave 2*
1	C_8	A_8
2	E_4	C_8
3	A_8	B_8
4	D_8	E_4
5	B_8	D_8

*Subscripts show the number of specimens submitted for chemical analysis. See Table 2.4A for conditions specified by the letters A-E.

2.1.3.3 Results

Tables 2.4 through 2.8 present the results of each experimental condition. The data presented in the tables are the changes in weight and changes in pH, calculated as initial value minus final value, and the solution chemistry, presented as the fraction of material lost. This value was obtained by subtracting the elemental "blank" analysis from the solution analysis and dividing that difference by the original weight of each element in the glass sample, then multiplying by 10^4.

Some of the fraction elemental loss data listed in Tables 2.4 through 2.8 are negative. Such results are not entirely unexpected for samples exposed to the simulated basalt water. In that case, elements removed from the glass could react with elements in the solution to cause precipitation. Alternately, precipitation on cooling to room temperature could remove species from solution. The "blank" should not be subject to these situations and would retain most of the original species in solution. When this blank value is subtracted in the fraction lost calculation, then a negative value would result.

This interpretation is consistent with the weight-loss data. Nine of the weight changes, or 25 percent of the data, for basalt water were positive, indicative of a net weight gain. Of these, four have negative fractions lost for calcium and, usually, sodium. Such data imply that species originally present in the basalt solution have precipitated onto the glass specimen. Also, one of the "blank" measurements for basalt waters had erratic values for sodium and calcium, and these data have not been included in Table 2.5 However, since the basalt water contains no boron or molybdenum, those data in that table are acceptable.

Table 2.4. Leaching pilot experimental results for both replicates at 90 C and 0.1 MPa nominal conditions.

Temperature, C: 88.8 ± 0.2 Pressure, MPa: 0.1
90 ± 0.3* 0.1*

Water	S/V	Δweight, %	ΔpH	Fraction Lost x 100**					
				Si	B	Sr	Mo	Na	Ca
Deionized	.001	-.634	1.157	.968	.115	1.034	1.053	0.000	-4.410
		-.113	2.066	.690	.218	1.199	1.498	1.967	5.860
	.010	-.376	3.250	.050	.067	.075	.318	.450	.583
		-.322	2.893	.043	.174	.086	.401	.347	2.644
Basalt	.001	.455	-.321	.193	.054	.351	.030	-7.400	16.660
		.279	-.415	.740	.052	.517	.715	54.100	1.138
	.010	.094	-1.415	.030	.046	.050	.273	3.423	1.04
		-.172	-.233	.040	.023	.051	.255	2.804	1.03
Deionized*	.001	-1.108	.746	0.000	.022	.875	1.163	0.000	-2.460
		-.850	1.006	0.000	-.010	-.020	0.000	0.000	-1.660
	.010	-.225	1.636	0.000	.029	.049	.517	.315	-.100
		-.301	1.646	.002	.039	.026	.707	.602	-.120
Basalt*	.001	-.802	-.500	.022	.046	.475	.516	0.000	.501
		.926	-.480	-.070	.029	.484	.672	0.000	-2.830
	.010	.065	-.530	-.0022	.015	.035	.145	-2.930	-.250
		.041	-.505	-.0003	.017	-.058	.209	-.610	-.250

*Second replicate.
**Values of 0.000 are analyses that were below detection limit of ICAP but set to zero for statistical treatment.

Table 2.5. Leaching pilot experimental results for both replicates at 90 C and 34.0 MPa nominal conditions.

Temperature, C: 90 ± 0.3 Pressure, MPa: 34
90 ± 0.1* 34*

Water	S/V	Δ weight, %	ΔpH	Fraction Lost x 100**					
				Si	B	Sr	Mo	Na	Ca
Deionized	.001	-2.017	1.306	1.438	.153	1.573	2.129	0.000	1.896
		-1.389	1.261	0.000	.048	1.820	2.174	0.000	1.637
	.010	-.322	1.986	.050	.076	.064	.688	.511	.064
		-.368	2.036	0.000	.154	.040	.795	.635	.067
Basalt	.001	.176	-1.055	.056	.056	.870	.894	--	--
		-.407	-1.050	.058	.039	.844	.827	--	--
	.010	-.101	-.320	.006	.035	.070	.229	6.051	.149
		-.126	-.580	0.000	.047	.086	.415	9.608	.154
Deionized*	.001	-.211	2.015	-1.75	.098	1.464	1.914	2.053	1.305
		-.080	1.945	-1.48	.030	.725	.825	.722	.747
	.010	-.322	2.395	-.090	.021	.178	.467	.632	.226
		.209	2.735	-.110	.069	.022	.697	.640	.110
Basalt*	.001	.018	-.224	-.56	.021	.268	.461	-35.510	-2.410
		.73	-.314	-.36	.019	.252	.686	-36.390	-3.380
	.010	-.0295	-.234	-.02	.017	.064	.415	.857	-.220
		-.0284	-.224	-.02	.005	.062	.360	.660	-.190

*Second replicate.

**Values of 0.000 are analyses that were detection limit of ICAP but set to zero for statistical treatment.

Table 2.6. Leaching pilot experimental results for both replicates at 225 C and 2.6 MPa nominal conditions.

Temperature, C: 229 ± 0.2 Pressure, MPa: 2.6
229 ± 0.1* 2.6*

				Fraction Lost x 100**					
Water	S/V	Δweight, %	ΔpH	Si	B	Sr	Mo	Na	Ca
Deionized	.001	-21.462	2.893	.00419	8.034	.484	36.518	40.152	.360
		-22.290	2.612	-.0044	14.175	.675	20.349	20.355	.352
	.010	-2.313	3.228	.041	.222	.046	3.719	4.130	.046
		-6.031	3.309	.004	.391	.036	3.959	4.555	.046
Basalt	.001	-11.37	-.154	-.01	1.389	.553	23.891	144.89	1.969
		-21.95	-.153	-.065	8.584	.923	33.026	173.38	1.431
	.010	-4.130	-.411	.009	2.018	.122	3.433	11.641	.234
		-7.679	-.583	.031	.296	.081	2.959	2.091	.167
Deionized*	.001	-25.73	1.262	0.000	2.407	1.879	35.527	36.027	.806
		-28.78	1.538	0.000	3.041	1.787	16.862	15.524	1.632
	.010	-2.79	2.181	.002	.538	.071	3.887	4.543	.096
		-2.522	1.272	.004	.639	.059	3.864	4.452	.068
Basalt*	.001	-13.370	-.629	.028	1.625	.346	16.695	-47.400	-6.650
		-10.427	-.639	-.010	1.935	.305	15.821	9.179	-7.000
	.010	-2.084	-.458	.005	.189	.185	3.222	3.378	-.17
		-2.178	-.368	.005	.168	.178	3.441	3.616	-.14

*Second replicate.

**Values of 0.000 are analyses that were below detection limit of ICAP but set to zero for statistical treatment.

Table 2.7. Leaching pilot experimental results for both replicates at 225 C and 34.0 MPa nominal conditions.

Temperature, C: 225 ± 1.2   Pressure, MPa: 34
218 ± 0.4*   34*

				Fraction Lost x 100**					
Water	S/V	Δ weight	Δ pH	Si	B	Sr	Mo	Na	Ca
Deionized	.001	-5.490	2.316	2.347	-.010	2.847	13.954	6.309	.309
		-20.320	2.120	-1.080	1.647	-1.080	29.204	29.870	.110
	.010	-2.38	2.480	-.070	.037	.070	3.576	3.870	.128
		-2.45	2.380	-.070	.064	.049	3.457	3.798	.035
Basalt	.001	-18.830	-.666	-.159	.243	.159	24.300	27.025	-.230
		-21.260	-.996	-1.930	.683	-1.930	30.570	36.654	-.430
	.010	-2.920	-.496	-.100	.177	.102	4.016	5.070	.402
		-2.580	-.496	-.090	.048	-.090	3.794	4.598	-.190
Deionized*	.001	-22.3844	2.275	.290	12.092	28.598	34.329	.892	.734
		-19.1062	2.295	-.040	4.243	22.403	28.607	.171	.472
	.010	-3.14	2.735	.002	.211	.077	2.648	3.211	.168
		-2.05	2.775	.005	.285	.076	3.705	3.630	1.55
Basalt*	.001	-11.24	-.874	.034	2.031	.682	18.270	44.457	0.000
		-13.24	-.894	.429	1.436	.818	26.999	51.500	-.960
	.010	-2.150	-.384	.004	.263	.138	4.616	-3.310	.213
		-1.875	-.324	.019	.339	.135	4.148	5.647	.183

*Second replicate.
**Values of 0.000 are analyses that were below detection limit of ICAP but set to zero for statistical treatment.

Table 2.8. Leaching pilot experimental results for both replicates at 170 C and 17.0 MPa nominal conditions.

Temperature, C: 159 ± 0.1 Pressure, MPa: 17
156 ± 0.7* 17*

				Fraction Lost x 100**					
Water	S/V	Δ weight, %	Δ pH	Si	B	Sr	Mo	Na	Ca
Deionized	.001	-8.290	2.261	-.00046	.874	1.938	8.341	5.118	1.108
		-7.11	2.277	-.00048	1.636	1.408	11.956	9.852	.278
	.010	-1.410	2.341	.002	.448	.022	2.516	2.720	.028
		-1.574	2.433	.0000	.631	.021	2.514	2.741	.010
Basalt	.001	-1.754	.015	.053	.190	.308	3.457	-3.710	-2.920
		-.828	.006	-.010	.285	.350	1.983	-13.230	-2.530
	.010	-.593	-.085	.011	.09	.086	1.083	1.560	.240
		-.610	-.086	.001	.163	.044	1.053	-2.100	-.240
Deionized*	.001	-6.77	1.670	.125	3.098	.910	10.594	8.492	.470
		-8.29	1.940	-.00338	.540	.885	11.525	8.797	.049
		23.62	2.400	.005	.132	.036	3.174	3.411	.043
		-1.61	2.300	.001	.087	.036	2.637	2.637	.060
Basalt*	.001	-6.67	-.486	-.020	.419	10.020	12.046	-1.100	.617
		-6.80	-.556	-.020	.498	10.534	12.894	-1.140	.552
	.010	-1.360	-.426	.0003	.055	2.162	2.237	.010	.050
		-1.320	-.316	.008	.135	2.162	2.615	-.00335	.046

*Second replicate.

**Values of 0.000 are analyses that were below detection limit of ICAP but set to zero for statistical treatment.

The negative values for deionized water are more troublesome because they imply that species are being removed from the TEFLON parts. If this is the case, then the TEFLON cleaning procedure, which includes autoclaving at 120 C for one hour, is not adequate for removing all contamination. These procedures were based on those used by most investigators in this area, but modified to include the autoclaving. On inspection after each run, many of the TEFLON containers showed visible penetration of the leaching solution, especially those exposed to high pressure. This penetration manifested itself in increased opacity of the containers, and in some cases, as visible pockets of liquid. All these containers returned to their original appearance after going through the cleaning procedure. Yet the data imply that residual contamination remained. Therefore, the number of repeat uses of TEFLON containers is limited after exposure to high pressure.

2.1.3.4 Statistical Analysis of Data

The purpose of the main pilot waste-form leaching experiment was to screen a subset of the large number of environmental factors that potentially could affect the extent and rate of leaching of the glass waste form into groundwater. The environmental factors included were: temperature (TEMP), pressure (PRESS), ratio of surface area of glass to volume of solution (SAV), and water type (WATER).

2.1.3.4.1 Weight-Change Data

Because of the obvious and large effect of temperature, the weight-change data for the two different temperatures are analyzed separately. The analysis of variance (ANOVA) for the 90 C data is presented in Table 2.9. In addition to the previously mentioned experimental factors (PRESS, SAV, WATER), an autoclave effect (ACLAVE) has also been included in the model. The top portion of the table contains the ANOVA table corresponding to the entire model being fitted to the data. All main effects and interactions of ACLAVE, PRESS, SAV, and WATER have been included in the model. The "ROOT MSE" value of 0.31 is an estimate of the standard deviation of an individual percentage weight-increase observation.

The bottom portion of the table contains information on the individual main effects and interactions included in the model. Because the ACLAVE and PRESS main effects are whole-plot effects, the corresponding sums of squares are compared to the ACLAVE*PRESS interaction sum of squares for testing purposes. All other effects are compared to the mean square error term of 0.094 from the top portion of the table. The values in the "PR > F" column are the observed significance levels or P-values of the tests of the hypotheses that the corresponding main effect or interaction is not present in the model. A small value (< 0.05) is an indication that the corresponding main effect of interaction is present.

Table 2.9. Analysis of variance table for weight change data at 90 C.

```
TEMP = 90

                                          GENERAL LINEAR MODELS PROCEDURE

DEPENDENT VARIABLE:  WT

SOURCE                  DF    SUM OF SQUARES    MEAN SQUARE    F VALUE     PR > F

MODEL                   15        8.266            0.551         5.84      0.0006

ERROR                   16        1.510            0.094                   ROOT MSE

CORRECTED TOTAL         31        9.776                                    0.307


SOURCE                  DF    TYPE III SS       F VALUE      PR > F

ACLAVE                   1        0.522            0.54       0.597
PRESS                    1        0.119            0.12       0.786
ACLAVE-PRESS             1        0.972           10.30      -0.006
SAV                      1        0.129            1.37       0.260
WATER                    1        3.289           34.86      -0.000
SAV*WATER                1        1.411           14.95      -0.001
PRESS*SAV                1        0.147            1.56       0.230
PRESS*WATER              1        0.021            0.22       0.647
PRESS*SAV*WATER          1        0.013            0.14       0.710
ACLAVE*PRESS*SAV*WAT     6        1.643            2.90       0.041
```

The significant effects for PRESS, SAV, and WATER from Table 2.9 are the WATER main effect and the SAV*WATER interaction. To illustrate these effects, a tree diagram of the percentage weight increase averages is presented in Figure 2.3. The value plotted for each branch is the average response for all observations at the indicated conditions. For example, the average response for the eight observations at TEMP = 90, WATER = BASALT, and SAV = 0.010 is -0.03 percent. The main effect of WATER is illustrated by the first branches which show that the averages for the two water types differ by 0.64 percent. Note that in reagent water there was an average weight loss, while in basalt water there was an average weight gain. The interaction between WATER and SAV is illustrated by the fact that the SAV effect reverses itself for the two water types. The root MSE value of 0.31 from the ANOVA table is graphed in the lower left-hand corner for reference.

It should be noted that there was actually very little weight change activity at 90 C. All of the average values in Figure 2.3 are less than 1 percent. These averages should be contrasted with the averages at 225 C, presented below, which range from 1 to 25 percent.

The ANOVA table for the 225 C data is presented in Table 2.10 and a tree diagram of the average responses is shown in Figure 2.4. The significant effects at 225 C are a SAV main effect and a SAV*WATER interaction. The first branches of the tree in Figure 2.4 illustrate the SAV effect. The only other effect that appears significant is the WATER main effect at low PRESS and low SAV. This effect accounts for the SAV*WATER interaction.

2.1.3.4.2 pH Data

Due to the significantly different initial pH values for the two water types and the fact that the two solutions tend to similar equilibrium pH values, the observations for the two different water types were analyzed separately.

The ANOVA table for the reagent water data is shown as Table 2.11, and a tree diagram of the average responses is presented in Figure 2.5. The significant effects for SAV, TEMP, and PRESS from Table 2.11 are the TEMP main effect and the TEMP-SAV interaction. ACLAVE, TEMP, PRESS, and TEMP-PRESS are whole-plot effects and thus are compared to the ACLAVE*TEMP*PRESS interaction term to test their significance. All other terms are compared to the MSE value of 0.068 from the top portion of the table.

The main effect of SAV is illustrated by the first branches of the tree in Figure 2.5. The interaction of TEMP and SAV is shown in the second set of branches. The effect of temperature at SAV = 0.001 is much greater than the effect at SAV = 0.010 which accounts for the interaction.

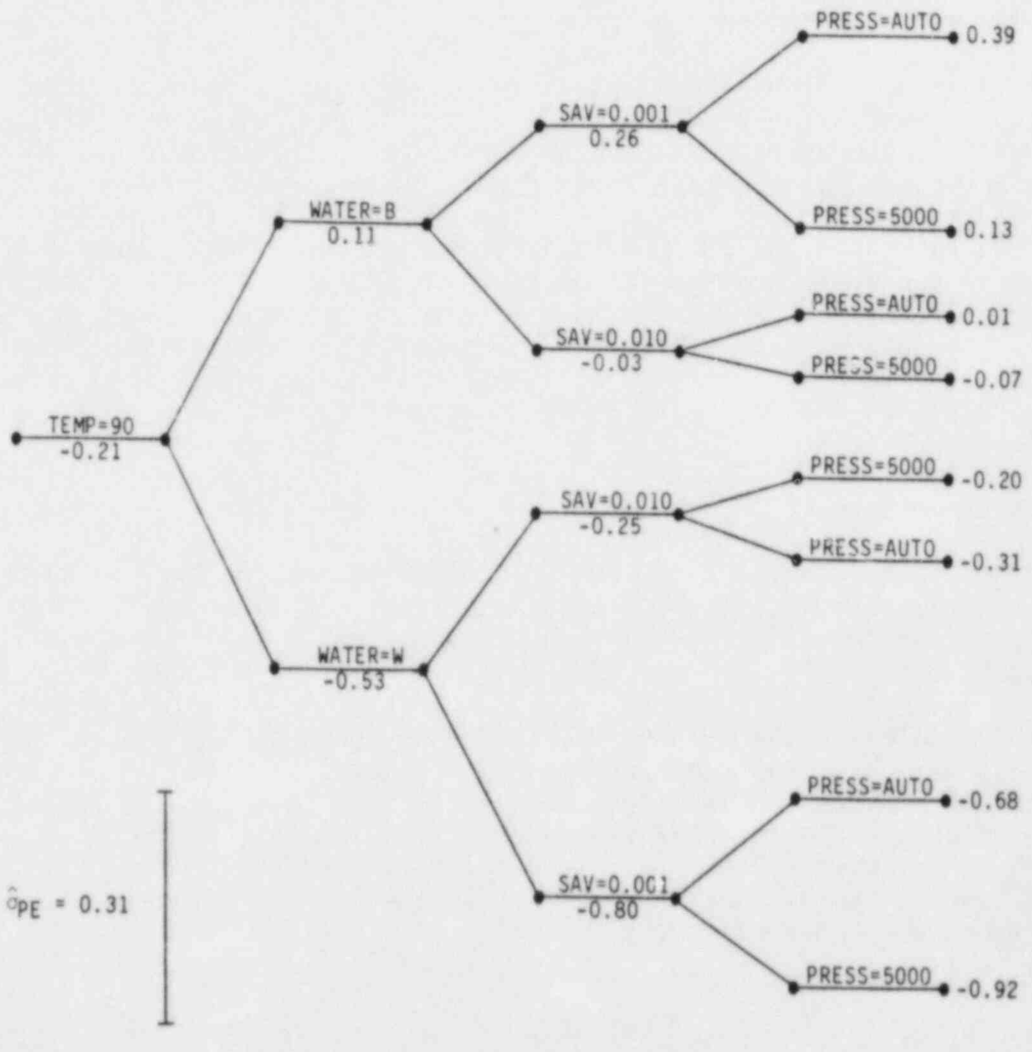

Figure 2.3. Tree diagram of percentage weight increase averages at 90 C.

Table 2.10. Analysis of variance table for weight change data at 225 C.

```
TEMP = 225

                                          GENERAL LINEAR MODELS PROCEDURE

DEPENDENT VARIABLE:  WT

SOURCE                  DF     SUM OF SQUARES     MEAN SQUARE     F VALUE      PR > F

MODEL                   15       2306.656          153.777        11.65        0.0001

ERROR                   16        211.189           13.199                     ROOT MSE

CORRECTED TOTAL         31       2517.844                                      3.63308787


SOURCE                  DF     TYPE III SS         F VALUE     PR > F

ACLAVE                   1         0.955            0.17        0.749
PRESS                    1        46.390            8.44        0.211
ACLAVE*PRESS             1         5.496            0.42        0.528
SAV                      1      1844.224          139.72       -0.000
WATER                    1        43.018          139.72       -0.000
SAV*WATER                1        80.121            6.07        0.026
PRESS*SAV                1         2.244            0.17        0.686
PRESS*WATER              1        51.151            3.88        0.067
PRESS*SAV*WATER          1        41.372            3.13        0.096
ACLAVE*PRESS*SAV*WAT     6       191.686            2.42        0.074
```

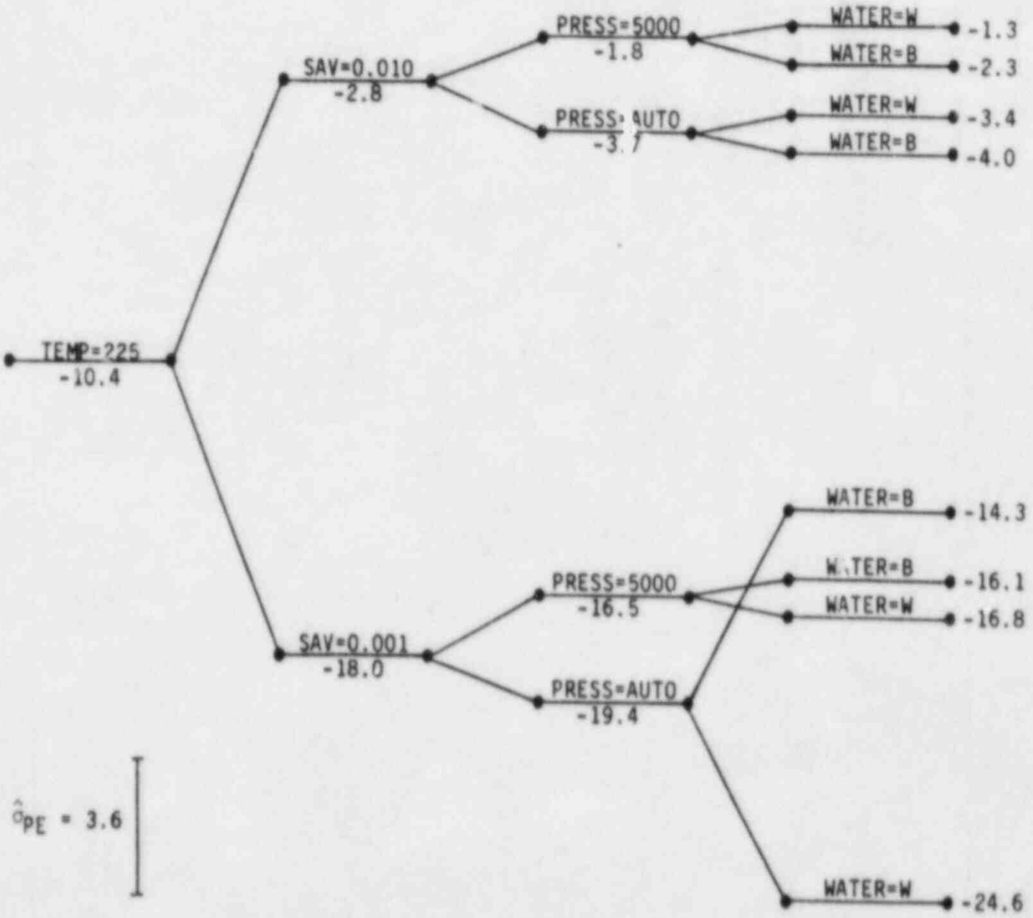

Figure 2.4. Tree diagram of percentage weight increase averages at 225 C.

Table 2.11. Analysis of variance table for change in pH data for reagent water.

```
WATER = W

                                               GENERAL LINEAR MODELS PROCEDURE

DEPENDENT VARIABLE:  PH

SOURCE                   DF      SUM OF SQUARES      MEAN SQUARE      F VALUE        PR > F

MODEL                    15      13.59584300         0.90638953       13.29          0.0001

ERROR                    16       1.09126700         0.06820419                      ROOT MSE

CORRECTED TOTAL          31      14.68711000                                         0.26115931


SOURCE                   DF      TYPE III SS         F VALUE          PR > F

ACLAVE                    1      0.31363200            0.13           0.7396
TEMP                      1      1.79835612            0.76           0.4470
PRESS                     1      0.173167613           0.07           0.8041
TEMP*PRESS                1      0.00130050            0.00           0.0927
ACLAVE*TEMP*PRESS         3      7.08109875           34.61           0.0001
SAV                       1      3.20677812           47.02           0.0001
TEMP*SAV                  1      0.50501250            7.40           0.0151
PRESS*SAV                 1      0.14311250            2.10           0.1668
TEMP*PRESS*SAV            1      0.07125313            1.04           0.3219
ACLAVE*TEMP*PRESS*SA      4      0.30213325            1.11           0.3870
```

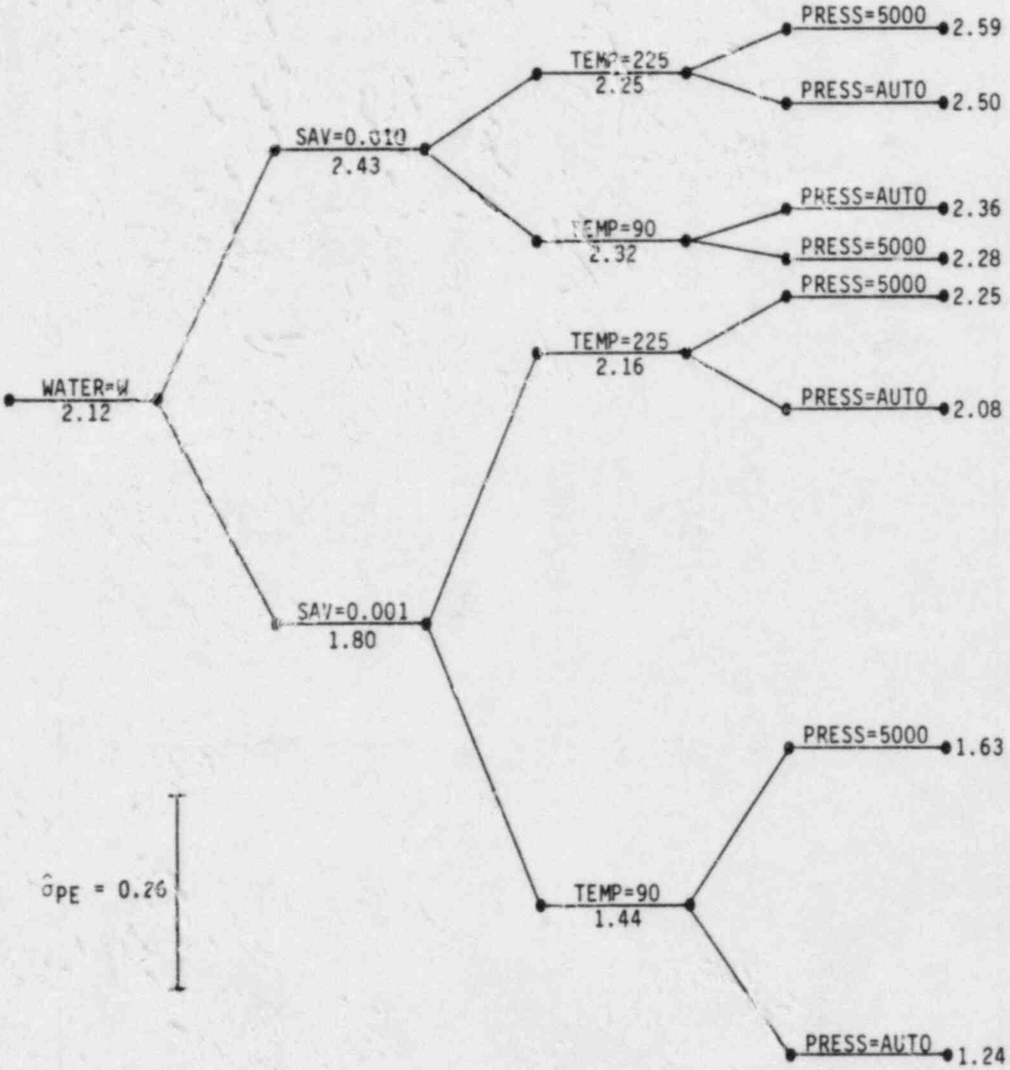

Figure 2.5 Tree diagram of pH increase averages for reagent water.

The ANOVA table for basalt water is presented as Table 2.12, and Figure 2.6 contains a tree diagram of the average responses. Here the only significant effect is the PRESS*SAV interaction. It should be noted that the root MSE value of 0.23 is very large is comparison with the change in pH data for basalt water; that is to say, the relative error in these observations is large. Thus, the only effect to be declared significant is the obvious interaction between PRESS and SAV. The effect of PRESS reverses itself for the two SAV values as illustrated in Figure 2.6.

2.1.3.4.3 Elemental Data

Because of the effect of temperature on the variability of the responses, the elemental responses for the two different temperature levels were analyzed separately. That is, two analysis-of-variance (ANOVA) tables were produced for each element, one at 90 C and the other at 225 C. Sample ANOVA tables are shown as Tables 2.13 through 2.18.

In each case, an autoclave effect (ACLAVE) has been included in the model in addition to the primary experimental factors PRESS, SAV, and WATER. The top portion of the table contains the ANOVA table corresponding to the entire model being fitted to the data. All main effects and interactions of ACLAVE, PRESS, SAV, and WATER have been included in the model. The "ROOT MSE" value is an estimate of the standard deviation of an individual observation.

The bottom portion of each table contains information on the individual main effects and interactions included in the model. Because the ACLAVE and PRESS main effects are whole-plot effects, the corresponding sums of squares are compared to the ACLAVE*PRESS interaction sum of squares for testing purposes. All other effects are compared to the mean square error term from the top portion of the table. The values in the "PR > F" column are the observed significance levels or P-values of the tests of the hypotheses that the corresponding main effect or interaction is not present in the model. A small value (< 0.05) is an indication that the corresponding main effect or interaction is present.

For two of the element-temperature combinations, a tree diagram was formed from the average responses to illustrate the effect of the experimental factors (PRESS, SAV, WATER) on the responses. The combinations illustrated in Figures 2.7 and 2.8 are boron and molybdenum. The value plotted for each branch is the average response for all observations at the indicated conditions. For example, the average percentage of boron lost times 100 for the eight observations at TEMP = 225, SAV = 0.001, and WATER = BASALT is 2.2 as illustrated in Figure 2.7.

Table 2.12. Analysis of variance table for change in pH data for basalt water.

```
WATER = B

                                   GENERAL LINEAR MODELS PROCEDURE

DEPENDENT VARIABLE:  PH

SOURCE                   DF      SUM OF SQUARES     MEAN SQUARE     F VALUE      PR > F

MODEL                    15      1.93588122         0.12905875      2.53         0.0376

ERROR                    16      0.81674750         0.05104672                   ROOT MSE

CORRECTED TOTAL          31      2.75262872                                      0.22593521


SOURCE                   DF      TYPE III SS        F VALUE         PR > F

ACLAVE                    1      0.27993903          2.59           0.2059
TEMP                      1      0.00048828          0.00           0.9506
PRESS                     1      0.05586153          0.52           0.5241
TEMP*PRESS                1      0.14217778          1.32           0.3345
ACLAVE*TEMP*PRESS         3      0.32415784          2.12           0.1383
SAV                       1      0.10158778          1.99           0.1775
TEMP*SAV                  1      0.04255903          0.83           0.3748
PRESS*SAV                 1      0.55836028         10.94           0.0045
TEMP*PRESS*SAV            1      0.00239778          0.05           0.8312
ACLAVE*TEMP*PRESS*SA      4      0.42835188          2.10           0.1286
```

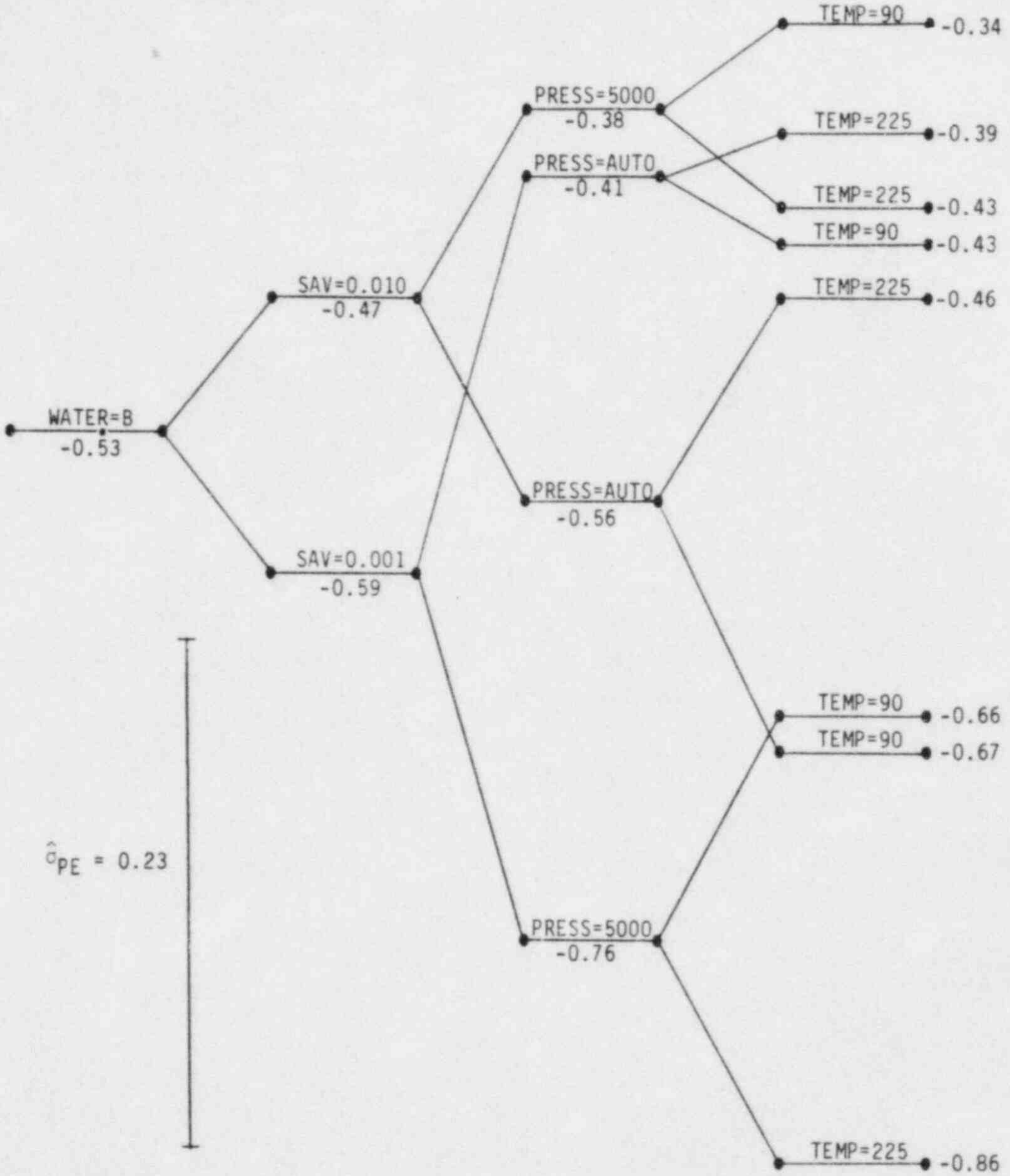

Figure 2.6. Tree diagram of pH increase averages for basalt water.

Table 2.13. Analysis of variance table for silicon at 90 C.

```
TEMP = 90

                                              GENERAL LINEAR MODELS PROCEDURE

DEPENDENT VARIABLE:  SI

SOURCE                   DF      SUM OF SQUARES       MEAN SQUARE      F VALUE        PR > F

MODEL                    15      8.51961327           0.56797422        7.08          0.0002

ERROR                    16      1.28439875           0.08027492                      ROOT MSE

CORRECTED TOTAL          31      9.80401201                                           0.28332829


SOURCE                   DF      TYPE III SS          F VALUE     PR > F

ACLAVE                    1      2.42026951              7.58     0.2217
PRESS                     1      0.94102394              2.95     0.3357
ACLAVE*PRESS              1      0.31910263              3.98     0.0635
SAV                       1      0.00003509              0.00     0.9836
WATER                     1      0.00284088              0.04     0.8531
SAV*WATER                 1      0.00048431              0.01     0.9391
PRESS*SAV                 1      0.71834795              8.95     0.0086
PRESS*WATER               1      0.11310838              1.41     0.2525
PRESS*SAV*WATER           1      0.08155852              1.02     0.3285
ACLAVE*PRESS*SAV*WAT      6      3.92284206              8.14     0.0004
```

Table 2.14. Analysis of variance table for silicon at 225 C.

```
TEMP = 225

                                               GENERAL LINEAR MODELS PROCEDURE

DEPENDENT VARIABLE:  SI

SOURCE                  DF      SUM OF SQUARES     MEAN SQUARE      F VALUE      PR > F

MODEL                   15          2.54289029      0.16951269      0.33         0.9809

ERROR                   16          8.18955989      0.51184749                   ROOT MSE

CORRECTED TOTAL         31         10.73225019                                   0.71543418

SOURCE                  DF      Type III SS         F Value        PR > F

ACLAVE                   1      0.08022115            1.06         0.4902
PRESS                    1      0.00055937            0.01         0.9453
ACLAVE*PRESS             1      0.07544573            0.15         0.7061
SAV                      1      0.00386738            0.01         0.9318
WATER                    1      0.26568223            0.52         0.4816
SAV*WATER                1      0.25307877            0.49         0.4921
PRESS*SAV                1      0.01395327            0.03         0.8709
PRESS*WATER              1      0.24503675            0.48         0.4989
PRESS*SAV*WATER          1      0.23362201            0.46         0.5089
ACLAVE*PRESS*SAV*WAT     6      1.37122363            0.45         0.8370
```

Table 2.15. Analysis of variance table for boron at 90 C.

```
TEMP = 90

                                          GENERAL LINEAR MODELS PROCEDURE

DEPENDENT VARIABLE:  B

SOURCE                  DF     SUM OF SQUARES      MEAN SQUARE       F VALUE       PR > F

MODEL                   15       0.06203300        0.00413553        2.72          0.0277

ERROR                   16       0.02431300        0.00151956                      ROOT MSE

CORRECTED TOTAL         31       0.08634600                                        0.03898157


SOURCE                  DF     Type III SS              F Value      PR > F

ACLAVE                   1     0.02475313                14.47       0.1637
PRESS                    1     0.00007200                 0.04       0.8712
ACLAVE*PRESS             1     0.00171112                 1.13       0.3044
SAV                      1     0.00076050                 0.50       0.4895
WATER                    1     0.01911013                12.58       0.0027
SAV*WATER                1     0.00013613                 0.09       0.7686
PRESS*SAV                1     0.00018050                 0.12       0.7348
PRESS*WATER              1     0.00004513                 0.03       0.8653
PRESS*SAV*WATER          1     0.00001512                 0.01       0.9218
ACLAVE*PRESS*SAV*WAT     6     0.01524925                 1.67       0.1919
```

Table 2.16. Analysis of variance table for boron at 225 C.

```
TEMP = 225

                                                GENERAL LINEAR MODELS PROCEDURE

DEPENDENT VARIABLE:  B

SOURCE                     DF     SUM OF SQUARES     MEAN SQUARE      F VALUE       PR > F

MODEL                      15       311.99353100     20.79956873      4.21          0.0034

ERROR                      16        78.95557300      4.93472331                    ROOT MSE

CORRECTED TOTAL            31       390.94910400                                    2.22142371


SOURCE                     DF     Type III SS           F Value       PR > F

ACLAVE                      1        1.34316050            0.02       0.9027
PRESS                       1       14.93584512            0.26       0.6980
ACLAVE*PRESS                1       56.65269013           11.48       0.0038
SAV                         1      103.93215312           21.06       0.0003
WATER                       1       22.09795200            4.48       0.0504
SAV*WATER                   1       25.94520612            5.26       0.0357
PRESS*SAV                   1        7.78940450            1.58       0.2270
PRESS*WATER                 1        0.00035112            0.00       0.9934
PRESS*SAV*WATER             1        0.04470050            0.01       0.9254
ACLAVE*PRESS*SAV*WAT        6       79.25206788            2.68       0.0540
```

Table 2.17. Analysis of variance table for molybdenum at 90 C.

```
TEMP = 90

                                             GENERAL LINEAR MODELS PROCEDURE

DEPENDENT VARIABLE:  MO

SOURCE                  DF    SUM OF SQUARES    MEAN SQUARE    F VALUE      PR > F

MODEL                   15     7.83498650       0.52233243      4.93        0.0015

ERROR                   16     1.69671700       0.10604481                  ROOT MSE

CORRECTED TOTAL         31     9.53170350                                   0.32564522


SOURCE                  DF    Type III SS         F Value     PR > F

ACLAVE                   1    0.26645000             2.98     0.3343
PRESS                    1    0.95358050            10.66     0.1892
ACLAVE*PRESS             1    0.08946450             0.84     0.3720
SAV                      1    2.35770613            22.23     0.0002
WATER                    1    2.13417800            20.13     0.0004
SAV*WATER                1    0.42458112             4.00     0.0627
PRESS*SAV                1    0.28918013             2.73     0.1182
PRESS*WATER              1    0.20801250             1.96     0.1804
PRESS*SAV*WATER          1    0.15764113             1.49     0.2404
ACLAVE*PRESS*SAV*WAT     6    0.95419250             1.50     0.2406
```

Table 2.18. Analysis of variance table for molybdenum at 225 C.

```
TEMP = 225

                                             GENERAL LINEAR MODELS PROCEDURE

DEPENDENT VARIABLE:  MO

SOURCE                   DF      SUM OF SQUARES       MEAN SQUARE     F VALUE       PR > F

MODEL                    15      3747.02552897       249.80170193     7.39          0.0001

ERROR                    16       541.10511850        33.81906991                   ROOT MSE

CORRECTED TOTAL          31      4288.13064747                                      5.81541657

SOURCE                   DF      Type III SS             F Value      PR > F

ACLAVE                    1        28.16063628             1.23       0.4669
PRESS                     1         0.26553828             0.01       0.9317
ACLAVE*PRESS              1        22.86739378             0.68       0.4230
SAV                       1      3497.46933903           103.42       0.0001
WATER                     1         5.30483878             0.16       0.6973
SAV*WATER                 1         6.71336403             0.20       0.6619
PRESS*SAV                 1         1.07567778             0.03       0.8607
PRESS*WATER               1        30.74260078             0.91       0.3546
PRESS*SAV*WATER           1        12.80306503             0.38       0.5470
ACLAVE*PRESS*SAV*WAT      6       141.62307519             0.70       0.6552
```

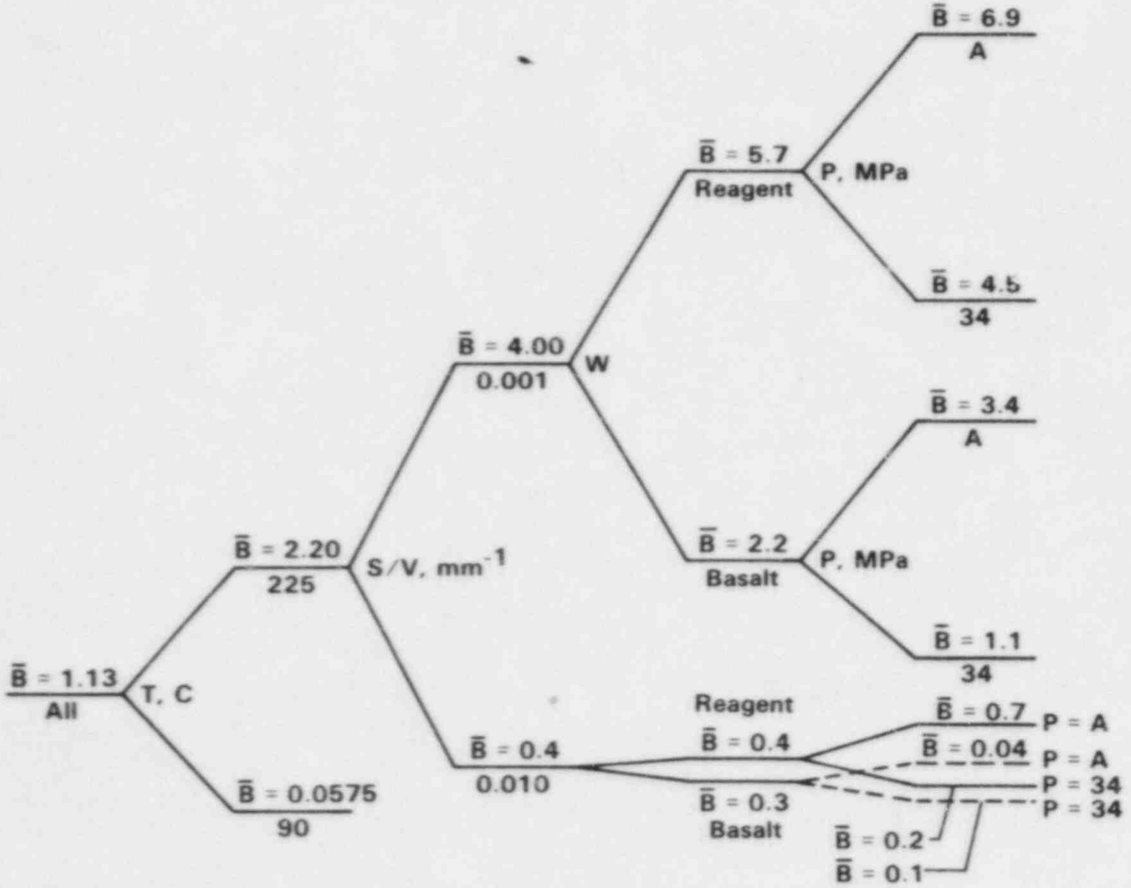

Figure 2.7. Tree diagram showing effect of experimental factors on boron.

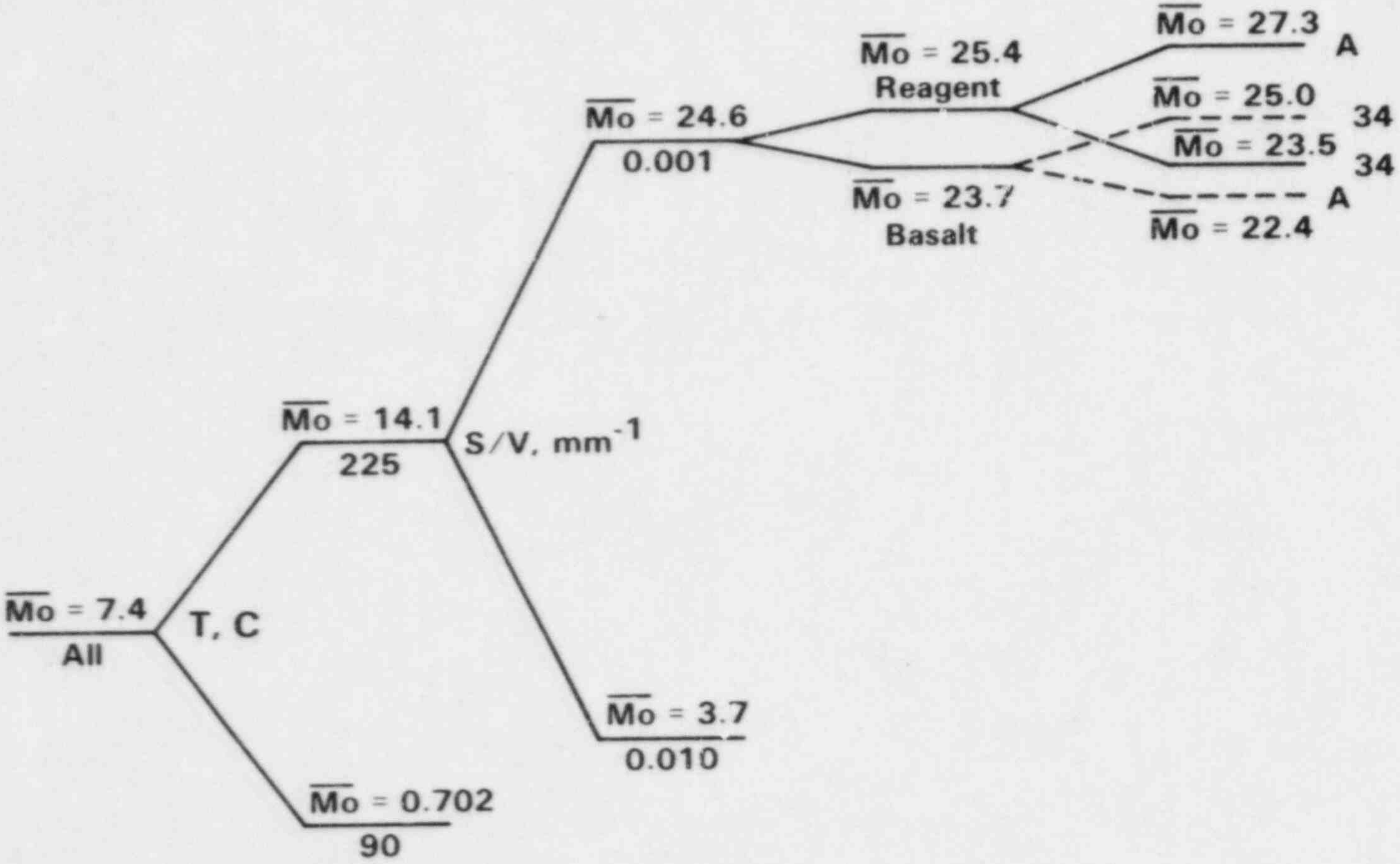

Figure 2.8. Tree diagram showing effect of experimental factors on molybdenum.

Summarizing the statistical analyses of the elemental data:

Silicon. All the average responses are smaller than 0.5. The only significant effect at either temperature was a PRESS*SAV interaction at 90 C.

Boron. At 90 C there is a significant WATER effect; however, all the average responses are smaller than 0.1 in magnitude. At 225 C, there are significant SAV and WATER effects as well as a significant SAV*WATER interaction. These effects are illustrated in Figure 2.7. The first branch of the tree illustrates the SAV main effect. The fact that there appears to be a large WATER effect at SAV = 0.001 and no WATER effect at SAV = 0.010 accounts for the SAV*WATER interaction.

Molybdenum. At 90 C there are significant SAV and WATER effects; however, all the average responses are smaller than 1.8. At 225 C there is a very strong SAV effect which is illustrated by the first branch in Figure 2.8.

Sodium. At 90 C, there are significant SAV and WATER main effects and SAV*WATER and PRESS*WATER interactions. SAV appears to have a strong effect in basalt water and PRESS appears to have a strong effect in basalt water at SAV = 0.001.

At 225 C, the SAV and WATER main effects are significant in addition to the SAV*WATER interaction. The fact that WATER has an effect at SAV = 0.001 but not at SAV = 0.010 accounts for the SAV*WATER interaction.

Calcium. At 90 C there are no significant effects, and all the average responses are smaller than 4. Actually, except for one value (3.86), all the average responses are smaller than 1.4. The large 3.86 value appears to be due to the one observed response exceeding 16. At 225 C, all the effects involving only SAV, WATER, and PRESS are significant; however, all the average responses are smaller than 0.8 in magnitude except for a single response of -2.56.

Strontium. At 90 C SAV, WATER, SAV*WATER, and PRESS*SAV are significant but all average responses are smaller than 1.4 in absolute value. At 225 C there are no significant effects and all average responses are small.

2.1.3.5 Conclusions

A number of conclusions can be drawn from the split-plot experiment in temperature, pressure, surface-to-volume ratio, and water chemistry. First, the effect of temperature is large and nonlinear, as illustrated in Figure 2.9. Exposure of the waste form to temperatures above ~125 C will result in significant removal of material from it. Second, the effect of change in surface area of glass to solution volume ratio for a given period of time is to change material removal proportionally.

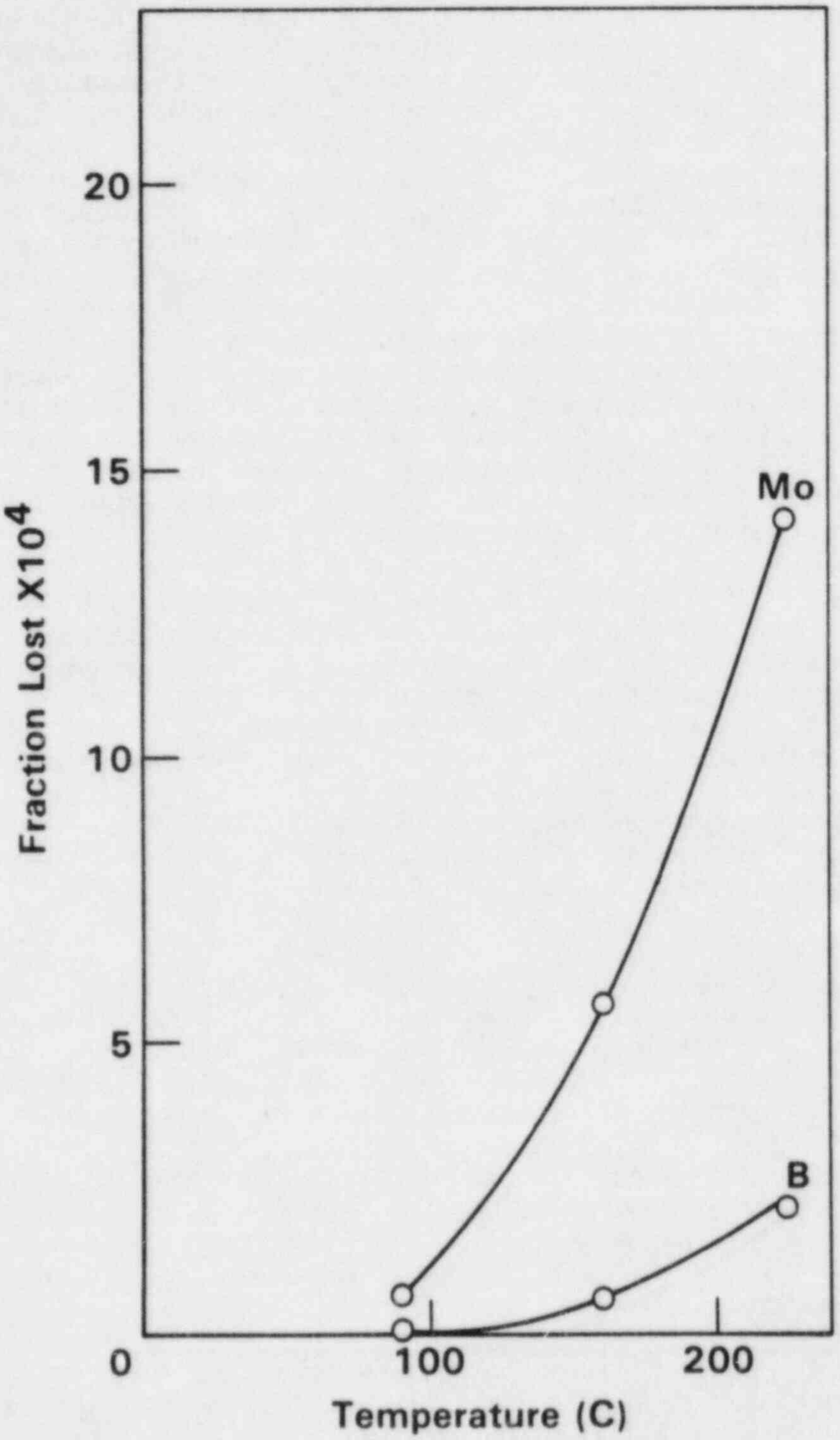

Figure 2.9. Nonlinear temperature relationship for boron and molybdenum.

Decreasing this ratio by a factor of 10 increases material removal rate, at least for boron and molybdenum, by a factor of 10. The influence of water chemistry is also important. In the cases tested, both solutions, reagent grade water and simulated Grande Ronde basalt water, quickly achieved a common pH of approximately 9.3, which seems to be the natural "buffering" level for MCC 76-68 glass. (Also, the reagent water is a more severe exposure condition.) Run-to-run variation was higher than within-run variation. This is a result similar to that seen in the MCC workshop.(2.5) As discussed by Kingston, et al, this result may well be caused by an intrinsic lack of homogeneity in the MCC 76-68 glass bars.(2.5) Finally, the continuous contact between the glass specimen and corroding solution may introduce unaccounted variation into the experiment, because reactions that occur during heating to experimental conditions and cooling from them are counted as influences at the experimental temperature. Also, material that precipitates onto the glass specimen cannot be digested, so it is not counted as part of the material removed from the specimen. This may be an especially significant problem in simulated repository water.

One of the goals of this experiment was to evaluate the interactive effects among the tested variables. The statistical analyses (ANOVA) did reveal a number of interactive effects. However, the magnitude of these interactions were small in comparison to the magnitude of the primary effects of temperature, surface-to-volume ratio, and water chemistry. Therefore, these interactions have a relatively small effect on material removal. Since the pressure effect only shows statistical significance as an interaction with the autoclave effect, and then only in a few cases (calcium at 225 C, sodium at 90 C and 225 C, boron at 225 C), it is considered a minor effect.

2.1.4 Future Work

During the coming year, interaction between modelers/experimenters and statisticians will continue with the purpose of updating and documenting plans and results for current experiments and planning future experiments. The following specific activities are expected:

(1) Design and conduct an experiment to study the influence of glass/water contact during the heatup and cooldown periods of leach testing on the measured elemental-mass loss and surface-layer formation. Statisticians will help analyze the data generated.

(2) Design and conduct an experiment to evaluate a proposed leaching/corrosion model. Statisticians will help analyze the data generated.

(3) Design and initiate an experiment to identify groundwater components that are likely to affect leaching of the waste form. Candidate components include organic acids and dissolved fluoride. Statisticians will analyze data generated by the experiment and assess the need for follow-on experiments.

(4) Design and conduct an experiment to study the extent and rate of leaching of a glass waste form into groundwater as a function of the volume fraction of crystallization. Statisticians will analyze the data generated by the experiment and assess the need for follow-on experiments.

2.2 Devitrification Evaluation for Glass Waste Forms

A detailed thermal analysis conducted in the first year of this program has shown that the cooling rate for nuclear waste glasses cast from the melt is exceedingly slow. Prolonged exposure of the glass at elevated temperatures is favorable for devitrification, the conversion of the material from the amorphous form to a partially crystalline form. If this crystallinity should occur to a volume fraction of 10 percent or more, then breakage and enhanced leaching could result. This situation has prompted an evaluation of the potential for devitrification of a full-sized defense waste form using cooling data based on thermal calculations using the TRUMP code.(2.6)

2.2.1 Methods

To calculate the volume fraction crystallized with temperature in a full sized waste form, the method developed by Onarato and Uhlmann(2.7) has been used. The volume fraction crystallized is represented by the following equation:

$$V_c = \int_{R^*}^{R_{max}} \frac{4}{3} \pi \psi R^3 \, dR$$

In this equation, ψ represents the crystal distribution function originally developed by Hopper and Uhlmann(2.8) and modified by Onarato and Uhlmann, and R represents the radius of the growing crystal. The crystal distribution function is calculated by the following equation:

$$\psi = \frac{I_\upsilon \ T(t)}{U \ T(t) \ - dR^*/dt}$$

In this equation, $[I_\upsilon \ T(t)]$ represents the nucleation rate, U T(t) represents the crystal growth rate, and dR*/dT represents change in the size of the critical nucleus with time. In these equations, the notation T(t) represents the change in temperature with time. In the previous equation, the integration is accomplished from R^* to R_{max}. The radii are determined from the crystal growth rate function as follows:

$$R = \int_{t_o}^{t} U\ T(t)\ dt + R^*_{t_o}$$

To accomplish this analysis for full-size waste form, the cylindrical shape of the waste form is subdivided into a number of cells at which the temperature change with time is determined by TRUMP calculations. These thermal data are then used to compute the volume fraction crystallized using the previously described equations and a computer code using the logic shown in Figure 2.10. For each cell, the temperature interval between T_g and T_ℓ, the range over which devitrification can occur, is divided into 100 equal intervals. Then, the previously described equations are used to calculate the volume fraction crystallized in each cell and the final radius of the crystals in that cell. Next, the volume percent crystallized is calculated by a rotational integration about the waste form's centerline, and the course of crystallization with time is determined by summing these variables over the time increments used in the analysis.

The integrations shown in the previous equations are accomplished with spline techniques.† The derivative of the critical nucleus size is calculated by taking spline derivatives of the radius size as a function of time, t. These radius sizes are calculated from the following equation at each temperature T = T(t):

$$R^* = \frac{0.5\ Vm^{1/3} Te}{No^{1/3} (T_\ell - T) T}$$

In this equation, Vm is the molar volume and No is Avogadro's number.

2.2.2 Data Sources

A number of separate data sources were used to conduct this devitrification evaluation. The data for the TRUMP calculation of heat flow are available and will be described briefly in the following section. Data for the crystallization approximation were difficult to obtain, and a number of approximations had to be developed.

---

†IMSL Library.

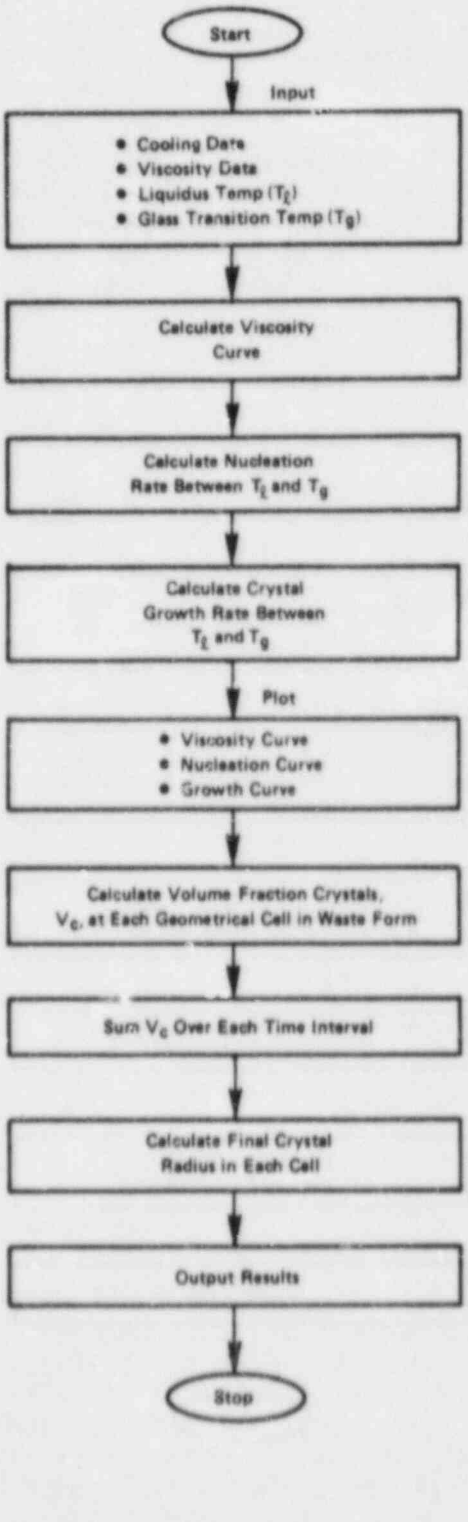

Figure 2.10. Simplified logic flow chart for devitrification analysis.

2.2.2.1 TRUMP Data

TRUMP(2.6) is a sophisticated computer code used to perform heat flow calculations for various geometries. In the case of the defense waste form, the cylinder size was 0.64 meters in diameter by 2.48 meters high of glass, poured into a canister 1 centimeter thick and 2.72 meters high. For the calculation, the entire volume of glass, in a cylindrical coordinate system, was subdivided into 186 cells approximately 6 centimeters x 8 centimeters in cross section. The whole of the glass volume was assumed to begin its cooling at 1150 C by radiation to air and conduction to the floor on which the waste form sat, both of which were infinite sinks. The calculation continued until the waste form temperature was approximately 200 C or lower throughout. The thermal data used for these calculations are shown in Table 2.19.

Table 2.19. Glass thermal data used for TRUMP calculations.

Temperature °C	Density (ρ), g/cc	Heat Capacity (C_p), cal/gm°C	Thermal Conductance (k), cal/cm hr°C
100	2.813	0.224	8.15
400	2.786	0.309	11.77
700	2.499	0.345	15.77
1000	2.204	0.363	30.43
1100	2.115	0.367	34.35
1200	2.031	0.371	45.09

The cooling curves and cooling rate curves are shown in Figure 2.11. Also plotted in that figure are the cooling data for a similar location in a full-sized waste form of similar composition.(2.9) These data are referenced to T_ℓ shown in that graph. The real cooling rate data closely match the calculated cooling curve, indicating that the TRUMP calculation is a very close facsimile to real cooling. More importantly, this close match indicates that cooling rate data generated by spline differentiation of the cooling curves is a very good approximation of actual cooling rates occurring during canister cooling.

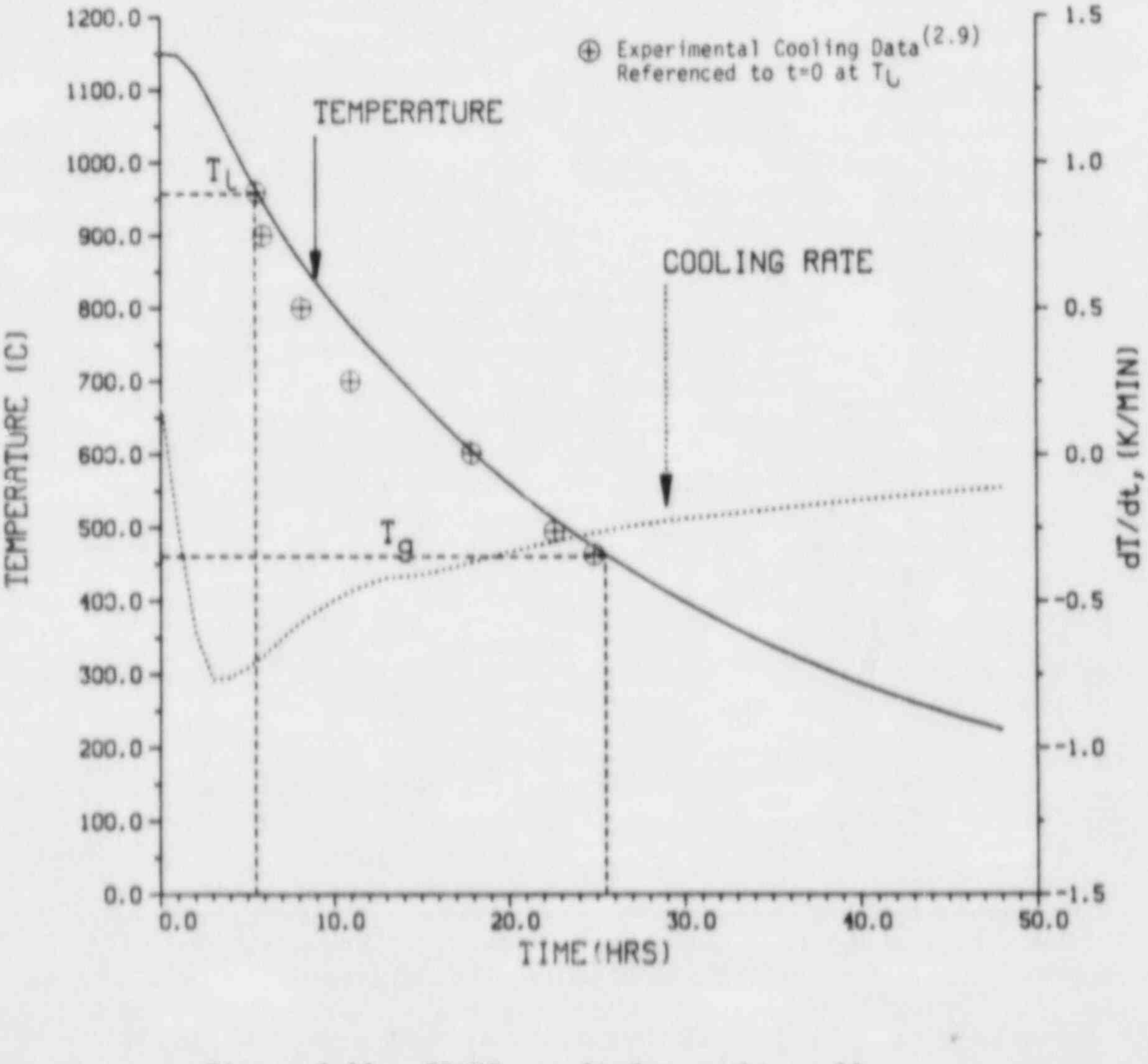

Figure 2.11. TRUMP result for center cell.

2.2.2.2 Crystallization Data

Neither growth rate data nor nucleation data are available for the glass composition in this particular waste form. Therefore, approximations were used in both instances. To approximate the crystal growth rate, u, the classical equation was used:

$$U \approx \frac{kT}{3\pi a_0^2 \eta} \left\{1 - \exp\left[\frac{-\Delta H_f (T_\ell - T)}{RTT_\ell}\right]\right\}$$

In this equation, k is the Boltzmann constant; T, the calculation temperature; ΔH_f, the heat of fusion of the crystallizing phase; T_ℓ, the glass liquidus temperature; a_0, the molar thickness of the growing crystal layer; η, the viscosity; and R, the gas constant.

A recent paper by Bickford and Jantzen$^{(2.10)}$ indicates that the primary phases crystallizing in this glass are spinel and acmite. The data used to accomplish this crystal growth calculation are listed in Table 2.20. As can be seen from reviewing that table, the viscosity data do not extend over the entire range of T_ℓ to T_g and had to be extrapolated to include that range. This extension was accomplished by first fitting a Fulcher equation to the viscosity data in Table 2.20 using standard techniques applied for ASTM reference materials. The Fulcher equation was used to extrapolate the viscosity data to the viscosity of 10^9 poise. The glass transition temperature, T_g, shown in Table 2.20, was assigned the viscosity value 10^{13} poise. Then, all of the viscosity data, the data provided in Table 2.20, the data extrapolated by the Fulcher equation, and the value at the glass transition, were used to accomplish a spline interpolation of viscosity in the crystal growth calculations. Figure 2.12 presents this spline fit to the data along with the actual and extrapolated data used to obtain that curve. As can be seen in Figure 2.12, the methods applied give a very good approximation for the viscosity curve over the range needed for the crystallization calculations.

The nucleation frequency, I_v, also presents a difficult data problem. One way of obtaining this value is to use the classical calculation as defined by the following equation:

$$I_v \approx 10^{34} \exp\left[\frac{-1.024\ T_\ell^5}{T^3 (T_\ell - T)^2}\right]$$

This equation presents a nucleation frequency that is monotonically decreasing with increasing temperature, and this value is in error near the glass transition. An alternative method for obtaining the nucleation rate is calculation from experimental data using the Avrami equation.

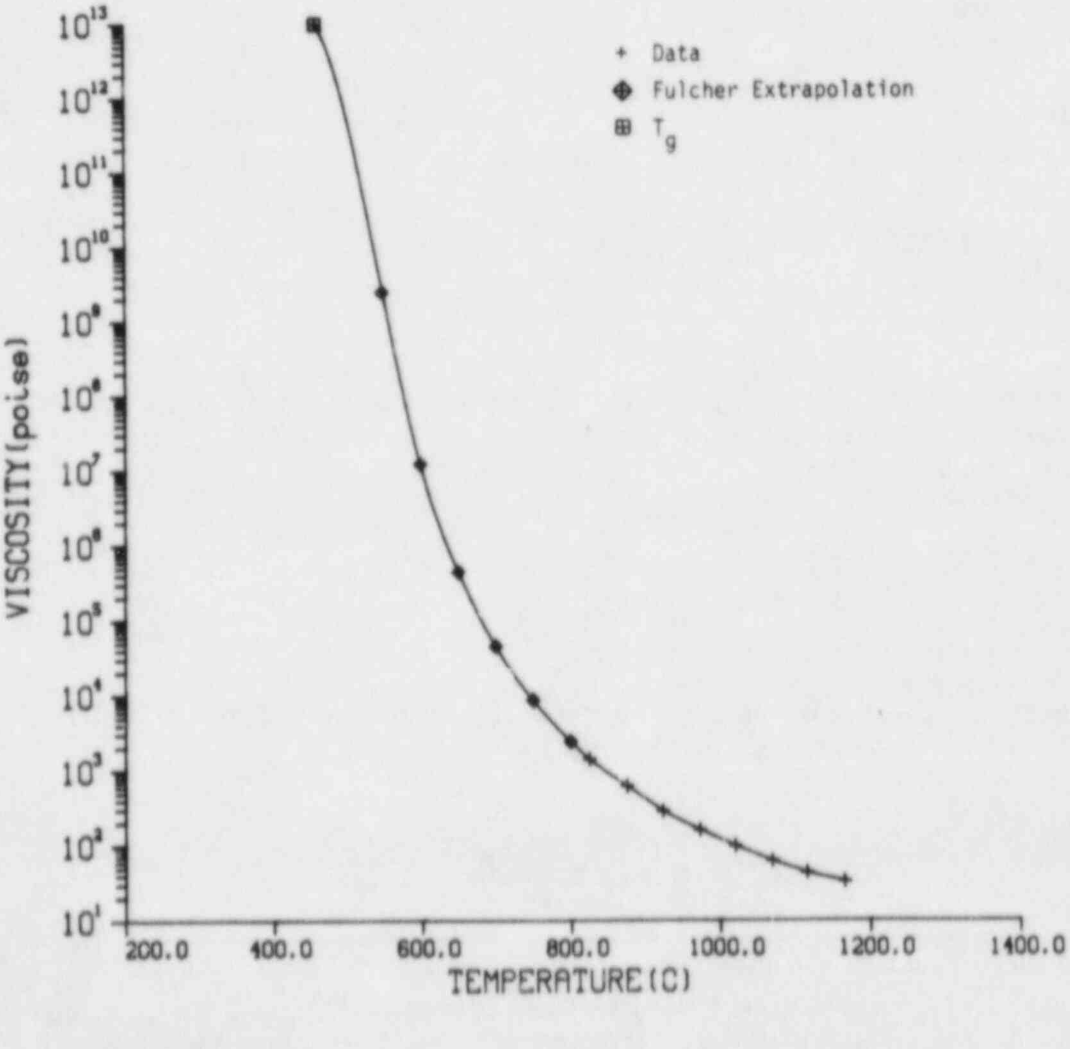

Figure 2.12. Spline fit to the viscosity curve for crystal growth calculations.

Table 2.20. Data used for crystal growth calculations.

T_ℓ = 957 C; a_o = 0.8 nm

Temperature T, ^oC	Viscosity η, poise
460*	10^{13}
825	1400
875	620
923	290
973	160
1020	98
1069	62
1116	43
1166	33

*T_g calculated from knee in plot of $1/\rho$ vs. T.

A recent publication(2.10) presents volume fraction crystallization data with time and temperature that can be used to solve for I_v in the following equation:

$$V_c = 1 - \exp\left(- \frac{\pi}{3} I_v U^3 t^4\right)$$

Then, according to Uhlmann's treatment, the following equation should provide the approximate nucleation rate:

$$I_v \approx \frac{C}{\eta} \exp\left(\frac{-B}{\Delta T_r^2 \; T_r^3}\right)$$

where, $T_r = T/T_\ell$ and $\Delta T_r = 1 - T_r$. The parameters C and B in this equation may be obtained by using viscosity data in a linear regression of $I_v\eta$ against the inverse of $\Delta T_r{}^2 T_r{}^3$.

2.2.3 Results

The results of the crystal growth and nucleation calculations are presented in Figure 2.13. Using the previously discussed data, the growth rate curve takes the expected shape. The rate is highest at a temperature just below T_ℓ and decreases slowly to approximately 750 C. At that point, the growth rate decreases rapidly until termination in invoked at Tg.

The nucleation rates are also presented in Figure 2.13. The solid line represents the value calculated from the classical equation. This rate is forced to a constant value above 860 C to avoid calculation errors that result from generating exceedingly small numbers above that temperature. The dashed line represents the value calculated from available data using the second equation on page 2-44. The data used for this solution(2.10) are for a case of heterogeneous nucleation, and as can be seen in Figure 2.13, it results in a different nucleation rate curve than that derived from the classical, homogeneous nucleation equation. At approximately 680 C, the two nucleation rate curves are very nearly the same.

Both sets of nucleation calculations were used with the crystal growth calculation to solve for the volume fraction crystallized in each cell. When the classical nucleation rate solution was used, the volume fraction crystallized increased slowly to about 5 percent at 780 C. In the next time step, the volume fraction changed immediately to very large values near 750 C. A similar result occurred when the calculated nucleation rate curve derived from literature data was used, except that the rapid changes occurred between 910 C and 880 C. These temperature ranges are associated with the "knee" in the respective nucleation rate curves shown in Figure 2.13. In other words, the lower temperature portions of both curves are unrealistically high. Obviously, these results make evaluation of the fraction of crystallization in the entire waste form intractable.

An alternate means of partially assessing the severity of the crystallization problem is to compare the results of published TTT curves to the temperature profiles generated by TRUMP. The data published by Bickford and Jantzen(2.10) can be used for this purpose. The temperature at the nose of the TTT curve, T_n, and the time needed to reach that temperature, t_n, can be used to approximate the cooling rate for avoiding a fixed fraction of crystallization by using the following equation:

$$\frac{dT}{dt} \approx \frac{T_n - T_\ell}{t_n}$$

For the referenced data, this value is -3.5 K/min for avoiding no more than 1 percent crystallization. For each cell, the cooling curve generated by TRUMP can be used to calculate the instantaneous derivative

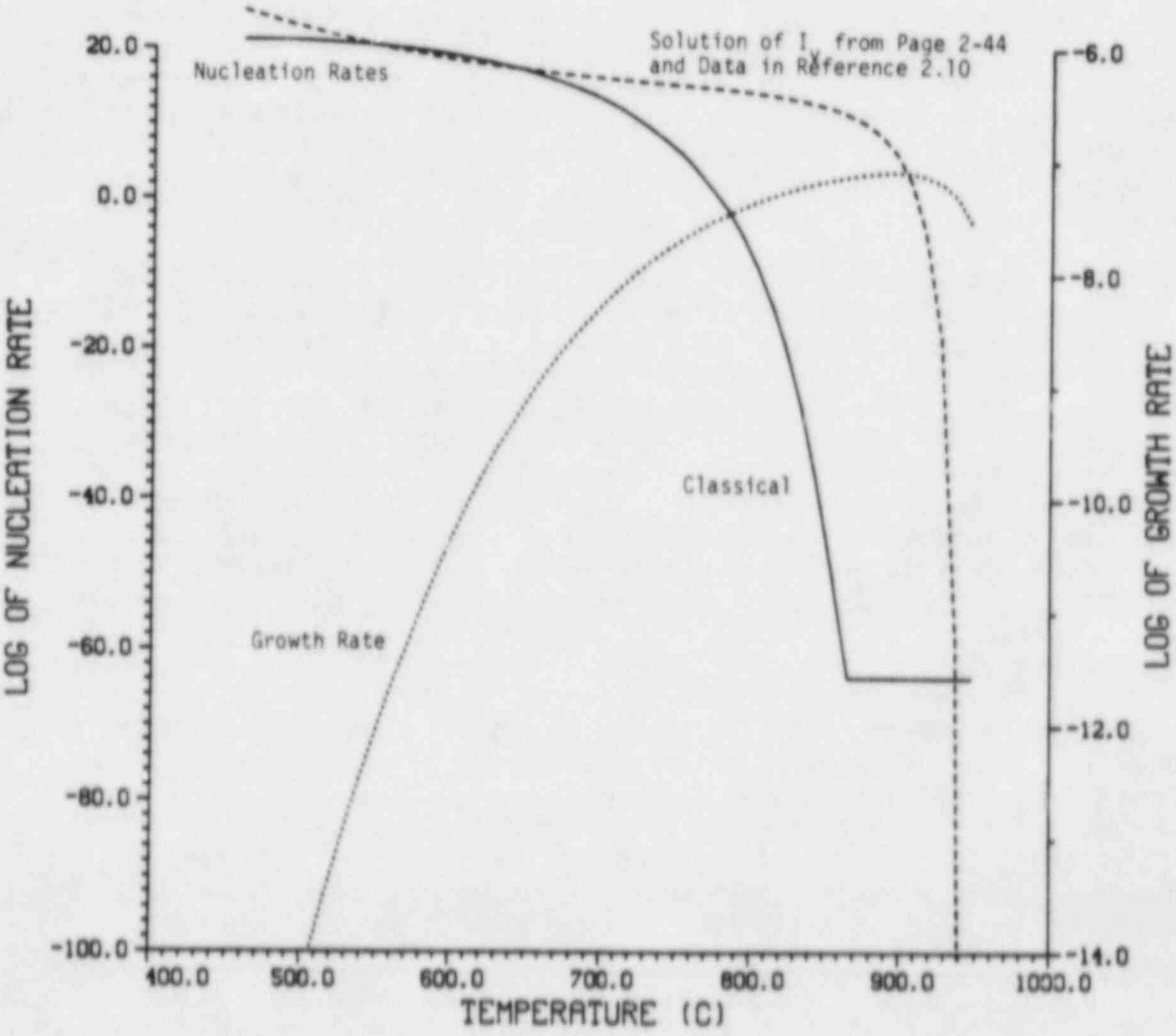

Figure 2.13. Comparison of crystallization data used in devitrification calculation.

using spline techniques.* These cooling rates can then be compared to that from TTT estimates to assess the potential severity of the devitrification problem.

The results of these calculations are presented in Figures 2.14 through 2.16 for the centerline and outside wall cells for cells in the top, middle, and bottom of the waste form. In these figures, the dotted line represents the critical cooling rate for avoiding approximately 1 percent crystallinity. Some peaks in these derivative curves are artifacts of the numerical techniques and do not influence the interpretation. Presented in Table 2.21 are the times required to reach the glass transition and liquidus temperature in each of these cells.

These data are taken directly from the TRUMP cooling curves for each cell.

Table 2.21 Time required to reach T_g and T_ℓ for selected cells in the waste form.

Cell Position	Hours to Reach: T_g	T_ℓ
Top of waste form:		
Centerline	5.25	1.0
Outside surface	2.50	0.5
Middle of waste form:		
Centerline	20.5	5.5
Outside surface	9.5	0.6
Bottom of waste form:		
Centerline	5.25	0.7
Outside surface	2.60	0.5

The cooling rates for all of these cells are generally less than the critical rate. Except for the more centrally located cells, the time spent between T_ℓ and T_g while cooling at these slow rates is brief: less than an hour for the outside cells at the bottom and top of the waste form, and only a few hours for the centerline cells in the top and bottom. The interior cells cool at very slow rates compared to the critical value and spend approximately 10 hours cooling at these slow rates.

---

*IMSL library.

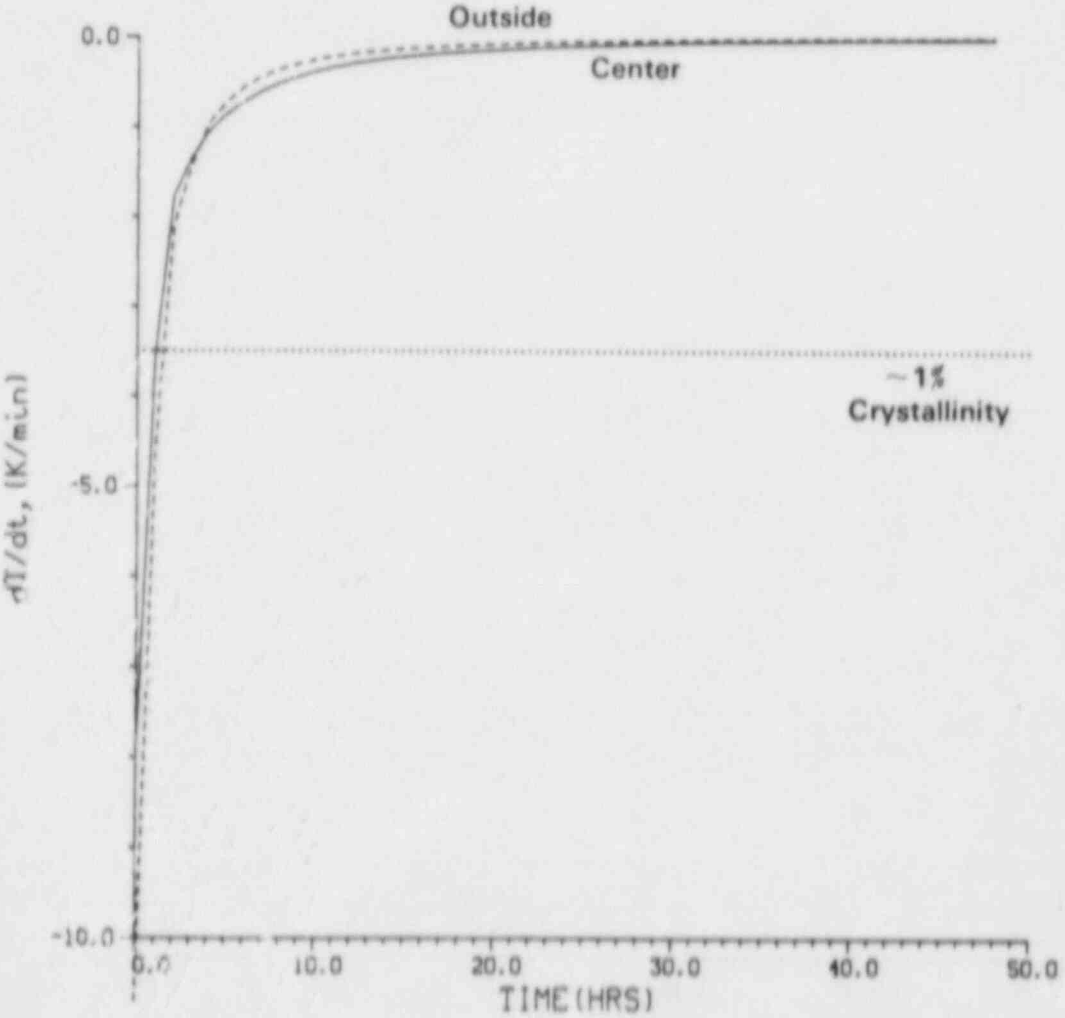

Figure 2.14. Cooling rate curve for top cells of defense waste form.

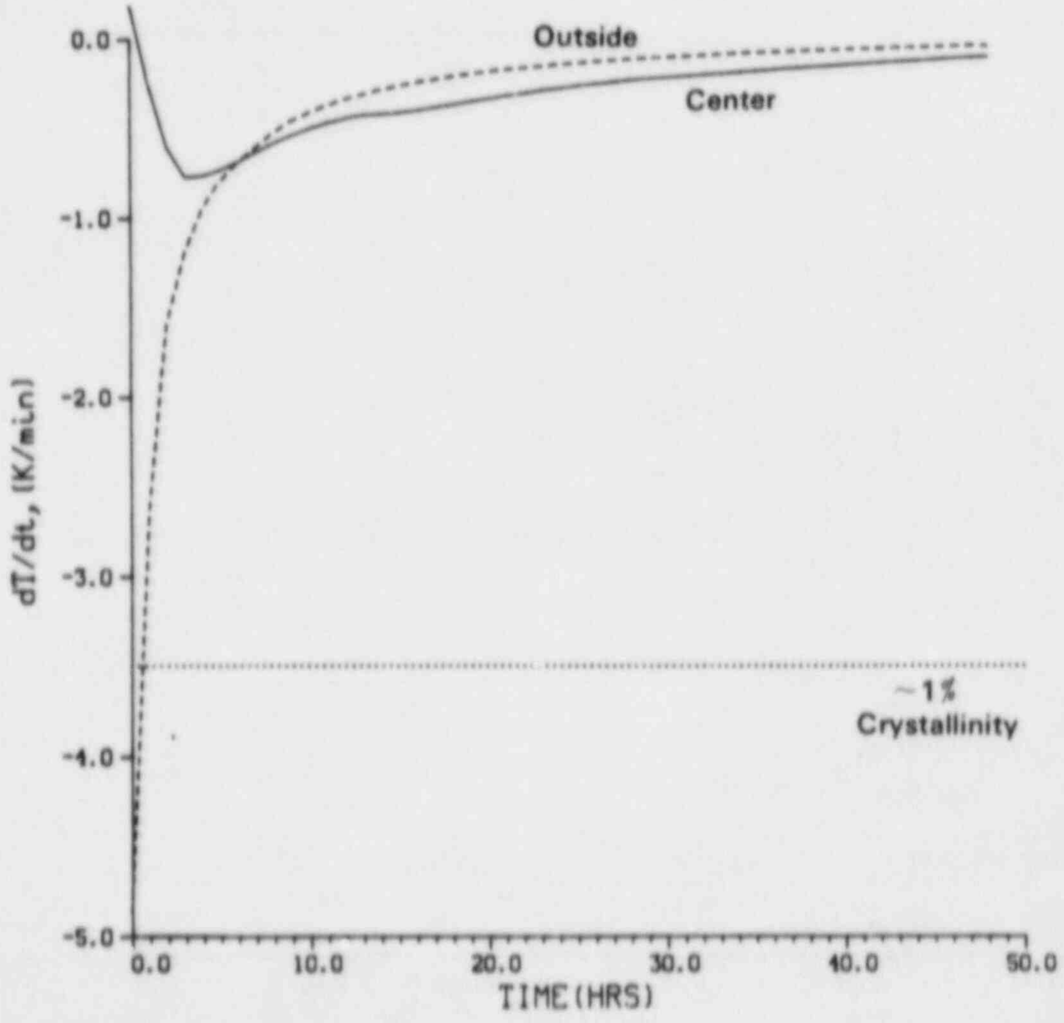

Figure 2.15. Cooling rate curve for middle cells of defense waste form.

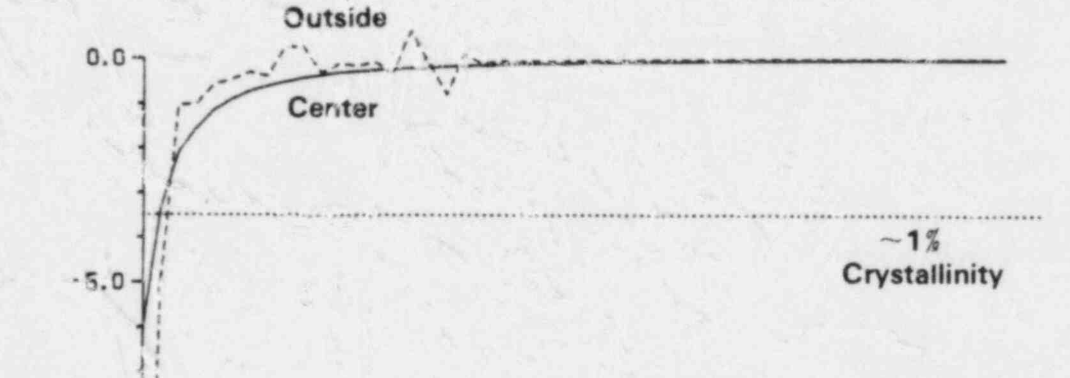

Figure 2.16. Cooling rate curve for bottom cells of defense waste form.

2.2.4 Conclusions

The calculation of the volume fraction crystallized in a full-sized waste form cannot be adequately approximated using currently available data and accepted classical approximations to the nucleation and growth rates. If this approximation is to be pursued, experimental nucleation and growth rate data are needed. Estimation of the severity of crystallization using TTT data and TRUMP-derived cooling rates indicate that only the more centrally located portions of the waste form are at risk of being more than 10 percent crystalline. The outer portions, especially those near the top and bottom of the waste form, are not likely to be more than a few percent crystalline. Therefore, the effect of the fraction of crystallization on leaching/corrosion will be assessed (see Section 2.1.4) before applying further efforts to obtain the crystallization data.

2.3 Transmutation Effects in Glass Waste Forms

As summarized in the first annual report, most individual radiation damage mechanisms are not harmful to the waste form. However, the combined effects of all these mechanisms operating simultaneously cannot be evaluated by simulation experiments. The evaluation of the literature pertinent to transmutation continued during this year.

The experimental study of radiation effects in glass waste forms will have to be deferred pending receipt of the real waste that has been produced by the MCC. This material is expected early in the third program year. The first portion of the third year's work will be devoted to developing appropriate experiments for this material. These experiments should begin approximately halfway tnrough the third year and continue into the fourth and possibly fifth program years.

Another possibility, which is beyond the scope of the present effort, is the study of transmutation effects in the nepheline syenite glass hemispheres containing strontium-90 which were formulated by AECL in June of 1960. This glass could offer a unique opportunity to study transmutation.

2.4 Implications for Waste-Form Performance

The results of the multivariate experiment in temperature, pressure, surface-to-volume ratio, and solution chemistry have several implications for waste-form performance. First, early container failure that would expose glass of high surface temperature, around 125 to 150 C or greater, to groundwater would result in rapid attack and removal of material. If this failure were a small hole which would expose minimum surface, then the problem would not be severe, since a deposit of leached material is likely to build around such a hole. However, if general loss of a large portion of the container is experienced, then the waste form will be attacked. The severity of such attack will increase nonlinearly with increasing temperature. In later years, when the outer temperature is below 100 C, material would be removed at a much lower rate.

Exposing a large surface area of waste form also will accelerate attack. Such acceleration is likely to be more pronounced if it occurs at higher temperatures. However, it is not expected to be more pronounced than the additive effect with temperature. In other words, a synergistic effect between surface-to-volume ratio and temperature is unlikely to be more than a second-order phenomenon. If cracking of the outer surfaces of the waste form can be minimized during casting, the influence of surface-to-volume ratio can also be minimized.

The solution chemistry will also have a large influence on waste-form performance. Performance predictions based on deionized-water studies should be conservative, since such water is a more severe condition than simulated basalt water. However, performance predictions based on static tests may be biased. Material that precipitates onto the glass is not adequately taken into account. If it is loosely attached, then it may become mobile even in slowly flowing groundwater. Tests performed in reused TEFLON containers may be subject to spurious results because of previously adsorbed species. Finally, the question of run-to-run variation in static tests needs to be taken into account. This accounting can be accomplished by increasing replications of experimental conditions (i.e., runs). Increasing replications within a condition will not properly account for this variation.

A number of interactions or synergisms were shown to be statistically significant. However, the magnitudes of these interactions were found to be only slightly larger than the prime effects of T, SA/V, and solution chemistry. A similar statement can be made about pressure above the autogeneous pressure of water at any given temperature. Therefore, that variable and the interactions can be considered minor influences and can probably be ignored.

The influence of devitrification could not be clearly and completely defined. The outer portion of the waste form is likely to be a few volume percent crystalline, and such a state should have very little effect on waste-form performance. The more central portions may be more crystalline, perhaps up to 10-15 volume percent. At those levels, cracking may occur during the thermal period, thereby raising the potential for increased attack because of increased exposed surface. Some work in this area(2.11) has shown that increasing the fraction crystallinity may accelerate materal removal. This acceleration needs to be more clearly defined. If such definition should show that the problem is severe, then a devitrification evaluation based on more precise nucleation and crystallization data should be conducted for each waste-form glass composition submitted for licensing.

2.5 Glass-Dissolution Kinetics

During the past year, separate-effects analyses of glass-dissolution kinetics were devoted to studies of three kinetic processes and their effects on the overall rate of glass dissolution:

- actual dissolution of the glass by transport of glass species across the glass/groundwater interface.
- convective flow of the groundwater.
- reprecipitation of dissolved glass species as a more stable phase than the original glass.

In order to maintain the interpretation of the results on a reasonably simple level, these processes were considered just two at a time, i.e., dissolution/convective-flow and dissolution/reprecipitation.

2.5.1 Dissolution Plus Convective Flow

Suppose that a volume V of groundwater is in contact with surface area S of glass and that the volumetric flow rate of the groundwater is $\dot{v}$. Let C be the instantaneous concentration, within the groundwater, of the glass component that controls the dissolution rate, and let C_0 be the equilibrium concentration of that component with respect to the glass. The concentration C is assumed to be spatially invariant within V. This is clearly a simplified treatment, in which possible reactions that the species controlling dissolution (assumed to be silica, in this case) may undergo, are not considered; it is assumed simply to accumulate, in solution, until its saturation level (which is, in general, temperature-dependent) is reached.

It is assumed further that the rate at which the species is transferred across the glass-water interface is directly proportional to the difference between its equilibrium and instantaneous concentrations in the groundwater. The net rate at which the total amount of the species within V varies with time t is equal to the rate at which new amounts are added by dissolution minus the rate at which already-dissolved species are transported away by flow, i.e.,

$$V \frac{dC}{dt} = KS\ (C_0 - C) - C\dot{v} \qquad (2.1)$$

where K is a temperature-dependent rate constant. The quantities K, S, V, and C_0 are all assumed here to be time-independent, although each may actually vary with time during the long lifetime of a waste package. "Loss" of the species, through processes such as radioactive decay or chemical reactions, is not considered here.

Equation 2.1 can be expressed in the alternative form

$$\frac{dC}{dt} + \frac{\alpha KS}{V} C = \frac{KS}{V} C_o \tag{2.2}$$

where

$$\alpha \equiv 1 + \frac{\dot{v}}{KS} \quad . \tag{2.3}$$

Equation 2.2 can easily be solved, subject to a given initial condition, taken here to be C (t = 0) = 0, to yield

$$C = \frac{C_o}{\alpha}\left[1 - \exp\left(- \frac{\alpha KS}{V} t\right)\right] \quad . \tag{2.4}$$

An expression similar to Equation 2.4 has also been derived by Machiels and Pescatore(2.12), albeit from a somewhat different point of view.

It is interesting to observe that Equation 2.3 can be expressed as

$$\alpha = 1 + \frac{\tau_d}{\tau_r}$$

where $\tau_d \equiv V/(KS)$ is a "characteristic time" for saturation of the liquid in V due to dissolution from the waste form and $\tau_r \equiv V/\dot{v}$ is essentially the "residence time" of solution within V. Clearly, if $\tau_d \ll \tau_r$, then dissolution kinetics controls the variation of C with time, whereas if $\tau_d \gg \tau_r$, it is the flow of solution that is controlling.

Equation 2.4 can be expressed in an alternative form using the concept of an "effective characteristic time", τ_{eff}, defined as

$$\tau_{eff} \equiv \left(\tau_r^{-1} + \tau_d^{-1}\right)^{-1} \quad ,$$

which can be applied to Equation 2.4 to yield

$$C = \frac{C_o}{\alpha}\left[1 - \exp\left(- \frac{t}{\tau_{eff}}\right)\right] \quad .$$

Let $\dot{Q}$ be the rate at which the species controlling dissolution is being dissolved from the glass. Clearly,

$$\dot{Q} = KS\ (C_o - C) \ . \tag{2.5}$$

Combining Equations 2.3 through 2.5,

$$\dot{Q} = \frac{KSC_o}{\alpha}\left[\frac{\dot{v}}{KS} + \exp\left(-\frac{\alpha KS}{V}\,t\right)\right] . \qquad (2.6)$$

Under steady-state conditions (that is, when the exponential term in Equation 2.6 becomes negligible), one obtains

$$\dot{Q} = C_o\dot{v}/\alpha . \qquad (2.7)$$

Combining Equations 2.3 and 2.7,

$$\rho = \frac{\nu}{1 + \nu} \qquad (2.8)$$

where ρ and ν are normalized, dimensionless expressions for the steady-state dissolution rate and the flow rate, respectively, and are given by

$$\rho \equiv \frac{\dot{Q}_d}{KSC_o} \qquad (2.9)$$

$$\nu \equiv \frac{\dot{v}}{KS} . \qquad (2.10)$$

Clearly, for $\nu << 1$, glass dissolution is flow-rate-controlled, with $\rho \approx \nu$, i.e., $\dot{Q} \approx C_0\dot{v}$. Conversely, for $\nu >> 1$, dissolution is controlled by transport of the species across the glass-water interface, with $\rho \approx 1$, i.e., $\dot{Q} \approx KSC_0$.

Equation 2.8 is plotted on logarithmic axes in Figure 2.17. At the lower flow rates, the curve is seen to approach a straight line having unit slope, whereas at the higher flow rates, it approaches a straight line having zero slope. These represent the two limiting cases discussed above.

The rate of release of the glass species to the environment external to the volume V can also be readily calculated, being equal to $C\dot{v}$. Under steady-state conditions, this quantity is equal to the rate of dissolution, as can be seen from Equation 2.1.

It is also of interest to determine the total amount of species which has dissolved as of time t, this being denoted as Q. Clearly,

$$Q = \int_0^t \dot{Q}dt . \qquad (2.11)$$

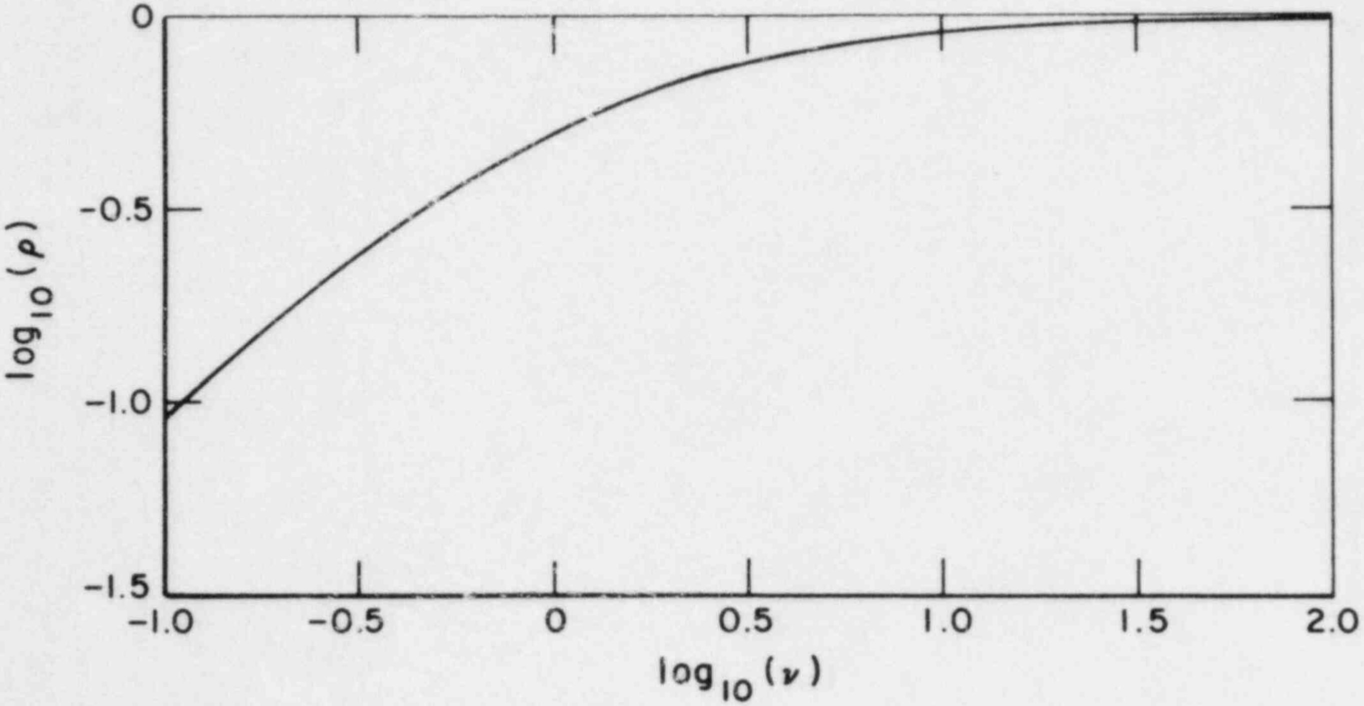

Figure 2.17. Logarithmic plot of ρ vs. ν (after Equation 2.8).

Combining Equations 2.6 and 2.11 and carrying out the resultant integration produces

$$Q = CV + Q_{\dot{v}} \tag{2.12}$$

where

$$Q_{\dot{v}} \equiv \frac{\dot{v}}{\alpha} \; C_o t - \frac{CV}{KS} \quad . \tag{2.13}$$

The first term on the right-hand side of Equation 2.12 is the instantaneous amount of dissolved species contained within volume V, so that $Q_{\dot{v}}$ must be the amount of dissolved species that has been carried out of V by the flowing water.

Some interesting limiting cases exist for the analysis presented above:

- $\underline{\alpha = 1}$. This case corresponds to completely stagnant groundwater, i.e., $\dot{v} = 0$, in which case Equation 2.4 reduces to

  $$C = Co \left[1 - \exp\left(-KSt/V\right)\right] \quad . \tag{2.14}$$

  Characteristics of this case, corresponding to asymptotically large times, are discussed below.

- $\underline{t \to \infty}$. As already discussed, this limiting case corresponds to steady-state conditions, for which the time-dependent contribution on the right-hand side of Equation 2.4 becomes negligible. Under this general heading, two cases are of interest:

  $\underline{\alpha = 1}$. Here, C asymptotically approaches the value C_o, meaning that dissolution in a stagnant solution continues only until the equilibrium solubility is reached. Clearly, for this case, Q asymptotically approaches the limiting value C_oV.

  $\underline{\alpha >> 1}$. This corresponds to very rapid flow of the groundwater (i.e., $\tau_d >> \tau_r$). From Equations 2.3 and 2.4, we find that

  $$C \approx KSC_o/\dot{v} << C_o \quad .$$

  Moreover, from Equations 2.3, 2.4, 2.12, and 2.13, we obtain

  $$Q_{\dot{v}} \approx Q \approx KSC_o t \quad .$$

  In this case, the dissolved species is transported out of V almost as fast as it goes into solution.

2.5.2 Dissolution Plus Reprecipitation

Reprecipitation of dissolved glass species as part of a more stable phase is a cause for concern in waste-package analysis. Basically, when dissolved species are removed from solution (as precipitates), the solution becomes additionally undersaturated with respect to the glass, so that the thermodynamic driving force for glass dissolution is increased. As a result, the rate at which the glass dissolves is greater than that which would have existed had no reprecipitation taken place.

Actually, processes associated with dissolution/reprecipitation have long been known in the geochemistry field, since they occur with various minerals in aqueous solution. One example of this sequence of processes consists of the dissolution of nepheline ($NaAlSiO_4$) followed by the precipitation of gibbsite ($Al(OH)_3$). As pointed out by Lasaga(2.11), the overall reaction is

$$NaAlSiO_4 + H^+ + 3H_2O \rightarrow Al(OH)_3 + Na^+ + H_4SiO_{4(aq)}.$$

However, this reaction proceeds in a sequence that consists of at least two steps. The first of these consists of nepheline dissolution,

$$NaAlSiO_{4(s)} + 4H^+ \rightarrow Na^+ + Al^{3+} + H_4Sio_{4(aq)}$$

and the second consists of the subsequent gibbsite-precipitation reaction,

$$Al^{3+} + 3H_2O \rightarrow Al(OH)_{3(s)} + 3H^+$$

where it has been assumed that the pH is low enough that Al^{3+} is a dominant species. Another example of this general nature, as pointed out by Lasaga(2.13), involves the silica content associated with interstitial waters in marine sediments, in which amorphous silica dissolves and is reprecipitated in another form.

2.5.2.1 Thermodynamic Basis

The thermodynamic basis for waste-form dissolution/reprecipitation is illustrated in Figure 2.18. As indicated there, the equilibrium solubility with respect to the glass (e.g., silica glass) of the species that controls glass dissolution is greater than that of that same species with respect to the precipitate (e.g., quartz).

During glass dissolution, there exist two regimes of interest that can be described in terms of the instantaneous concentration of the species in the solution. Referring to Figure 2.18, these regimes are:

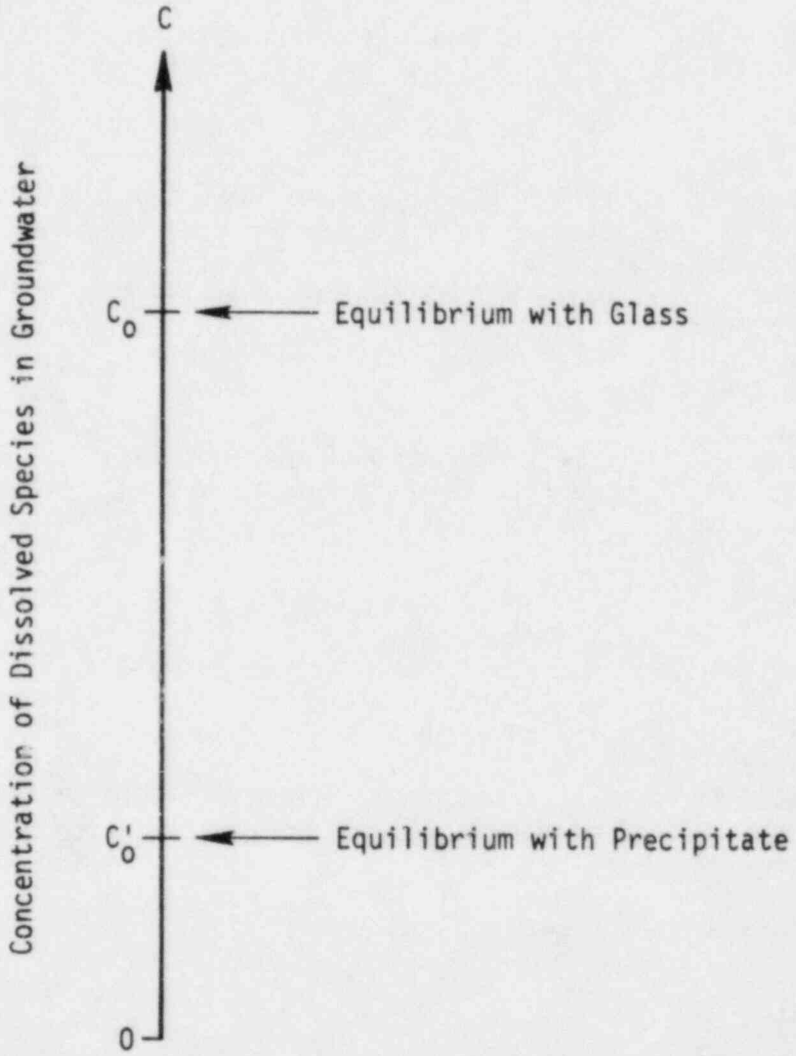

Figure 2.18. Illustration of equilibria associated with dissolution/reprecipitation.

$0 < C \leq C_0'$, for which the solution is undersaturated with respect to both the glass and the precipitate. Hence, assuming that no precipitates exist in the solution at the initiation of contact between glass and the water, the only kinetic process that takes place is glass dissolution.

$C_0' < C < C_0$, for which the solution is still undersaturated with respect to the glass, so that glass dissolution continues to take place. However, the solution is now supersaturated with respect to the precipitate, so that precipitate growth, in the form of layers on adjacent surfaces and/or colloids within the solution, is energetically favored to occur.

A semiempirical description of the kinetics of the dissolution process is presented in the following section.

2.5.2.2 Dissolution/Reprecipitation Model

Following the reasoning just presented, the kinetics of dissolution/reprecipitation of the waste form is treated here as occurring in two distinct sequential stages: glass-dissolution only, followed by dissolution/reprecipitation. A semi-empirical analysis of each of these stages is now presented.

2.5.2.2.1 $0 \leq C < C_0'$

Here the solution is undersaturated with respect to both the glass and the precipitate, which have saturation levels C_0 and C_0', respectively, as indicated in Figure 2.18. Within this regime,

$$\frac{dC}{dt} = \frac{KS}{V} (C_0 - C) \tag{2.15}$$

which is clearly equivalent to Equation 2.1 except that $\dot{v}$ is taken as zero for the case presently under consideration.

For the sake of simplicity, particularly in the analysis of the dissolution/reprecipitation regime, we now define dimensionless concentration and time variables as

$$s \equiv C/C_0 \tag{2.16a}$$

and

$$\tau \equiv KSt/V \quad . \tag{2.16b}$$

Combining Equations 2.15 and 2.16,

$$\frac{ds}{d\tau} = 1 - s \tag{2.17}$$

The solution of Equation 2.17, subject to the initial condition $s(\tau = 0) = 0$, is

$$s(\tau) = 1 - \exp(-\tau), \tag{2.18}$$

which is equivalent to Equation 2.14 above, as can be seen by combining Equations 2.16a and 2.16b with Equation 2.14.

In addition, let r be the value of s corresponding to the upper limit of this regime, i.e.,

$$r = C_o'/C_o \quad . \tag{2.19}$$

Moreover, let τ_p be the value of τ at which $s = r$.

From Equations 2.18 and 2.19, it follows directly that

$$\tau_p = \ln\left(\frac{1}{1-r}\right) \quad . \tag{2.20}$$

2.5.2.2.2 $C_o' < C < C_o$

In this regime, glass dissolution and precipitate formation occur simultaneously. It is assumed that the physical process of glass dissolution is essentially unaltered by the presence of the precipitate; however, the precipitate does indirectly influence the rate at which dissolution takes place because of its effect on C.

For the present purposes, it is assumed that, within this regime, Equation 2.15 is modified as follows:

$$\frac{dC}{dt} = \frac{KS}{V}(C_o - C) + K'(C_o' - C) \quad . \tag{2.21}$$

The first term on the right-hand side of Equation 2.21 is positive (since $C < C_o$) and is the rate at which the species is added to the solution from the glass. On the other hand, the second term is negative (since $C > C_o'$) and represents the rate at which the species is transferred out of solution into the precipitate, with K' being the effective rate constant for this latter process. Thus, Equation 2.21 is a mass-balance expression that describes the overall transfer of matter from the glass to the solution and from the solution to the precipitate.

A number of important observations should be made relative to the reprecipitation term in Equation 2.21:

- The term itself is semiempirical in the sense that no particular physical mechanism (e.g., layer growth on adjacent surfaces or colloid formation within the solution) was assumed for the mode by which reprecipitation occurs.

- The detailed nature of the effective rate constant, K', depends on the nature of the reprecipitation process itself. In general, K' can be expected to vary with time in a complex manner. It is also temperature-dependent.

- The rate of reprecipitation varies linearly with the difference between the saturation concentration, C_0', and the instantaneous actual concentration, C.

In order to proceed further, some assumption must be made regarding the time-dependence of K'. As a first attempt at describing reprecipitation kinetics, it is assumed here that K' is a constant. Such behavior may be more representative of layer growth on adjacent surfaces, which act as a pre-existing substrate for the precipitate. Colloid formation, on the other hand, involves the growth from solution of discrete particles starting from very small sizes. For this case, K' most likely increases with time as the colloids grow from solution.

Again, for the sake of simplicity, we cast Equation 2.21 in dimensionless form, i.e.,

$$\frac{ds}{d\tau} = 1 - s + \beta(r - s) \tag{2.22}$$

where

$$\beta \equiv \frac{K'V}{KS} \quad . \tag{2.23}$$

As seen from Equation 2.23, the parameter β is a measure of the ratio of the rate constant for reprecipitation relative to that for dissolution.

The solution of Equation 2.22, subject to the initial condition $s(\tau = \tau_p) = r$, can easily be shown to be

$$s = s_k \left\{ 1 - \frac{1}{1 + \beta r} \left(\frac{1}{1 - r} \right)^{\beta} \exp\left[- (1+\beta)\tau \right] \right\} \tag{2.24}$$

where

$$s_k \equiv s(\tau \to \infty) = \frac{1 + \beta r}{1 + \beta} \quad . \tag{2.25}$$

Combining Equations 2.16a, 2.19, and 2.15,

$$C(\tau \rightarrow \infty) \equiv C_k = \frac{C_o + \beta C_o'}{1 + \beta} \ . \qquad (2.26)$$

Thus, the value C_k, approached by C at asymptotically large times, is a constant, consisting of a weighted average of C_o and C_o'. In general, $C_o' < C_k < C_o$. Moreover, upon consideration of Equation 2.26, one sees that, if $\beta << 1$, then C_k is less than but close to C_o. On the other hand, if $\beta >> 1$, then C_k is greater than but close to C_o'. As can be seen from Equation 2.21, what is taking place at times for which $C \approx C_k$ is that the rate at which the species is being added to the precipitate is virtually the same as the rate at which it is leaving the glass by dissolution.

It should be emphasized that C_k is <u>not</u> a true equilibrium concentration, its magnitude being a function of the rate-constants K and K'. Rather, C_k is a "kinetic" parameter; hence the choice of subscript for this quantity. Further discussion of the nature of this saturation concentration has been presented by Lasaga$^{(2.13)}$.

As far as the net amount of glass dissolution is concerned, Equations 2.5 and 2.11 still apply. However, for $0 \leq \tau < \tau_p$, one uses Equation 2.18 to obtain s (i.e., C), whereas for $\tau > \tau_p$, one uses Equation 2.24 to obtain s. Carrying out this procedure, the final result for $0 \leq \tau < \tau_p$ is

$$q = 1 - \exp(-\tau), \qquad (2.27)$$

where q is a dimensionless form of Q, defined as

$$q = \frac{Q}{C_o V} \ . \qquad (2.28)$$

Likewise, for $\tau > \tau_p$, one obtains

$$q = r + \frac{1 - r}{1 + \beta}\left\{\beta(\tau - \tau_\rho) + \frac{1}{1 + \beta}\right. \qquad (2.29)$$

$$\left.\left\{1 - \left(\frac{1}{1 - r}\right)^{1 + \beta} \exp\left[-(1 + \beta)\tau\right]\right\}\right\}$$

One can readily show that the value of s, at a given value of τ ($> \tau_p$), is always smaller for the case in which reprecipitation takes place ($\beta \neq 0$) as compared to the case in which no precipitation occurs ($\beta = 0$). The significance of this result lies in the fact that the instantaneous rate of glass dissolution is proportional to $C_0 - C$ (after Equation 2.5). Consequently if s (and hence C) is maintained at smaller values, as is the case when reprecipitation takes places, then the rate of glass dissolution is increased, so that more glass goes into solution.

2.5.2.3 Results

Results for a specific example are illustrated in Figures 2.19 and 2.20. Here, the case of glass-dissolution only (i.e., no reprecipitation, or $\beta = 0$) is compared with that for which values of $\beta = 1$ and $r = 0.2$ were selected. Accordingly, one can use Equations 2.20 and 2.25 to obtain $\tau_p \simeq 0.223$ and $s_k = 0.6$, respectively, for this example.

Some principal features of the dissolution/reprecipitation model developed here are clearly illustrated in Figures 2.19 and 2.20. For example, in Figure 2.19 we find that the variation of s with τ is initially the same for both cases. However, when s exceeds r, they begin to diverge, with the value of s, at a given value of τ, being lower for the case in which reprecipitation takes place, as expected. In addition, the value of s asymptotically approaches a value of unity for the case in which glass dissolution alone takes place, and a value of 0.6 when both both dissolution and reprecipitation occur.

Likewise, in Figure 2.20, the amount of glass species dissolved away from the solid glass is the same for the two cases until τ exceeds τ_p, after which more of the species has gone into solution, at a given value of τ, for the case in which reprecipitation is taking place, again as expected. What is not shown clearly in Figure 2.20 is the fact that q asymptotically approaches a constant value of unity if no reprecipitation occurs, but asymptotically increases linearly with τ if reprecipitation does occur.

For purposes of further illustration, we refer again to the dissolution/reprecipitation reaction that was discussed above (after Lasaga$^{(2.13)}$), consisting of the dissolution of nepheline and subsequent precipitation of gibbsite. Shown in Figure 2.21, is the measured concentration of Al^{3+} in solution as a function of time (after Tole, as reported by Lasaga$^{(2.13)}$) for this particular set of reactions. Clearly, the data exhibit the general behavior predicted by Equation 2.24 (the Al^{3+} concentration rises from zero) and "saturates" at a level that lies between the saturation concentration for nepheline and that for gibbsite.

If we apply the dissolution/reprecipitation model developed above to the data shown in Figure 2.20, i.e., taking $C_0 \simeq 9790$ ppm, $C_0' \simeq 6$ ppm and $C_K \simeq 38$ ppm, then one can use Equation 2.26 to calculate a corresponding value for β, the result being $\beta \simeq 305$. This large value of β is consistent with the fact that C_k lies much closer to C_0' than it does to C_0 for this particular case.

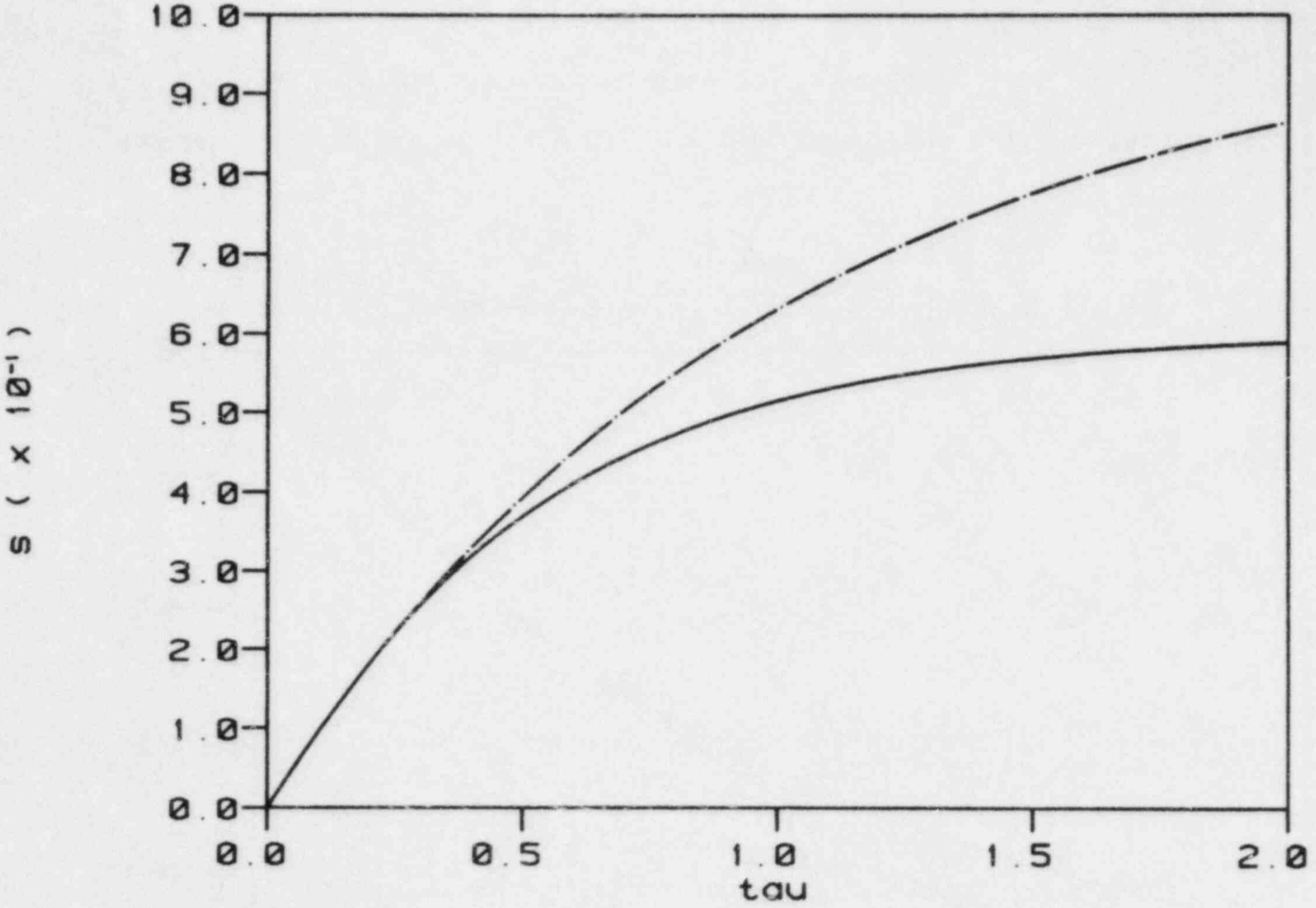

Figure 2.19. Variation of s with τ for two different cases: glass dissolution only (broken curve) and dissolution plus reprecipitation (solid curve).

For the solid curve, β = 1 and r = 0.2.

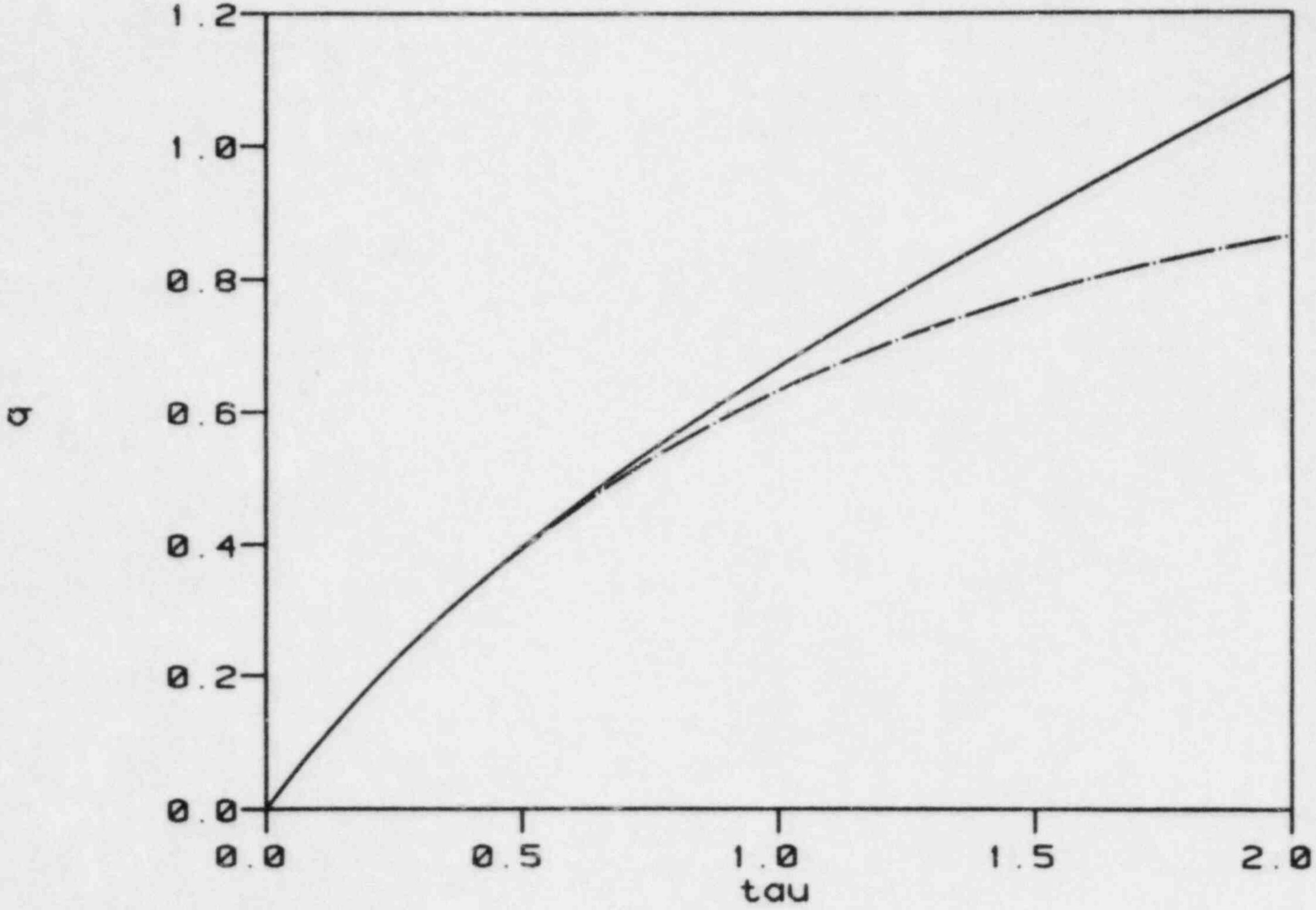

Figure 2.20. Variation of q with τ for the cases illustrated in Figure 2.24. For the solid curve, β = 1 and r = 0.2.

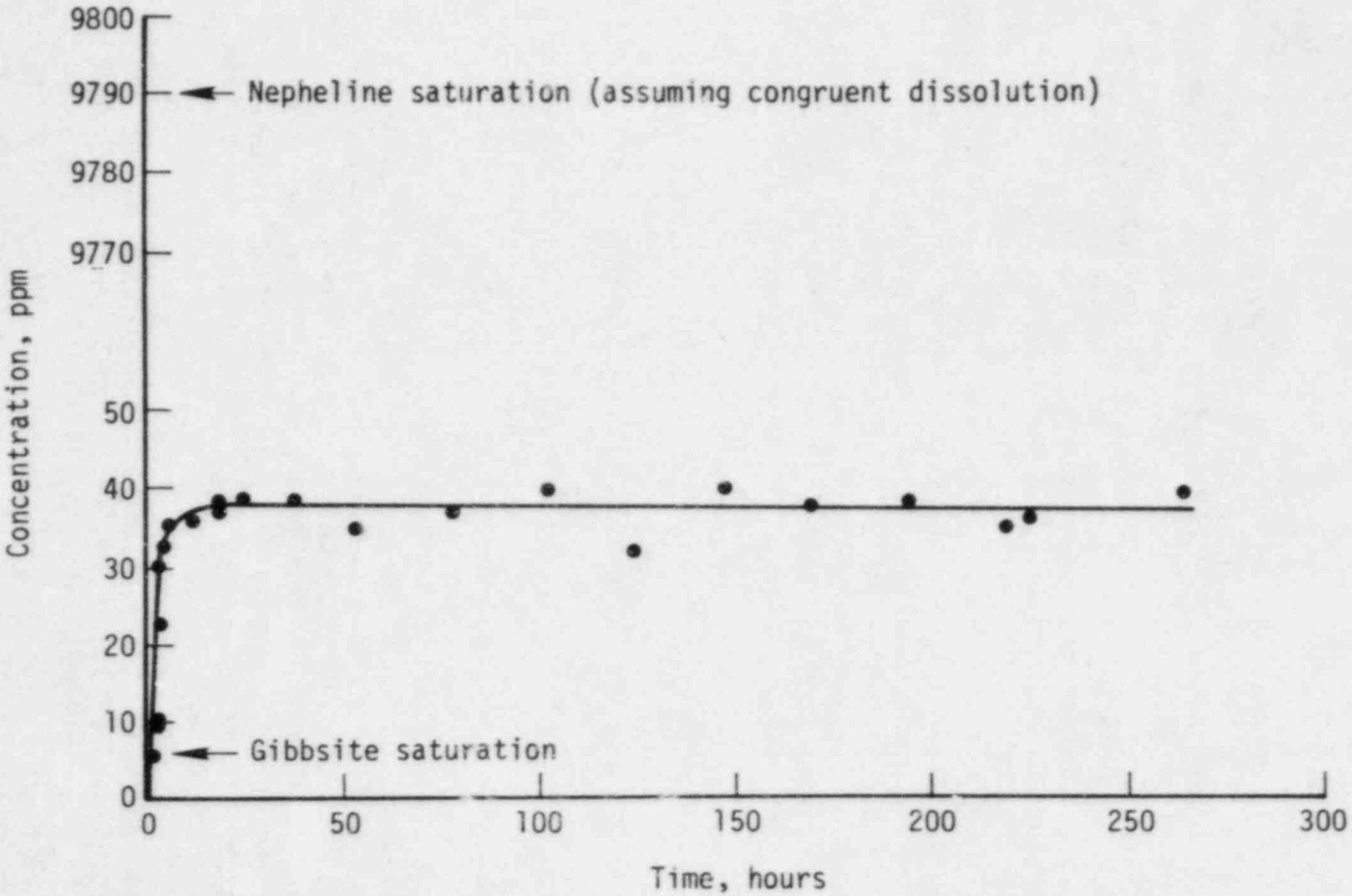

Figure 2.21. Variation with time of Al^{3+} in solution, at pH = 3.1 and 60 C, during gibbsite reprecipitation.

(After Tole, as reported by Lasaga$^{(2.13)}$. Reprinted by permission of the Mineralogical Society of America).

In the present state of development, the glass-dissolution model has satisfactorily described geochemical data. This represents a significant step toward the ultimate objective of being able to describe the performance of nuclear-waste glasses in repository environments and to assist the NRC in evaluating the long-term release of radionuclides from DOE's proposed waste package.

2.6 Spent Fuel as a Waste Form

Disposal of spent fuel is an alternative to reprocessing and disposal of high-level waste. As with other waste-form candidates, an important scenario which needs to be modeled and understood is one in which waste packages are breached after disposal and available groundwater causes leaching of radioactive elements. The amount of data available on leach rates of spent fuel and UO_2 is limited.(2.14) The available data will be summarized, probable leaching mechanisms discussed, and suggestions for further experimentation presented.

Spent fuel is largely UO_2, but the physical and chemical properties of irradiated fuel are significantly different from those of unirradiated UO_2. Use of UO_2 as a laboratory analog must take these property differences into account. Leaching mechanisms will depend on irradiation history, groundwater conditions, and the element under consideration, among other factors. In addition, when assessing the suitability of spent fuel as a waste form, the added barrier of the cladding material should be considered.

2.6.1 Cladding

Spent fuel will be disposed of in its cladding which, in most cases, is Zircaloy. (The specific alloy may depend on the reactor type.) This cladding provides a significant barrier to migration of fuel and fission products after disposal provided that it is intact. Fuel rods may degrade due to external corrosion and to various internal mechanisms.

Spent fuel rods are typically stored in water pools following reactor discharge. Pool storage is intended for relatively short periods of time, but no evidence of fuel rod degradation or failure after approximately 20 years of storage in water has been observed.(2.15) A repository will not be available until the end of the century, so fuel rods may remain in pool storage for longer times than originally intended. If times extend well beyond 20 years, the importance of slow degradation mechanisms in water needs to be examined.

Some of the important potential cladding degradation mechanisms for long-term storage identified by Blackburn, et al(2.16) are: mechanical overload (principally from internal pressure); internal hydriding or hydrogen embrittlement; cladding oxidation; stress rupture; and stress-corrosion cracking or chemical attack by fission products (e.g., cesium, iodine). Most of these are temperature-dependent, and the last two are the most likely to be operative.

Breach tests of spent fuel rods at elevated temperatures were conducted by Einziger, et al(2.17), who found that the rods did not fail as expected. They observed no gross changes in rod condition and furthermore noted 1.5-2.0 percent cladding creep with an attendant 31 percent decrease in hoop stress. This value of cladding creep was 6 times higher than predicted and explains the lack of breach. The test temperatures used (480-570 C) were sufficient to anneal in-reactor radiation damage. More recent tests at 325 C were conducted at Battelle-Columbus by Einziger and Kohli(2.18). No cladding breaches and minimal creep (< 0.2 percent) were observed after 2100 hours. Geologic disposal temperatures may be low (< 400 C) and may not result in the same values of creep and stress reduction. In most cases the cladding will remain intact and will serve as an additional barrier to groundwater attack in the event of canister breach.

2.6.2 Characteristics

Although general characteristics of spent fuel can be described, significant physical and chemical differences exist among fuels from different reactors. These differences arise primarily from differences in fabrication or irradiation history of the fuel pellets. Differing irradiation history in particular will affect spent fuel characteristics and, hence, leaching behavior.

Spent fuel pellets are physically and chemically heterogeneous due to the steep thermal gradient across them during irradiation (hottest near center, cooler around periphery). An extreme example of the physical changes accompanying irradiation can be seen in Figure 2.22(2.19) and include:

- Grain growth--producing long, columnar grains near the pellet center (at high temperature) followed by equiaxed grains, with the original grain structure near the periphery of the pellets
- Cracking--resulting in high surface area material
- Closed and open porosity--some pellets have a central cavity
- Fission gas bubbles at grain boundaries.

The chemistry of spent fuel is equally heterogeneous, but pellets are essentially heavily sintered UO_2 with ~4.5 percent fission products and actinides. A variety of distributions and phases is expected for the fission products and actinides, including:

- Solid solutions with UO_2
- Metallic inclusions
- Oxide phases distinct from UO_2
- Gases.

A given element may be present in more than one chemical form within an individual fuel pellet, and the specific behavior of a given fission product is difficult to predict. Behavior depends on:(2.19)

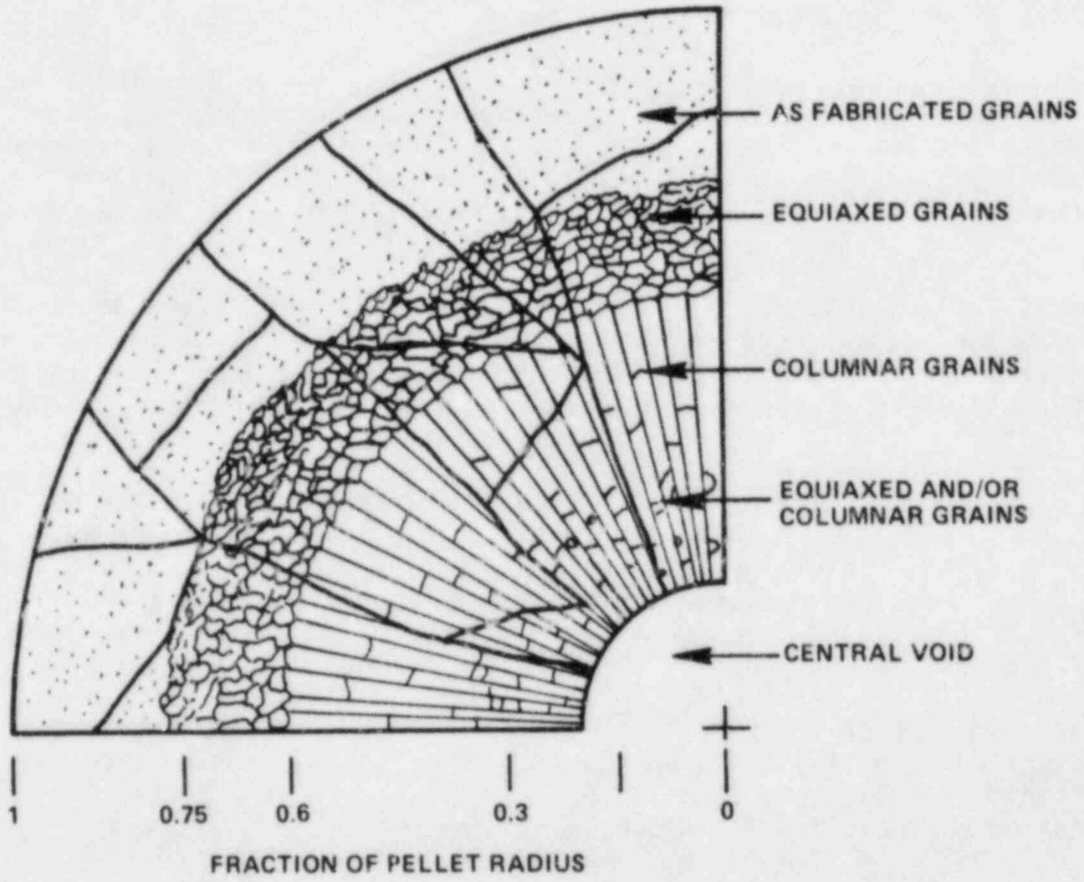

Figure 2.22. Cross-section of an oxide fuel pellet from high-power light-water reactor or fast breeder reactor fuel.

(Adapted from Reference 2.19).

- Birth location of fission product in fuel pellet
- Temperature distribution within pellet
- Fission product concentration (increases with burn-up)
- Oxygen-to-metal ratio (increases with burn-up).

The latter two conditions increase with increased fuel-burnup rate. Generally, the fission product content is greatest in the non-restructured region around the periphery of a pellet. In particular, cesium-137 concentrates at the fuel/cladding interface and in grain boundaries near the fuel-pellet periphery. Little information is available regarding unambiguous descriptions of the chemical state of fission products.

2.6.3 Testing Conditions

The conditions under which spent fuel is leach-tested will influence the elemental release rates obtained. In addition, problems arise when attempts are made to duplicate chemical and physical characteristics of spent fuel using simulated material.

Although most leach tests use fragments of unclad fuel, results of leach tests using fuel plus cladding display important differences. The latter case is closer to the actual disposal scenario but, for testing purposes, the surface area of the fuel (which is highly cracked) is unknown, and comparison of data becomes difficult. Fuel-plus-cladding tests, however, give a more accurate account of the preferential leaching of cesium-137 from the fuel/cladding interface. Unclad-fuel tests permit measurement of surface area, but the effects of the cladding are not measured. The fuel fragments themselves are inhomogeneous, and large numbers of them are required for a representative spent-fuel sample.(2.20)

The grain structure, fission-product distribution, and effects of radioisotopes in spent fuel are probably not amenable to accurate simulation. Simulated materials made to date are essentially chemically and physically homogeneous; spent fuel contains grain boundaries, large inhomogeneities, and radiation damage. Leaching mechanisms of spent fuel will probably be more complex than those for simulated material, and direct evaluation of spent fuel and spent fuel plus cladding is required. Unfortunately, relatively few surface analyses can be performed on spent fuel due to a lack of radiation-shielded analytical techniques. Leach rates of spent fuel also are influenced by factors which affect leach testing in general, including:

- Type of test--static vs. dynamic, duration
- Chemical composition of leachate--especially oxidizing or reducing capacity
- pH of leachate
- Temperature of tests
- Irradiation history of fuel
- Element considered--different elements display different leach rates.

2.6.4 Leaching Mechanism

The amount of data available on leach rates of spent fuel and UO_2 is limited. Most of the leach tests have been performed at room temperature, although some data are available at temperatures up to approximately 200 C.(2.21-2.23) However, each investigator has used different samples and experiments, so direct comparison of results is difficult. The most detailed studies of leaching mechanisms appear to have been done by Johnson, et al (AECL-Whiteshell)(2.22) and by Wang and Katayama and their associates at Battelle's Pacific Northwest Laboratories.(2.23-2.27) In these studies, UO_2 is used as a model to investigate leaching mechanisms. Since the chemistry of spent fuel is dominated by the chemistry of UO_2, this is a suitable starting point and provides guidelines for the probable leaching mechanisms of spent fuel. There is a need for further studies using spent fuel to improve understanding of the details of spent fuel leaching, including(2.23)

- The roles of grain boundaries, microcracks and pores
- The effects of surface segregation and solid solutions
- The effects of radiation
- The interactive effects between spent fuel and cladding.

Some general observations on spent-fuel leaching by various investigators are:

1. Leaching is initially incongruent. Elements such as $^{134,\ 135,\ 137}Cs$, ^{90}Sr, ^{129}I and inert gases, which tend to migrate to gaps in the fuel and to the fuel/cladding interface, are leached more rapidly from the fuel in the short term. This initial release tends to be from leachable phases, especially in the case of cesium, and matrix breakdown is not required.

2. At longer times, congruent dissolution is approached.

3. In general, leach rates are not strongly temperature-dependent.

4. Surface films on UO_2 and spent fuel play an important role in the dissolution process. Hydrolyzed, gelatinous UO_2 films may lower the release of uranium to the leachate, while other radionuclides may pass through the film.

5. The effects of oxygen on spent fuel leaching are significant. UO_2 is quite insoluble in neutral and alkaline solutions under reducing conditions, but solubility increases rapidly even under mildly oxidizing conditions because of formation of U(VI) species.

The dissolution mechanism proposed by Wang and Katayama(2.23,2.24) for UO_2 and spent fuel was developed following observations of surface films produced during leaching studies of UO_2 single crystals. The initial dissolution of UO_2 involves oxidation of U^{4+} (solid) to U^{6+} (aqueous) through formation of uranyl ions. Subsequent hydrolysis reactions lead to the formation of solid uranyl hydrates or related complex compounds that deposit onto the surface of the UO_2. The thickness of these coatings is a function of temperature, solution pH, and time. The dissolution of UO_2 will increase with temperature due to enhanced diffusion of oxygen and H^+ ions to the UO_2 surface. However, the solubility of uranyl ions is inversely related to temperature, so most of the dissolution products end up on uranyl hydrate deposits.(2.27) The presence of H_2O_2, expected from radiolysis of water, enhances the oxidation-dissolution of UO_2 and increases the formation of hydrate deposits.

The observed leach rate of UO_2 is dependent on formation/dissolution and also partial spallation of the hydrate films. Even after the solubility limits of uranyl ions have been reached, dissolution can still occur as long as precipitation is still occurring. As dissolution/precipitation continues, other elements, whose solubility limits may not have been reached, are released to solution. Katayama(2.25) has also observed a rise in the leach rate after several hundred days of cumulative leaching. During this accelerated leaching period, there is an increase in the leach rates for all radionuclides. Evidence suggests that this phenomenon is due to exposure of new surfaces to leachant as a result of cracking and spallation of the protective surface film.

Preliminary studies of spent fuel leaching(2.22,2.24) indicate that leaching mechanisms are similar to those found for UO_2, but this requires further investigation. Better understanding of leachate composition effects is needed. In general, leach rates in deionized water are higher than those in groundwaters for most elements. However, the leach mechanisms for all radionuclides may not be similar, and their dependence on leaching solution is still unclear. In particular, more experimentation with groundwaters is necessary. Katayama(2.25) has reported that burnup has no measurable effect on leach rates of ^{137}Cs, $^{239+240}Pu$, and uranium, but does affect the leach rate of ^{244}Cm. No other data are available on the influence of burnup, and further experimentation is warranted.

2.6.5 Conclusions and Recommendations

The effectiveness of spent fuel as a waste form lies in its ability to prevent release of radioactive elements to the environment. Both the spent UO_2 fuel itself and the fuel cladding serve as barriers to fission product release. Therefore, the condition of the cladding, the features of the fuel-cladding interface, and the chemical and microstructural characteristics of the spent fuel must be examined and understood.

Experiments to date with both the spent fuel and simulated spent fuel have attempted to characterize the factors which will influence the leaching/dissolution behavior and to develop models describing the leaching/dissolution mechanism. Although numerous influencing factors have been identified, further systematic studies of their effects are necessary. Models which have been developed to describe the dissolution

(2.7) Onorato, Uhlmann, and Hopper, "A Kinetic Treatment of Glass Formation: IV, Crystallization on Reheating Glass," *J. Non-Crystal Sol. 41*, p 189-200, 1980.

(2.8) Hopper, Scherer, and Uhlmann, "Crystallization Statistics, Thermal History, and Glass Formation", *ibid 15* pp 45-62, 1974.

(2.9) M. J. Plodinec, G. G. Wicks, and N. E. Bibler, "An Assessment of Savannah River Borosilicate Glass in the Repository Environment", DP-1629, April 1982.

(2.10) Bickford and Jantzen, "Devitrification Behavior of SRL Defense Waste Glass", Materials Research Society Annual Meeting, Boston, Massachusetts, November 14-17, 1983.

(2.11) Hench and Clark, "Surface Properties and Performance Prediction of Alternative Waste Forms", Report to U.S. Nuc. Reg. Comm. (Contract No. NRC-04-78-252), March 1983.

(2.12) A. J. Machiels and C. Pescatore, *Mater. Res. Soc. Symp. Proc. 15*, 1983, p. 209.

(2.13) A. C. Lasaga, in Reviews in Mineralogy, Vol. 8: Kinetics of Geochemical Processes, A. C. Lasaga and R. J. Kirkpatrick (editors), Mineralogical Society of America (Washington D.C., 1981), pp. 10-11.

(2.14) "An Assessment of the Proposed Rule (10CFR60) for Disposal of High Level Radioactive Wastes in Geologic Repositories" NUREG/CR-3111/2 of 2, November 1983.

(2.15) A. B. Johnson, Jr., "Behavior of Spent Nuclear Fuel in Water Pool Storage", BNWL-2256 (1977). Also A. B. Johnson, Jr., W. J. Bailey, E. R. Gilber, and J. T. Mayer, "Materials Behavior in Interim Storage of Spent Fuel", Trans Am. Nuclear Soc. *43*, pp 314-315, 1982.

(2.16) L. D. Blackburn, D. G. Farwick, S. R. Fields, L. A. James, and R. A. Moen, "Maximum Allowable Temperature for Storage of Spent Nuclear Reactor Fuel--An Interim Report", HEDL-TME 78-37 UC-70, May 1978.

(2.17) R. E. Einziger, D. A. Cantley, J. C. Krogness, D. E. Stellrecht, and V. Pasupathi, "Spent Fuel Resistance to Internally Produced Cladding Degradation", CONF-8005107, May 1980.

(2.18) R. E. Einziger and R. Kohli, "Low Temperature Rupture Behavior of Pressurized Water Reactor Spent Fuel Rods Under Dry Storage Conditions", submitted to Nuclear Technology.

through formation of uranyl ions. Subsequent hydrolysis reactions lead to the formation of solid uranyl hydrates or related complex compounds that deposit onto the surface of the UO_2. The thickness of these coatings is a function of temperature, solution pH, and time. The dissolution of UO_2 will increase with temperature due to enhanced diffusion of oxygen and H^+ ions to the UO_2 surface. However, the solubility of uranyl ions is inversely related to temperature, so most of the dissolution products end up on uranyl hydrate deposits.(2.27) The presence of H_2O_2, expected from radiolysis of water, enhances the oxidation-dissolution of UO_2 and increases the formation of hydrate deposits.

The observed leach rate of UO_2 is dependent on formation/dissolution and also partial spallation of the hydrate films. Even after the solubility limits of uranyl ions have been reached, dissolution can still occur as long as precipitation is still occurring. As dissolution/precipitation continues, other elements, whose solubility limits may not have been reached, are released to solution. Katayama(2.25) has also observed a rise in the leach rate after several hundred days of cumulative leaching. During this accelerated leaching period, there is an increase in the leach rates for all radionuclides. Evidence suggests that this phenomenon is due to exposure of new surfaces to leachant as a result of cracking and spallation of the protective surface film.

Preliminary studies of spent fuel leaching(2.22,2.24) indicate that leaching mechanisms are similar to those found for UO_2, but this requires further investigation. Better understanding of leachate composition effects is needed. In general, leach rates in deionized water are higher than those in groundwaters for most elements. However, the leach mechanisms for all radionuclides may not be similar, and their dependence on leaching solution is still unclear. In particular, more experimentation with groundwaters is necessary. Katayama(2.25) has reported that burnup has no measurable effect on leach rates of ^{137}Cs, $^{239+240}Pu$, and uranium, but does affect the leach rate of ^{244}Cm. No other data are available on the influence of burnup, and further experimentation is warranted.

2.6.5 Conclusions and Recommendations

The effectiveness of spent fuel as a waste form lies in its ability to prevent release of radioactive elements to the environment. Both the spent UO_2 fuel itself and the fuel cladding serve as barriers to fission product release. Therefore, the condition of the cladding, the features of the fuel-cladding interface, and the chemical and microstructural characteristics of the spent fuel must be examined and understood.

Experiments to date with both the spent fuel and simulated spent fuel have attempted to characterize the factors which will influence the leaching/dissolution behavior and to develop models describing the leaching/dissolution mechanism. Although numerous influencing factors have been identified, further systematic studies of their effects are necessary. Models which have been developed to describe the dissolution mechanism of UO_2 and simple simulated fuel systems must be extended to include the effects of more complicated chemical and microstructural features of actual spent fuel elements. Leaching mechanisms for all radionuclides are not the same, although the leach rate for the majority of the fission products and actinides appears to be controlled by the dissolution of the UO_2 matrix. Additional information on the leaching mechanism of spent fuel is necessary.

The chemical and physical features of spent fuel are difficult to simulate. Experiments with simulated spent fuel are necessary for development of behavior models, but additional studies with real spent fuel should be conducted to test the validity of these models.

Further leaching and dissolution experiments should be designed to address the following areas:

- The roles of surface area, grain boundaries, microcracks and pores
- The effect of fuel burnup on the leach rates of specific elements
- The interactive effects between spent fuel and cladding
- The effects of leachate composition, particularly for groundwaters
- The effects of elevated temperatures, up to and including predicted storage temperatures.

2.7 References for Section 2

(2.1) Nuclear Waste Materials Handbook Test Methods, "MCC-IP Static Leach Test Method," Section 4.1.

(2.2) "Evaluation of Bulk Properties of Radwaste Glass and Ceramic Container Materials to Determine Long-Term Stability," prepared by P. B. Macedo and A. Barkatt, p. 45-46 (NUREG/CR-2737).

(2.3) Jones, T. E., "Reference Material Chemistry--Synthetic Groundwater Formulation", Report from Rockwell International to U.S. DOE under Contract DE-AC06-77RL01030 April, 1982.

(2.4) Engineered Waste Package Conceptual Design, DHLW, CHLW, SF, Disposal in Basalt; AESD-TME-3113; p 3-15, September 1981.

(2.5) "Materials Characterization Center Workshop on Leaching Mechanisms of Nuclear Waste Forms", J. E. Mendel (Compiler), PNL-4382, August 1982.

(2.6) A. L. Edwards, "TRUMP--A Computer Program for Transient and Steady-State Temperature Distributions in Multidimensional Systems", UCRL-14754, Rev. 3, September 1972.

(2.7) Onorato, Uhlmann, and Hopper, "A Kinetic Treatment of Glass Formation: IV, Crystallization on Reheating Glass," J. Non-Crystal Sol. 41, p 189-200, 1980.

(2.8) Hopper, Scherer, and Uhlmann, "Crystallization Statistics, Thermal History, and Glass Formation", ibid 15 pp 45-62, 1974.

(2.9) M. J. Plodinec, G. G. Wicks, and N. E. Bibler, "An Assessment of Savannah River Borosilicate Glass in the Repository Environment", DP-1629, April 1982.

(2.10) Bickford and Jantzen, "Devitrification Behavior of SRL Defense Waste Glass", Materials Research Society Annual Meeting, Boston, Massachusetts, November 14-17, 1983.

(2.11) Hench and Clark, "Surface Properties and Performance Prediction of Alternative Waste Forms", Report to U.S. Nuc. Reg. Comm. (Contract No. NRC-04-78-252), March 1983.

(2.12) A. J. Machiels and C. Pescatore, Mater. Res. Soc. Symp. Proc. 15, 1983, p. 209.

(2.13) A. C. Lasaga, in Reviews in Mineralogy, Vol. 8: Kinetics of Geochemical Processes, A. C. Lasaga and R. J. Kirkpatrick (editors), Mineralogical Society of America (Washington D.C., 1981), pp. 10-11.

(2.14) "An Assessment of the Proposed Rule (10CFR60) for Disposal of High Level Radioactive Wastes in Geologic Repositories" NUREG/CR-3111/2 of 2, November 1983.

(2.15) A. B. Johnson, Jr., "Behavior of Spent Nuclear Fuel in Water Pool Storage", BNWL-2256 (1977). Also A. B. Johnson, Jr., W. J. Bailey, E. R. Gilber, and J. T. Mayer, "Materials Behavior in Interim Storage of Spent Fuel", Trans Am. Nuclear Soc. 43, pp 314-315, 1982.

(2.16) L. D. Blackburn, D. G. Farwick, S. R. Fields, L. A. James, and R. A. Moen, "Maximum Allowable Temperature for Storage of Spent Nuclear Reactor Fuel--An Interim Report", HEDL-TME 78-37 UC-70, May 1978.

(2.17) R. E. Einziger, D. A. Cantley, J. C. Krogness, D. E. Stellrecht, and V. Pasupathi, "Spent Fuel Resistance to Internally Produced Cladding Degradation", CONF-8005107, May 1980.

(2.18) R. E. Einziger and R. Kohli, "Low Temperature Rupture Behavior of Pressurized Water Reactor Spent Fuel Rods Under Dry Storage Conditions", submitted to Nuclear Technology.

(2.19) R. C. Hoyt and B. W. Rhee, "Review of Literature for Dry Reprocessing Oxide, Metal and Carbide Fuel--the Airox, Rahyd and Carbox Pyrochemical Processes", ESG-DOE-13277, Rockwell International, Energy Systems Group, Canoga Park, California, 1979.

(2.20) J. F. Kircher, D. P. Moak, and D. E. Clark, "Waste Package Materials Testing for a Salt Repository: 1982 Status Report", ONWI-490, August 1983.

(2.21) A. E. Norris, "Fission Product Release: Progress Report, April 1-June 30, 1979", LA-7969-PR, Los Alamos National Laboratory, August 1979.

(2.22) L. H. Johnson, D. W. Shoesmith, G. E. Lunansky, M. G. Bailey, and P. R. Tremaine, "Mechanisms of Leaching and Dissolution of UO_2 Fuel", Nuclear Technology, 56, February 1982, pp 238-253.

(2.23) R. Wang and Y. B. Katayama, "Probable Leaching Mechanisms for Spent Fuel", CONF-8005107, April 1981.

(2.24) R. Wang and Y. B. Katayama, "Dissolution Mechanisms for UO_2 and Spent Fuel", Nuclear and Chemical Waste Management, 3, 1982, pp. 83-900

(2.25) Y. B. Katayama, "Spent Fuel (LWR) Leach Tests", PNL-2982, April 1979.

(2.26) Y. B. Katayama, D. J. Bradley and C. O. Harvey, "Status Report on LWR Spent Fuel IAEA Leach Tests", PNL-3173, March 1980.

(2.27) R. Wang, "Spent Fuel Special Studies Progress Report: Probable Mechanisms for Oxidation and Dissolution of Single Crystal UO_2 Surfaces", PNL-3566, March 1981.

3. CONTAINER MATERIALS

The container consists of two or more concentric metallic enclosures that act as a barrier against the ingress of groundwater or brine to the waste form and the egress of radionuclides to the repository.

During this project year, the possible internal corrosion of the canister by the waste form has been studied. The canister is the innermost metallic enclosure and is in direct contact with the waste. With a borosilicate glass waste form, the most probable canister material is Type 304L stainless steel. Canister corrosion could occur during the relatively short period of time when the glass is molten. Corrosion can also occur during the long period of time when the glass is still hot, e.g., when it is in storage awaiting final disposition. To determine the long-term corrosive effects of the waste form on the canister materials, coupons of Type 304L stainless steel and its casting equivalent, CF8 alloy, were exposed to PNL 76-68 waste glass at elevated temperatures. The pits produced by corrosion were measured, and the mechanism of corrosive attack was studied.

The general and localized corrosion of the outer metallic enclosure, or overpack, by water in the repository has also been studied. At the outset of the project, a potential overpack consisted of a thick-walled steel container covered by a thin shell of a titanium alloy. This was considered for use in a salt repository. To study overpack corrosion in the titanium - salt system, coupons of Titanium Grade 12 were exposed in an autoclave to high-temperature simulated brines. However, the use of a titanium shell has subsequently been in less favor by the DOE, so the effort has shifted from titanium to cast and wrought low-carbon steels, which are being considered for use in a basalt repository. To study corrosion in the steel - basalt system, steel coupons were exposed in an autoclave to high-temperature simulated basalt groundwaters of varying concentration. The steel coupons were cast and wrought specimens of two different compositions, one ("doped") approximating the composition of 1018 steel, and the other ("clean") containing lower levels of phosphorus and sulfur. The effect of groundwater on the relevant electrochemical and mechanical behaviors of these steels is being evaluated, along with the possible embrittlement of a cast steel overpack by hydrogen generated during corrosion reactions, and radiolysis.

Closely related to these experimental efforts is the ongoing development of a mathematical description of general corrosion and pitting corrosion of container materials. The general-corrosion correlation has been refined and simple test cases are being evaluated. Efforts in developing the pitting-corrosion correlation have focused on the kinetics of pit generation and pit growth.

3.1 Internal Corrosion

The experimental investigation of internal corrosion of the canister was carried out by exposing metal coupons to a reference waste glass under a range of temperature conditions. The corrosive effects of the waste glass on the coupons were determined by measurement of pit depths. The mechanism of the corrosive attack was studied by analysis of the corrosion products using energy dispersive X-ray analysis in the scanning electron microscope.

3.1.1 Materials

Coupons of Type 304L stainless steel in the shape of rectangular solids having the nominal dimensions 3.81 cm x 2.54 cm x 0.238 cm were used for the experiments. The specimens were polished to a 600 grit finish before use. Crucibles of Type 304L stainless steel were fabricated by welding bases on short lengths of tubing. The certified analysis for the stainless steel sheet and tubing that were used for the specimens and the crucibles are shown in Table 3.1.

Table 3.1 Certified analyses of Type 304L stainless steel

	Composition, weight percent	
	Sheet	Tubing
Carbon	0.017	0.016
Manganese	1.44	1.72
Phosphorus	0.026	0.024
Sulfur	0.010	0.013
Silicon	0.58	0.43
Chromium	18.29	18.64
Nickel	8.63	8.66
Molybdenum	0.29	--

A few specimens also were prepared from CF8 alloy, which is the casting equivalent of Type 304L stainless steel. Some consideration has been given to casting high-level waste canisters from the large supply of contaminated Type 304 stainless steel. Thus some evaluation of CF8 alloy was made in this study. The composition of the CF8 alloy is shown in Table 3.2. This alloy contained substantially more chromium and slightly less nickel than the Type 304L stainless steel.

A supply of PNL 76-68 reference simulated waste glass, obtained from Battelle's Pacific Northwest Laboratories, was used for the coupon exposures. This glass is composed of two parts Frit 76-101 and one part Waste Type PW-8a. The chemical composition of the particular lot from which the supply was obtained is shown in Table 3.3.

Table 3.2 Certified analysis of CF8 alloy

Component	Composition, weight percent
Carbon	0.052
Manganese	0.069
Phosphorus	0.119
Sulfur	0.017
Silicon	0.93
Chromium	20.59
Nickel	8.48
Molybdenum	0.11

3.1.2 Accelerated Test Planning/Statistics

A baseline experiment for the program was developed. The responses were the extent of pitting corrosion and chemical species present in pitted areas. The primary experimental variables were exposure temperature and time. For each temperature, the extent of corrosion was studied at multiple times. The maximum test temperature was 900 C. Based on data reported in the literature, a tentative average trend curve of general corrosion versus time was derived for planning purposes. Tentative exposure times at 900 C were established based on this curve. These exposure times proved to be adequate.

3.1.3 Experimental Procedure

The metal coupons were exposed to the waste glass by heating in muffle furnaces at temperatures of 900, 700, 500, and 300 C. Approximately 120 g of the glass was melted in each crucible at 1000 C, and two metal specimens were then immersed in each crucible. The exposure times for the different temperatures were based on the assumption of an Arrhenius relationship for temperature effects and were as follows:

900 C	700 C	500 C	300 C
400 hrs	470	620	974
750	890	1172	1826
1330	2664	2065	3273
1930			

The third set of specimens at 700 C was inadvertently exposed longer than the planned 1580 hours.

Six specimens were removed from exposure at each of the times indicated, and they were taken from different regions of the furnace. When the specimens were removed from the crucibles, the glass adhered to the

Table 3.3 Composition of PNL 76-68 glass

Oxide	Average Analysis of 3 Bars (%)	Standard Deviation (%)
Al_2O_3	0.84	0.03
B_2O_3	8.65	0.06
BaO	0.62	0.01
CaO	2.29	0.04
CdO	0.05	0.01
Cr_2O_3	0.50	0.02
Cs_2O	1.21	0.08
Dy_2O_3	0.01	0.00
Eu_2O_3	0.01	0.00
Fe_2O_3	9.08	0.12
Gd_2O_3	0.03	0.01
K_2O	0.09	0.03
La_2O_3	4.89	0.06
MgO	0.18	0.01
MnO_2	0.06	0.00
MoO_3	2.17	0.01
Na_2O	11.60	0.95
Nd_2O_3	1.65	0.01
NiO	0.25	0.03
P_2O_5	0.56	0.08
SiO_2	40.33	0.81
SrO	0.49	0.01
TiO_2	2.86	0.04
ZnO	4.75	0.08
ZrO_2	2.33	0.04
Total	95.50	

surfaces in different amounts for the various specimens. Most of this glass could be broken away, but enough remained so that weight change measurements could not be used as a measure of the metal corrosion. Consequently, pit-depth measurements were made to determine the extent of corrosive attack on the specimens.

Each specimen was sectioned across the width at the center line and one of the cut surfaces was mounted and polished. The edges which had been in contact with the glass were then examined for pitting attack, using an optical microscope. The measurements were made at a magnification of 200X, using an eyepiece equipped with a reticle.

3.1.4 Pit-Depth Measurements

In all specimens, a relatively large number of small pits having depths of 5-10 μm were observed. The numbers of such pits increased with exposure time at each temperature, as would be expected. The effect of exposure time on pit development at 900 C is shown in Figure 3.1, where the pit distribution along the center line of the two worst specimens is plotted for each of the four exposure times. There was a reasonably uniform increase in the number of pits less than 20 μm depth as the time increased from 400 to 1930 hours. However, for deeper pits the growth pattern was erratic. There was a large increment in the moderate-depth pitting between 400 and 750 hours, after which the numbers stayed about the same. The deeper pits (60-150 μm) were relatively few, and the increase with time was small. Nevertheless, the deep pits are the most important in determining the rate at which the stainless steel will be penetrated by the corrosive attack of the waste glass.

The results at 700 C are shown in Figure 3.2. More small pits were observed at this temperature than at 900 C, but there were very few pits deeper than 10 μm in the 700 C specimens. This rapid drop in pit-depth growth at the lower temperature indicates that although pit initiation occurs readily at 700 C, there is little driving force to increase the pit depth. As Figure 3.2 illustrates, there were very few pits deeper than 20 μm, with a single pit that reached a depth of 100 μm.

At 500 C, the number of 5-10 μm pits was approximately proportional to exposure time, as shown in Figure 3.3. As at the other temperatures, there was a sharp drop in the number of larger pits, and in spite of the long exposure time only one was detected that grew as deep as 40 μm.

The pit development at 300 C is presented in Figure 3.4. As at the other temperatures, there was a significant increase in the number of small pits as the exposure time was lengthened. However, in this case no pits greater than 20 μm depth were observed, and there were relatively few pits in the 15-20 μm range.

When the maximum pit depths for each time-temperature combination are converted to penetration rates in micrometers/year, the resultant data produce the curves shown in Figure 3.5. The maximum penetration rates

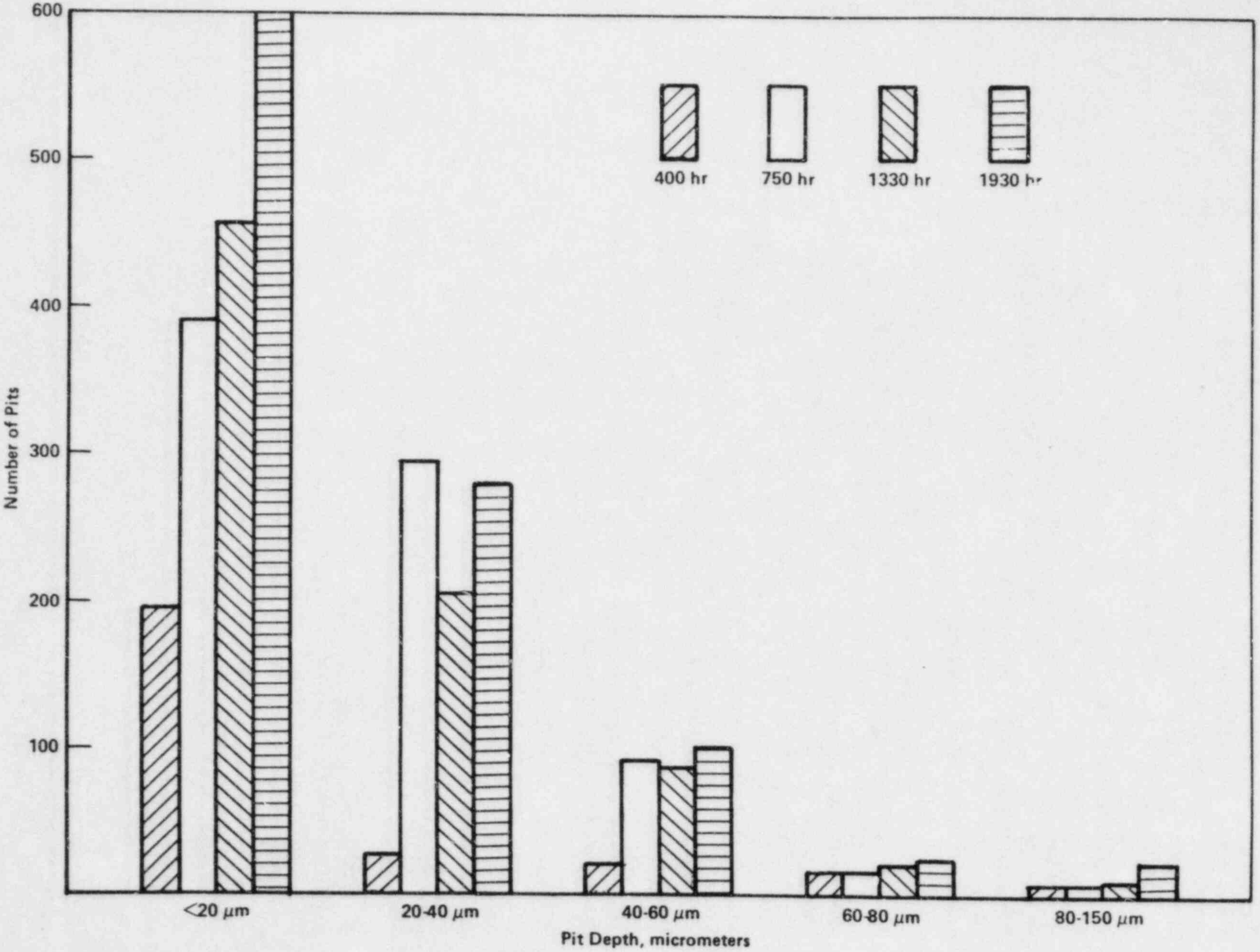

Figure 3.1 Effect of exposure time on pit development at 900 C.

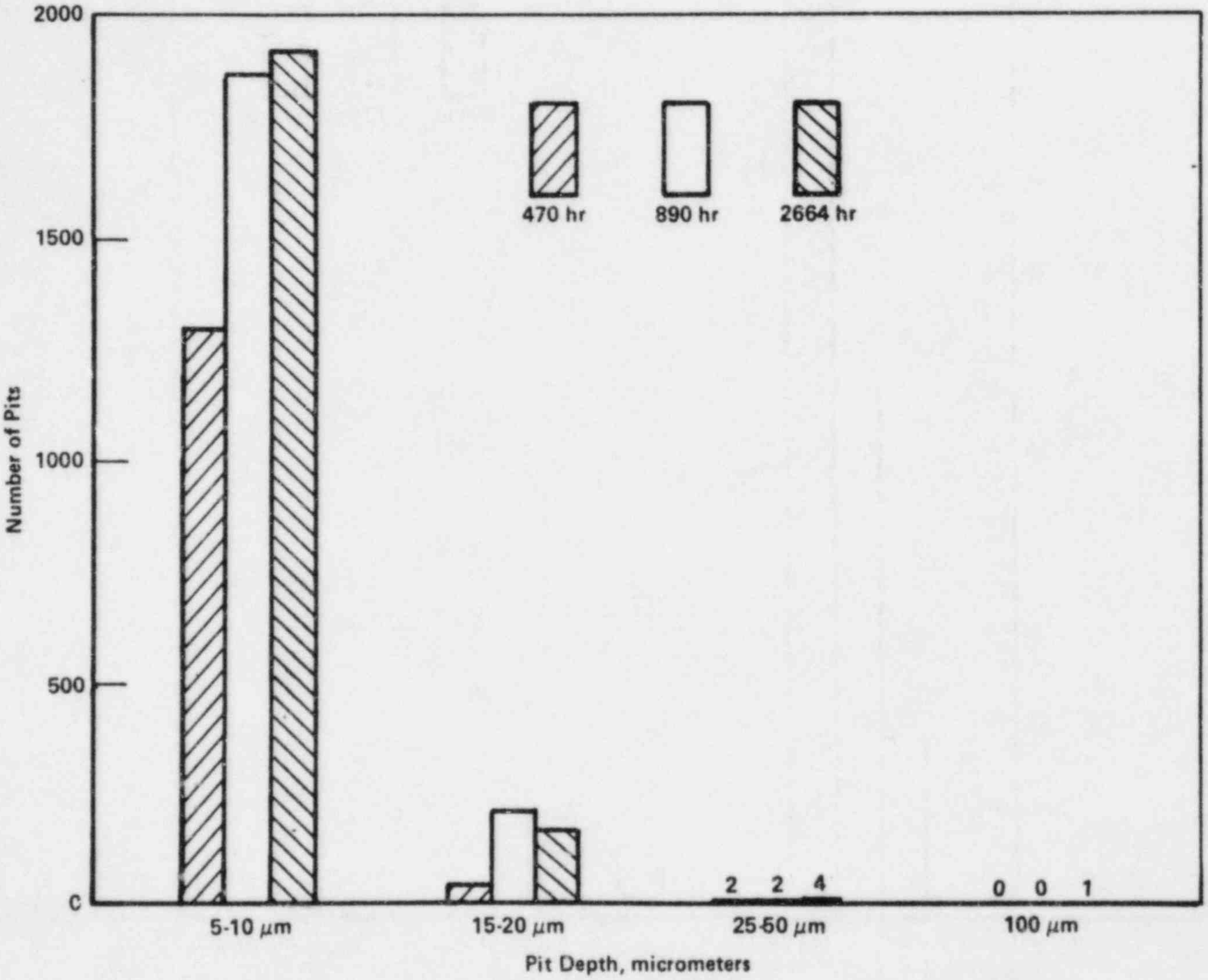

Figure 3.2 Effect of exposure time on pit development at 700 C.

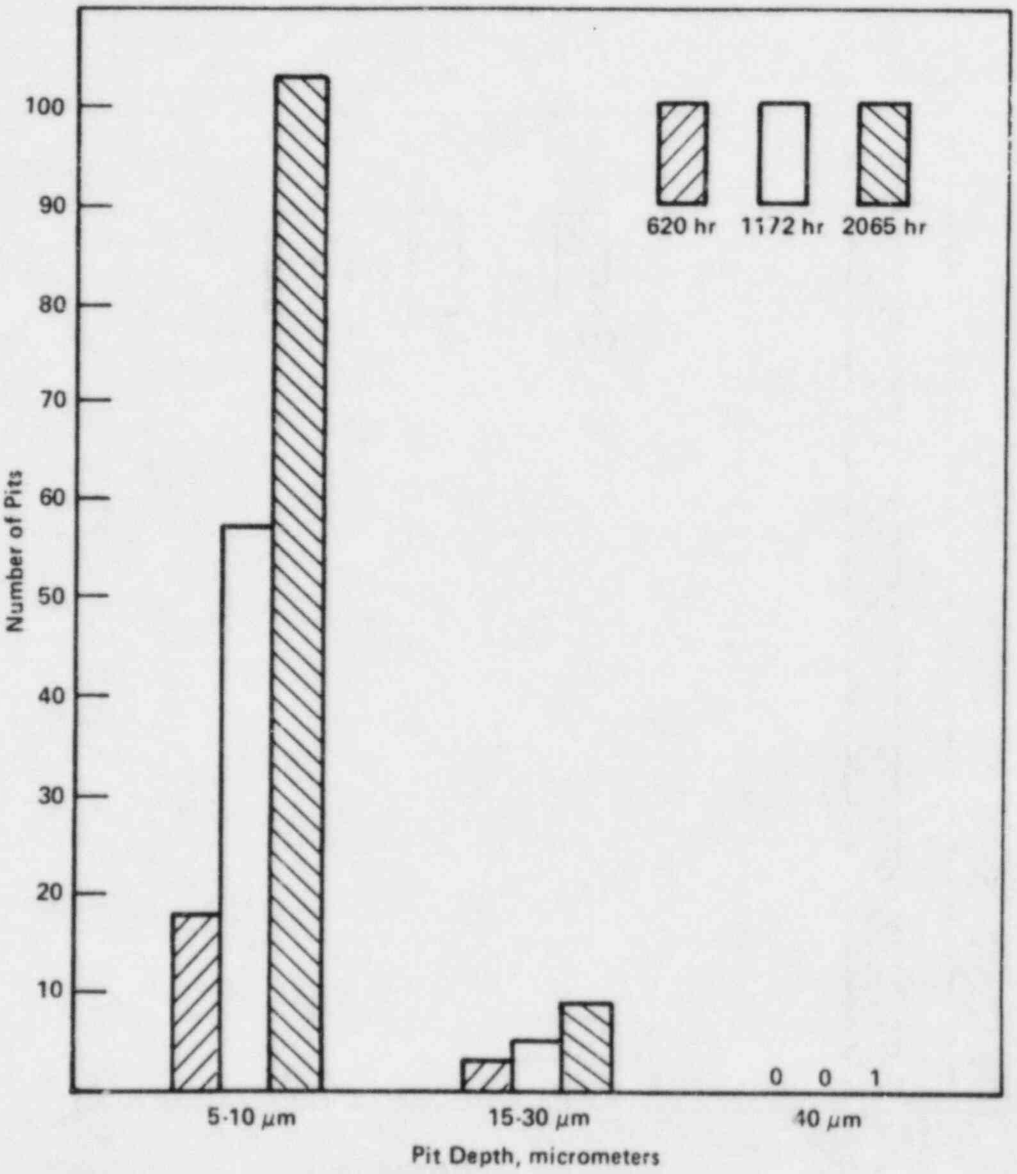

Figure 3.3 Effect of exposure time on pit development at 500 C.

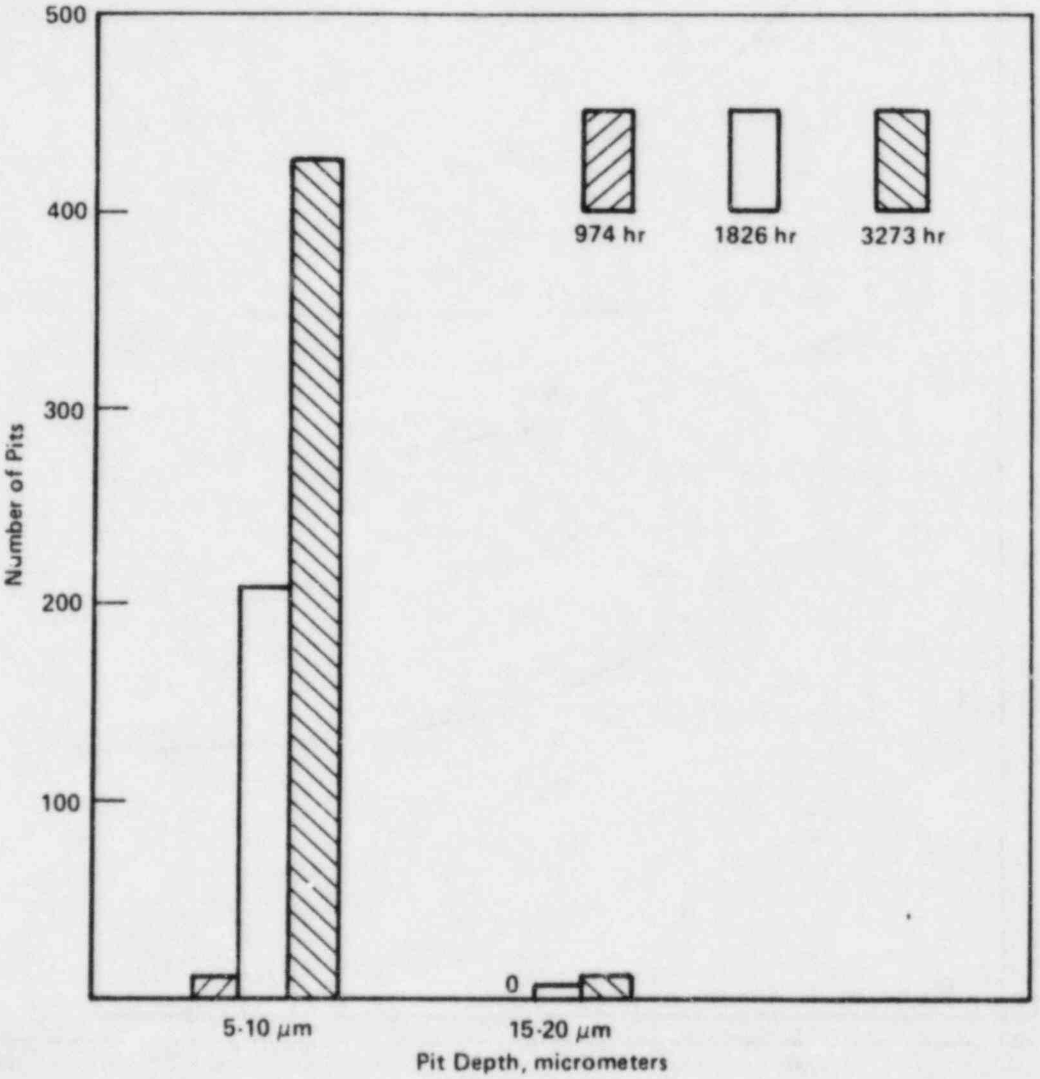

Figure 3.4 Effect of exposure time on pit development at 300 C

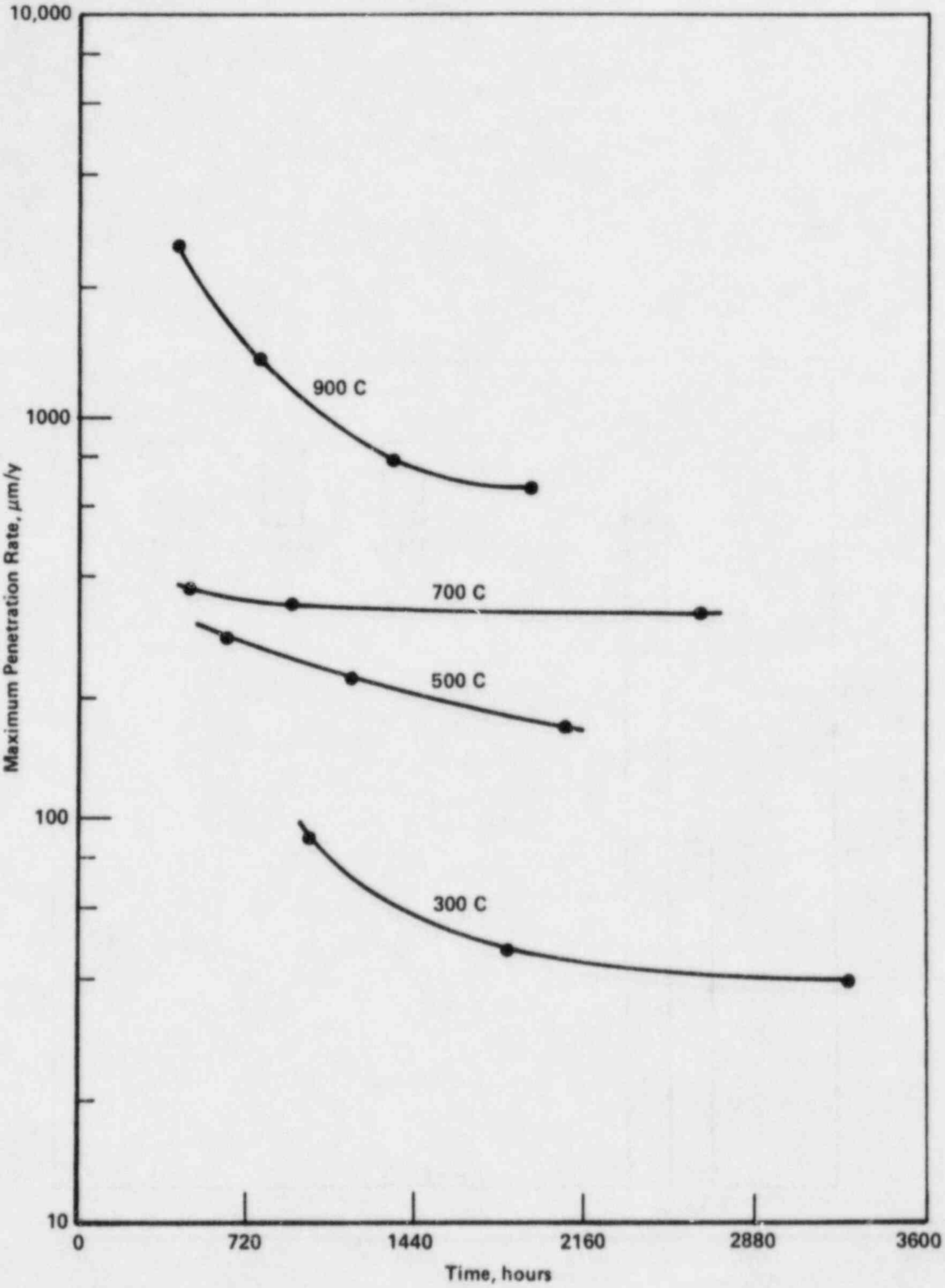

Figure 3.5 Pitting penetration rates as a function of time

plotted as a function of exposure time at the four temperatures make a family of curves that illustrates the rapid decrease in corrosive attack on the stainless steel as the temperature is lowered. From the trend of these curves it could be estimated that at a canister wall temperature of 100-150 C, the long-term rate of attack would be of the order of 10-15 μm/year.

The maximum penetration rates for the longest exposure times at each of the four temperatures are plotted as a function of temperature in Figure 3.6. These data result in a curve which indicates that a penetration rate of 15-20 μm/year would occur at a temperature of 200 C.

When a curve was fitted to these four points, the best fit proved to be an exponential having the equation:

$$\text{Rate, } \mu\text{m/yr} = 878.734\left(\frac{1000}{^{\circ}\text{C}}\right)^{-2.535}.$$

Calculation of the penetration rate at 200 C from this equation gives a value of 14.8 μm/yr. At 150 C, the rate would drop to 7.2 μm/yr from this calculation. This latter value is somewhat lower than that estimated in Figure 3.5. The result obtained from the curve fitting is probably more valid than that obtained by estimation of the temperature trends shown in Figure 3.5.

It has been suggested that a 3/8-inch (9525-μm) wall thickness of the stainless steel be used for the canister. If there were to be a constant pit penetration rate as high as 14.8 μm/year, such a wall thickness would be penetrated in 643 years. If the rate were only 7.2 μm/year, it would take 1330 years for penetration. These times may be conservatively short, because they assume a constant diffusion of corrosive agents to the glass-metal interface.

It should be emphasized that the maximum rates used to get the plots in Figures 3.5 and 3.6 occurred for only a few pits at each temperature. Consequently, if such attack rates were achieved at the canister wall for the long term, there would still only be relatively few points of penetration.

3.1.5 Corrosion-Product Analysis

One of the mounted and polished specimens from each time-temperature combination was examined in the scanning electron microscope. Typical pits were selected, and the composition of the corrosion products in these pits was determined by energy dispersive x-ray analysis.

The scanning electron micrographs for the specimens at 900 C are shown in Figures 3.7-3.11, together with the elemental analysis of the corrosion products. A typical pit in a specimen exposed for 400 hours

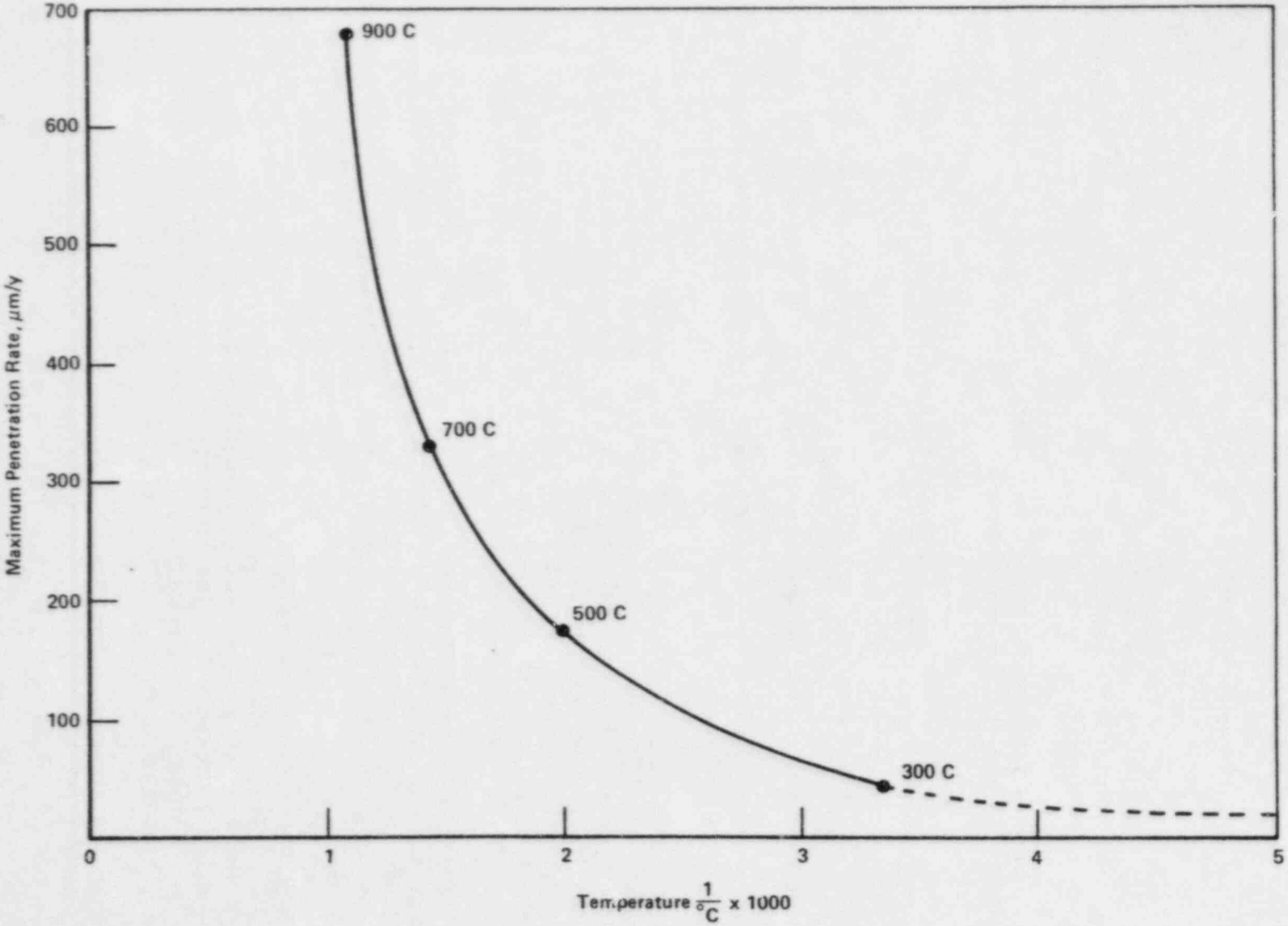

Figure 3.6 Pitting penetration rates for longest exposure times as a function of temperature.

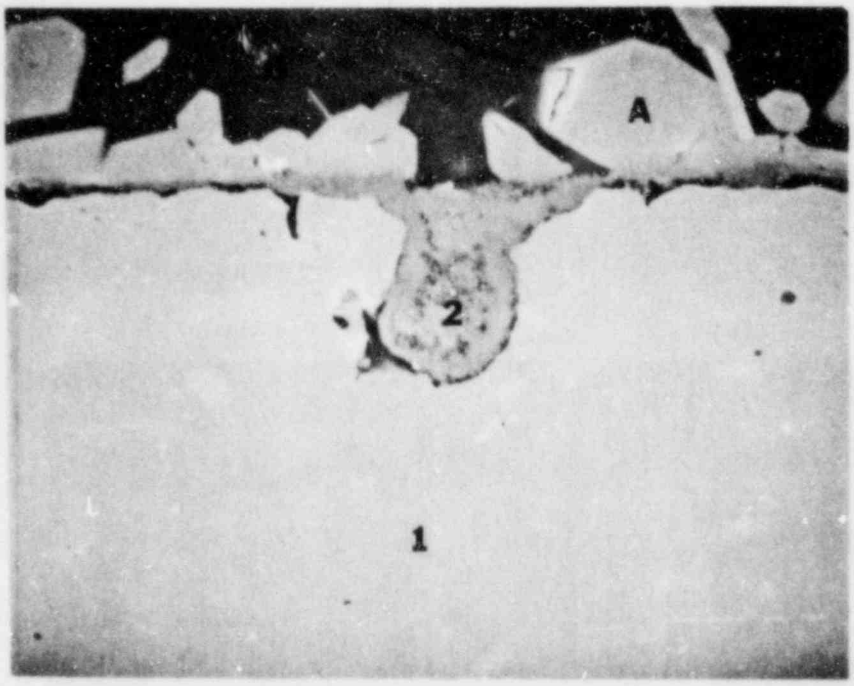

Component	Composition, weight percent			
	Base Metal (Area 1)	Corrosion Pit (Area 2)	Glass (Phase A)	Glass (Phase B)
Fe	71.69	8.23	12.10	17.17
Cr	18.48	62.76	5.18	--
Ni	9.83	10.54	2.49	0.71
Si	--	17.23	20.18	50.74
Zn	--	1.24	--	8.71
Pb	--	--	--	8.18
Ti	--	--	25.51	--
Ca	--	--	4.29	3.73
Pr	--	--	24.49	4.01
Gd	--	--	2.68	--
P	--	--	3.08	4.61
Cs	--	--	--	1.87
K	--	--	--	0.27

Figure 3.7 Energy dispersive x-ray analysis of 900 C specimen (400-hour exposure)

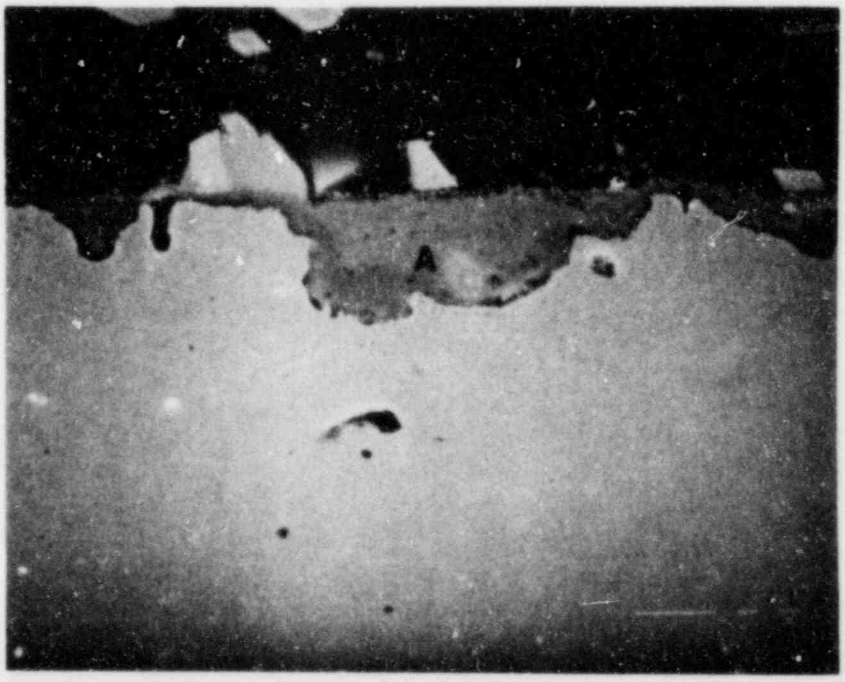

42005 1000X

Component	Composition (Area A), wt. percent
Fe	19.56
Cr	44.63
Ni	10.77
Zn	21.36
Pb	1.84
Si	1.46
Ti	0.39

Figure 3.8 Energy dispersive x-ray analysis of corrosion products in 900 C specimen (400-hour exposure)

42376 1000 X

Component	Composition (Area A), wt. percent
Cr	64.83
Ni	12.45
Fe	11.23
Zn	7.63
Si	2.78
S	1.08

Figure 3.9 Energy dispersive x-ray analysis of 900 C specimen (750-hour exposure)

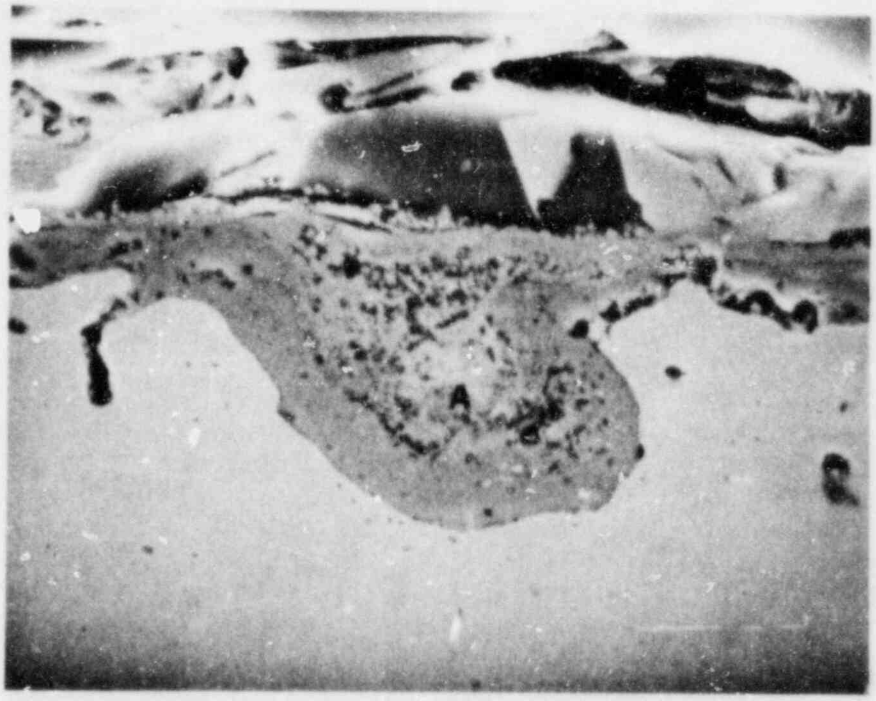

42374 1000 X

Component	Composition (Area A), wt. percent
Cr	62.04
Ni	11.21
Fe	7.50
Si	11.82
Zn	7.15
Ti	0.28

Figure 3.10 Energy dispersive x-ray analysis of 900 C specimen (1330-hour exposure)

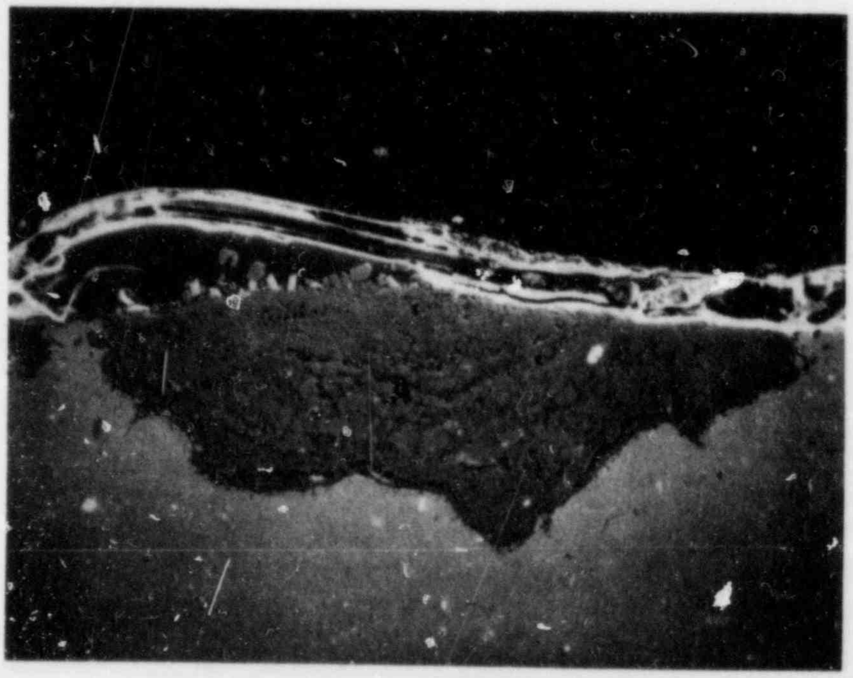

45756 200 X

Component	Composition (Area A), wt. percent
Cr	34.11
Fe	33.16
Ni	14.91
Si	10.61
Zn	7.09
Ti	0.13

Figure 3.11 Energy dispersive x-ray analysis of 900 C specimen (1930-hour exposure)

(Figure 3.7) contained the iron, chromium, and nickel of the base metal, plus silicon and zinc from the glass. Two distinct phases were observed in the glass which adhered to the specimen. The light-colored phase A was largely silicon, titanium, praseodymium, and iron. The dark-colored phase B was mostly silicon and iron, with moderate amounts of zinc and lead. Neither of these compositions is typical of the bulk glass, and it is likely that other phases exist in the waste glass. Another pit in the same specimen contained a large amount of zinc in addition to the base metal components (Figure 3.8). This 21.36 percent concentration of zinc is 5.6 times that which is present in the waste glass.

A comparison of Figure 3.9 with Figure 3.7 illustrates the increased pit growth with exposure of 750 hours as compared to 400 hours. The longer exposure also resulted in a higher concentration of zinc in the pit. A small amount of sulfur also was present in the 750-hour specimen.

Extending the exposure to 1330 hours (Figure 3.10) resulted in a typical pit having a greater volume but not greater depth than that at 750 hours. The zinc concentration was about the same in both cases, but the longer exposure resulted in more silicon in the corrosion products. Titanium appeared instead of sulfur.

After 1930 hours (Figure 3.11), the pit depth was substantially greater, and to include the entire pit in the micrograph it was necessary to reduce the magnification to 200X. The amounts of silicon, zinc, and titanium in the pit were very close to those found in the previous analysis (Figure 3.10). The distribution of base metal elements was quite different, however.

Pits developed at 700 C are shown in Figures 3.12-3.14. At 470 hours (Figure 3.12) the pit was small, but there was grain boundary penetration to 7 μm. In addition to the elements found in the pits at 900 C, sodium and vanadium were detected in small amounts. The greater pit development after 890 hours at 700 C can be seen in Figure 3.13. The levels of silicon, zinc, titanium, and sulfur all were higher in this case, with phosphorus and calcium appearing as well. Pitting after 2664 hours at 700 C is shown in Figure 3.14. This analysis is the first that did not show the presence of zinc, although silicon, titanium, and sulfur were present in small amounts, along with aluminum.

The analysis of the corrosion products in a pit on a specimen exposed at 500 C for 620 hours is shown in Figure 3.15. The pits on this specimen were shallow compared to many of those formed at higher temperatures, but the zinc content of the corrosion product layer was high. After 1172 hours at 500 C (Figure 3.16), the pit depth was slightly greater, and more elements were detected in the pit. However, the only one not previously detected in corrosion products was potassium. The pits were still rather shallow after 2065 hours at 500 C (Figure 3.17). In this case a large amount of zinc was found, together with the usual silicon and titanium. Molybdenum was observed for the first time in a corrosion product layer.

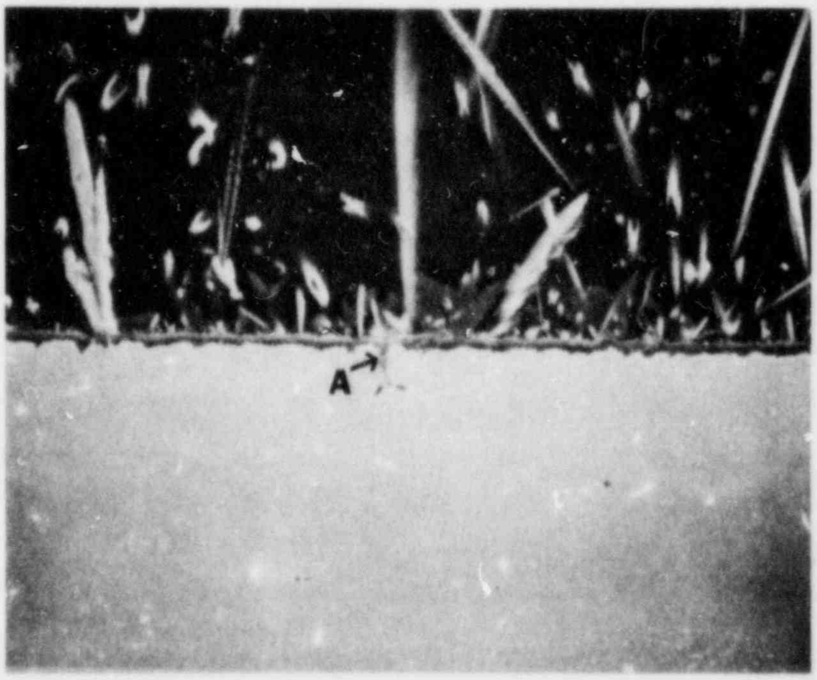

45397 1000 X

Component	Composition (Area A), wt. percent
Cr	69.54
Fe	9.11
Ni	1.40
Si	11.18
Na	3.47
Zn	1.92
Ti	1.69
S	1.00
V	0.69

Figure 3.12 Energy dispersive x-ray analysis of 700 C specimen (470-hour exposure)

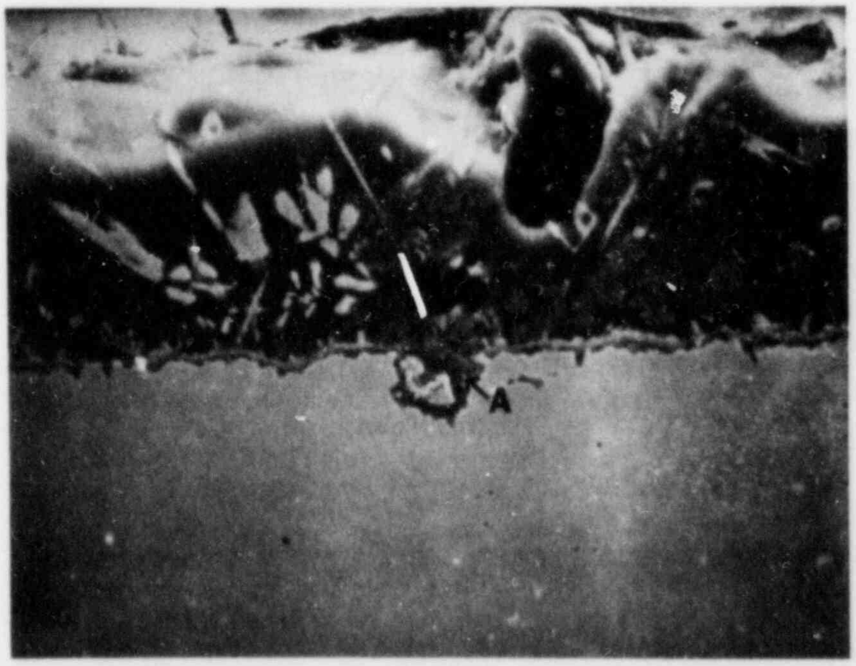

45758 1000 X

Component	Composition (Area A), wt. percent
Cr	27.12
Fe	20.05
Ni	2.78
Si	28.79
Zn	9.36
P	3.76
Ti	3.11
S	2.64
Ca	2.40

Figure 3.13 Energy dispersive x-ray analysis of 700 C specimen (890-hour exposure)

45395 1000 X

Component	Composition (Area A), wt. percent
Cr	47.16
Fe	29.25
Ni	14.16
Si	5.71
Al	2.30
Ti	0.74
S	0.68

Figure 3.14 Energy dispersive x-ray analysis of 700 C specimen (2664-hour exposure)

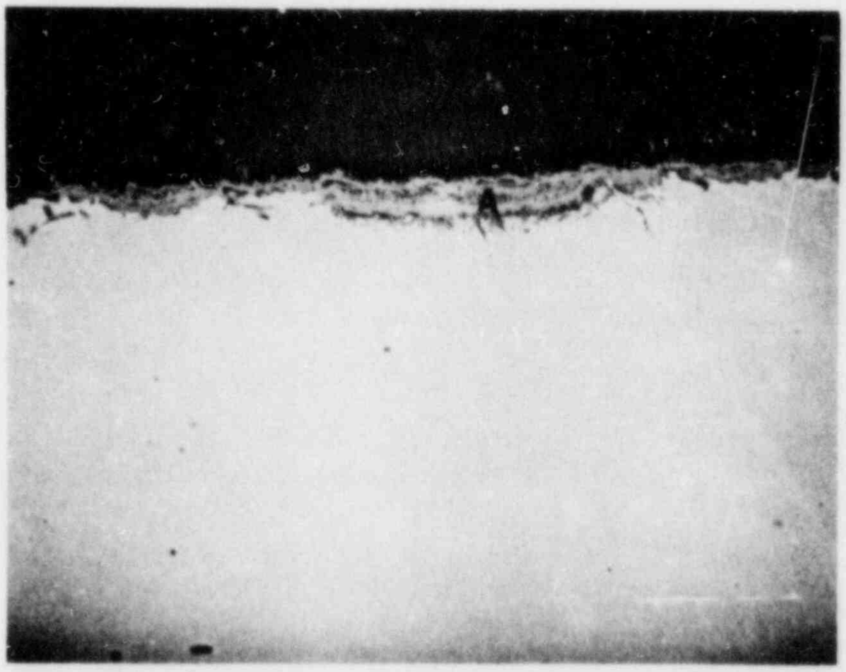

Component	Composition (Area A), wt. percent
Fe	19.02
Cr	46.18
Ni	1.45
Si	10.93
Zn	17.68
Pb	4.05
Ti	0.70

Figure 3.15 Energy dispersive x-ray analysis of corrosion products on 500 C specimen (620-hour exposure)

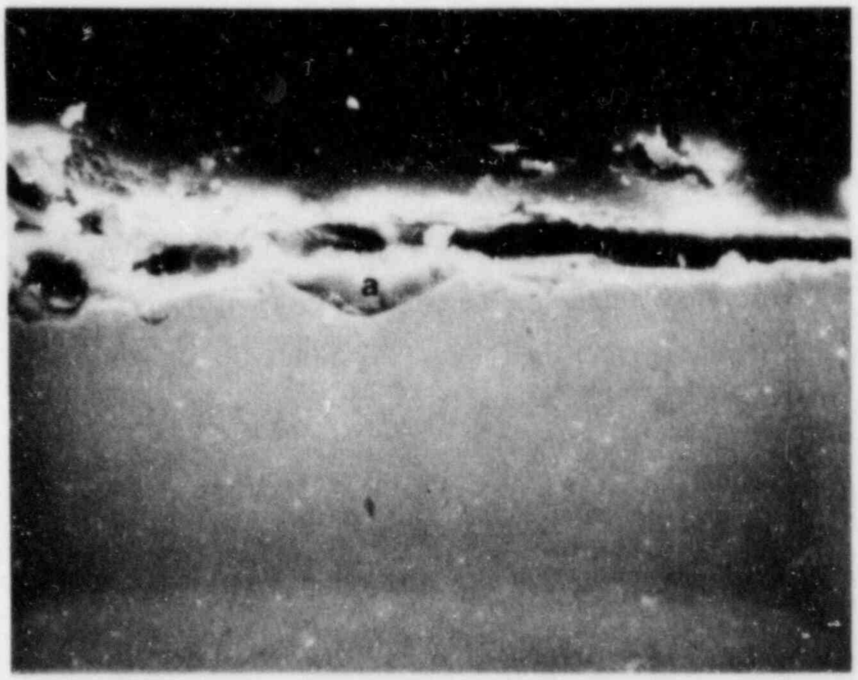

44749 1000 X

Component	Composition (Area a), wt. percent
Fe	17.39
Ni	1.66
Si	47.44
Zn	7.92
Ti	6.91
P	6.42
S	4.51
Ca	4.22
V	2.10
K	1.44

Figure 3.16 Energy dispersive x-ray analysis of 500 C specimen (1172-hour exposure)

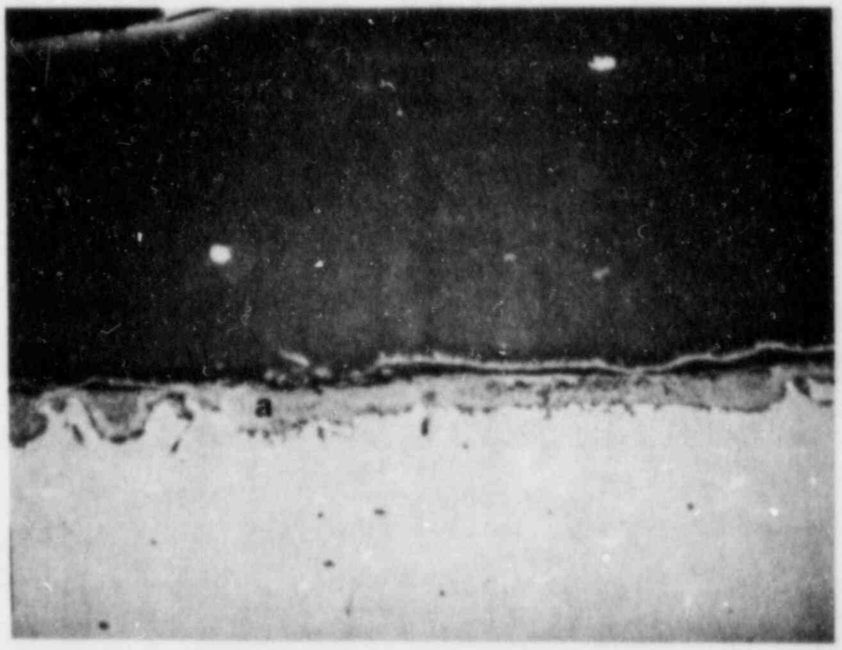

42775 1000 X

Component	Composition (Area a), wt. percent
Cr	49.15
Zn	19.06
Fe	17.69
Si	6.99
Mo	3.31
Ni	2.64
Ti	1.16

Figure 3.17 Energy dispersive x-ray analysis of 500 C specimen (2065-hour exposure).

Although pits developed on the 300 C specimens during the 974-hour exposure, (Figure 3.18), most of them were in the early stages of growth, and the corrosion layer contained a variety of elements. None of these were new, but the high silicon and sodium contents were unusual. It should be noted that this area required greater magnification (2500 X) than pits formed at the higher temperatures. A large amount of zinc was found in the products on the 1826-hour specimen at 300 C (Figure 3.19). The other elements present were typical of those found for other specimens that were analyzed. Only a thin corrosion-product layer was found on the specimen exposed at 300 C for 3273 hours (Figure 3.20). However, there was grain boundary penetration as deep as 10 µm. Only small concentrations of silicon and zinc were found in this case.

These analyses demonstrated that silicon, zinc, and titanium were almost always present in the corrosion products, sometimes in large amounts. Although a few other elements were detected in addition to these three, the silicon, zinc, and titanium must play a major role in the pitting attack on the stainless steel.

3.1.6 CF8 Alloy Exposure

Enough material was available to prepare 6 specimens of the CF8 alloy for comparison with the Type 304L stainless steel. These specimens were exposed at 900 C for 750 hours, thus providing data under the same exposure conditions as those for one set of the Type 304L specimens. On completion of the exposure it was found that very little glass adhered to the CF8 alloy, in contrast to the strong bonding of the waste glass to the Type 304L alloy. Pit-depth measurements for the two worst specimens are shown below with comparable data for the corresponding exposure of the Type 304L stainless steel:

	Number of Pits	
Pit depth, µm	CF8	304L
20	644	390
20-40	68	295
40-60	15	90
60-80	2	15
80-150	-	10

Many more small pits were initiated in the CF8 alloy, but few of these pits increased in depth during the exposure, as compared to the Type 304L stainless steel. Apparently the inability of the waste glass to bond to the CF8 alloy resulted in superficial pitting, with little penetration into the metal surface.

Metallographic examination of the CF8 alloy showed that its microstructure was distinctly different from that of the Type 304L stainless steel. The photomicrographs shown in Figure 3.21 illustrate this difference. The Type 304L had a typical austenitic structure, with small equiaxed grains and annealing twins. On the other hand, the CF8

42006 2500X

Component	Composition (Area A), wt. percent
Fe	31.79
Cr	5.93
Ni	3.11
Si	37.61
Zn	1.68
Ti	1.26
Na	13.34
Al	3.56
Ca	1.53
K	0.19

Figure 3.18 Energy dispersive x-ray analysis of corrosion products on 300 C specimen (974-hour exposure)

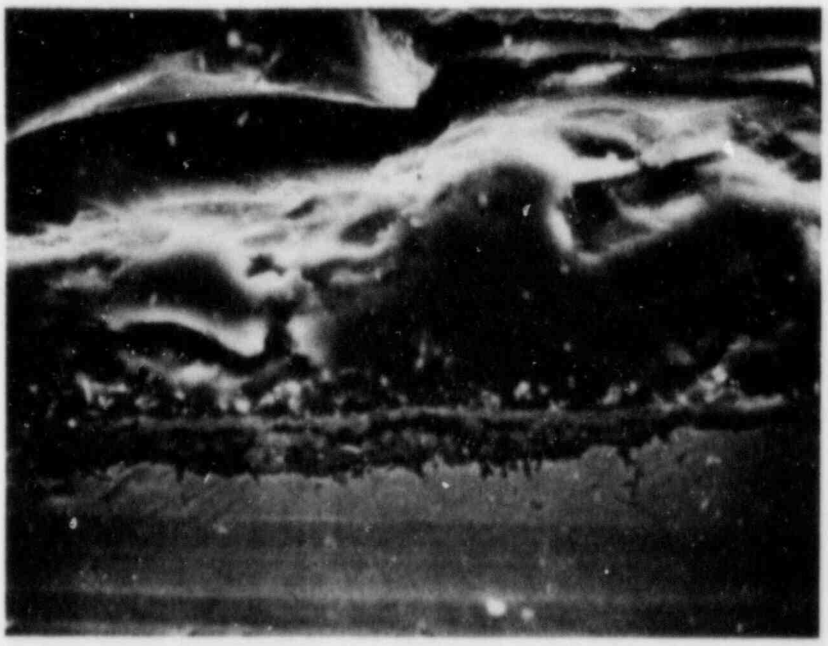

42772 1000 X

Component	Composition (Area a), wt. percent
Cr	49.17
Fe	21.04
Zn	16.89
Si	7.42
Ni	3.65
Ti	1.03
S	0.79

Figure 3.19 Energy dispersive x-ray analysis of 300 C specimen (1826-hour exposure).

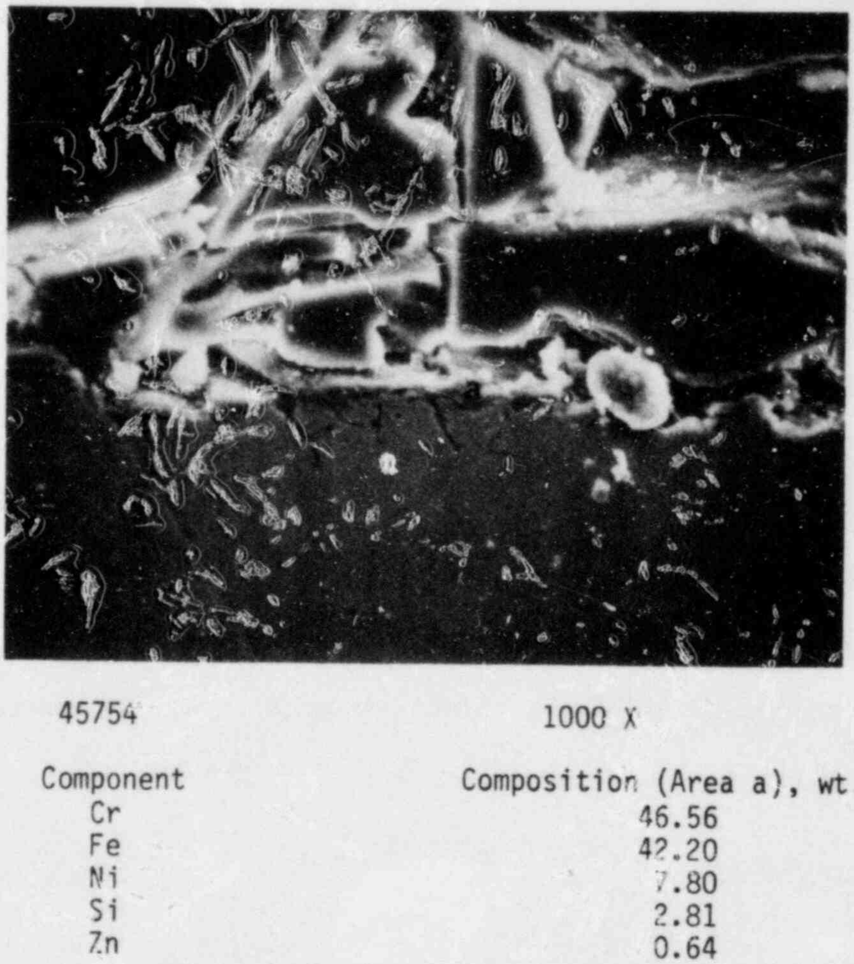

45754 1000 X

Component	Composition (Area a), wt. percent
Cr	46.56
Fe	42.20
Ni	7.80
Si	2.81
Zn	0.64

Figure 3.20 Energy dispersive x-ray analysis of 300 C specimen (3273-hour exposure).

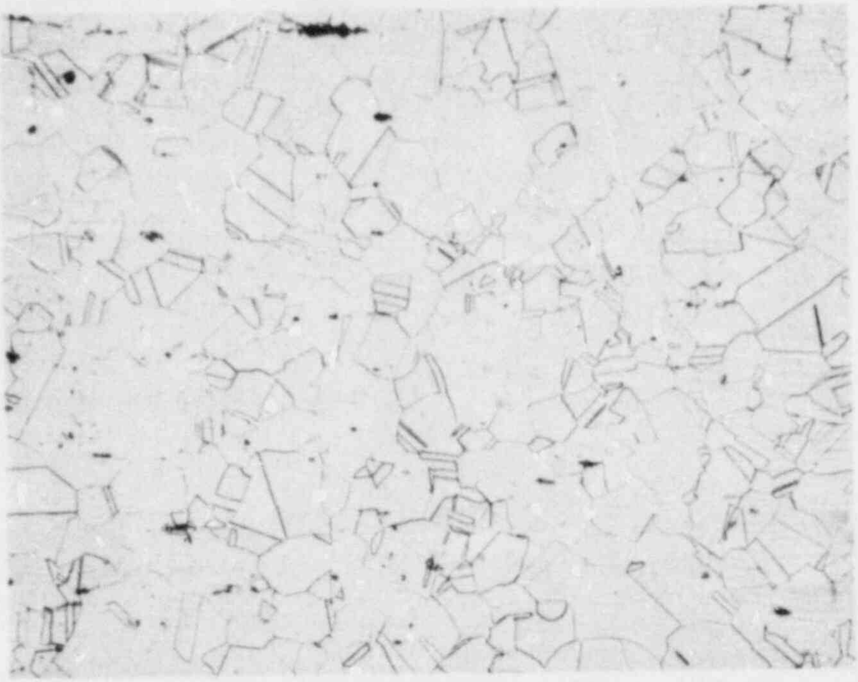

304L 200X

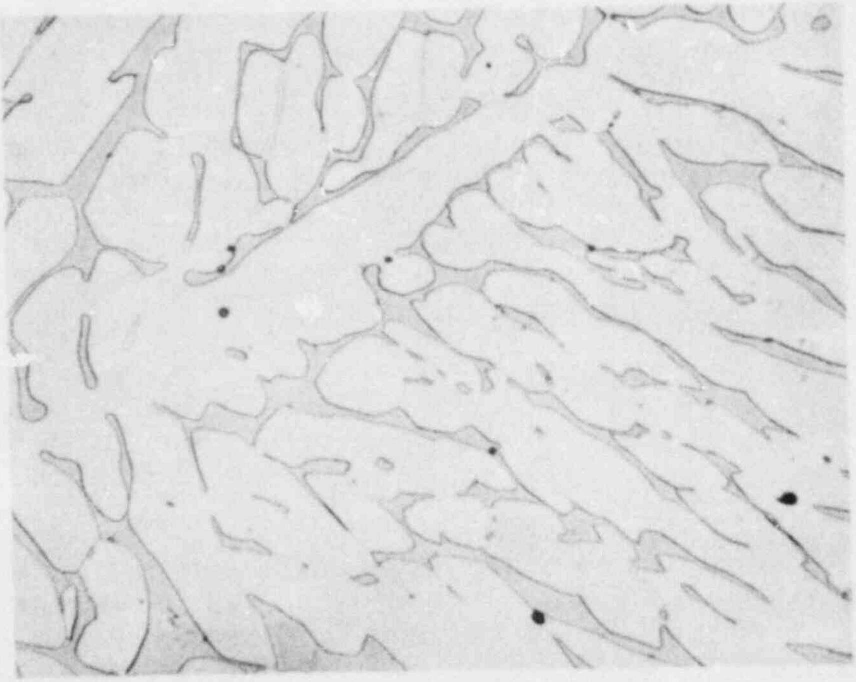

CF8 200X

Figure 3.21 Photomicrographs of Type 304L and CF8 stainless steels alloy had large grains, with ferrite islands (dark) in a matrix of austenite. This structural difference would provide a surface on the Type 304L alloy with more grains per unit area, which could account for greater bonding of the glass to the metal. The small difference in chemical composition of the two alloys (Tables 3.1 and 3.2) would not be expected to influence the bonding to any great extent, and it is more likely that surface effects are responsible for the lack of adherence of the glass to the CF8 alloy.

3.1.7 Conclusions

From the results of the exposures of the Type 304L stainless steel to the waste glass over a range of temperatures, the following conclusions can be reached:

1. Pits initiate rapidly on the metal surface at the exposure temperatures of 300-900 C, with more pits forming as the temperature is increased.
2. The increase in pit depth with time of exposure is slow, so that few deep pits are formed even at higher temperatures.
3. The pitting attack results in maximum penetration rates of the order of 10-20 μm/year. A 3/8-inch stainless steel canister would be penetrated in about 500 years at the higher rate and 1000 years at the lower rate.
4. Silicon, zinc, and titanium from the waste glass were found in the corrosion products at all temperatures, indicating that these elements play a role in the attack on the metal.
5. The presence of the same elements in the corrosion products at all temperatures indicates that the corrosion mechanism does not change with temperature.
6. Limited experiments indicate that the glass does not attack CF8 cast stainless steel as much as it does the Type 304L stainless steel; CF8 may be preferable for canister use.

3.2 External Corrosion

The objective of the overpack corrosion effort is to develop an understanding of the corrosion processes which can lead to overpack failure. This objective is being achieved through continued perusal of the relevant literature and experimental evaluation. Two systems have been investigated: Titanium Grade 12 - salt and steel - basalt.

Emphasis in the program was shifted from the Titanium Grade 12 - salt system to the steel - basalt system this year at the request of the NRC. Two autoclave exposures on the former system were completed early in this year, and an additional three autoclave exposures were completed on the steel - basalt system. Electrochemical and slow strain rate evaluations also were performed on the latter system. Significant results of these studies are given below. Detailed procedures are available in the quality assurance documents listed in Section 5.

3.2.1 Titanium Grade 12 - Salt System

At the end of the first year, an autoclave exposure was completed in which the effects of heat transfer and thermal gradients on corrosion of Titanium Grade 12 in deaerated Brine A (see Table 3.4) were studied. This test was performed at 250 C under autogenous pressure for 1000 hours. As described in the 1982-1983 Annual Report(3.1), deposits built up on the heated-specimen surface exposed to the vapor phase, and pressure buildup was noted in the autoclave during the test.

Analysis of the solution from this autoclave experiment was completed early in the second year. Results, given in Table 3.5, indicated the presence of significant quantities of nickel, chromium, and iron. As discussed in the 1982-1983 Annual Report(3.1), this contamination apparently occurred as a result of the unexpected generation of HCl in the vapor phase in the autoclave because of hydrolysis of $MgCl_2$ on the heated surfaces. This HCl promoted severe attack of the HASTELLOY* Alloy C-276 autoclave head. The presence of nickel corrosion products is especially significant since nickel is an inhibitor of localized corrosion of titanium. Thus, the validity of the low corrosion-rate data reported for Titanium Grade 12 in this autoclave experiment is questionable.

Analysis of the electrochemical data from this autoclave exposure also was completed. Two types of electrochemical measurements were performed: galvanic current and polarization resistance. The objective of the galvanic-current experiment was to evaluate the potential influence of variation in the overpack skin temperature, as a function of location, on corrosion rates; this phenomenon is sometimes referred to as thermogalvanic corrosion. The galvanic current between a heated and an unheated specimen, having equal surface areas, was measured periodically by means of a zero-resistance ammeter. The heated specimen was maintained at 270 C by an internal resistance heater; the unheated specimen was equilibrated at the autoclave temperature (250 C). Before each measurement, the polarity of the electrodes also was measured.

It was found that the heated specimen was noble to the unheated one by about 90 mV throughout the exposure, and that the galvanic-current flow was in the direction of the unheated specimen; i.e., the unheated specimen was undergoing galvanic corrosion when contacted by the heated specimen, assuming that the current measured was a corrosion current. Actual current measurements are given in Figure 3.22. These data show that the current fluctuated over the initial 400 hours' exposure around

---

* HASTELLOY is a registered trademark of the Cabot Corporation.

Table 3.4 Nominal composition of Brine A.

Component	Concentration, wppm
Na^+	42,000
K^+	30,000
Mg^{+2}	35,000
Ca^{+2}	600
Sr^{+2}	5
Cl^-	190,000
SO_4^{-2}	3,500
I^-	10
HCO_3^-	700
Br^-	400
BO_3^{-3}	1,200

pH at 25 C = 6.5.

Table 3.5 Results of inductively coupled argon plasma analyses of test solution from the autoclave exposure of Titanium Grade 12 in Brine A where effect of heat transfer was studied.

Element*	µg/ml (ppm)
Arsenic	4.7
Boron	210
Calcium	560
Cobalt	590
Chromium	2,600
Copper	310
Iron	3,600
Magnesium	22,000
Manganese	210
Molybdenum	<8.0
Sodium	37,000
Nickel	9,100
Phosphorus	8.3
Palladium	3.9
Selenium	2.5
Strontium	13.0
Zinc	7.6

*Only elements having a concentration greater than 1 ppm are reported

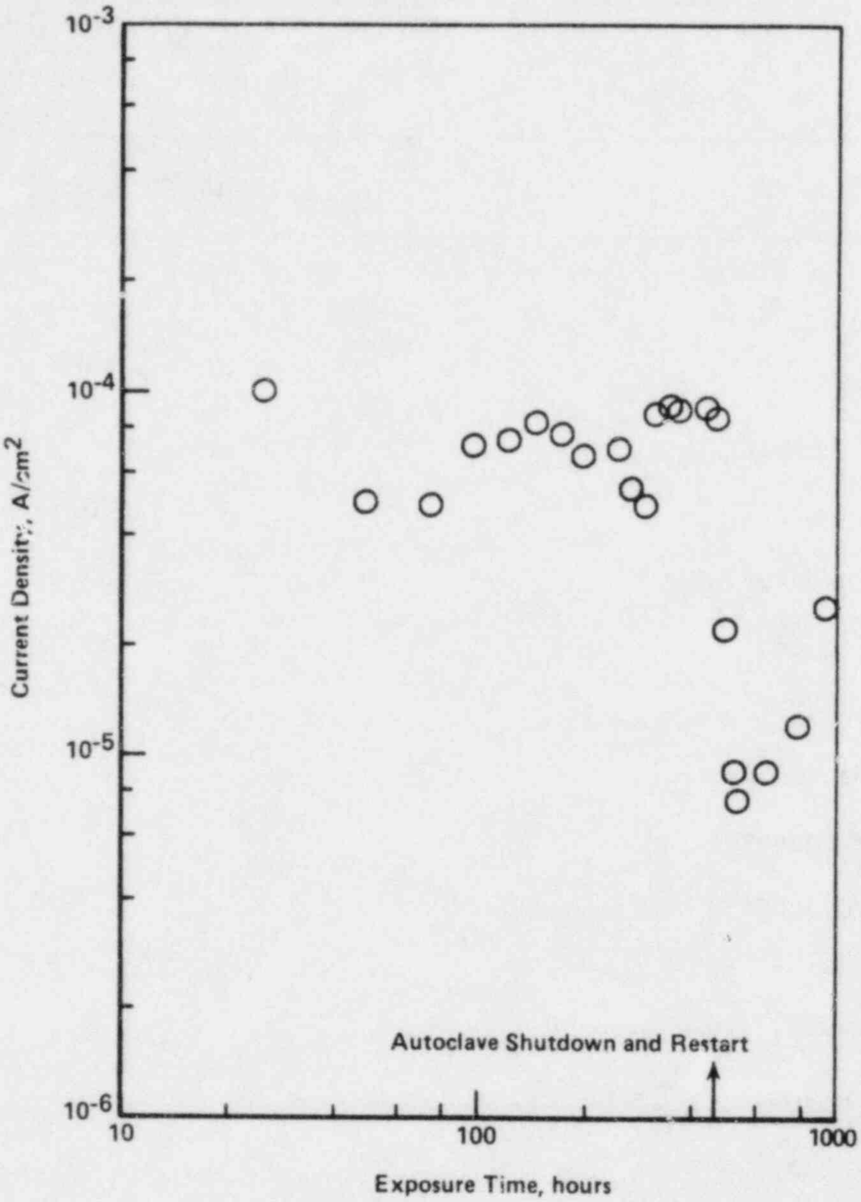

Figure 3.22 Galvanic current density as a function of exposure time for a heated Titanium Grade 12 specimen coupled to an unheated specimen (ΔT = 20 C) having equal surface areas in deaerated Brine A at 250 C.

Heated specimens were noble to unheated specimens throughout exposure.

a value of 8×10^{-5} A/cm^2. Converting this current to a corrosion rate by means of Faraday's Law, and assuming an ionic valence state of +4 for titanium, gives a value of 6.5×10^2 μm/year. This value is more than two orders of magnitude greater than the corrosion rate of the unheated specimen as measured gravimetrically (1.72 μm/year). As discussed in the First Annual Report(3.1), a similar discrepancy was observed between corrosion rates of Titanium Grade 12 in Brine A predicted by polarization resistance and those predicted gravimetrically. This discrepancy was attributed to parasitic redox reactions in the solution which contributed a net current.

The corrosion rate of the unheated thermogalvanic specimen measured gravimetrically was greater, by an order of magnitude, than the corrosion rate of the gravimetric specimen from the previous autoclave exposure, or from immersed U-bend specimens in this autoclave exposure. Thus it appears that the galvanic current measurement successfully predicted the direction of the galvanic effect, but not its magnitude. However, in this autoclave exposure, deposits built up on the heated specimens in the vapor phase, which apparently led to hydrolysis of salts in the deposits and to generation of HCl. The HCl in the vapor may have accelerated the corrosion rate of the electrodes, which pass through the vapor phase, more than that observed with the immersed U-bend specimens.

During this second autoclave exposure, pressure buildup in the autoclave promoted a leak after approximately 450 hours of exposure. As shown in Figure 3.22, galvanic currents measured after restarting the autoclave were considerably lower than those measured before shutdown. The data taken after autoclave startup, however, are not considered to be reliable since deposit buildup may have impinged on the autoclave head by this time and affected the measurements.

Results of the polarization resistance (PR) measurements performed in this autoclave exposure are summarized in Figure 3.23. These data show that the polarization resistance values for the heated specimens are higher (i.e., 1/PR values are lower) than those for the unheated specimens. This suggests that corrosion rates for the heated specimens were lower than those of the unheated specimens, a suggestion which is qualitatively consistent with the results of the galvanic-current measurements. Serious problems exist with the data, however. First of all, corrosion rates predicted from the polarization-resistance measurements are several orders of magnitude higher than those predicted gravimetrically, as was observed in the previous autoclave exposure. In addition, the polarization-resistance values for the unheated specimens measured in this autoclave exposure do not agree well with those reported in the first autoclave exposure. This effect may result from the increased concentration of metal ions in the solution, as shown in Table 3.5. Finally, the measured polarization resistance values for the heated specimens decreased with exposure time after about 300 hours; this may have been a real effect but more probably was a result of impingement of vapor-phase deposits onto the autoclave head.

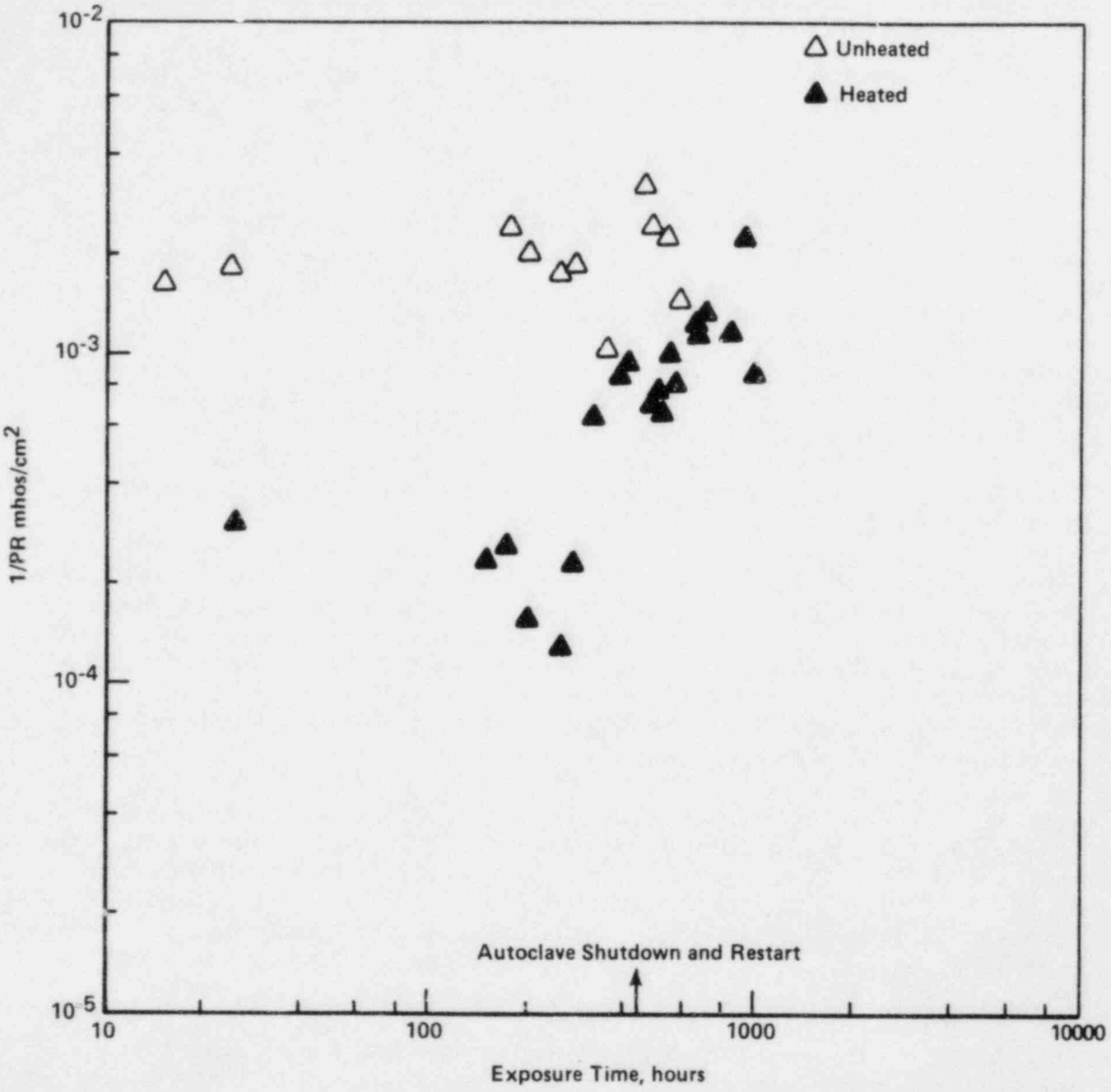

Figure 3.23 1/PR as a function of exposure time for heated and unheated (ΔT = 20 C) Titanium Grade 12 specimens exposed in deaerated Brine A at 250 C.

The final autoclave exposure for the Titanium Grade 12 - salt system also was completed this year. This exposure was identical to the previous exposure in which the effect of heat transfer on corrosion performance was evaluated, with one exception: a sealed internal canister of Titanium Grade 12 was fitted inside the HASTELLOY Alloy C276 autoclave so that the test environment was isolated from the autoclave head and body. This precaution was taken to prevent contamination of the test solution by corrosion products from the autoclave head, as occurred in the previous autoclave exposure. Included in the canister were duplicate U-bend and crevice specimens in the vapor and the liquid, and four gravimetric specimens in each phase.

Unlike the results of the previous autoclave exposure, the pressure within the canister in this exposure did not increase with exposure time. When the autoclave was opened at the end of the exposure, a deposit was found to have built up on the outside of the internal canister (see Figure 3.24). This region of the autoclave was filled with an aqueous solution of 1,000 g/l sodium chloride; this solution was selected to match the vapor pressure of Brine A but to prevent HCl generation by hydrolysis of magnesium salts.

The internal canister, which contained the actual specimens and Brine A, was cut open, and only a small amount of deposit was found on the heated specimen (see Figures 3.25 and 3.26). The solution pH was measured using a glass electrode and was found to be 5.7. These observations suggest that the internal canister had become isothermal during the test and that the majority of the temperature drop had occurred between the outside surface of the canister and the wall of the autoclave.

All of the specimens were found to have gained weight as a result of the exposure, and the weight changes were comparable with those previously reported, although the values for the gravimetric specimens which were immersed in the liquid were somewhat higher than those previously reported (see Table 3.6).

The specimens were optically examined and as in the previous exposures, evidence of incipient attack was found within the crevices (see Figure 3.27). This attack appeared to have been somewhat more severe on the specimens exposed in the liquid, although the gravimetric results did not reflect this. Colored interference spots were evident on the specimens exposed to the vapor, suggesting that an aggressive condensate had formed on them (see Figure 3.28).

In support of the autoclave exposures on the Titanium Grade 12 - salt system, the effect of temperature difference between a heated specimen and the bulk solution (ΔT) on the rate of deposit build up on the surface exposed to vapor was studied. The tests were performed for three hours at ambient pressure over a solution temperature range of 40-100 C and a ΔT range of 5-15 C.

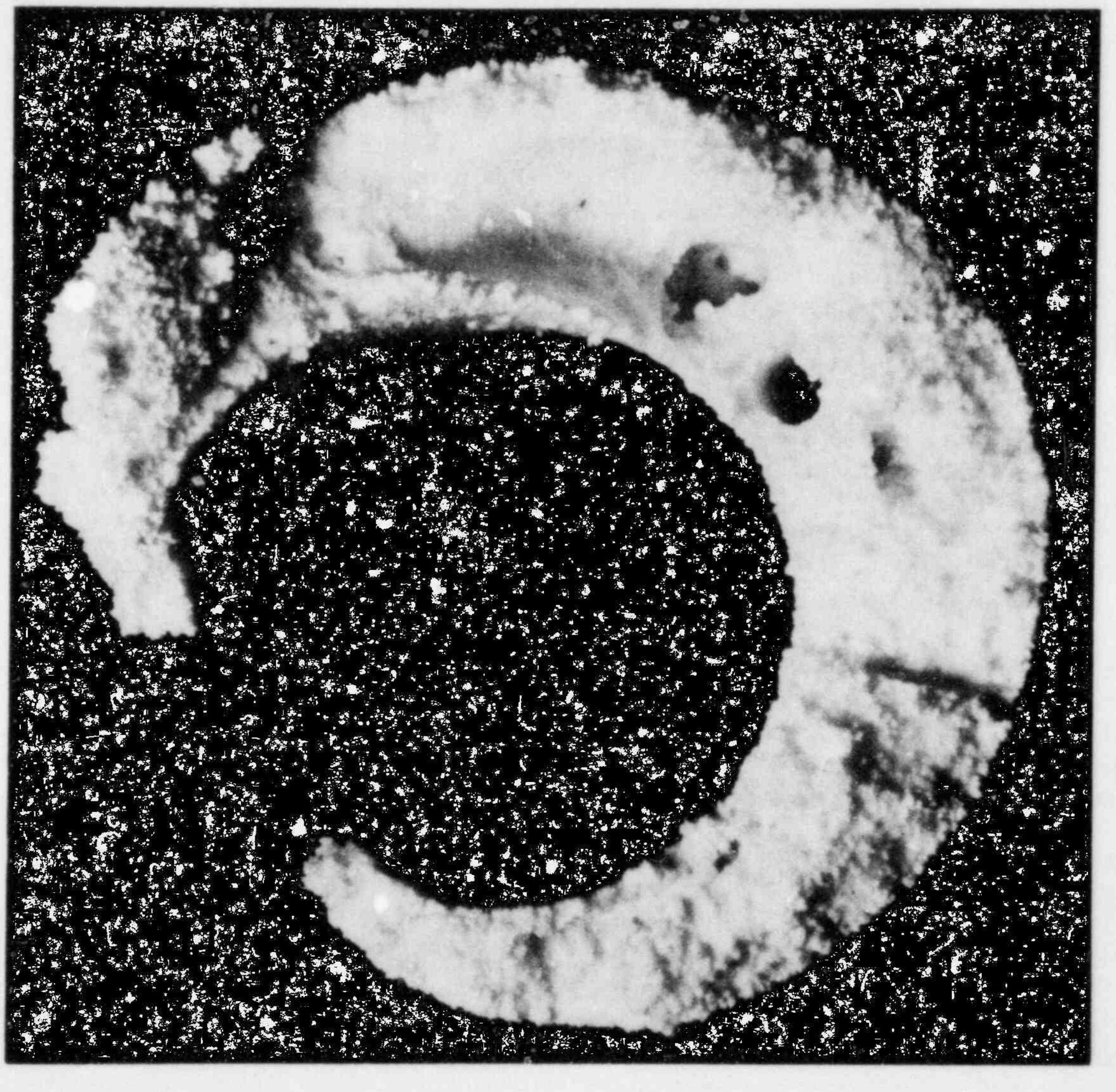

1X

2L353

Figure 3.24 Low-power optical photograph of deposit found on the outer diameter of the internal canister.

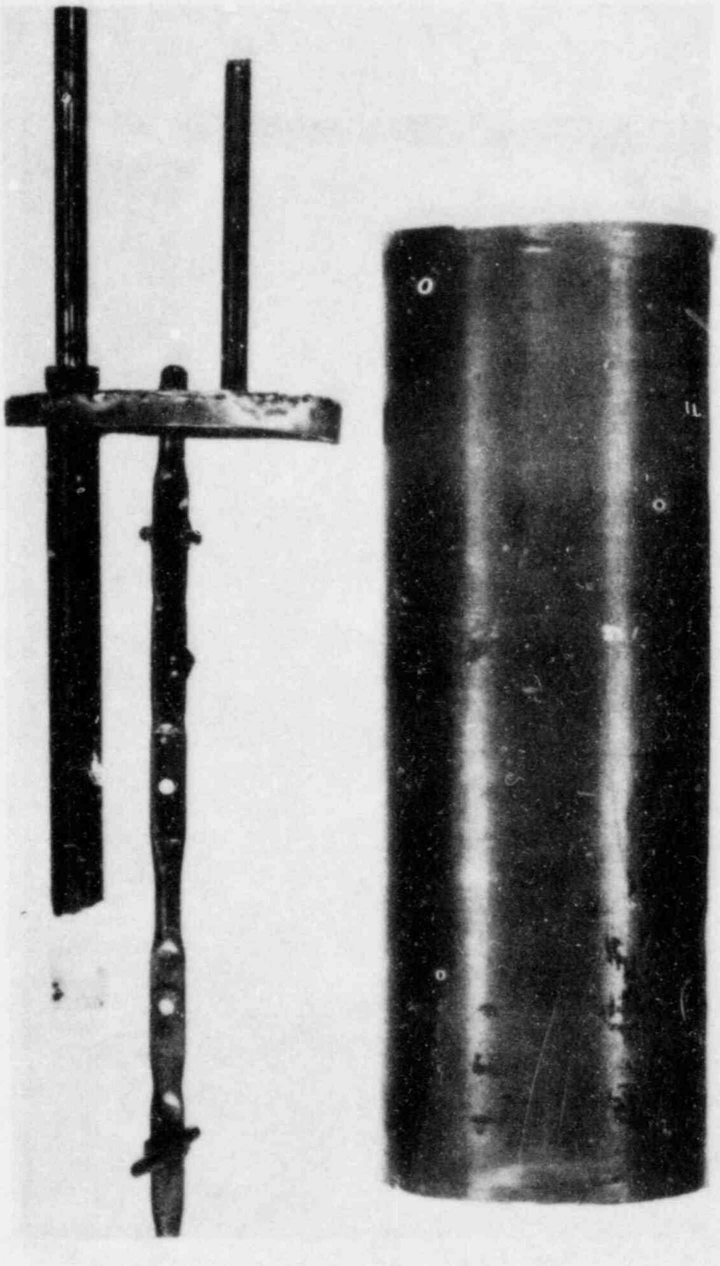

0.5X

2L354

Figure 3.25 Low-power optical photograph of canister, specimen rack, and heat transfer specimen following testing.

Note the small amount of deposit present on the heat transfer specimen (lower left).

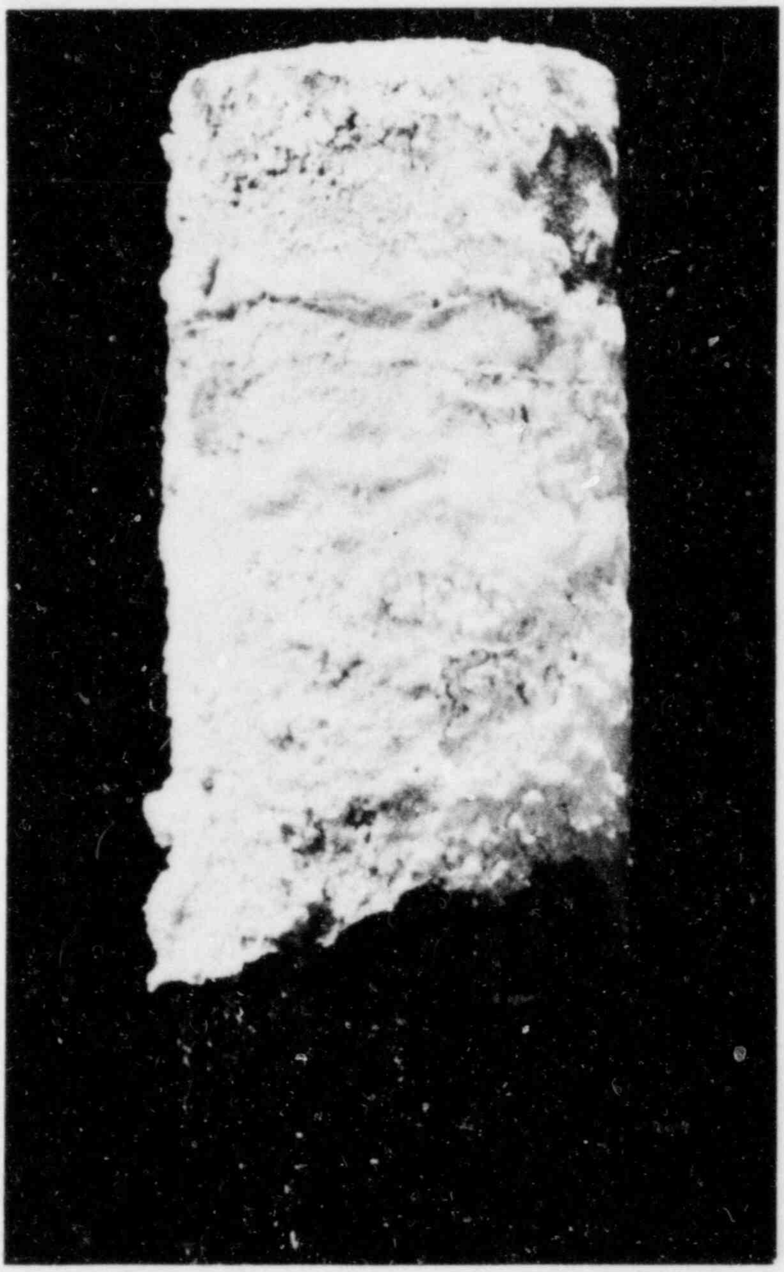

4X 2L352

Figure 3.26 Higher-power optical photograph of deposit found on heat transfer specimen

Table 3.6 Results of gravimetric measurements performed on Titanium Grade 12 specimens exposed for 1000 hours to deaerated Brine A at 250 C (final autoclave exposure).

Specimen Type	Phase	Weight Change g/cm^2	Corrosion Rate μm/y(a)
gravimetric	vapor	1.09×10^{-4}(b)	1.27
crevice	vapor	3.68×10^{5}(c)	4.29
gravimetric	liquid	4.09×10^{-5}(b)	4.77
crevice	liquid	3.95×10^{-5}(c)	4.61

(a) Calculated assuming the weight gain was the result of TiO_2 formation.

(b) Averaged for 4 specimens.

(c) Averaged for 2 specimens.

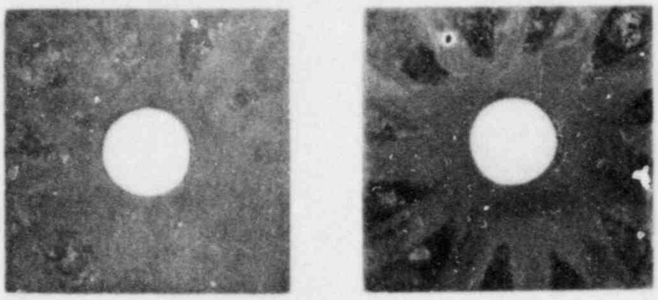

vapor liquid

3X 2L464

Figure 3.27 Low-power optical photograph of crevice specimens exposed to vapor and liquid phases in the final autoclave exposure.

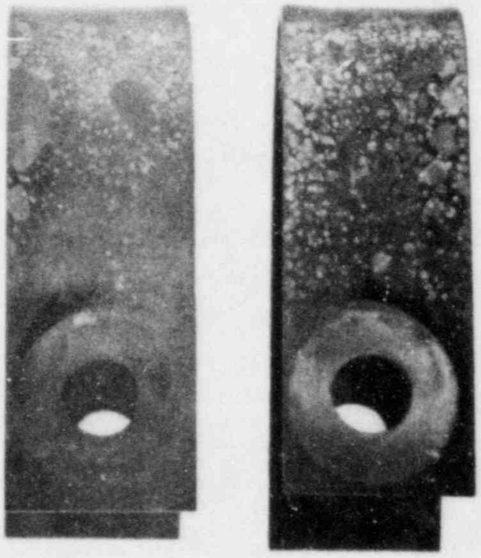

2X 2L465

Figure 3.28 Low-power optical photograph of U-bend specimens exposed to vapor in the final autoclave exposure

Results given in Figure 3.29 show that the rate of deposit growth increased with increasing temperature and ΔT. The data were plotted as a function of $1/T$ to determine whether the rate of deposit buildup could be described by a thermally activated process having a single activation energy. Figure 3.30 shows that the data for $\Delta T = 5$ C do fall on a reasonably straight line, with an activation energy of approximately 13 kcal/mole. Data for $\Delta T = 10$ C and 15 C have considerably more scatter and appear to fit lines having smaller slopes, indicating lower activation energies.

The deposits which formed on the specimens were optically examined, and selected samples were analyzed. In contrast to the multicolored deposits which formed in the autoclave tests, where significant contamination of the system had occurred by reactions with the autoclave head, deposits formed at ambient pressure were of a uniform white color (see Figure 3.31). The deposits were found to contain approximately 68 percent chlorine, 15 percent potassium, 13 percent magnesium, 4 percent sodium, and a trace of sulfur, as determined by energy dispersive X-ray spectroscopy. X-ray diffraction analyses of the deposits indicated the presence of KOH, NaCl and two hydrated magnesium chlorides.

From optical examination of the specimens during deposit formation, it appears that the mechanism of formation is related to a wicking action whereby a thin deposit initially forms on the specimens at the vapor-liquid interface, and solution then migrates up the specimen in the thin layer between the specimen and the deposit, ultimately depositing on the specimen. Such a mechanism may be driven by a large thermal gradient on the specimen surface. Accordingly, thermocouples were attached to the specimen in the vapor space, and the temperature was measured as a function of distance from the solution-vapor interface. Typical results of these measurements, given in Figures 3.32 and 3.33, show that the temperature of the specimen in the vapor was indeed much greater than that in the liquid and reached a maximum at about 2.5 cm from the solution-vapor interface.

3.2.2 Steel - Basalt System

3.2.2.1 Autoclave Exposures

A matrix of autoclave exposures is being performed on the steel-basalt system. The experimental variables are steel composition, steel microstructure, and solution composition. Results of experiments completed to date are discussed below.

Two carbon-steel compositions are being used in this study: one ("doped") approximating 1018 carbon steel, and one ("clean") with similar composition but with low phosphorus and sulfur. The compositions of these steels are given in Table 3.7. Both cast and wrought specimens are included in the experimental matrix. Cast specimens are machined directly from the billets, while wrought

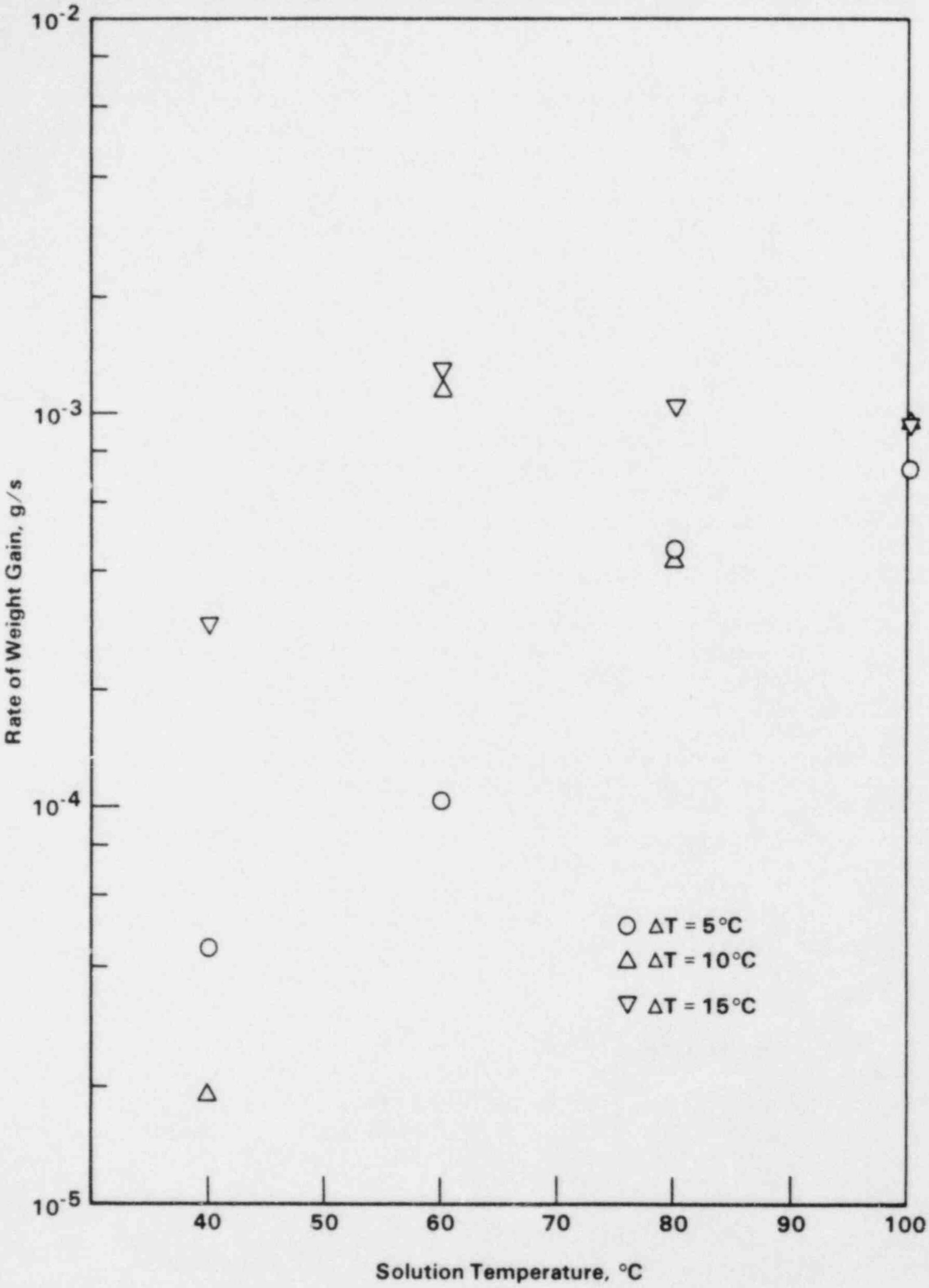

Figure 3.29 Rate of deposit growth, averaged over 3-hour tests, as a function of solution temperature and ΔT on a Titanium Grade 12 specimen exposed to naturally aerated Brine A.

$\Delta T = T_{\text{specimen in solution}} - T_{\text{solution}}$.

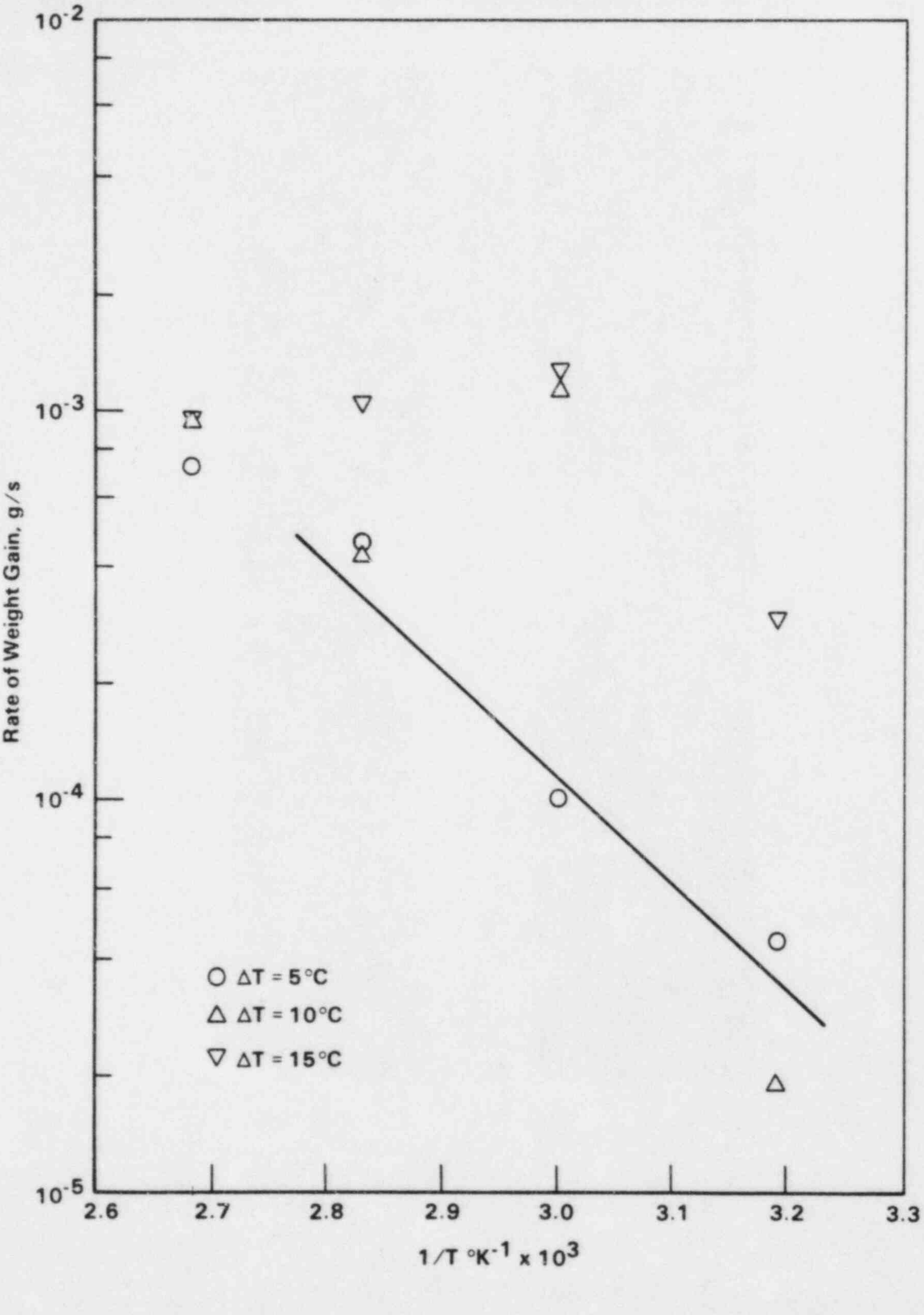

Figure 3.30 Data shown in Figure 3.29, reported as rate of weight gain as a function of 1/T.

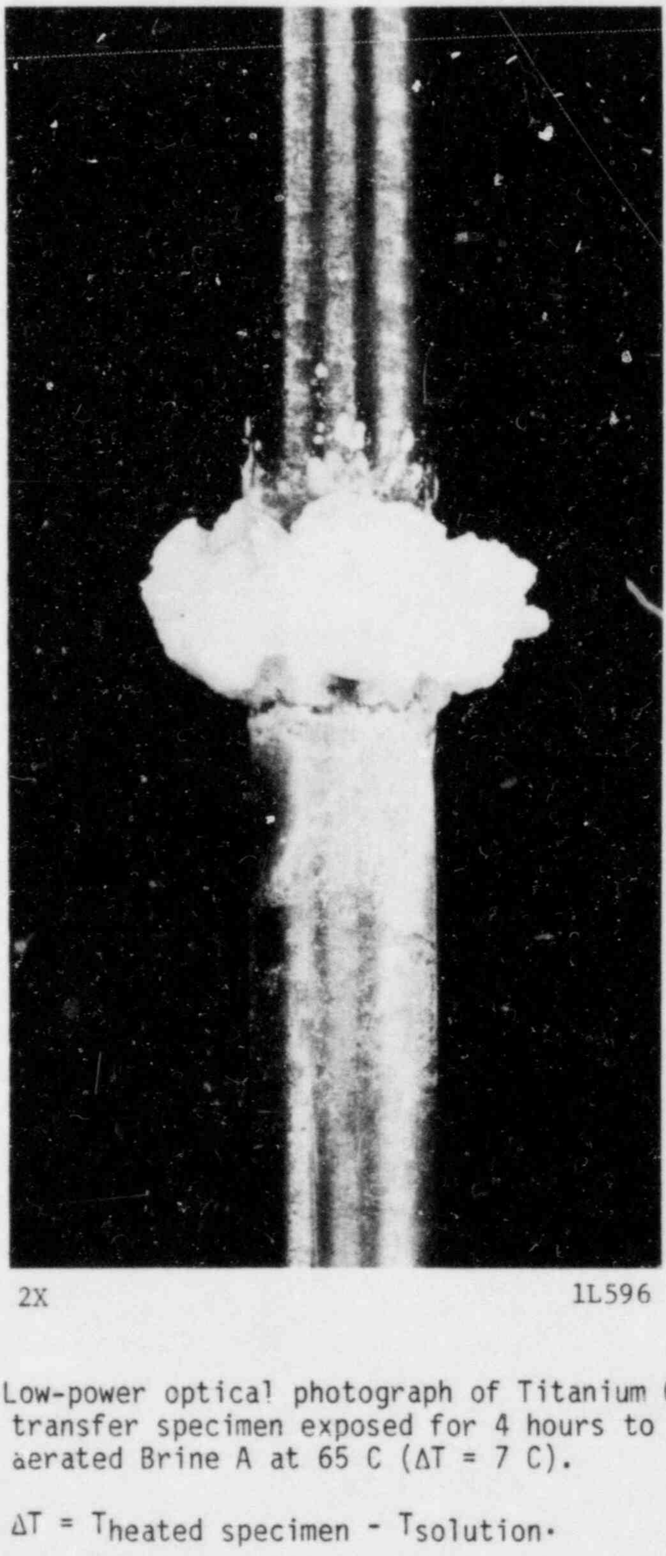

2X 1L596

Figure 3.31 Low-power optical photograph of Titanium Grade 12 heat transfer specimen exposed for 4 hours to naturally aerated Brine A at 65 C (ΔT = 7 C).

$\Delta T = T_{\text{heated specimen}} - T_{\text{solution}}$.

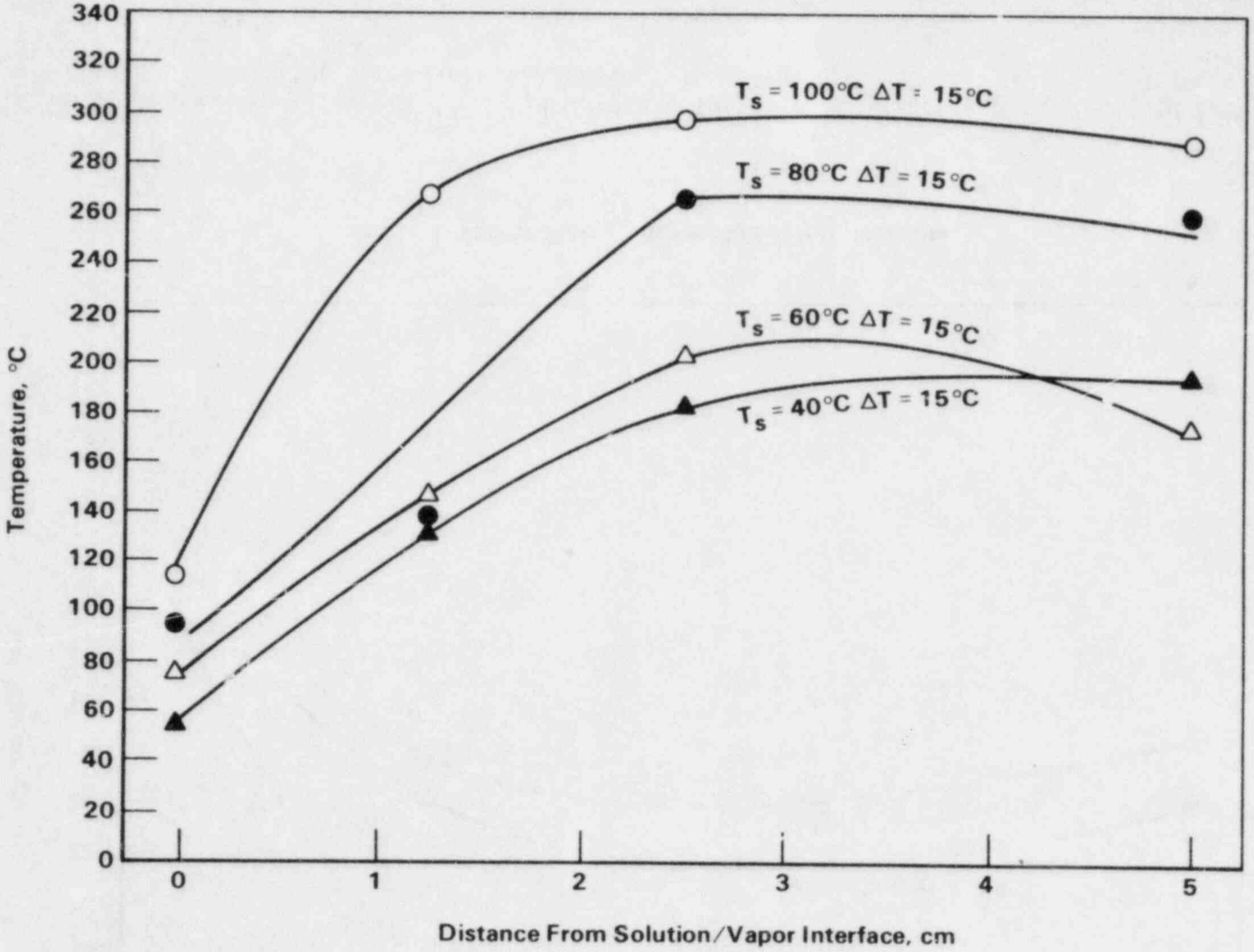

Figure 3.32 Specimen temperature as a function of distance from solution/vapor interface and solution temperature for Titanium Grade 12 in Brine A with a fixed ΔT = $T_{\text{specimen in solution}} - T_{\text{solution}}$.

Measurements were taken after an exposure time of 10 minutes.

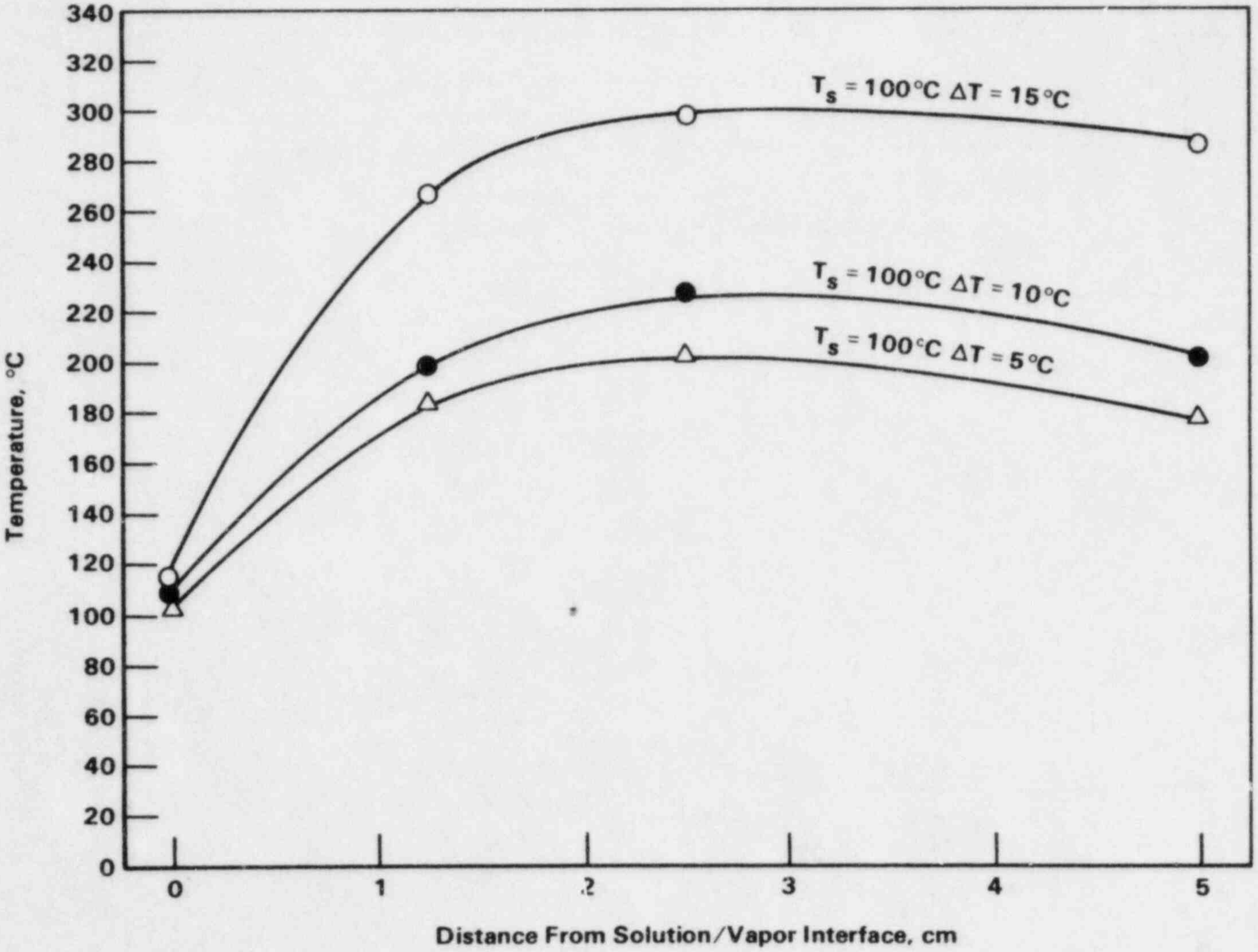

Figure 3.33 Temperature of Titanium Grade 12 specimen as a function of distance from solution/vapor interface and ΔT in Brine A at 100 C.

$\Delta T = T_{\text{specimen in solution}} - T_{\text{solution}}$.

Table 3.7 Chemical compositions in weight percent of reference steels and steels used in the experimental program.

Element	Proposed DOE Reference Steel	Clean BCL Steel (Actual)	Doped BCL Steel (Actual)	1018 Steel
Carbon	0.15-0.20	0.18	0.17	0.15-0.20
Manganese	0.90 max	0.49	0.55	0.60-0.90
Phosphorus	0.04 max	0.004	0.029	0.040 max
Sulfur	0.045 max	0.002	0.036	0.050 max
Silicon	0.60 max	0.30	0.35	-
Aluminum	-	0.10	0.14	-
Copper	-	0.006	0.007	-
Nickel	-	0.002	0.004	-
Chromium	-	0.007	0.011	-
Molybdenum	-	0.000	0.000	-
Vanadium	-	0.000	0.006	-

specimens are machined from sections of the billets which are hot-reduced approximately 87 percent. Four types of specimens are included in the autoclave exposures: gravimetric specimens, crevice specimens, 3-point bend specimens, and polarization resistance (PR) specimens. The crevice-corrosion specimens have a boldly-exposed-surface-area to crevice-surface-area ratio of 10 and were made by attaching serrated TFE washers to thin, rectangular specimens of the steels.

One-thousand-hour autoclave exposures were completed on 1018 steel specimens in two simulated basalt groundwater compositions at 250 C under stagnant deaerated conditions. Basalt rock, taken from an outcropping of the Umtanum flow, was present in the bottom of the autoclave during the exposures. One simulated basalt groundwater was a 1X solution prepared according to a Rockwell-Hanford Procedure(3.2); the other was a 10X concentration of that solution. The nominal composition of the 1X simulated basalt groundwater is shown in Table 3.8.

Results of the gravimetric measurements performed on the specimens which were exposed in the simulated groundwaters are given in Tables 3.9 through 3.12. These data show that general-corrosion rates were quite low in these environments under deaerated conditions and were similar for the two materials. Surprisingly, general-corrosion rates were somewhat higher in the unconcentrated groundwater. The PR specimens tested in the concentrated groundwater also exhibited somewhat higher weight losses than the other specimens. These rates of general attack in the unconcentrated groundwater are comparable, in most instances, to those reported by Bradley, et al(3.3) for ductile iron in a basalt groundwater*.

Specimens were optically examined following exposure to find evidence of pitting, crevice corrosion, and stress-corrosion cracking and to characterize any surface films present. No evidence of stress-corrosion cracking was found on any of the 3-point bend specimens. The depths of pits were measured with a microscope having a calibrated stage. Results of the analyses are given in Tables 3.9 through 3.12, where it can be seen that shallow pits were detected on most specimens. Pitting was somewhat more severe in the more concentrated solution and was similar for the two materials. The pits on the specimens exposed in the less concentrated groundwater appeared to be more prevalent in or near the crevices. A typical photograph of one such pit is given in Figure 3.34.

Tenacious black surface films were present on all the steel specimens following exposure to the basalt groundwater. The surface films on a cast specimen of the clean steel which was exposed in the unconcentrated groundwater were analyzed by energy dispersive x-ray (EDX) spectroscopy

---

*The O_2 concentration of the groundwater in the tests by Bradley, et al was not well controlled. A refreshed system was used with aerated makeup water, but the basalt rock in the autoclave rapidly consumed the oxygen.

Table 3.8 Nominal composition of 1X simulated basalt groundwater

Component	Concentration, wppm
Na^+	360
K^+	3.4
Mg^{+2}	0.03
Ca^{+2}	2.8
F^-	33
Cl^-	310
SO_4^{-2}	175
C	-*
SiO_2	76

* Total inorganic carbon = 9 10^{-4} mole/liter.
pH at 25 C = 9.8.

Table 3.9 Corrosion rates calculated from weight loss and pit depths for cast specimens of clean 1018 steel exposed for 1000 hours to a deaerated simulated basalt groundwater at 250 C.

Specimen Type	Number of Specimens[a]	Corrosion Rate μm/y[b]	Average[c] Pit Depth μm	Maximum Pit Depth
Gravimetric	3	15.64	6.0	9.0
Crevice	2	12.64	8.0	18[d]
3-Point Bend	2	13.10	-	-
Polarization Resistance	2	7.42	-	-

(a) Some specimens were reserved for future analyses and thus the number of specimens of each type which were descaled and weighed varied.

(b) Weight losses were converted to depths of penetration assuming uniform attack and extrapolated linearly to give annual rates of penetration.

(c) For 5 deepest pits.

(d) In crevice region of specimen.

Table 3.10 Corrosion rates calculated from weight loss and pit depths for wrought specimens of 1018 steel exposed for 1000 hours to deaerated simulated basalt groundwater at 250 C.

Specimen Type	Number of Specimens(a)	Corrosion Rate μm/y(b)	Average(c) Pit Depth, μm	Maximum Pit Depth, μm
Gravimetric	2	22.46	8.7	17
Crevice	2	22.49	8.3	15
3-Point Bend	1	15.35	-	-

(a) Some specimens were reserved for future analyses and thus the number of specimens of each type which were descaled and weighed varied.

(b) Weight losses were converted to depths of penetration assuming uniform attack and extrapolated linearly to give annual rates of penetration.

(c) For 5 deepest pits.

Table 3.11 Corrosion rates calculated from weight loss and pit depths for cast specimens of clean 1018 steel exposed for 1000 hours to deaerated 10X simulated basalt groundwater at 250 C.

Specimen Type	Number of Specimens(a)	Corrosion Rate µm/y(b)	Average(c) Pit Depth, µm	Maximum Pit Depth, µm
Gravimetric	3	5.59	18	30
Crevice	1	5.83	13	20
3-Point Bend	2	7.46	-	-
Polarization Resistance	2	18.1	12(d)	>1,000

(a) Some specimens were reserved for future analyses and thus the number of specimens of each type which were descaled and weighed varied.

(b) Weight losses were converted to depth of penetration assuming uniform attack and extrapolated linearly to give annual rates of penetration.

(c) For 5 deepest pits.

(d) Average for PR specimen which did not contain the deep pits.

Table 3.12 Corrosion rates calculated from weight loss and pit depths for wrought specimens of 1018 steel exposed for 1000 hours to deaerated 10X simulated basalt groundwater at 250 C.

Specimen Type	Number of Specimens[a]	Corrosion Rate μm/y[b]	Average[c] Pit Depth, μm	Maximum Pit Depth, μm
Gravimetric	3	6.40	18	25
Crevice	1	3.92	21	25
3-Point Bend	2	6.78	-	-

(a) Some specimens were reserved for future analyses and thus the number of specimens of each type which were descaled and weighed varied.

(b) Weight losses were converted to depths of penetration assuming uniform attack and extrapolated linearly to give annual rates of penetration.

(c) For 5 deepest pits.

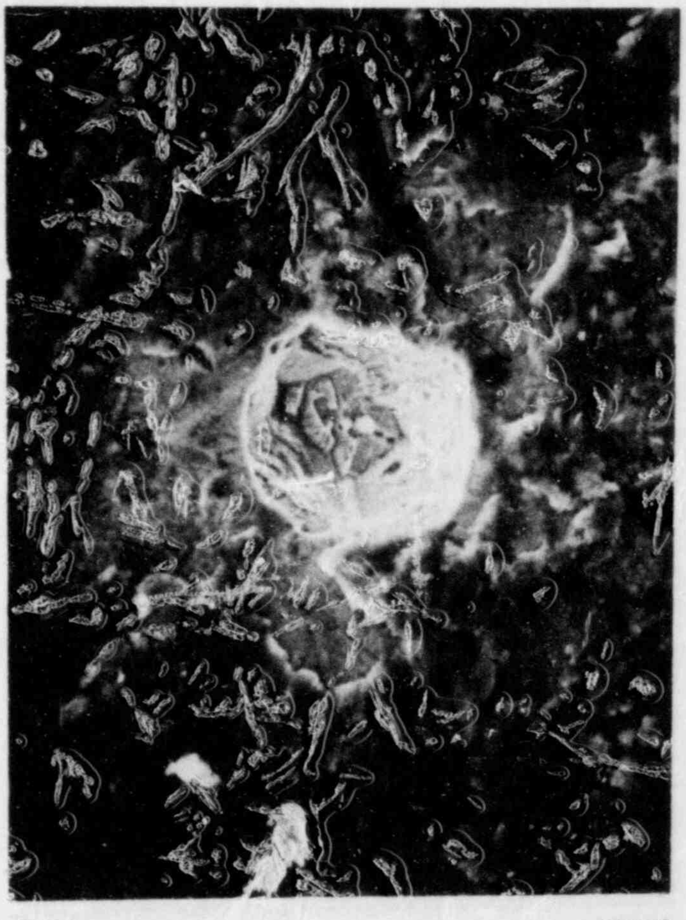

Figure 3.34 SEM photograph of pit found in the crevice region of a cast steel specimen exposed for [illegible]000 hours in 250 C deaerated simulated basalt groundwater containing crushed basalt.

and x-ray diffraction (XRD). The results of the analyses are summarized in Table 3.13. These data indicate that the compounds present in these films were primarily Fe_3O_4. The presence of surface films on the specimen is consistent with the observed low rates of general attack and the occurrence of pitting; pitting corrosion is normally associated with the breakdown of passive films. The absence of any higher oxidation states for iron is good evidence that oxygen was successfully excluded from the autoclaves during the tests. In the presence of oxidants generated by radiolysis of the groundwater, higher-oxidation-state oxides, such as Fe_2O_3 or FeOOH, probably would be generated. Although Fe_2O_3 is much less soluble than Fe_3O_4 and thus potentially more protective, the corrosion performance of carbon steel in the presence of oxygen and chlorides is generally poor because of local breakdown of these oxide films.

Deep pits were observed on one of the polarization-resistance specimens of the cast clean steel which had been exposed to the concentrated groundwater. This attack reached depths greater than 1000 µm and was localized in the region of the specimen that had been exposed to the vapor space in the autoclave. All other specimens in the autoclave were fully submersed.

An additional autoclave exposure was performed to investigate further the vapor-phase corrosion behavior of the steels in the concentrated groundwater. Gravimetric and crevice specimens of cast and wrought clean and doped 1018 carbon steel were exposed for 1000 hours in the vapor and in the liquid at 250 C. Results given in Tables 3.14 through 3.17 do not indicate a significant or consistent effect of exposure to liquid as compared to vapor on general, pitting, or crevice corrosion for any of the four materials. Thus, the "pits" observed in the PR specimen from the previous autoclave exposure probably were simply metallurgical flaws in the specimen.

3.2.2.2 Electrochemical Measurements

Electrochemical measurements were performed during the autoclave test with the unconcentrated groundwater. The polarization resistance (PR) of the cast steel specimens was measured as a function of exposure time in the basalt groundwater using a two-electrode technique. Results given in Figure 3.35 show that the value of 1/PR, which is proportional to the corrosion rate, increased over the first 50 hours of exposure and decreased over the remaining 950 hours. The polarization resistance of platinum electrodes also was measured as a function of exposure time, and values of 1/PR were found to be lower than values for cast steel, as anticipated, and appeared to achieve a maximum after about 250 hours of exposure.

The PR measured on the platinum electrode indicates the magnitude of the exchange current, i_0, for the primary reducible species in the solution. This is represented graphically in Figure 3.36, where the reduction reaction is $Ox + ne^- \rightarrow Red$. This measurement is not particularly

Table 3.13 Results of EDX and XRD analyses of cast steel specimen exposed for 1000 hours in 250 C deaerated simulated basalt groundwater containing crushed basalt.

EDX

Composition, weight percent

Al	Si	S	K	Ca	Fe
8.97	26.0	7.58	1.71	1.31	54.43

XRD

Compound	Powder Diffraction Number
Fe_3O_4	19-629
Fe_2SiO_4	29-720

Table 3.14 Corrosion rates calculated from weight loss and pit depths for specimens of clean cast 1018 steel exposed for 1000 hours to deaerated 10X simulated basalt groundwater at 250 C.

Specimen Type	Phase	Corrosion Rate[a] μm/y	Average Pit[b] Depth μm	Maximum Pit Depth μm
Gravimetric	V	9.47	10	14
Gravimetric	L	10.21	6.8	8
Crevice	V	12.16	10	13
Crevice	L	9.54	14	20

(a) Weight losses were converted to depths of penetration assuming uniform attack and extrapolated linearly to give annual rates of penetration.

(b) For 5 deepest pits.

Table 3.15 Corrosion rates calculated from weight loss and pit depths for duplicate specimens of clean wrought 1018 steel exposed for 1000 hours to deaerated 10X simulated basalt groundwater at 250 C.

Specimen Type	Phase	Corrosion Rate[a] μm/y	Average Pit[b] Depth μm	Maximum Pit Depth μm
Gravimetric	V	12.4	9.4	12
Gravimetric	L	9.49	11	14
Crevice	V	10.8	10	13
Crevice	L	8.14	14	18

(a) Weight losses were converted to depths of penetration assuming uniform attack and extrapolated linearly to give annual rates of penetration.

(b) For 5 deepest pits.

Table 3.16 Corrosion rates calculated from weight loss and pit depths for duplicate specimens of cast 1018 steel exposed for 1000 hours to deaerated 10X simulated basalt groundwater at 250 C.

Specimen Type	Phase	Corrosion Rate[(a)] µm/y	Average Pit[(b)] Depth µm	Maximum Pit Depth µm
Gravimetric	V	9.07	9.4	11
Gravimetric	L	8.52	12	16
Crevice	V	11.1	15	27
Crevice	L	9.44	16	22

(a) Weight losses were converted to depths of penetration assuming uniform attack and extrapolated linearly to give annual rates of penetration.

(b) For 5 deepest pits.

Table 3.17 Corrosion rates calculated from weight loss and pit depths for specimens of wrought 1018 steel exposed for 1000 hours to deaerated 10X simulated basalt groundwater at 250 C.

Specimen Type	Phase	Corrosion Rate[(a)] µm/y	Average Pit[(b)] Depth µm	Maximum Pit Depth µm
Gravimetric	V	8.36	5.6	10
Gravimetric	L	7.35	8.6	10
Crevice	V	11.9	12	15
Crevice	L	8.42	9.8	12

(a) Weight losses were converted to depths of penetration assuming uniform attack and extrapolated linearly to give annual rates of penetration.

(b) For 5 deepest pits.

accurate, because i_0 Red/Ox values on platinum may differ significantly from those on the corroding metal surface. In this system, the primary reduction reaction under deaerated conditions is probably H_2O reduction, but in the presence of radiation, many other reducible species may be generated.

Elecrochemical potentials of the cast steel and platinum also were measured as a function of exposure time with respect to an external (25 C) Ag/AgCl (0.1 M KCl) reference electrode. The measurement performed on the steel specimen is referred to as the corrosion or open-circuit potential and is indicated graphically in Figure 3.36 as E_{corr} for a metal corroding under activation control.* The measurement performed on the inert platinum electrode indicates the E_0 value for the dominant reduction reaction (see Figure 3.36). This value is sometimes referred to as the solution Eh. It must be cautioned that there are many problems associated with the use of a platinum electrode to measure solution Eh, such as filming of the electrode, but the measurement does provide an indication of the oxidizing power of the solution.

To convert the potential values to the standard hydrogen electrode (SHE), a correction must be made for the thermal junction potential and the standard potential difference between the two electrodes. These corrections nearly cancel each other out, and thus the Ag/AgCl (0.1 M KCl at 25 C) reference electrode is equal to +0.22 V (SHE) for the reference electrode at 25 C and the test solution at 250 C.

Results of the measurements, given in Figure 3.37, show that the potentials for the platinum were consistently more noble than those of the cast steel, as anticipated, and the values for both materials exhibited a peak after about 250 hours of exposure. The increase in potential over the first few hundred hours of exposures is common in systems where film formation or passivation occurs. It should be noted that deposits had formed on both cast steel and platinum electrodes during the exposure. It was thought that the drop in the potential over the remainder of the exposure may have been the result of degradation of the reference electrode, and accordingly, the potential of the electrode was planned to be measured with respect to a saturated calomel electrode (SCE) at 25 C, following exposure, to determine whetner or not degradation had occurred. Unfortunately, gas bubbles had formed in the electrode upon depressurization and cooling, and a final potential reading could not be made.

---

*Activation control refers to a condition where the rate-limiting step for the reaction is charge transfer across the metal-solution interface.

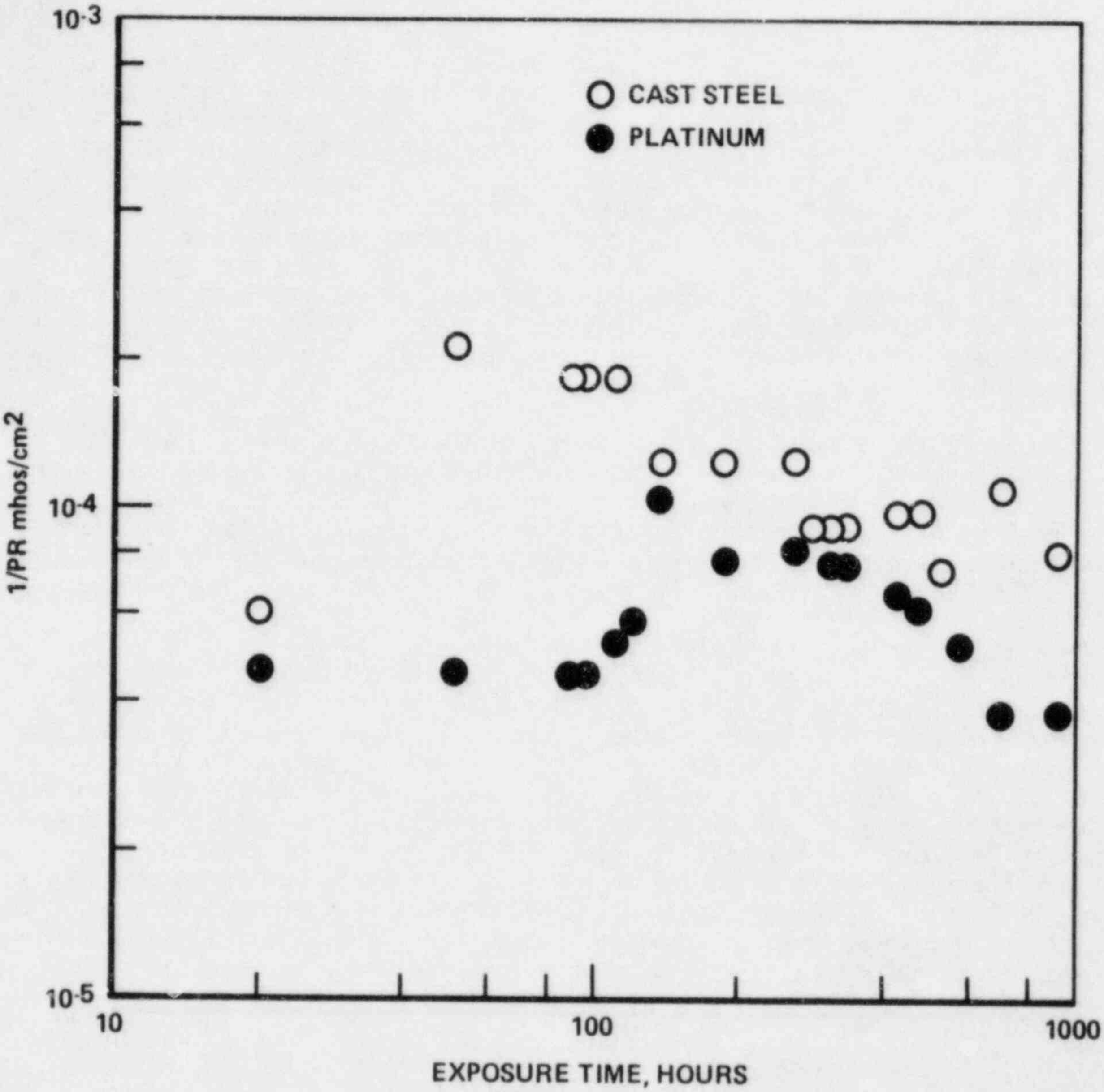

Figure 3.35 1/PR as a function of exposure time for cast steel and platinum exposed in deaerated simulated basalt groundwater at 250 C containing crushed basalt.

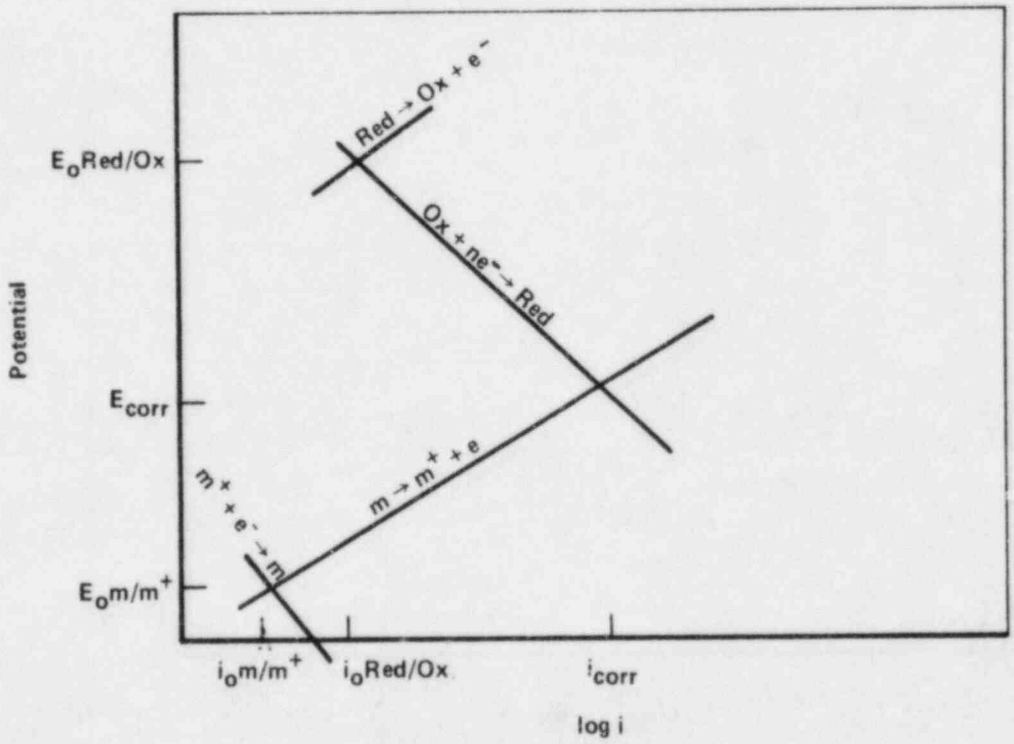

Figure 3.36 Graphical representation of electrode kinetics for a corroding metal where the oxidation and reduction reactions are under activation control.

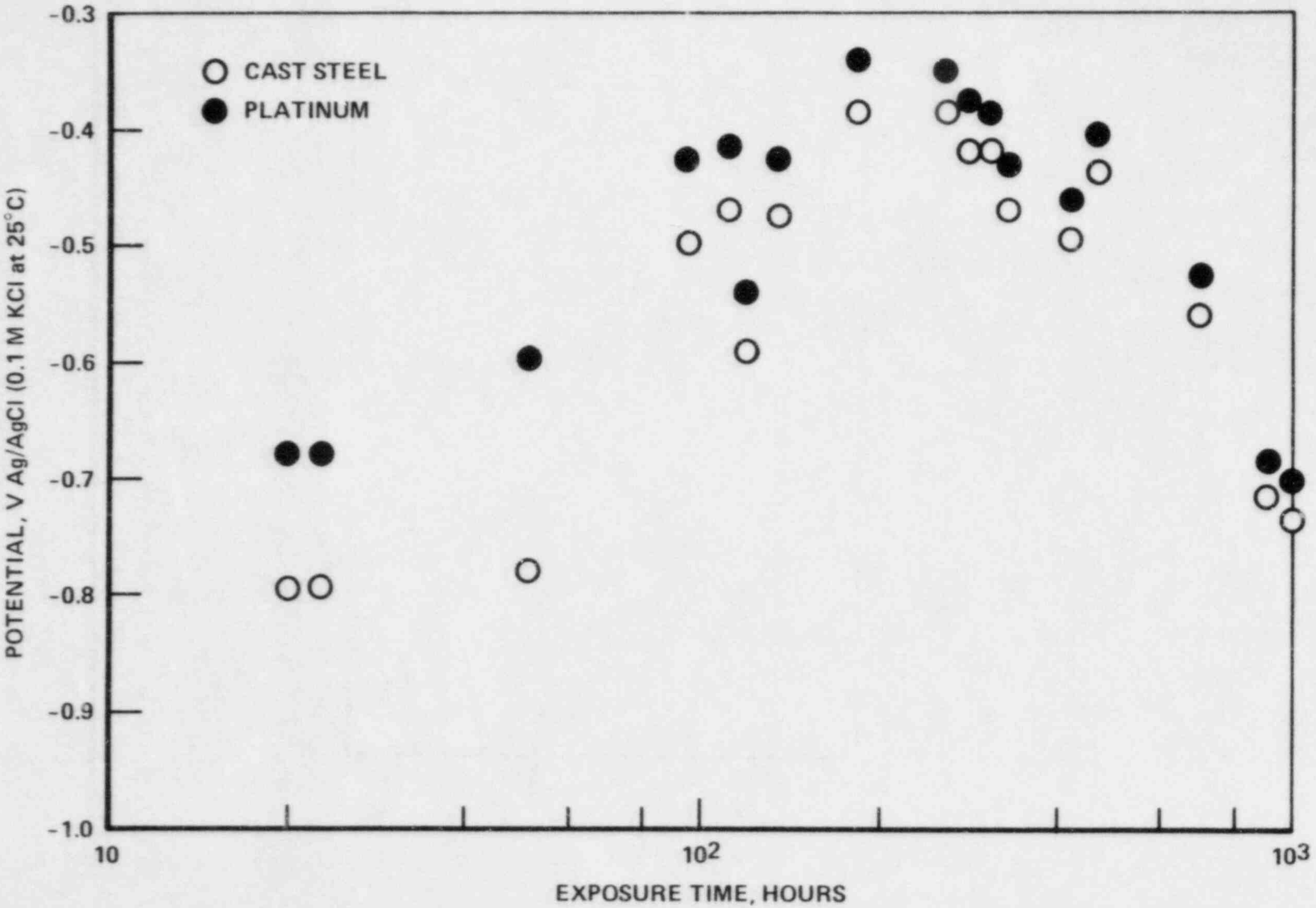

Figure 3.37 Potential as a function of exposure time for cast steel and platinum exposed in deaerated simulated basalt groundwater at 250 C containing crushed basalt.

3.2.2.3 Potentiodynamic Polarization Experiments

A matrix of potentiodynamic polarization experiments, which is similar to the matrix of autoclave exposures, is being performed at 90 and 250 C. In this test procedure, the polarity and magnitude of the current density flowing between a specimen of the material of interest and an inert counter electrode is measured as a function of electrochemical potential. For the anodic portions of the curve, the current measured is equal to the corrosion rate of the electrode if two conditions are met: (1) the electrochemical potential is sufficiently far away from the open-circuit potential that the rate of the cathodic reaction is negligible; and (2) the rates of parasitic oxidation reactions are negligible.

Schematics of anodic polarization curves showing several types of behavior are given in Figure 3.38. For the active-corrosion case, the anodic curve is linear on an E-log i plot, and the forward and reverse scans are coincident. The presence of a nose in the anodic portion of the curve is generally indicative of the onset of passivation. The passive current density is indicated in the figure. Generally, this value decreases with decreasing potential scan rate and may be negligibly small for a highly corrosion-resistant material. The occurrence of hysteresis between the forward and reverse scans is indicative of pitting. Where the hysteresis loop is very large, the protection potential may be very close to the open-circuit potential, indicating a high probability of pitting in service.

Preliminary tests were completed on specimens in four types of deaerated basalt groundwaters at 90 C:

- Basalt groundwater (1X)
- 10X concentration of basalt groundwater
- 1X basalt groundwater containing crushed basalt
- 10X concentration of basalt groundwater containing crushed basalt.

Results of the experiments are given in Figures 3.39 to 3.42 and Tables 3.18 and 3.19. Reproducibility of the data was quite good in general. The most striking conclusion from the data is that the steel undergoes passivation and is highly susceptible to localized forms of corrosion, such as pitting, in these basaltic environments. The latter conclusion is based on the large hysteresis observed between the forward and reverse scans and the fact that the values for E_{prot} were very close to values for E_{corr} for most of the test conditions. It should also be pointed out that gelatinous deposits formed on the surfaces of the specimens during the tests and that severe localized attack occurred beneath these deposits.

In other findings, the presence of the basalt rock or the concentration of the groundwater did not have a consistent or large effect on corrosion behavior. Qualitatively, this is consistent with the results

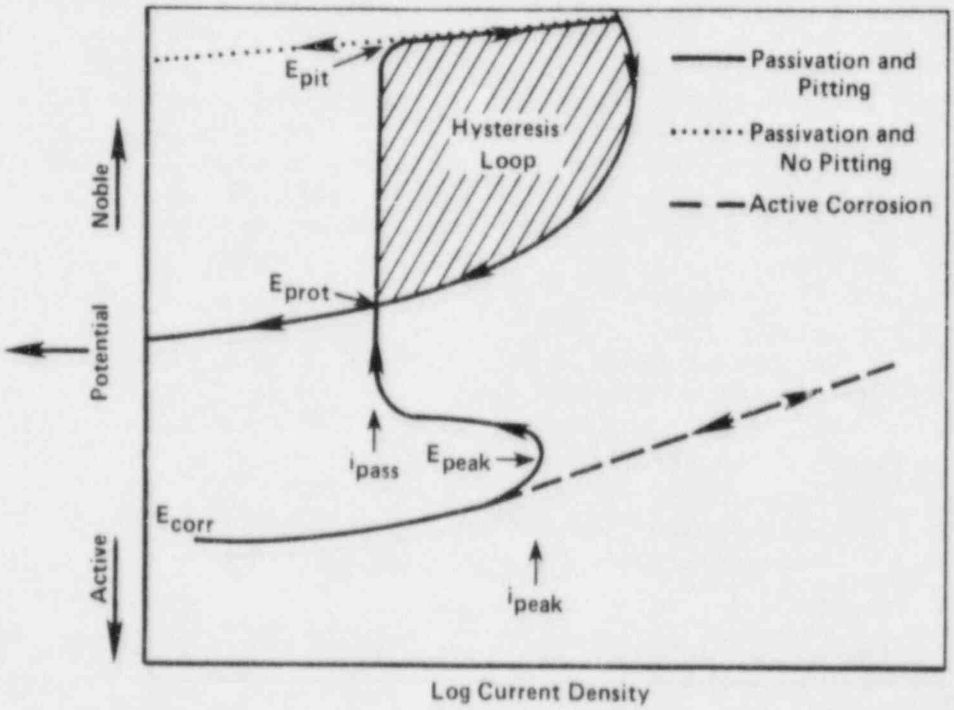

Figure 3.38 Schematic of typical anodic potentiodynamic polarization curves

E_{corr} = corrosion potential; E_{pitt} = potential at which pits initiate on forward scan; E_{prot} = potential at which pits repassivate on reverse scan; i_{peak} = current density at active peak; i_{pass} = current density in passive range.

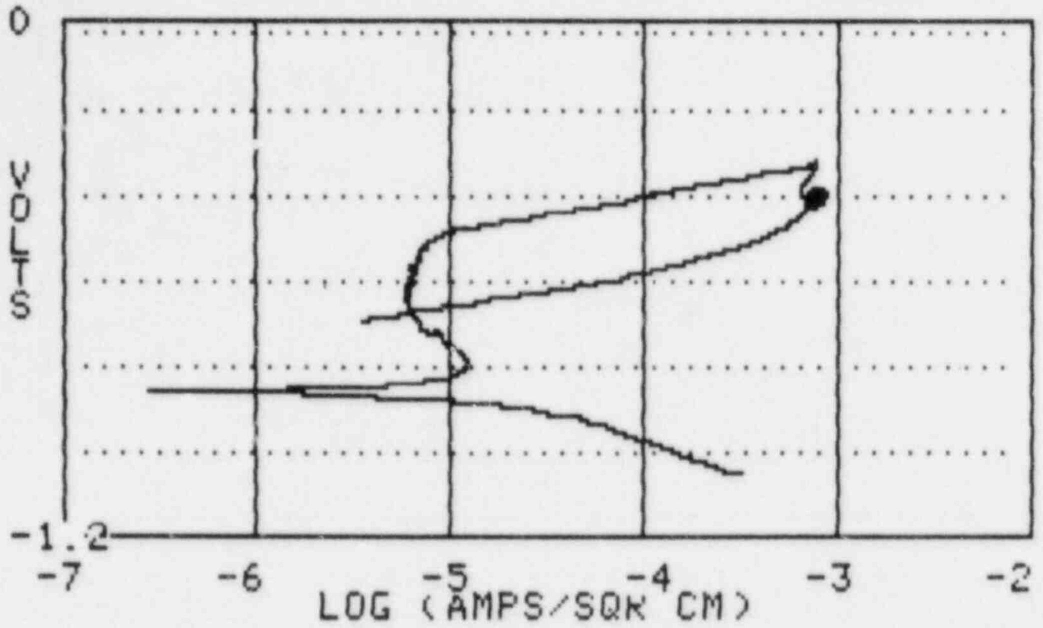

a. Without Basalt

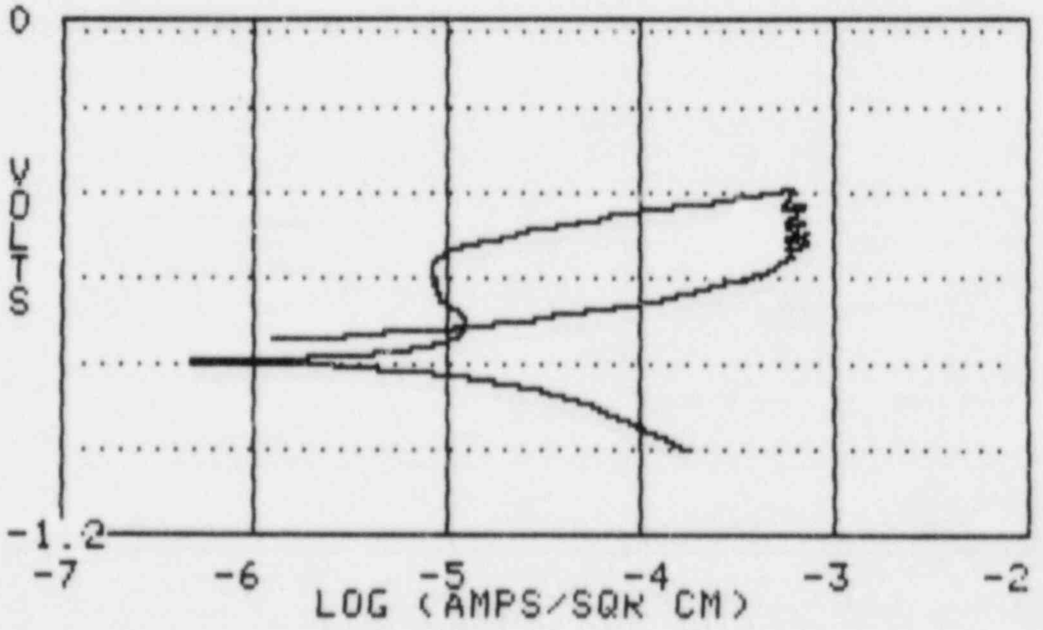

b. With Basalt

Figure 3.39 Potentiodynamic polarization curve for wrought 1018 steel in deaerated 1X basalt groundwater at 90 C with and without crushed basalt at scan rate of 0.6 V/hr.

All potentials measured with respect to SCE.

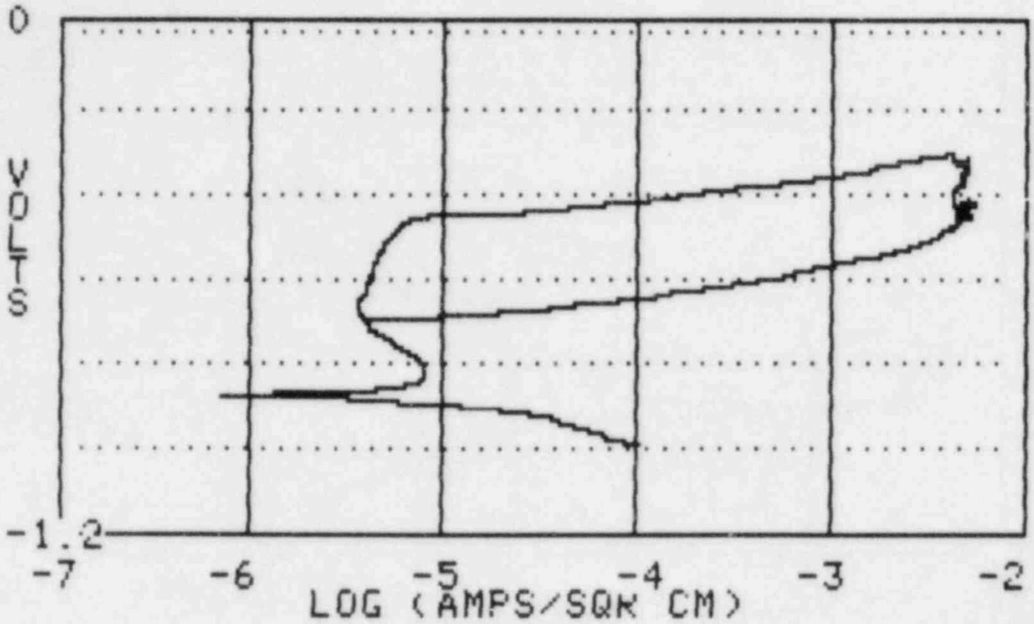

a. Without Basalt

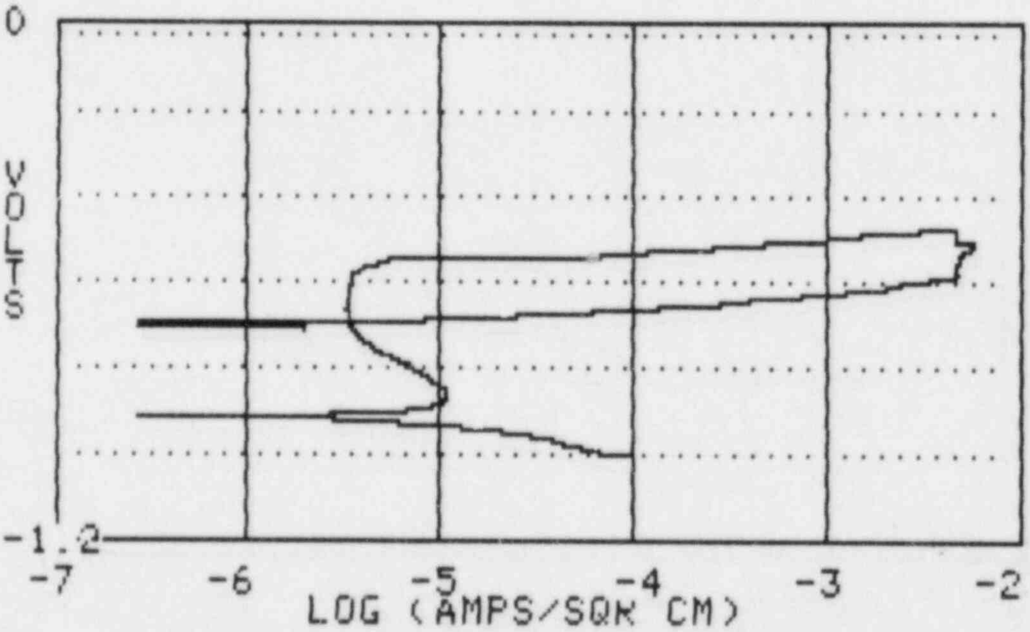

b. With Basalt

Figure 3.40 Potentiodynamic polarization curve for wrought 1018 steel in deaerated 10X basalt groundwater at 90 C with and without crushed basalt at scan rate of 0.6 V/hr.

All potentials measured with respect to SCE.

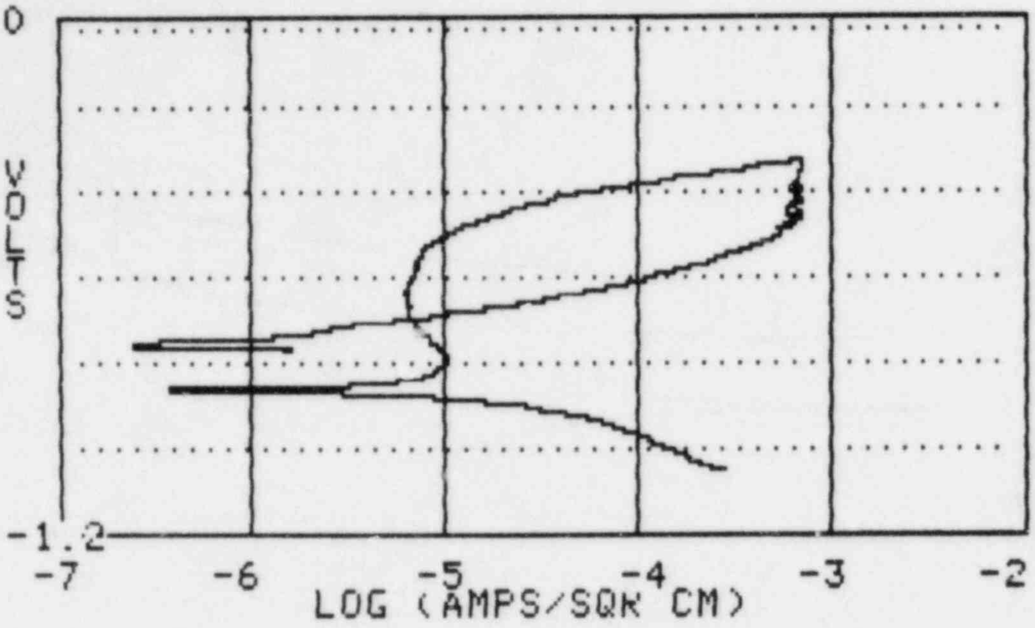

a. Without Basalt

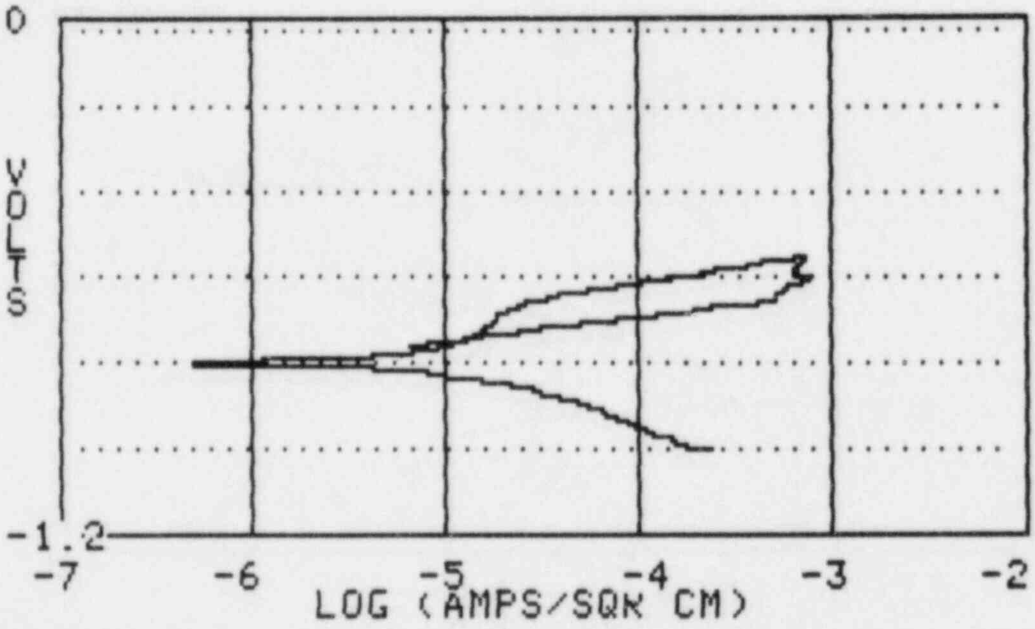

b. With Basalt

Figure 3.41 Potentiodynamic polarization curve for clean cast 1018 steel in deaerated 1X basalt groundwater at 90 C with and without crushed basalt at scan rate of 0.6 V/hr.

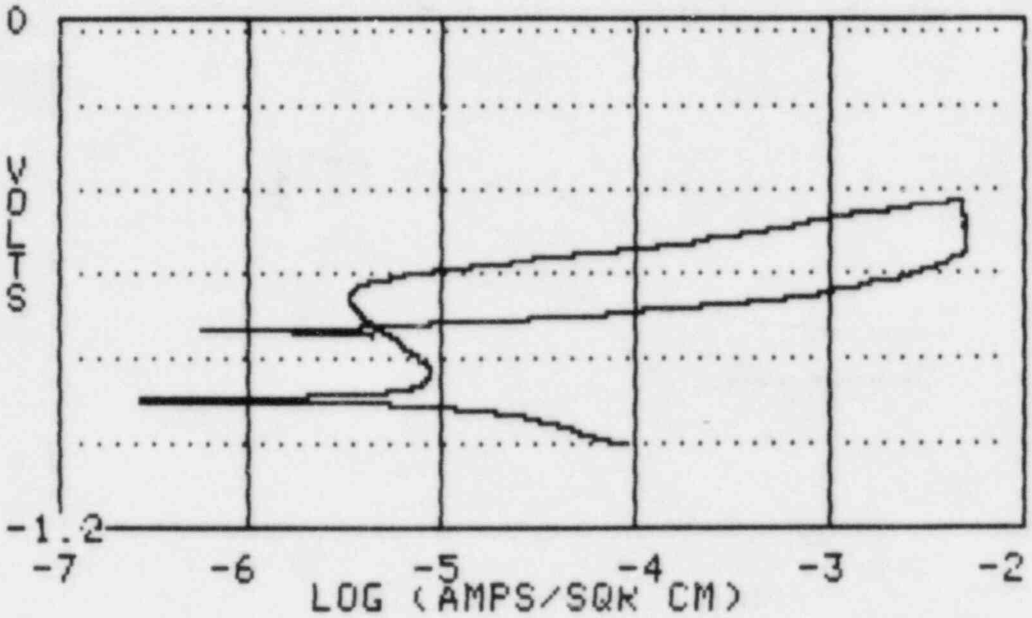

a. Without Basalt

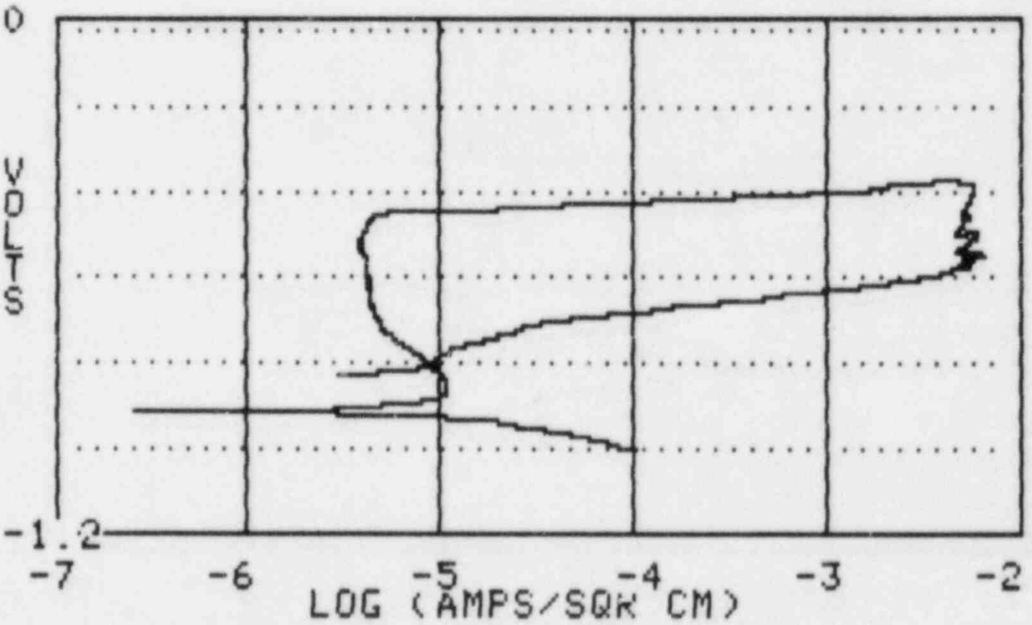

b. With Basalt

Figure 3.42 Potentiodynamic polarization curve for clean cast 1018 steel in deaerated 10X basalt groundwater at 90 C with and without crushed basalt at a scan rate of 0.6 V/hr.

Table 3.18 Summary of results of potentiodynamic polarization tests on clean cast 1018 steel in deaerated basalt groundwater at 90 C and a scan rate of 0.6 V/hr.

Solution	E_{corr} V (SCE)	E_{pitt} V (SCE)	E_{prot} V (SCE)	i_{corr} A/cm^2	i_{peak} A/cm^2	i_{pass} A/cm^2
1X	-0.86	-0.47	-0.68	6.3×10^{-6}	1.0×10^{-5}	6.3×10^{-6}
1X + Basalt	-0.80	-0.66	-0.72	5.7×10^{-6}	--	--
10X	-0.87	-0.62	-0.72	6.3×10^{-6}	8.8×10^{-6}	3.3×10^{-6}
10X + Basalt	-0.92	-0.45	-0.75	7.2×10^{-6}	1.1×10^{-5}	3.9×10^{-6}

E_{corr} = corrosion potential.

E_{pitt} = potential at which pits initiate on forward scan.

E_{prot} = potential at which pits repassivate on reverse scan.

i_{corr} = corrosion rate at the free-corrosion potential.

i_{peak} = current density at active peak.

i_{pass} = current density in passive range.

Table 3.19 Summary of results of potentiodynamic polarization tests run on wrought 1018 steel in deaerated basalt groundwater at 90 C and a scan rate of 0.6 V/hr.

Solution	E_{corr} V (SCE)	E_{pitt} V (SCE)	E_{prot} V (SCE)	i_{corr} A/cm^2	i_{peak} A/cm^2	i_{pass} A/cm^2
1X	-0.86	-0.48	-0.66	6.8×10^{-6}	1.3×10^{-5}	5.7×10^{-6}
1X + Basalt	-0.80	-0.53	-0.72	5.5×10^{-6}	1.2×10^{-5}	7.8×10^{-6}
10X	-0.90	-0.45	-0.69	5.5×10^{-6}	7.8×10^{-6}	3.5×10^{-6}
10X + Basalt	-0.91	-0.55	-0.70	6.3×10^{-6}	1.0×10^{-5}	3.1×10^{-6}

E_{corr} = corrosion potential.

E_{pitt} = potential at which pits initiate on forward scan.

E_{prot} = potential at which pits repassivate on reverse scan.

i_{corr} = corrosion rate at the free-corrosion potential

i_{peak} = current density at active peak.

i_{pass} = current density in passive range.

of the exposure studies. However, longer equilibration times between the basalt rock and the groundwater at the test temperature may alter the corrosion behavior.

Potentiodynamic-polarization data also are useful in assessing materials' susceptibility to stress-corrosion cracking. The presence of an active-passive transition in the potentiodynamic-polarization curves is an indication that stress-corrosion cracking may occur. However, the magnitudes of the peak current density and the active-to-passive transition are small, indicating low susceptibility to stress-corrosion cracking at 90 C.

3.2.2.4 Slow Strain Rate Tests

Slow strain rate tests were performed on cold-rolled 1018 carbon steel specimens (obtained from a commercial supplier) in the standard basalt groundwater at 90 C and a strain rate of $6x10^{-7}$/sec. The weight percent composition of the steel used in these tests is: carbon, 0.18; manganese, 0.72; phosphorus, 0.0007; sulfur, 0.010.

The tests were performed over a potential range of -0.5 to -0.7 V (SCE) which was selected on the basis of the results of the potentiodynamic-polarization behavior. This potential range lies in the region of the active-passive transition in the anodic polarization curve, a potential region where stress-corrosion cracking of carbon steel is observed in all the cracking environments that have been studied electrochemically (see Section 3.2.2.5). Results of the tests, which are given in Table 3.20, show that the mechanical properties of the materials were similar in the basalt environment and in the inert environments. Moreover, optical examination of the specimens did not indicate any evidence of susceptibility to stress-corrosion cracking. The small values of elongation to failure were the result of the use of cold-worked, rather than hot-worked, material. Use of this material had the advantage that failure times were reasonably short, even though the strain rate was quite low.

3.2.2.5 Literature Survey of Stress-Corrosion Cracking

A survey of the literature was performed on stress-corrosion cracking (SCC) of low-strength carbon steels in repository environments. This survey has been submitted to NRC as a topical report.

It was found that SCC of low-strength carbon steels has been observed in a number of environments. Some of the cracking agents identified for carbon and low-alloy steels are:

Table 3.20 Effect of electrochemical potential on the time to failure and the mechanical properties of cold-rolled 1018 carbon steel specimens in slow strain rate tests in 1X basalt groundwater at 90 C at a strain rate of 6×10^{-7}/sec.

Potential V(SCE)	Time to Failure, Hours	Percent Elongation
-0.50	26.2	4.21
-0.60	26.6	3.95
-0.70	28.5	5.29
Oil at 90 C	26.2	4.75
Air at 25 C	24.0	4.31

- NO_3^-
- OH^-
- $CO_3^= - HCO_3^-$
- $CO - CO_2 - H_2O$
- PO_4^{-3}
- Water - O_2
- Water - Cl^- - Oxidant
- $MgCl_2$ (Ni Alloys)
- H_2SO_4 - KI
- Non-aqueous liquid NH_3.

In all the environments in which electrochemical studies have been performed, stress-corrosion cracking occurs over an electrochemical potential range in which there is a critical balance between active and passive behavior, which is reflected in the potentiodynamic-polarization curves. This relationship between passivation and stress-corrosion cracking is the basis for the dissolution mechanism for stress-corrosion cracking.(3.4) The essence of this mechanism is that the walls of the crack are passivated while plastic deformation continually bares unfilmed metal at the crack tip, which undergoes rapid dissolution. In this mechanism, environmental parameters play a role in cracking through their influence on the chemistry and electrochemistry of the system, whereas physical and metallurgical parameters affect the mechanical response at the crack tip as well as the electrochemical behavior of the material. A detailed discussion of this mechanism and additional supporting evidence are given by Parkins.(3.4)

The results of the mechanical-effects studies of stress-corrosion cracking in these systems also are quite consistent with the above mechanism. Stresses approaching the yield stress apparently are necessary for SCC to initiate in most of the systems studied. This behavior may simply reflect the necessity for significant plastic deformation to occur in order for the cracking to initiate. Historically, the utilization of this knowledge to limit SCC either by decreasing the applied residual stresses or by increasing the yield stress of the material have met with only limited success. Among the reasons for this is the detrimental effect of cyclic loading on threshold stresses for cracking. Moreover, the presence of notches in a structure can cause local stresses to exceed the yield stress, even when static nominal stresses are considerably lower. Finally, altering the composition or microstructure of an alloy to increase its yield stress may actually increase the probability that cracking will occur because of detrimental effects of the alteration on the electrochemical behavior of the material or the increased likelihood of hydrogen embrittlement.

One desirable feature of the dissolution model for stress-corrosion cracking is that it enables a rapid prediction of the potency of an environment on the basis of electrochemical measurements. Possible stress-corrosion cracking environments are those in which a pronounced active-to-passive transition is observed in the potentio-dynamic polarization curves or in current-time data. Actual cracking velocities also can be estimated on the basis of electrochemistry. Indeed, Parkins(3.5) found a good correlation between the peak current densities measured on relatively bare metal surfaces with measured cracking velocities, as shown in Figure 3.43. The straight line in Figure 3.43 is calculated from Faraday's Law,

$$v = \frac{i_a M}{ZFd} ,$$

where

i_a = anodic current density
M = atomic weight
Z = valency
F = Faraday's constant
d = alloy density

demonstrating the excellent correlation between the measured cracking velocities and those predicted on the basis of the proposed mechanism.

Results of the preliminary electrochemical studies performed on a 1018 carbon steel in a basaltic groundwater suggest that some slight susceptibility to SCC may exist in the bulk environments. However, most stress-corrosion cracking problems of technological importance occur in systems where the bulk environment is relatively innocuous, but where potent cracking environments develop locally, e.g., caustic cracking in boilers and carbonate/bicarbonate cracking of pipeline steels. Thus, one must examine the bulk environment to identify potential cracking agents and also to examine possible mechanisms for concentration of these agents.

Unfortunately, a number of potential cracking agents are present at low concentrations in the candidate repository environments. These include carbonates, hydroxides, phosphates, nitrates, chlorides, and oxygen. Phosphates and nitrates may enter a repository by the intrusion of groundwater containing fertilizers, although it appears that cracking induced by phosphates is only significant at low temperatures. Moreover, nitrate may be generated by radiolysis of N_2. To complicate the problem further, species other than those currently identified as potential cracking agents also may promote cracking, because any species capable of promoting passivation also is a candidate stress-corrosion cracking agent. Koch and Thompson(3.6) recently performed a literature survey of inorganic ionic species that affect corrosion of iron and iron-base alloys. A summary of their findings is given in Table 3.21. These data show that the cracking agents NO_3^-, $CO_3^=$, $PO_4^{\equiv}$, and I^- are inhibitors of general corrosion of steels, as is well known. Other general corrosion inhibitors of steels which are present in repositories include Mg^{++} and Ca^{++}, silicates, and $BO_3^{\equiv}$.

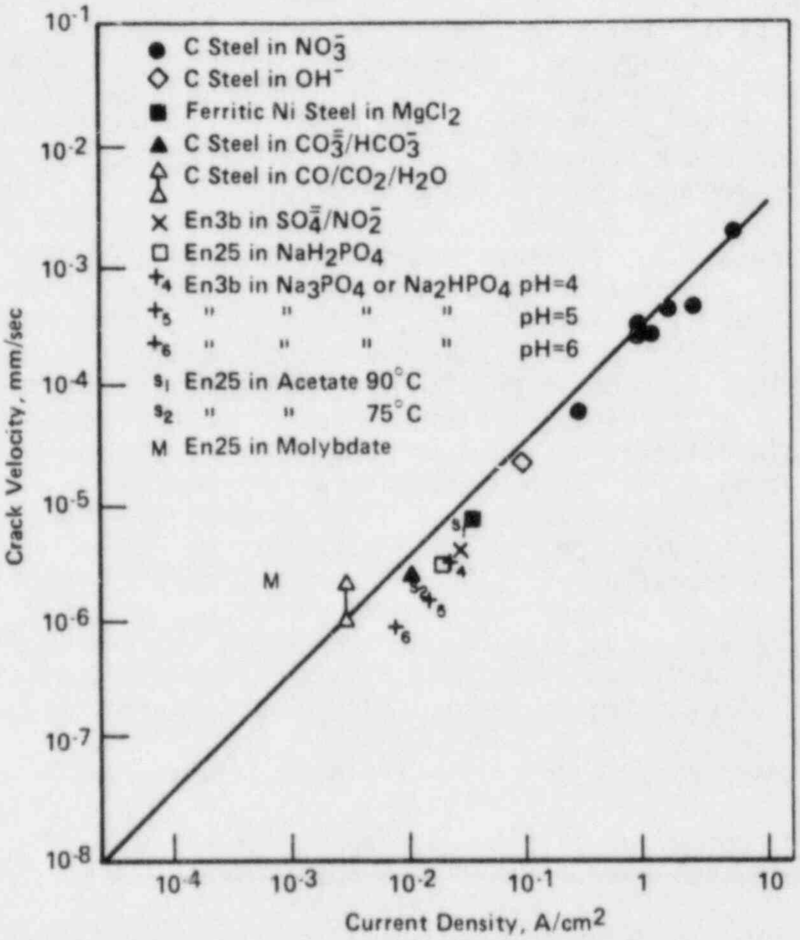

Figure 3.43 Measured stress corrosion crack velocities and current densities passed at a relatively bare surface for ferritic steel in a variety of solutions(3.5).

A number of potential concentrating mechanisms for the cracking agents may operate in a waste repository. For example, during the thermal period but prior to pressure buildup, boiling and resulting concentration may occur at, or near, the waste package. Localized corrosion is likely, and anions will migrate into pits and crevices to maintain charge neutrality where hydrolysis occurs. Thermogalvanic corrosion, which can occur where there are gradients in the skin temperature of the overpack, separates the oxidation and reduction reactions, resulting in acidification at the anodic sites and hydroxide buildup at the cathodic sites.

One problem with relating concentration mechanisms to stress-corrosion cracking susceptibility is in identifying upper limits for concentration. Clearly, this would require extensive physical modeling of the transport of the species. On the other hand, only limited data are available in the literature concerning lower limits in concentration for established cracking agents. Synergistic effects of the species present in the groundwater also must be considered.

Finally, the relationship between radiation and SCC warrants further amplification. In addition to the previously discussed effect of generating potential cracking agents, radiation also will move the Eh of the groundwater in the noble direction. Ford(3.7) in a review of the stress-corrosion cracking of ferritic steels, overlaid the pH-potential domains for SCC of ferritic steels in a number of environments on a single Pourbaix diagram, as shown in Figure 3.44. These data show that the cracking domain for phosphates, carbonates, and caustic lie along the water or H^+ reduction line and the domains for the latter two systems correspond with the region of stability of Fe_3O_4. Although data on Eh values in repositories are limited and of questionable accuracy, many repository environments are considered to be highly reducing, and thus the radiation fields may move the Eh values into these cracking domains. Furuya(3.8) demonstrated a similar effect in studies of the stress-corrosion cracking of sensitized Type 304 stainless steel.

This literature survey leads to the following conclusions:

- A number of potential cracking agents are present at low concentrations in repository environments.
- Stress-corrosion cracking of mild steel is relatively unlikely in bulk repository environments because of the low concentrations of the cracking species.
- The most serious threat to the integrity of a carbon-steel overpack with respect to stress-corrosion cracking is through concentration of the cracking species.
- Potential concentrating mechanisms include heat transfer, pitting, crevice corrosion, and thermogalvanic corrosion.

Table 3.21 Summary of the effects of various ions on the corrosion of iron-base alloys.

Anion	Effect	Cation	Effect
Cl^-	Accelerate	Cu^{+2}	Accelerate
Br^-	Accelerate	Cu^{+2}	Inhibit
I^-	Accelerate	Zn^{+2}	Accelerate
I^-	Inhibit	Ca^{+2}	Inhibit
F^-	Accelerate	Mg^{+2}	Inhibit
SO_4^{-2}	Accelerate	Fe^{+2}	Accelerate
SO_3^{-2}	Accelerate	Cr^{+3}	Accelerate
ClO_3^-	Accelerate		
ClO_3^-	Inhibit		
TcO_4^-	Inhibit		
CrO_4^{-2}	Inhibit		
$Cr_2O_7^{-2}$	Inhibit		
NO_3^-	Inhibit		
NO_2^-	Inhibit		
MnO_4^-	Inhibit		
IO_3^-	Inhibit		
AsO_2^-	Inhibit		
AsO_4^{-3}	Inhibit		
AsO_4^{-3}	Decrease Strength		
PO_4^{-3}	Inhibit		
HPO_4^{-2}	Inhibit		
$H_2PO_4^-$	Inhibit		
CO_3^{-2}	Inhibit		
B_4O^{-2}	Inhibit		
BO_3^{-3}	Inhibit		
MoO_4^{-2}	Inhibit		
WO_4^{-2}	Inhibit		
Silicate	Inhibit		

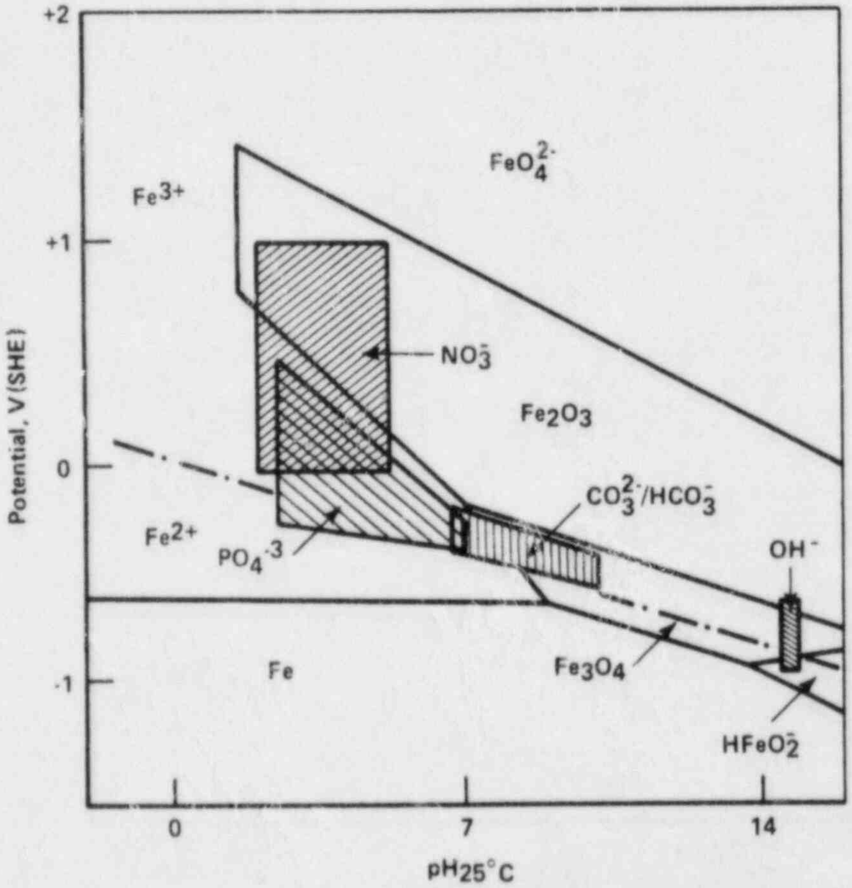

Figure 3.44 Potential-pH diagram for iron with cracking domains for some of the potent cracking agents(3.7).

- The influence of radiation fields on stress-corrosion cracking is not fully understood, but limited experimental data suggest that one likely influence is in moving the free-corrosion potential in the noble direction, which may increase the probability of SCC.

- Another effect of radiation fields may be to generate cracking agents such as nitrates.

- Stresses approaching the yield stress generally are required for cracking to initiate, even where the cracking agents are present at high concentrations.

These conclusions suggest a number of data needs. First, experimental and modeling studies are needed to assess the likelihood of stress-corrosion cracking of carbon steel in waste-repository environments. For the cracking agents identified in waste repositories, lower limits in concentration needed to promote cracking must be established. It is important to establish these data under realistic conditions where synergistic effects of other species present in the waste repository are considered. These studies can be accomplished through electrochemical screening of the environments, followed by selected stress-corrosion tests. The slow strain rate test technique for stress-corrosion testing is probably the most promising because it is an accelerated test and it allows a rapid evaluation to be made. Where evidence of cracking susceptibility is observed, it may be desirable to perform fracture-mechanics tests to measure cracking velocities accurately.

Physical modeling of possible concentrating mechanisms needs to be performed to more accurately assess the likelihood that these proposed mechanisms operate and to bound the upper limits of concentration for each mechanism. Identifying and quantifying mechanisms where selective concentration of a single or of a few species occurs are especially important in relating the modeling to the laboratory studies. Finally, the model should be verified through experimentation.

3.2.3 Future Work

External-corrosion studies during the third year will focus on stress-corrosion cracking and pitting kinetics of cast and wrought low-carbon steels in basaltic environments.

The objective of stress-corrosion cracking studies will be to identify species and environmental conditions (such as electrochemical potential and species concentration) which will promote stress-corrosion cracking (SCC) of steels in basaltic repositories. Electrochemical screening tests will identify particularly deleterious species and concentrations of those species. Selection of species for study will be based on the recently-completed SCC literature survey and on studies of radiolysis and groundwater composition being conducted in the System Performance Task of this project. Slow strain rate tests will be performed to confirm cracking under the most aggressive conditions. The planned experiments have the advantage of generating a wealth of electrochemical data that will be useful in developing the general- and pitting-corrosion correlations.

The objectives in the studies of pitting kinetics during the third year will be to obtain experimental data for use in validating the current model of pit-propagation kinetics and in understanding the relationship between pitting kinetics and geometrical, environmental, and metallurgical parameters. An electrochemical pitting-corrosion monitor will be developed and tested for use in the autoclave, based on a design currently used at Battelle's Columbus Laboratories to study the pitting kinetics of natural gas pipelines. Once developed, tested, and proven, the monitor will provide information on the effects of the above-mentioned parameters on pitting of carbon steels in repository environments.

3.3 Hydrogen Embrittlement of Cast-Steel Overpacks

Hydrogen embrittlement of steel overpacks is a significant concern with regard to container integrity because of the high hydrogen fugacity that could develop in a repository environment as a result of corrosion and/or radiolytic reactions. The extent of hydrogen degradation of the properties of any steel that is exposed to hydrogen depends on numerous material and environmental factors. Material factors that influence hydrogen embrittlement include alloy composition, microstructure, impurity segregation, and yield strength. Other factors such as hydrogen fugacity, temperature, the presence of stress concentrators or cracks, and the plastic-deformation rate also play a major role in hydrogen embrittlement. The influence of many of these factors on hydrogen embrittlement of cast-steel overpacks in high-level-waste containers is being studied in this program.

Hydrogen embrittlement of steels has been studied for over 50 years. The technical literature contains considerable information regarding hydrogen-induced loss of ductility and fracture toughness (embrittlement) in low-to-medium-strength wrought steels. In the area of cast steels, early work by Sims and his co-workers at Battelle identified steel-industry programs with heavy castings as a hydrogen-embrittlement phenomenon(3.9). Other similar studies have been conducted since that time; however, there has been no research effort toward understanding embrittlement of cast steels and the effects of material and environmental factors on that embrittlement. Therefore, Battelle has undertaken an investigation of hydrogen embrittlement of cast steel to develop an understanding of the effects of some material factors on embrittlement. In addition, in an effort to make use of the information available in the technical literature on hydrogen embrittlement of wrought steels, a comparison of the embrittlement susceptibilities of cast and wrought steels of identical chemical composition has been made.

3.3.1 Materials

To determine whether cast-steel overpacks will be particularly sensitive to hydrogen embrittlement and to identify the factors that contribute to hydrogen-embrittlement susceptibility in cast steels, two carbon-steel castings were prepared with nominal compositions that conform to ASTM Standard A27-81a, "Specification for Mild- to Medium-Strength Carbon-Steel Castings for General Application"; the compositions of the castings also conform to ASTM Standard A216 Grade WCA, which is being considered by DOE as a specification for a potential overpack material(3.10). The castings were sand-cast with approximately 8-inch-square cross sections in an attempt to simulate the slow cooling that is likely to be experienced in casting an overpack.

The effect of casting cleanliness with regard to metalloid impurity content was studied by preparing the castings with two impurity levels from a split heat: (1) "clean", which represents a high level of cleanliness and (2) "doped", which represents more typical commercial cleanliness levels, but actually was prepared by purposely adding sulfur and phosphorus to one half of the clean-steel melt. The compositions of the steels are summarized in Table 3.22, which includes for comparison the specified compositions of the other cast steels mentioned above. To provide a comparison with wrought-steel behavior, the castings were sectioned longitudinally, and one half of each casting was hot-rolled parallel to the pouring direction (8:1 reduction) to plate form; the temperature of each plate during rolling was between approximately 900 C and 1000 C. In addition, portions of the as-cast halves of the castings were annealed by heating in argon to 900 C, holding at temperature for two hours, and furnace-cooling to room temperature.

The microstructures of the clean and doped steels are shown in Figures 3.45 and 3.46, respectively. In those figures it can be seen that the clean-steel casting had a feathery, Widmanstatten-like microstructure, whereas the doped-steel casting had a more equiaxed-grain microstructure. The difference in structure would suggest a higher cooling rate for the clean steel. However, the heat records from the casting operation indicated that the cooling rates of all the castings were similar. Therefore, the solidification structure probably was affected by the presence of impurities which may provide nucleation sites for the formation and growth of equiaxed grains in the doped steel.

The microstructures of both steels consisted of ferrite (light constituent in Figures 3.45 and 3.46) and pearlite (dark constituent). In the as-cast condition there was considerable difference in the morphology of those microconstituents, as discussed above. After annealing, the ferrite and pearlite grains were much finer than in the as-cast condition. However, the differences in the ferrite/pearlite morphology observed between the clean and doped steels as cast were reflected in the annealed condition. In the clean steel, the pearlite appeared to be "banded", but the bands were oriented randomly, unlike

Table 3.22 Chemical compositions of steel castings and specified compositions of ASTM standards.

Steel Designation	Content, weight percent										
	C	Mn	P	S	Si	Al	Cu	Ni	Cr	Mo	V
Clean Steel	0.18	0.49	0.004	0.002	0.30	0.10	0.006	0.002	0.007	0.000	0.000
Doped Steel	0.17	0.55	0.029	0.036	0.35	0.14	0.007	0.004	0.011	0.000	0.006
ASTM A27 Grade U-60-30	0.25 max	0.75 max	0.05 max	0.06 max	0.80 max	--	--	--	--	--	--
ASTM A216 Grade WCA	0.25 max	0.70 max	0.04 max	0.045 max	0.60 max	--	0.50 max*	0.50 max*	0.40 max*	0.25 max*	0.03 max*

* The sum of the contents of these elements shall not exceed 1.00 weight percent, and those contents shall satisfy the following:

$$\text{Carbon equivalent} = C + \frac{Mn}{6} + \frac{Cr + Mo + V}{5} + \frac{Ni + Cn}{15} \qquad 0.50.$$

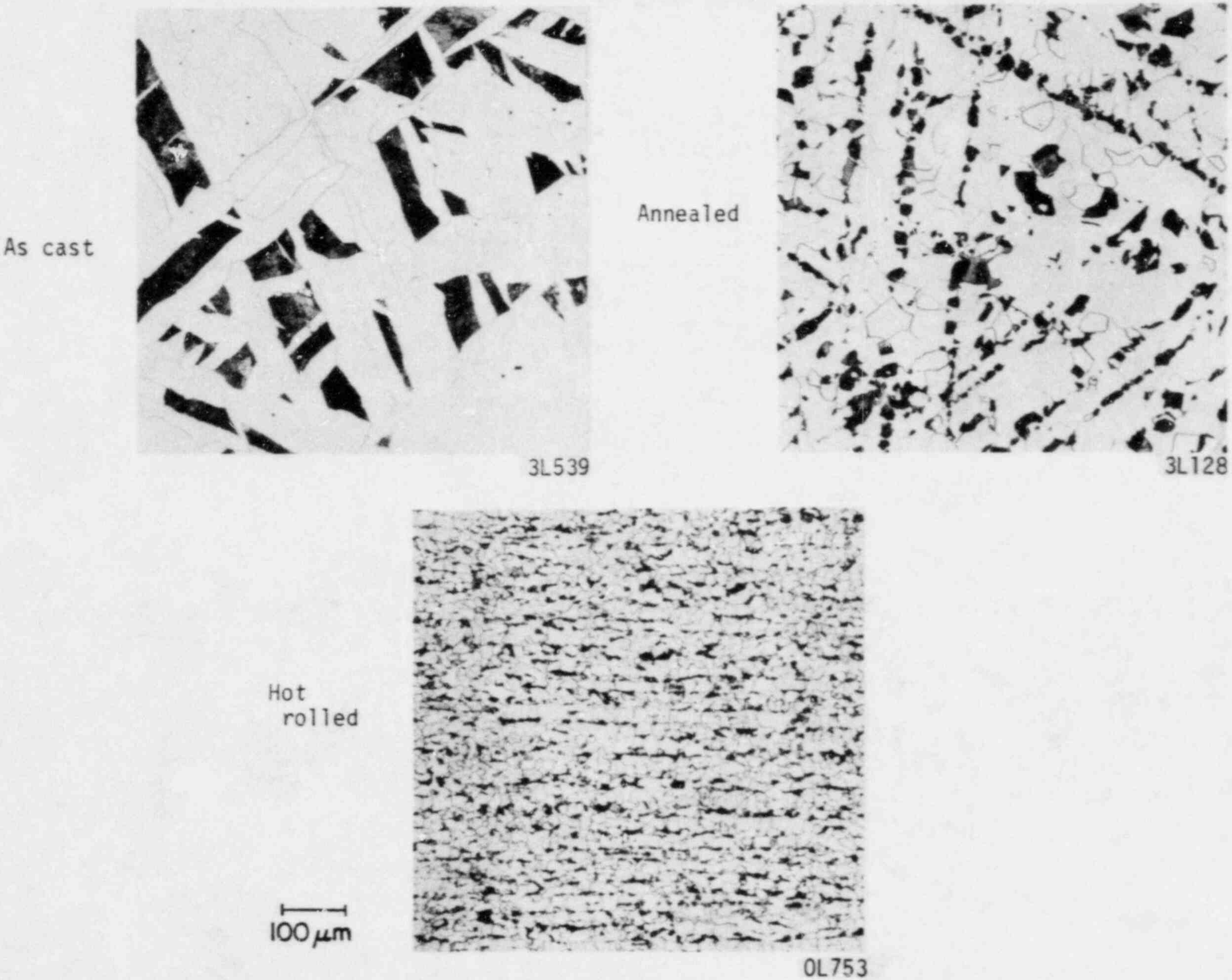

Figure 3.45 Microstructure of clean steel etched with picral and nital.

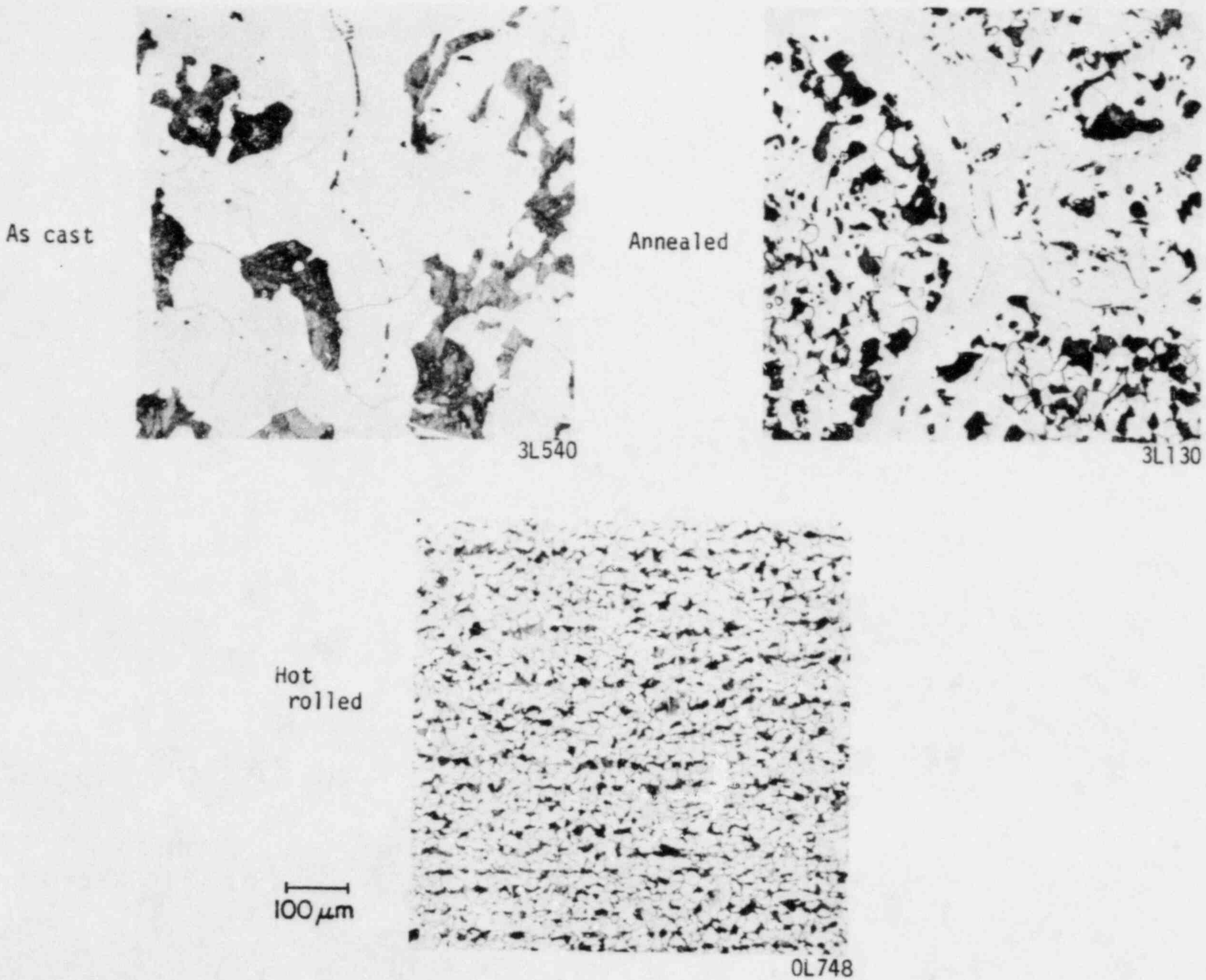

Figure 3.46 Microstructure of doped steel etched with picral and nital.

bands in a rolled-steel product. The pearlite in the doped steel was more evenly distributed, having formed from the more equiaxed cast structure. In the hot-rolled condition, the ferrite and pearlite constituents were banded in the direction of rolling for both steels.

In addition to differences in the configuration of microstructural constituents in the as-cast condition, there were significant differences in inclusion content. The doped casting contained numerous manganese sulfide inclusions that were aligned on as-cast grain boundaries. Those inclusions are visible in Figure 3.46a. The manganese sulfide and other inclusions that were present in the as-cast doped steel were not affected by the annealing heat treatment. The manganese sulfide inclusions still were situated on as-cast grain boundaries and formed a nearly continuous film on those boundaries, as shown in Figure 3.46b. The clean-steel casting had very few of those manganese sulfide inclusions. When the steels were hot-rolled, the manganese sulfide inclusions were elongated in the rolling direction, and the resulting microstructures exhibited little difference in morphology of the inclusions apart from the number of inclusions present. Both clean and doped castings also contained clusters of alumina-type inclusions which were strung out during rolling. The alumina-type inclusions appeared to be more prevalent in the doped steel.

Sensitivity to hydrogen embrittlement was evaluated by conducting tension and fracture-toughness tests in gaseous-hydrogen and inert environments and measuring the extent of degradation of properties by hydrogen. Testing in gaseous hydrogen separated the effects of hydrogen from corrosion effects, such as stress-corrosion cracking, that could occur in prototypic repository environments. In addition, the content of hydrogen absorbed as a result of corrosion reactions with basaltic groundwater was measured; parallel studies are being conducted at Brookhaven National Laboratory to determine the effect of radiolytic reactions on hydrogen absorption.

3.3.2 Tension Tests

Smooth, cylindrical tension specimens with a 0.25-inch-diameter (0.635-cm) gage section were machined from samples of the clean and doped steels in the as-cast, annealed, and hot-rolled conditions. The axes of the specimens were oriented longitudinally (i.e., parallel to the direction of pouring or hot-rolling) or transversely (i.e., perpendicular to the direction of pouring or hot-rolling). Duplicate tension tests were conducted at room temperature in hydrogen and in nitrogen (reference environment) at a pressure of 1000 psig and at an engineering-strain rate of 10^{-4} sec^{-1}. Strength and ductility properties were measured, and the fracture surfaces were examined in a scanning-electron microscope (SEM) to determine whether hydrogen affected the fracture mode.

3.3.2.1 Effect of Hydrogen on Tensile Properties

Tables 3.23 and 3.24 present the tensile data for the cast and wrought steels, respectively. Table 3.23 includes for comparison the specified properties for ASTM A216 Grade WCA steel. The table shows that the strengths of the steels as cast, annealed, and hot rolled were not affected significantly by impurity content, specimen orientation, or test environment. The average yield and ultimate tensile strengths for each material condition in hydrogen and in nitrogen were:

Material Condition	Yield Strength, ksi (MPa)	Ultimate Tensile Strength, ksi (MPa)
As cast	22 (149)	50 (345)
Annealed	31 (215)	58 (398)
Hot rolled	41 (284)	64 (442)

In the as-cast condition, the steels studied by Battelle did not meet the strength requirements of the Grade WCA steel, although they did meet the specification for chemical composition. However, annealing the steels increased the strength to approximately the minimum specified level. Heat treating to meet strength specifications is a common practice in the casting industry.

The ductilities of the steels were influenced by many factors, especially impurity content and environment. Figure 3.47 compares the reduction in area for each material condition. For material in the as-cast condition, considerable scatter in the ductility data was observed for replicate specimens, presumably as a result of the inhomogeneity of the castings and the small specimen size relative to the grain size. To reduce the scatter in the data, the results in Figure 3.47 were obtained by averaging the data for both orientations. Averaging may mask to some extent the effect of structure (orientation) on ductility; however, the variation with orientation was small compared with the effects of processing and of impurity content. For the clean steel, annealing increased the ductility when tested in nitrogen over that for the as-cast condition and decreased slightly the ductility loss when tested in hydrogen. Hot rolling further increased the ductility when tested in nitrogen and decreased the ductility loss when tested in hydrogen. The doped steel exhibited considerably less ductility than did the clean steel in either test environment, particularly in the as-cast and the annealed conditions. The inherent ductility was so low for the doped steel in those conditions that the effect of hydrogen on ductility was minimal, as is illustrated in Figure 3.47. This low ductility was related to the manganese sulfide inclusions that were on the as-cast grain boundaries, as is discussed in the following section. No beneficial effect on ductility by annealing was observed for the doped steel. However, hot rolling provided some improvement in ductility.

Table 3.23. Tensile properties of cast steels.

Casting and Condition	Test Environment	UTS, ksi	Yield Strength, ksi	Percent Elongation in 1 inch	Reduction in Area, percent
			Longitudinal Orientation		
Clean, as cast	1000 psig N_2	48	19	23	31
	1000 psig H_2	49	18	15	20
Clean, annealed	1000 psig N_2	58	30	37	56
	1000 psig H_2	59	31	36	59
Doped, as cast	1000 psig N_2	51	24	26	36
	1000 psig H_2	50	22	15	18
Doped, annealed	1000 psig N_2	55	32	14	28
	1000 psig H_2	56	32	13	23
			Transverse Orientation		
Clean, as cast	1000 psig N_2	50	21	29	50
	1000 psig H_2	51	22	28	41
Clean, annealed	1000 psig N_2	58	30	39	67
	1000 psig H_2	59	30	32	37
Doped, as cast	1000 psig N_2	51	25	13	16
	1000 psig H_2	50	22	15	20
Doped, annealed	1000 psig N_2	58	32	17	20
	1000 psig H_2	59	32	15	23
			ASTM A216 Grade WCA - Unspecified Orientation		
As cast or heat treated	Laboratory Air	60-85	30 Min	24 Min	35 Min

Table 3.24 Tensile properties of wrought steels.

Steel Identification	Test Environment	UTS, ksi	Yield Strength, ksi	Percent Elongation in 1 inch	Reduction in Area, percent
			Longitudinal Orientation		
Clean	1000 psig N_2	63	42	39	66
	1000 psig H_2	62	42	40	63
Doped	1000 psig N_2	67	42	34	53
	1000 psig H_2	67	43	34	40
			Transverse Orientation		
Clean	1000 psig N_2	64	41	41	63
	1000 psig H_2	62	39	35	48
Doped	1000 psig N_2	65	39	39	63
	1000 psig H_2	65	41	34	37

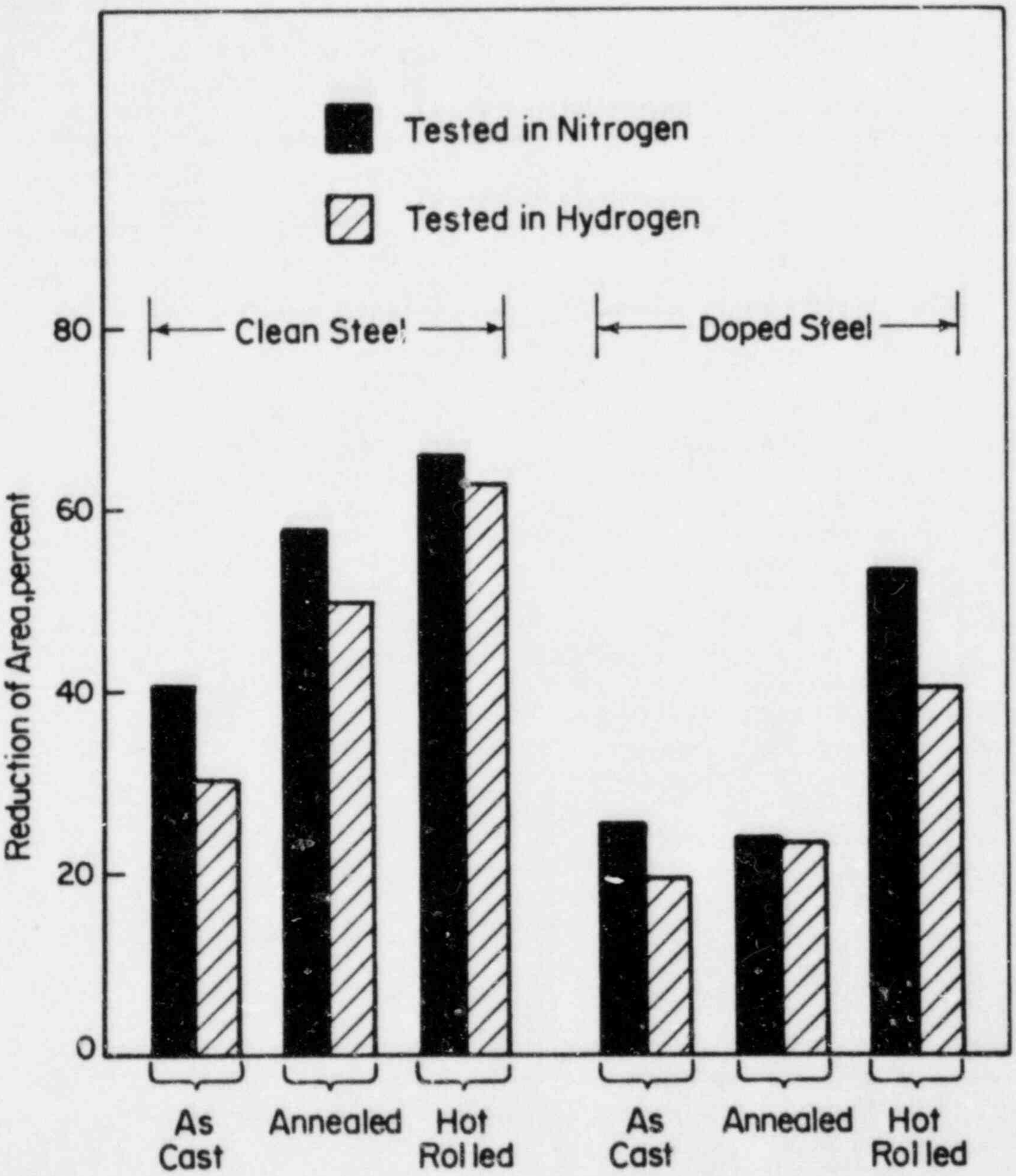

Figure 3.47 Ductility of clean and doped steels tension tested in 1000 psig hydrogen or nitrogen.

3.3.2.2 Fractography of Tensile Specimens

Fracture surfaces were examined in the scanning electron microscope to determine the dominant fracture mode for each material condition and environment. For the clean steel, fracture was strongly influenced by the hydrogen environment. In nitrogen, the as-cast clean steel fractured by a combination of tearing (failure with limited ductility) and some ductile dimpled rupture. In hydrogen, the clean steel failed by tearing in some regions and cleavage (brittle fracture) in others. Hydrogen also reduced local plastic deformation in the annealed clean steel. Annealing caused the fracture behavior in nitrogen to change to completely dimpled rupture, whereas the fracture mode in hydrogen changed to dimpled rupture plus tearing. Figure 3.48 presents examples of dimpled rupture, tearing, and cleavage in the clean steel. The figure shows the extent to which localized plastic deformation was reduced by hydrogen. This reduction was more pronounced in the as-cast condition than in the annealed condition. The refinement of the grains and redistribution of segregated impurities during annealing probably account for the increased resistance of the annealed steel to degradation by hydrogen. The fractographic evidence shown in Figure 3.48 suggests that the inherent resistance to fracture of the clean steel may be affected strongly by hydrogen as a result of reduced crack-tip deformation; this was studied further with fracture-toughness tests with precracked specimens, as is discussed in Section 3.3.3.

The doped steel in both the as-cast and annealed conditions fractured primarily along as-cast grain boundaries by delamination at manganese sulfide inclusions (i.e., separation at the matrix-inclusion interfaces), as is shown in Figure 3.49. In addition, some tearing was observed. The fractographic appearances of as-cast and annealed doped-steel specimens tested in hydrogen and nitrogen were virtually identical. Hydrogen apparently had little effect on the process of delamination at manganese sulfide inclusions. It is not clear at this time to what extent the effects observed with respect to the manganese sulfide inclusions are representative of other cast steels with similar compositions but with inclusions that are more uniformly distributed.

In the hot-rolled condition, the clean and doped steels fractured by dimpled rupture, or microvoid coalescence, both in hydrogen and in nitrogen. This behavior is consistent with that of other wrought steels reported widely in the literature(3.11). In the hot-rolled condition, the doped steel was slightly more susceptible to hydrogen-induced ductility losses than the clean steel. The dimples on the fracture surfaces of the doped steel consisted of a mixture of fine (initiated at carbide-ferrite interfaces) and coarse (initiated at MnS-matrix interfaces) dimples, whereas the dimples in the clean steel were almost uniformly fine.

3.3.3 Fracture-Toughness Tests

Fracture-toughness tests were conducted following ASTM Standard E813-81, "Standard Test Method for J_{IC}, a Measure of Fracture Toughness", using

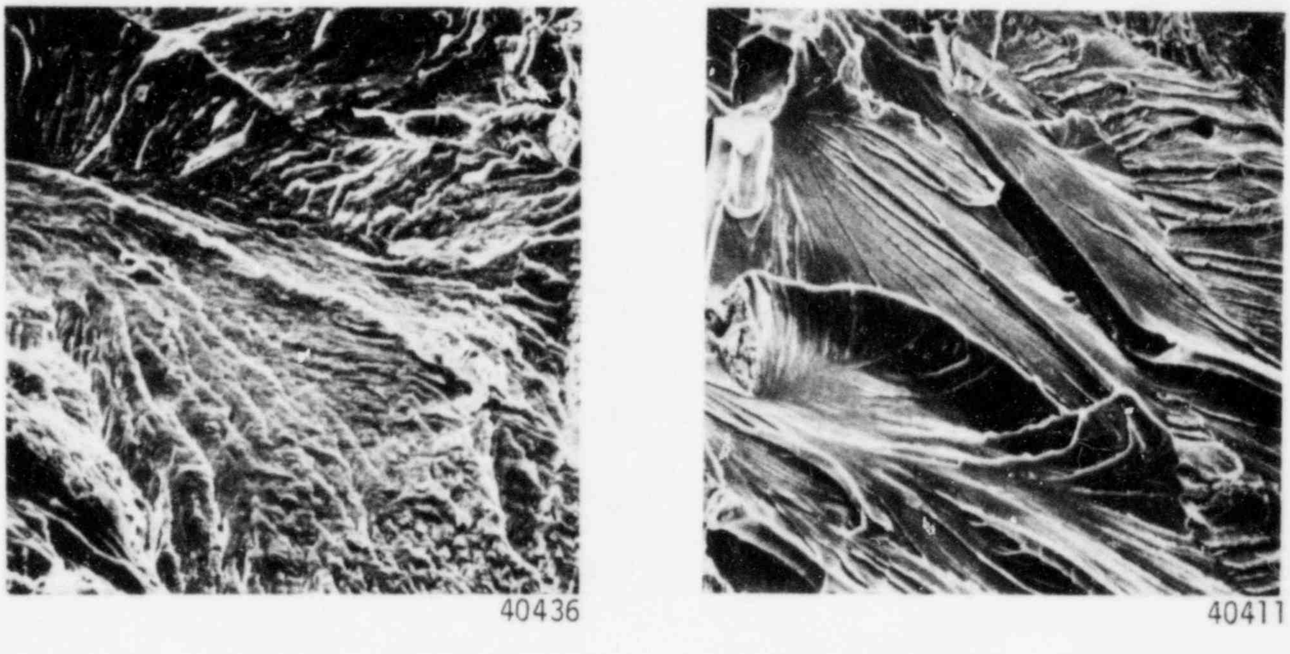

a. As cast; tested in nitrogen.

b. As cast; tested in hydrogen.

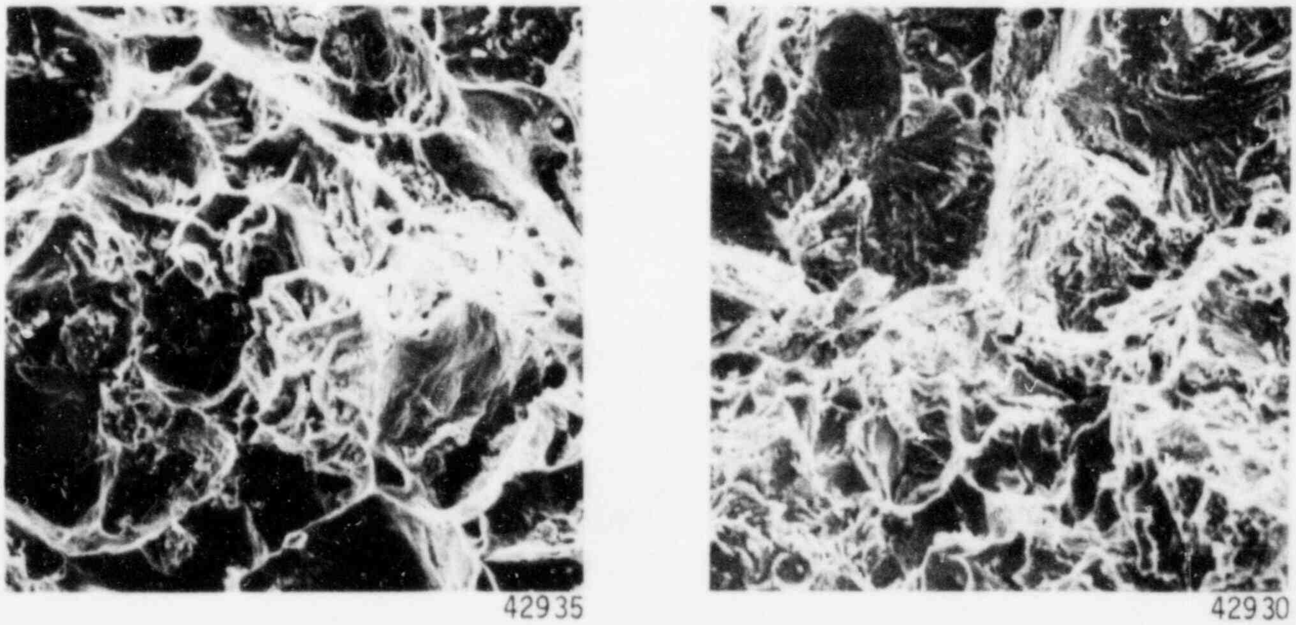

c. Annealed; tested in nitrogen.

d. Annealed; tested in hydrogen.

Figure 3.48 Fracture surfaces of clean, cast steel.

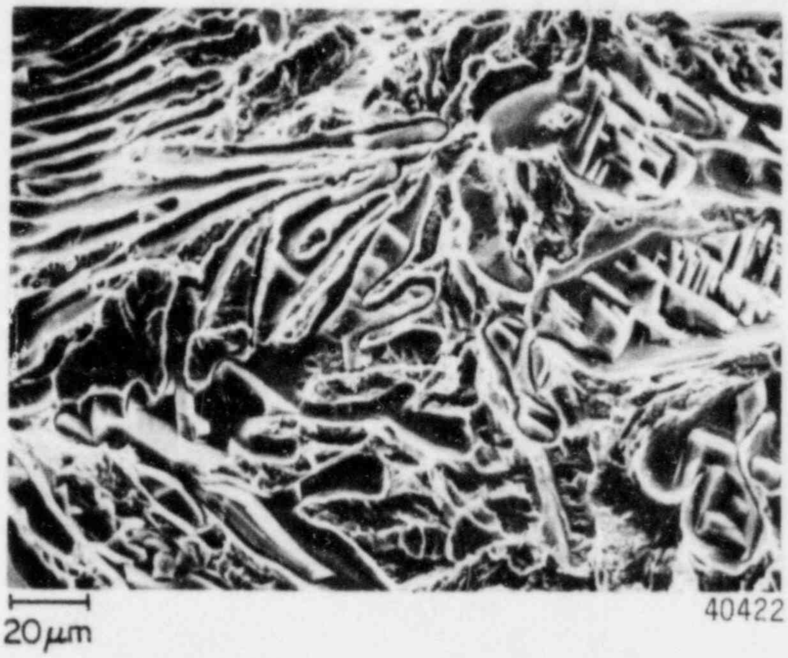

a. Tested in nitrogen.

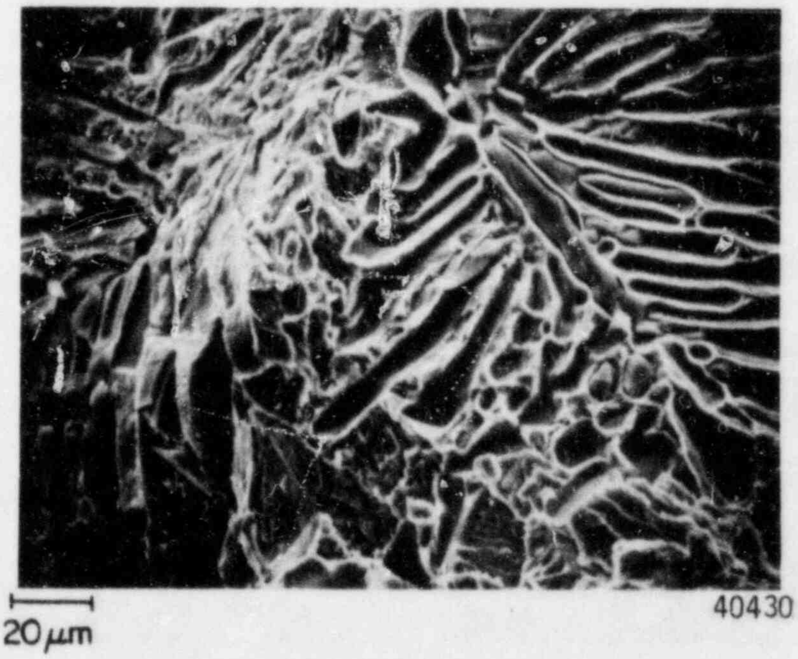

b. Tested in Hydrogen.

Figure 3.49 Fracture surfaces of doped, as-cast steel.

1-T (i.e., one-inch (2.54-cm) thick) compact-tension specimens. The type of test described in ASTM Standard E813-81 is the preferred method for characterizing the crack-extension behavior of a ductile metal. The information obtained from such testing provides an indication of the work required to initiate a ductile crack (J_{IC}, the energy-release rate when the crack is formed) and the resistance of the metal to subsequent unstable plastic crack growth (T, the tearing modulus, which is proportional to the slope of the J-resistance curve)(3.12).

The as-cast and the annealed specimens were oriented so that cracks would grow from the outer surface toward the interior of the casting; that is, parallel to the columnar grains of the casting. This crack-growth direction is representative of the type of cracking that is most likely to cause a breach in the overpack. Wrought specimens were in the T-L orientation, which results in crack growth parallel to the rolling direction. Tests were conducted in 1000 psig hydrogen and, as an inert reference environment, in 1000 psig nitrogen. Crack length was monitored using a d.c. electric-potential-drop method so that J-resistance curves could be developed from a single specimen.

3.3.3.1 Effects of Hydrogen on Fracture Toughness

The results of tests on the as-cast clean steel are presented in Figure 3.50. From that figure, the value of J_{IC} for each environment is determined by the intersection of the J-resistance curve for that environment and the blunting line for the particular material. The blunting line is an approximation of the apparent crack growth resulting from crack-tip blunting, Δa_B, and is defined by the expression

$$\Delta a_B = \frac{J}{2\sigma_0} ,$$

where σ_0 is the flow stress (given by the average of the yield strength and the ultimate tensile strength). The tearing modulus T is given by the following expression(3.12):

$$T = \frac{E}{\sigma_0 2} \frac{dJ}{da} ,$$

where E is Young's modulus and dJ/da is the slope of the J-resistance curve. T is a non-dimensional material parameter. A horizontal J-resistance curve (T=0) would indicate that the material is subject to time-dependent crack growth under a sustained load. This phenomenon, also referred to as delayed failure, is one of the more serious concerns with regard to overpack failure by hydrogen embrittlement.

The data in Figure 3.50 indicate a moderate reduction in fracture toughness by hydrogen for the as-cast clean steel. J_{IC} was reduced from approximately 575 psi-inch (0.105 MN/m) in nitrogen to approximately 420 psi-inch (0.076 MN/m) in hydrogen. In an earlier report it was observed that hydrogen reduced the tearing modulus of the steel by approximately 50 percent; however, during a Quality-Assurance review of that data, an error in the crack-length data for hydrogen that caused this apparent reduction was detected. Actually, hydrogen did not significantly influence the tearing modulus, as is shown in Figure 3.50 and as has been observed in previous studies at Battelle. However, for the annealed specimens a substantial reduction in the tearing modulus was observed. Table 3.25 summarizes the J_{IC} and tearing modulus data for the as-cast clean steel and the other material conditions, and includes for comparison data from an earlier Battelle study on a low-strength pipe steel.

As Table 3.25 shows, hydrogen reduced the fracture toughness, J_{IC}, for all material conditions except the annealed clean steel. For that material, J_{IC} was extremely low in both nitrogen and hydrogen. The fact that J_{IC} was higher in hydrogen than in nitrogen may have been a result of scatter in a low-toughness material. However, it is believed that the annealed clean steel should have toughness at least as high as that of the annealed doped steel, and that the low toughness was an experimental artifact. An additional test in nitrogen will be conducted to verify this possibility. Another inconsistency in Table 3.25 is with the effect of hydrogen on the tearing modulus of the as-cast doped steel. The data in the table suggest that exposure to hydrogen caused the tearing modulus to double, an effect that clearly is unrealistic, and this suggests a testing-related source for the inconsistency. Those experiments also will be repeated.

The effects of hydrogen shown in Table 3.25 are summarized below:

Steel Condition	Percentage Reduction Due to Hydrogen	
	J_{IC}	T
Clean; As cast	27	-7
Clean; Annealed*	-225	51
Clean; Wrought	95	27
Doped; As cast*	65	-64
Doped; Annealed	88	80
Doped; Wrought	58	-9
X42 Pipe Steel	64	14

---

* Verification tests to be conducted.

The fracture toughness, J_{IC}, was in most cases reduced substantially by hydrogen. The exceptions are the clean steel in the as-cast condition, which exhibited a modest reduction in J_{IC}, and the clean steel in the annealed condition, in which the measured J_{IC} in the reference environment was extremely low and must be verified. The results overall suggest that castings with low impurity contents will be relatively resistant to embrittlement. In fact, based on comparisons between the

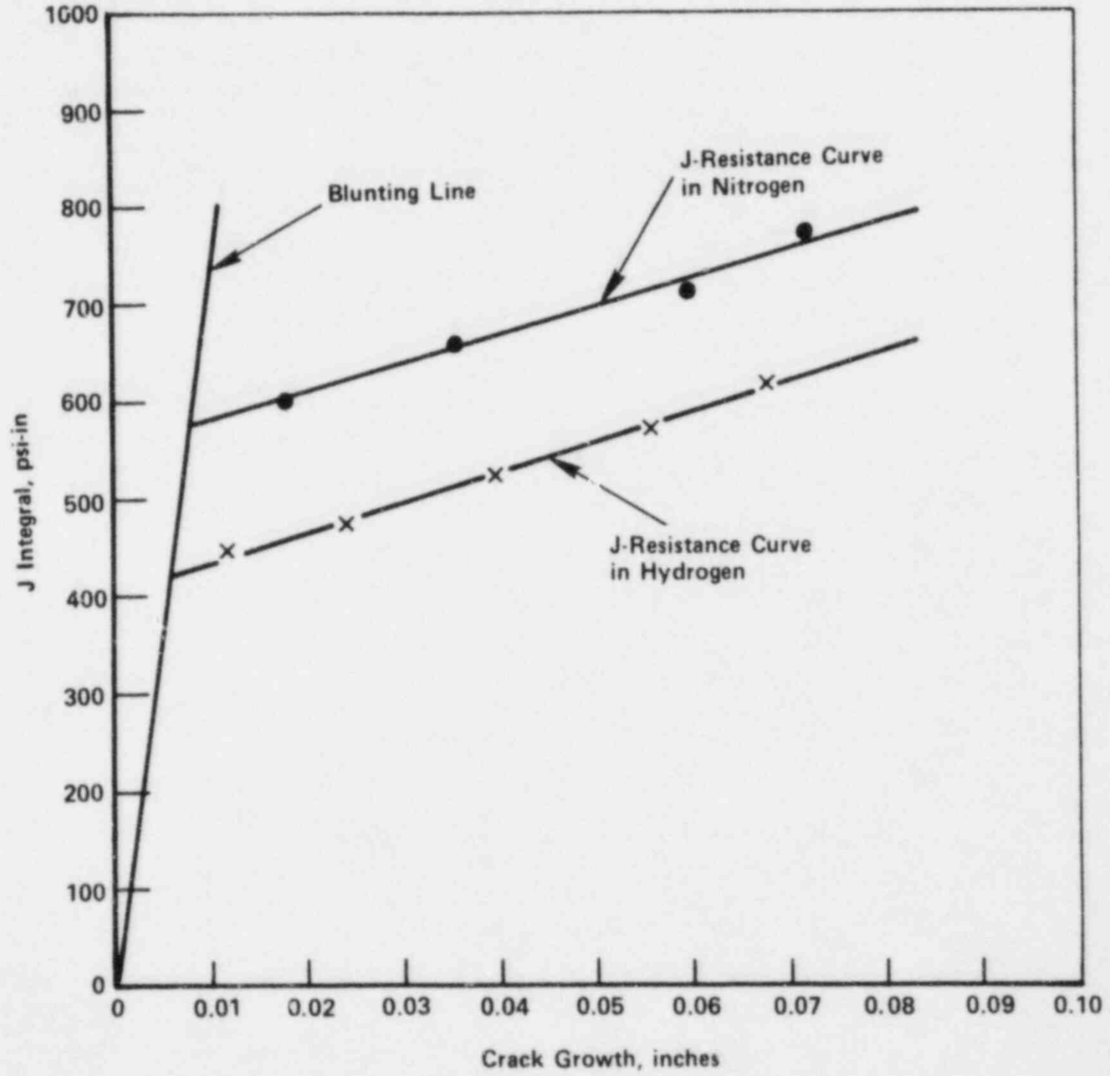

Figure 3.50 J-resistance curves for the as-cast clean steel tested in nitrogen and hydrogen.

Table 3.25. Fracture-toughness data for clean and doped steels.

Steel Condition	Test Environment	Fracture Toughness (J_{IC}), psi-inch (MN/m)	Tearing Modulus (T)
		Clean Steel	
As cast	1000 psig N_2	575 (0.105)	67
	1000 psig H_2	420 (0.076)	72
Annealed	1000 psig N_2	20 (0.004)	74
	1000 psig H_2	65 (0.012)	36
Wrought	1000 psig N_2	1,265 (0.230)	117
	1000 psig H_2	65 (0.012)	85
		Doped Steel	
As cast	1000 psig N_2	245 (0.045)	58
	1000 psig H_2	85 (0.015)	95
Annealed	1000 psig N_2	245 (0.045)	181
	1000 psig H_2	30 (0.005)	36
Wrought	1000 psig N_2	360 (0.065)	54
	1000 psig H_2	150 (0.027)	59
		X42 Pipe Steel(a)	
As fabricated	1000 psig N_2	800 (0.145)	87
	1000 psig H_2	290 (0.053)	75

(a) H. J. Cialone and J. H. Holbrook, "Effects of Gaseous Hydrogen on Fatigue-Crack Growth in Pipeline Steels", to be published in Metallurgical Transactions A.

steels in the as-cast and wrought conditions, castings with low impurity content should be more resistant to embrittlement than are their wrought counterparts. The rather surprising result for the wrought clean steel--a very large reduction in J_{IC} in hydrogen--was verified by repeating the tests on the wrought-steel specimens. There appear to be no distinct correlations in the present work between data for the wrought and the cast steel that would allow other hydrogen-embrittlement data in the literature for wrought steels to be utilized directly.

The effect of hydrogen on the tearing modulus was expected to be small, based on an earlier hydrogen-embrittlement study on low-strength pipe steel (data supplied in Table 3.25). Tearing-modulus data have not been catalogued widely, and therefore the implications of a specific percentage reduction in T are not known at present. Thus, the tearing modulus was viewed as a relatively coarse measure of hydrogen-embrittlement sensitivity, with differences on the order of 20 percent to be considered insignificant. Thus, the tearing-modulus values for most of the steels were not affected significantly by hydrogen; the exceptions were the doped, as-cast steel, for which additional tests must be conducted because of the apparent increase in T in hydrogen, and the annealed steels. Surprisingly, the annealed steels exhibited large reductions in T when tested in hydrogen. A large reduction in T may indicate that the material will be susceptible to delayed failure in a hydrogen or hydrogen-bearing environment. Although the annealed clean steel must be retested in nitrogen to verify the low toughness in that reference environment, the tentative indication is that, at least for steels with impurity levels typical of current commercial practice, the thermal history of the casting may be very important. Microstructural changes and/or repartitioning of impurities during welding or with long-term exposure to low-level heat from the waste form may dramatically reduce the resistance of the steel to hydrogen embrittlement.

3.3.3.2 Fractography of Fracture-Toughness Specimens

The fracture surfaces of the as-cast and the wrought fracture-toughness specimens in the region of steady crack growth were examined in the scanning-electron microscope. Those fracture surfaces were similar to the fracture surfaces of the tensile specimens made from the same material and tested in the same environment. The exceptions were the as-cast clean steel tested in nitrogen and the wrought clean steel tested in hydrogen. In both cases, the fracture surface in the region of steady crack growth exhibited an appreciable proportion of cleavage fracture which was not observed or the fracture surfaces of the corresponding tensile specimens. The annealed specimens are currently being examined fractographically for evidence of the reason for the reduced tearing modulus in hydrogen.

3.3.4 Hydrogen Absorption During Corrosion Reactions

Because hydrogen may be absorbed by the cast steel during corrosion reactions with groundwater, hydrogen-absorption determinations were made on as-cast and wrought specimens exposed to simulated basaltic groundwater at 250 C to determine whether significant concentrations of hydrogen could be developed in cast-steel overpacks. In addition, some specimens were exposed to more concentrated basaltic groundwater containing ten times the nominal concentrations of the various components, as described in Section 3.2.2. Coupons 1/4-inch (0.635 cm) in diameter by 1 inch (2.54 cm) long were machined from both the clean and the doped steels. The coupons were exposed to the simulated basaltic groundwater environment under stagnant conditions for 500 to 2,000 hours. Some of the as-cast coupons were thermally outgassed under vacuum for 24 hours at 250 C prior to insertion in the autoclave to remove any diffusible hydrogen that might be present. After removal from the autoclave, the coupons were stored in liquid nitrogen to retain the hydrogen until they could be analyzed. Prior to analysis, the surfaces of the coupons were abraded with a file to remove oxide or other corrosion products that might influence the results of the analysis. The hydrogen contents of the coupons were determined using an Ithac-01 Hydrogen Determinator. The hydrogen was extracted from each coupon by an inert-gas-fusion method, and the amount present was determined by the change in thermal conductivity of the carrier gas; the sensitivity of the unit is 0.01 ppm hydrogen.

Table 3.26 presents the results of the hydrogen analyses. Three coupons were evaluated for each material condition. In addition, at least three coupons that were not exposed to the basaltic environment were analyzed to determine the initial hydrogen contents. The hydrogen concentration due to exposure was determined from the difference between those two values.

The data in Table 3.26 exhibit wide scatter for replicate conditions. This scatter is particularly evident for the unexposed clean steel in the as-cast condition, which contained considerable dissolved hydrogen, the content of which varied widely from one location in the casting to another (from 0.32 to 3.39 ppm). Thermal outgassing did not reduce the hydrogen content of the as-cast clean steel; in fact, the average hydrogen content of outgassed specimens was more than twice that of specimens that were not outgassed. This indicates that most of the pre-existing hydrogen probably was nondiffusible, i.e., in the form of gaseous hydrogen in pores or at internal interfaces. Specimen-to-specimen variations in the initial hydrogen content of the clean steel may then be related to variations in porosity or interface content, although such a correlation was not attempted.

Hot rolling eliminated virtually all the pre-existing hydrogen in the clean steel. The doped steel contained very little hydrogen in the as-cast condition (less than 0.1 ppm average) and exhibited little scatter in initial hydrogen content. However, after exposure to the simulated basaltic groundwater, both the clean and doped steels in the as-cast

Table 3.26 Hydrogen absorbed during exposure to simulated basalt groundwater

Material	Thermally Outgassed Before Exposure[a]	Hydrogen Content of Exposed Specimens, ppm by weight		Hydrogen Content of Unexposed Specimens, ppm by weight		Average Hydrogen Concentration Absorbed During Exposure, ppm by weight
		Range	Average	Range	Average	
2,000-Hour Exposure (Nominal Groundwater Composition)						
Clean Steel						
As cast	Yes	3.29-5.74	4.65	2.78-5.73	4.43	0.22
As cast	No	3.92-4.99	4.43	0.32-3.39	1.98	2.45
Wrought	No	0.34-0.50	0.42	0.00-0.00	0.00	0.42
Doped Steel						
As cast	Yes	0.56-2.89	1.86	0.00-0.05	0.02	1.84
Wrought	No	0.00-0.17	0.09	0.00-0.09	0.02	0.07
1,100-Hour Exposure (Nominal Groundwater Composition)						
Clean Steel						
As cast	No	0.88-1.20	0.99	0.32-3.39	1.98	-0.99[b]
Wrought	No	0.21-0.42	0.31	0.00-0.00	0.00	0.31
Doped Steel						
As cast	No	0.34-0.60	0.49	0.00-0.33	0.07	0.42
Wrought	No	0.28-0.39	0.34	0.00-0.09	0.02	0.32
550-Hour Exposure (Nominal Groundwater Composition)						
Clean Steel						
As cast	No	6.49-7.10	6.69	0.32-3.39	1.98	4.71
As cast	Yes	4.48-6.80	5.67	2.78-5.73	4.43	1.24
Doped Steel						
As cast	Yes	1.04-3.56	2.61	0.00-0.05	0.02	2.59
1,000-Hour Exposure (10X Nominal Groundwater Composition)						
Clean Steel						
As cast	No	0.81-2.29	1.42	0.32-3.39	1.98	-0.56[b]
Doped Steel						
As cast	No	0.00-0.44	0.20	0.00-0.33	0.07	0.20

(a) Thermal outgassing was performed by heating to 250 C in a vacuum for 24 hours to drive off diffusible hydrogen.

(b) Probably an anomaly resulting from the wide specimen-to-specimen variation in initial hydrogen content.

condition exhibited considerable scatter in hydrogen content. The magnitude of the scatter was comparable for both steels, as illustrated in Figure 3.51; since thermal outgassing apparently had no effect on initial hydrogen content, data for outgassed specimens were not differentiated from data for specimens that were not outgassed. For either steel in Figure 3.51, the hydrogen content did not increase with greater exposure time over the level achieved with 550 hours' exposure, suggesting that an "equilibrium" level of hydrogen was reached within 550 hours.

The scatter in the data for the doped steel after exposure to the basaltic groundwater, compared with the reproducibility of the data for unexposed doped-steel specimens, indicates that the scatter in hydrogen contents results primarily from specimen-to-specimen variability in reactions with the groundwater or in absorption of hydrogen produced by those reactions. However, since concentrating the groundwater composition to ten times the nominal composition had little, if any, effect on hydrogen absorption, the variability of reaction was probably related to the specimens rather than the environment. The corrosion data, discussed in Section 3.2, did not exhibit much specimen-to-specimen variability. Therefore, the scatter observed in the hydrogen-absorption determinations probably arose from variations in the absorption of hydrogen that was generated by the corrosion reactions, and may be related to differences in the surface chemistries of the specimens.

The scatter in the hydrogen-absorption data causes difficulty in evaluating the effect of corrosion reactions with groundwater on hydrogen absorption by cast-steel overpacks. It appears, however, that the steels absorbed approximately 3 ppm or less hydrogen in the as-cast condition and approximately 0.5 ppm or less hydrogen in the wrought condition. Therefore, cast-steel overpacks might be expected to absorb several times more hydrogen from groundwater corrosion reactions than would their wrought-steel counterparts. However, in either case the concentration of hydrogen absorbed was not particularly high in comparison with that which could be obtained with cathodic charging methods (by which hydrogen contents of 5 to 10 ppm usually can be generated), so that testing of cathodically charged specimens would not be representative of anticipated repository conditions. Therefore, future hydrogen-embrittlement studies will involve tests conducted in high-pressure hydrogen. This should provide a realistic assessment of embrittlement characteristics in a repository for two reasons: (1) hydrogen pressures of approximately 1000 to 2000 psi as a result of radiolytic reactions have been estimated for a sealed repository, and (2) the absorption of up to approximately 3 ppm of hydrogen from corrosion reactions should have little impact on the embrittlement observed in gaseous hydrogen because the solubility of hydrogen at 1000 psi is 0.5 to 1.0 ppm(3.13) in α-iron (ferrite), and presumably would be higher in steel. Any direct influence of the groundwater on the integrity of the overpack should be observed in slow strain rate tests in the corrosion studies.

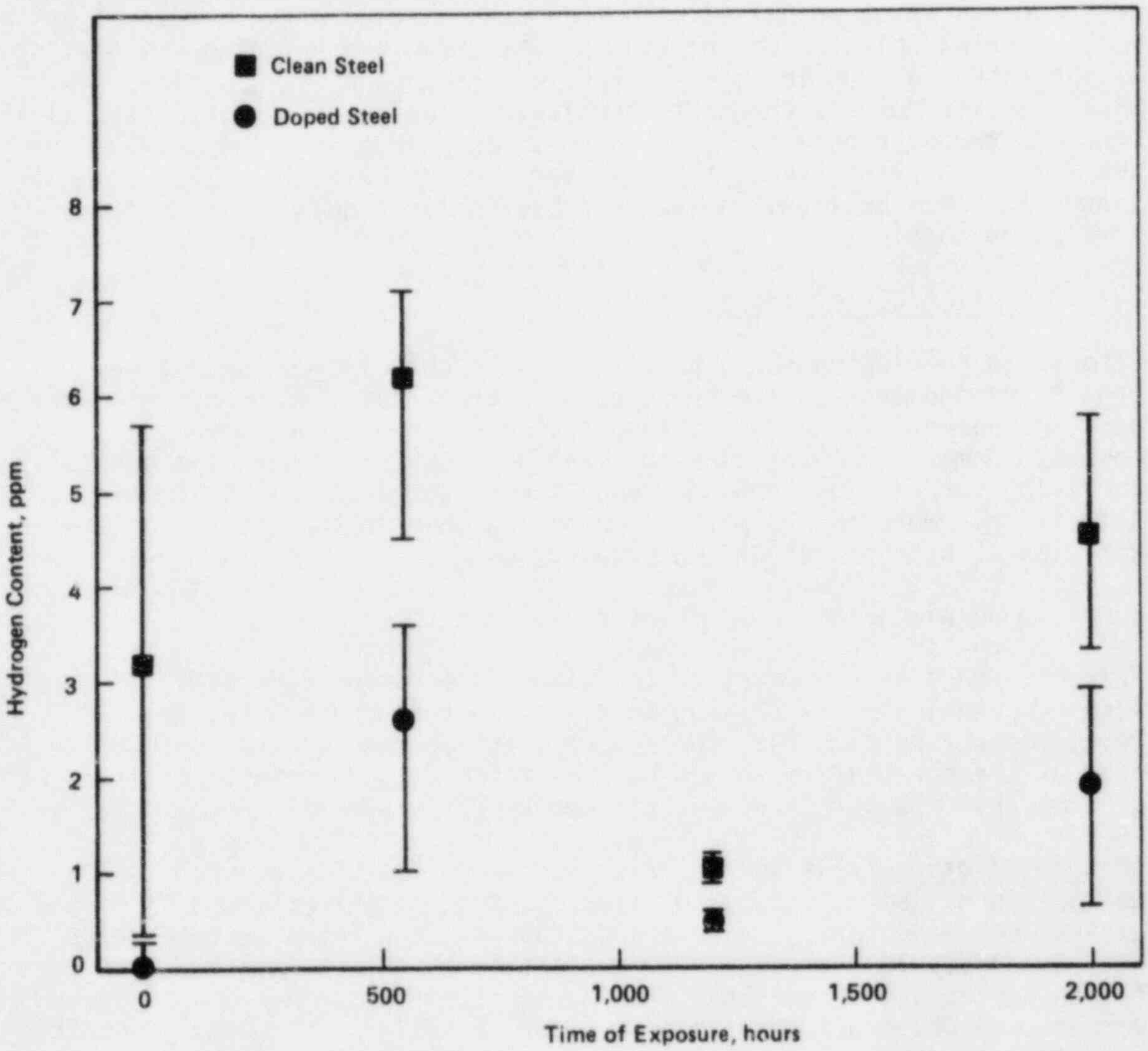

Figure 3.51 Hydrogen absorbed during exposure to simulated basaltic groundwater by clean and doped steels as cast.

3.3.5 Future Work

The results of the tests with the as-cast clean steel suggest that cast-steel overpacks can be made that are resistant to hydrogen embrittlement. However, the data for the annealed steel indicate that thermal history can adversely affect resistance to embrittlement. Therefore, further studies will be conducted to determine the effects on resistance to embrittlement of heating from welding and from long-term exposure to the waste form after emplacement in the repository. These studies will be conducted in coordination with the investigation being conducted by Manufacturing Sciences Corporation on the effects of welding and heating by the waste form on the microstructure of overpack steels. In addition, because DOE may choose to specify a pure-iron overpack, tests will be conducted on a relatively pure iron. This iron is being provided by the Armco Stainless Steel Division, and it will have a chemical composition that Armco believes can be produced in large quantities at relatively low cost.

3.4 Corrosion Correlations

Efforts in developing the general-corrosion correlation include several ongoing refinements in the correlation's treatment of convective transport and potential gradients, temperature gradients, and coupling phenomena. Some sample calculations have been performed with the general-corrosion correlation, and the results were compared to data from the literature. Work on the pitting-corrosion correlation focused on the kinetics of pit initiation and propagation.

3.4.1 General-Corrosion Correlation

Presented here is a summary of the general-corrosion correlation. Although usable in its present form, it is still under intensive development. As a result, the descriptions of the current implementation of the correlation should be considered as a "snapshot" of its present state rather than as a statement of its ultimate form.

This description falls into five sections. First, the general mathematical formalism is described. Second, some recent refinements of the general-corrosion correlation are discussed. The third section deals with the possible experimental verification of the correlation. In the fourth section, the numerical methods appropriate to the general-corrosion problem are briefly presented. Finally, a few sample results are given to demonstrate the current capabilities of the general-corrosion correlation.

3.4.1.1 Mathematical Formalism

The foundation of the mathematical correlation is a set of mass transport equations which can be used to compute the fluxes of corrosive species to the container surface, taking into account the fact that certain corrosive species may be generated by radiolysis within the backfill, i.e.,

$$H_2O \xrightarrow{\gamma} O_2,\ O_2^-,\ H^+,\ H_2O_2,\ HO_2^-,\ H_2,\ OH^-,\ e_{aq}^-,\ H,\ \ldots$$

and consumed by chemical reaction, e.g.,

$$H_2 + 1/2\ O_2 \rightarrow H_2O$$

$$H_2O_2 \rightarrow H_2O + 1/2\ O_2$$

$$H + H_2O + e_{aq}^- \rightarrow H_2 + OH^-$$

$$\vdots$$

If chemical diffusion is the only mode of transport, then the concentration of the ith species, $C_i(r,t)$, at radial position r from the center of the container (assuming an axially symmetric system, and neglecting end effects) and at time t, is described by a second-order partial differential equation of the form

$$\frac{\partial C_i}{\partial t} = \nabla \cdot \left(\frac{D_i}{\xi} \nabla C_i \right) + \sum_j \left(\frac{\partial C_i}{\partial t} \right)_{\text{production}} - \sum_k \left(\frac{\partial C_i}{\partial t} \right)_{\text{consumption}} \qquad (3.1)$$

where D_i is the diffusivity of the ith species within the groundwater and ξ is the local tortuosity of the pores in the backfill or host rock. In general, D_i will be a function of the local temperature and ξ will be a function of position.

The set of differential equations for the $C_i(r,t)$ must be solved, subject to appropriate boundary conditions, and the solution can then be used to compute the cathodic current, I_c, as

$$I_c = - \sum_j n_j D_j F \left(\frac{\partial C_j}{\partial r} \right)_{r = r_o} \qquad (3.2)$$

where n_j is the number of electrons involved with the reduction of species j at the container/liquid interface, $r = r_0$, F is the Faraday constant, and the summation over j is taken over all electroactive species (i.e., those that can corrode the container). The boundary conditions that must be used to solve the set of equations represented by Equation 3.1 also include an explicit function for the kinetics of the corrosion reaction itself; in the original formulation of the general-corrosion model, this was expressed as

$$I_c = -I_a = -(n_a F \rho / M)(dL/dt)$$

where I_a is the anodic current, n_a is the number of electrons involved in the anodic reaction, ρ and M are the density and average atomic weight of the metal, and dL/dt is the rate of penetration into the container. For passive corrosion (that is, for the growth of a coherent oxide film on the surface) we assumed that the thickness of the film could be computed from the point-defect model(3.14) as

$$dL/dt = A(B - 1)/[\exp(2KL) - 1] \tag{3.3}$$

where $K = F\epsilon/(RT)$, with ϵ being the electric field within the film (a constant, $\sim 10^6$ V/cm), A and B are constants which depend upon the redox potential at the container/backfill interface, R is the gas constant, and T is the absolute temperature. Equation 3.3 reduces to the familiar logarithmic growth law

$$L = \left\{ \ln\left[2KA(B - 1)\right] + \ln t \right\} / (2K)$$

for films of thickness greater than a few tens of angstroms.

Because A and B are potential-dependent parameters, it is necessary to compute the redox potential at the container surface. This can be accomplished using the mixed potential model developed by Macdonald et al,(3.15) which utilizes the concentrations for the electroactive species (principally O_2 and H_2) computed from Equation 3.1. Thus, it is evident that the problem presented in solving Equation 3.1, subject to the appropriate boundary conditions, will require the use of numerical iterative techniques in which the iterations will be required to converge on the redox potential at the container/backfill interface.

3.4.1.2 Refinements of the General-Corrosion Correlation

During recent months, it has become apparent that certain refinements of the general-corrosion correlation are necessary in order that it may be used to describe accurately the physical behavior of a container situated in a repository. These efforts are in progress, so that only brief details are provided in this report. The refinements themselves deal with convective transport and potential gradients, temperature gradients, and coupling phenomena.

3.4.1.2.1 Convective Transport and Potential Gradients

It is well recognized that some flow of water will occur through the backfill. Accordingly, Equation 3.1 will be modified to take into account convective transport of corrosive species to the container surface. In addition, because of the existence of a temperature gradient in the region outside the container wall, a gradient of electrical potential will also exist and may indeed have an important effect on the transport of charged species therein. Hence, Equation 3.1 must be generalized to

$$\frac{\partial C_i}{\partial t} = \left(\frac{\partial C_i}{\partial t}\right)_{D/C} + \left(\frac{\partial C_i}{\partial t}\right)_{\text{convection}} + \left(\frac{\partial C_i}{\partial t}\right)_{\text{pot. grad.}} , \qquad (3.4)$$

the first term on the right-hand side of Equation 3.4 representing the entire right-hand side of Equation 3.1. The effect of fluid flow may be readily handled by specifying an average mass-flow rate of water through the backfill, whereas the effect of the potential gradient will require some knowledge of the phenomenon of thermal diffusion.

Recent work by Macdonald et al,(3.15) as well as work by the same authors which has not yet been published, has shown that, for a number of electrolytes (including LiCl, NaCl, KCl, RbCl, and CsCl), the variation of potential, ϕ, with temperature T in degrees Kelvin, can be expressed in the form

$$\phi = A_1 (\Delta T) + A_2 (\Delta T)^2 + A_3 (\Delta T)^3$$

$$\Delta T = T - 298.15 \text{ K}$$

in which the coefficients (A_1, A_2, A_3) are independent of concentration and are only weakly dependent on the identity of the cation. Thus, the variation of electrical potential with distance is readily expressed as

$$\frac{\partial \phi}{\partial r} = \frac{\partial \phi}{\partial T} \frac{\partial T}{\partial r}$$

where $(\partial T/\partial r)$ is the local temperature gradient.

Because a temperature gradient (and hence a potential gradient) exists at the container surface, the flux expressed by Equation 3.2 must be appropriately modified to account for this fact.

3.4.1.2.2 Temperature Gradients

Since the rate of transport of chemical species depends upon the local temperature field, it is important that the temperature function, $T(r,t)$, for the groundwater outside the container be known. For this purpose, we shall either use existing temperature data or generate such data using available computer codes.

3.4.1.2.3 Coupling Phenomena

Because heat flow and mass flow take place simultaneously within the backfill, an alternative approach to describing the transport of aggressive species to the container surface is to use the formulations of irreversible thermodynamics, in which coupling between heat flux and mass flux is accounted for by the familiar phenomenological equations of Onsager. Minimum effort is being expended on this approach at this time, since we believe that the direct solution of the convective diffusion equations is preferable; however, we will hold this option open, subject to future developments.

3.4.1.3 Possible Experimental Verification of the Correlation

Two crucial aspects of the general-corrosion correlation being developed in this program are the generation of corrosive (electroactive) species in the backfill due to radiolysis of water, and the establishment of an electrical-potential gradient normal to the container surface due to the temperature gradient. The latter phenomenon results in thermal diffusion which may enhance or oppose the transport of corrosive species, depending upon the properties of the system. Radiolysis is important, not only because it generates corrosive species, but also because it almost certainly establishes the redox potential at the container/backfill interface and hence determines the driving force for various forms of corrosion. We believe that these two phenomena are subject to direct experimental observation which would provide direct tests of the validity of the model. A brief outline of an experimental program designed to accomplish this task has been presented elsewhere(3.16).

3.4.1.4 Numerical Methods

The model for general corrosion requires the solution of partial differential equations (PDEs). In the case of temperature, one must solve the heat equation subject to given initial and boundary conditions. In the case of concentrations, one must again solve the heat equation, although the problem is stated in terms of diffusion and modified by the addition of production and consumption terms for the radiolytic species. We solve the PDEs on a grid, i.e., the instantaneous temperature and concentration profiles are described by the values of temperature and concentration at a discrete set of positions corresponding to a certain instant of time. This profile is used to calculate a new profile for a later instant of time.

The qualitative behavior of a second-order PDE is determined by the coefficients of the second derivatives. Second-order PDEs are frequently classified as elliptic, parabolic, or hyperbolic solely on the basis of the these coefficients. Both the heat equation and the PDEs for the general-corrosion problem are parabolic, so similar methods apply to both. Accordingly, the discussion below is written as if the problem in question were the standard one-dimensional heat equation (which is written below for a thermal diffusivity of unity)

$$\left(\frac{\partial^2 u}{\partial x^2}\right)_t - \left(\frac{\partial u}{\partial t}\right)_x = 0$$

even though the actual PDEs to be solved are different due to non-constant diffusivity, the cylindrical geometry, and, in the case of the concentration PDE, the existence of production and consumption terms.

In order to solve the heat equation, it is necessary to evaluate both time and space derivatives. Time derivatives pose no particular problem since they are obtained from explicit expressions such as Equation 3.1. Space derivatives may be evaluated using one of a variety of formulas derived from the theory of interpolation. We presently use the central difference approximations

$$\left(\frac{\partial u}{\partial x}\right)_t (x,t) = \frac{u(x+h,t) - u(x-h,t)}{2h} + O(h^2)$$

and

$$\left(\frac{\partial^2 u}{\partial x^2}\right)_t (x,t) = \frac{u(x+h,t) - 2u(x,t) + u(x-h,t)}{h^2} + O(h^2)$$

where h is the distance corresponding to one step of the space grid and $O(h^2)$ denotes terms of order h^2. These approximations provide modest accuracy but exceptional ease of use with boundary conditions. For all points x in the interior of the region over which the PDE is to be solved, x + h and x - h are either also in the interior or on the boundary. If more advanced approximations were to be used, special treatments would be necessary for points near the boundaries.

By solving the heat equation on a grid of points, the PDE is converted to a system of ordinary differential equations (ODEs). The simplest method for solving the ODEs is to apply the Euler-Cauchy method(3.17) at each point independently:

$$u(x,t+k) = u(x,t) + k\left(\frac{\partial u}{\partial t}\right)_x (x,t)$$

where k is the size of the time step. This method is certainly simple, but it provides accuracy of only O(k). An additional difficulty with this method is that it is unstable for $k/h^2 > 0.5$.

A better approach to this problem is to use the Crank-Nicholson method.(3.18) The trapezoidal method(3.19) for solving an ODE is used with this method, i.e.,

$$u(t+k) = u(t) + \frac{1}{2}k\left(\frac{du}{dt}(t) + \frac{du}{dt}(t+k)\right) .$$

The trapezoidal method provides accuracy of $O(k^2)$, and more importantly, it is stable for all values of k. Note that this is an implicit method; it is necessary to know the new value u(t + k) in order to calculate (du/dt) (t + k) so that u(t + k) can be calculated. In addition, use of the Crank-Nicholson method couples the ODEs for all points into a system of ODEs. In the case of the heat equation, this causes no particular difficulty. The implicit equations result in a tridiagonal system of linear equations which may be solved very easily. However, the Crank-Nicholson method is more difficult to apply to the general-corrosion problem, for two reasons. First, chemical reactions such as those listed in Section 3.4.1.1 cause difficulties. If several radiolytic species are considered, there will be an ODE for each species at each point. Reactions among the various species result in coupling of the concentration ODEs for a given point. The coupling of the ODEs results in a much larger linear system. Rather than a tridiagonal system with rank m, where m is the number of points at which the PDE is to be solved, one has a band diagonal system with bandwidth 2n + 1, where n is the number of coupled species, and rank nm, where m is the number of grid points. This results in a greatly increased computational load. Second, the approach described above for the Crank-Nicholson method is applicable only to linear PDEs, and the kinetics of the chemical reactions may not be linear. These difficulties may be overcome by using an iterative predictor-corrector technique, and we may use such a technique in the future.

At present, we are using a Runge-Kutta technique with accuracy of $O(k^4)$. This method provides good accuracy, and since it is an explicit method, it has the advantage that the ODEs do not couple. However, it also shares with other explicit methods the disadvantage that it is unstable for large step sizes. The time derivatives are calculated four times for each step:

$$z_1 = k\ f(t,u)$$
$$z_2 = k\ f(t + k/2,\ u + z_1/2)$$
$$z_3 = k\ f(t + k/2,\ u + z_2/2)$$
$$z_4 = k\ f(t + k,\ u + z_3)$$
$$u(t + k) = u(t) + (z_1 + 2z_2 + 2z_3 + z_4)/6$$

where

$$\frac{du}{dt} = f(t,u) \quad .$$

3.4.1.5 Results of Sample Calculations

Rather than attack the full general problem described in Section 3.4.1.1, we have chosen to start our study by treating only a portion of this problem. We have written computer codes in such a way that it will be straightforward to generalize them. This approach maximizes the effectiveness of our programming effort and allows us to study the qualitative features of the model before attempting to solve actual corrosion problems. On the other hand, it must be understood that the calculations presented here describe the qualitative response of the corrosion model to variations of some of the parameters. The results given here are not a quantitative assessment of general-corrosion kinetics.

For our initial calculations we made a number of assumptions. Some of these may not correspond to reality, but they are appropriate for testing a program. Note that these assumptions are described in terms of dimensionless variables, so units may not always appear to conform to customary usage.

3.4.1.5.1 Heat-Transfer Calculations

As an initial test of the program, we studied the heat-transfer problem only. The problem was described in terms of dimensionless parameters. For these calculations, thermal diffusivity was assumed to be constant, although the program allows non-constant diffusivities. The value chosen for the thermal diffusivity was 1.

The region of integration of the PDE was $0 \leq t \leq 1$, $1 \leq r \leq 5$, where t is time and r is radial position in waste package radii. One unit of time is the square of the waste-package radius divided by the thermal diffusivity.

The time step was chosen as 0.005, and the radius step as 0.1.

The initial temperature T was taken to be

$$T\ (r = 1,\ t = 0) = 1$$
$$T\ (1 < r < 5,\ t = 0) = 0.$$

The boundary conditions were taken to be

$$T\ (r = 1,\ t > 0) = \exp\ (-t/\tau)$$
$$T\ (r = 5,\ t > 0) = 0$$

where τ is the characteristic decay time for the temperature at the surface of the waste package.

The description of the system in terms of dimensionless variables may appear to be cryptic, but it allows one to describe the system in terms of a minimum number of variables. In this case, the heat-transfer problem is reduced to a single parameter, τ, which compares the rate at which the waste package cools to the rate at which heat diffuses.

In Figures 3.52-3.54 we show temperature profiles for various times and for $\tau = 0.1$, 1.0, and 10. Except near $t = 1$, diffusion of heat away from the waste package is sufficiently slow that the fixed temperature at the outer boundary will have a negligible effect on the calculations. For significantly longer times, a larger radius for the outer boundary would be desirable.

Close examination of Figure 3.52 shows that is is possible to choose τ so that it does not describe a physical waste package. Between $t = 0.1$ and $t = 0.2$, the temperature gradient at $r = 1$ changes from negative to positive. This is correct for the boundary conditions that were specified, but it implies that, at short times, heat flows out of the waste package, whereas at longer times, heat flows from the surroundings into the package. It is conjectured that this will occur at sufficiently long times for any value of $\tau > 0$. In future work, we may use a different boundary condition at the inner boundary.

3.4.1.5.2 Mass-Transport Calculations

As a second test of the program, we solved the PDE for the concentration of a radiolytic species as a function of time and position. The program is capable of solving the coupled temperature and concentration PDEs, but the coupled PDEs have not yet been studied systematically. To eliminate the effects of heat conduction, we chose the initial and boundary conditions as

$$T\ (1 < r < 5,\ t = 0) = T\ (r = 1,\ t > 0) = T\ (r = 5,\ t > 0) = k$$

where k is a constant. Integration of the temperature PDE produced a constant function, as expected.

The region of integration was the same as for the temperature problems, $1 \leq r \leq 5$, $0 \leq t \leq 1$. Time and radius step sizes were also unchanged.

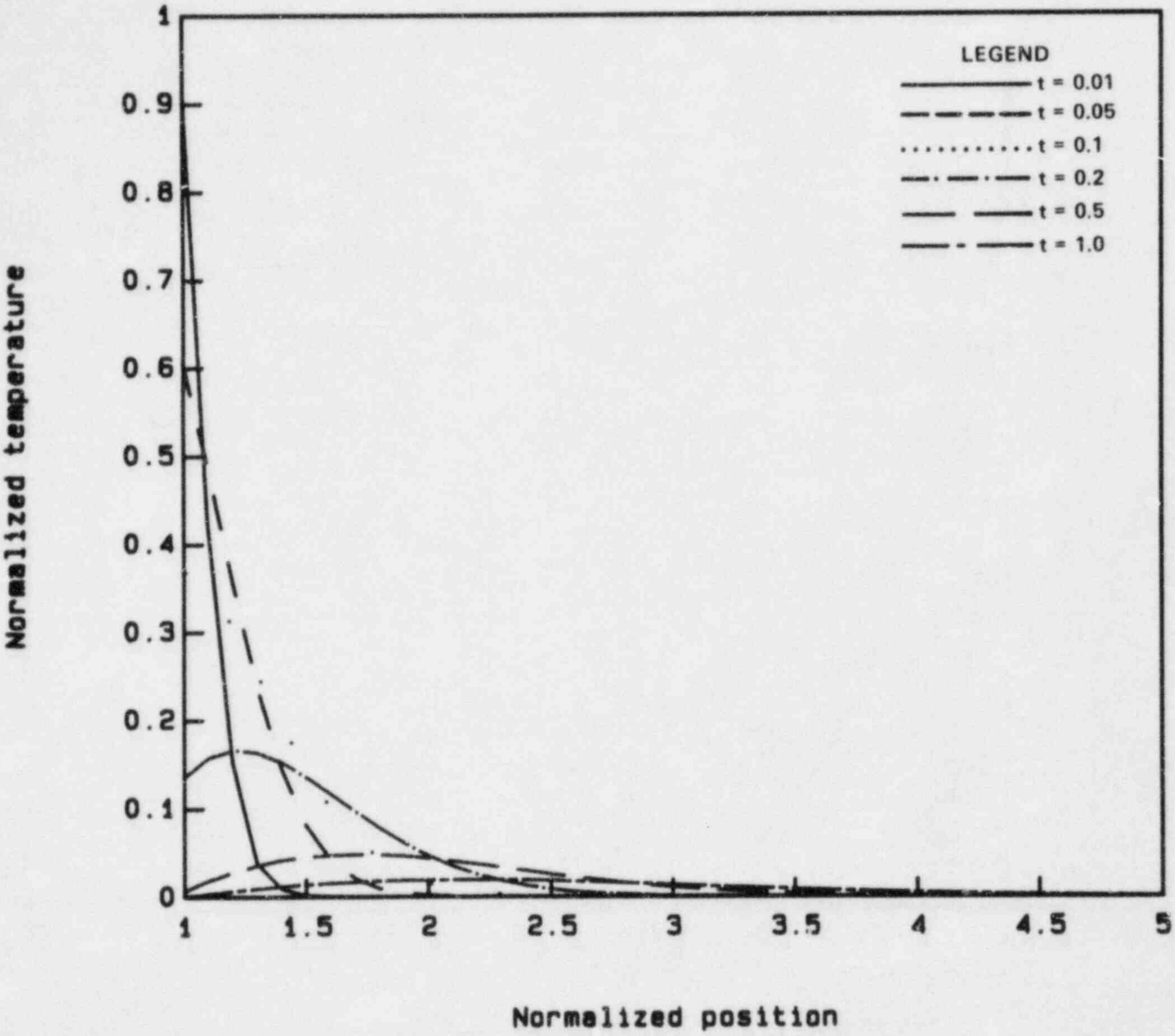

Figure 3.52. Temperature profiles near waste package, calculated with $\tau = 0.1$.

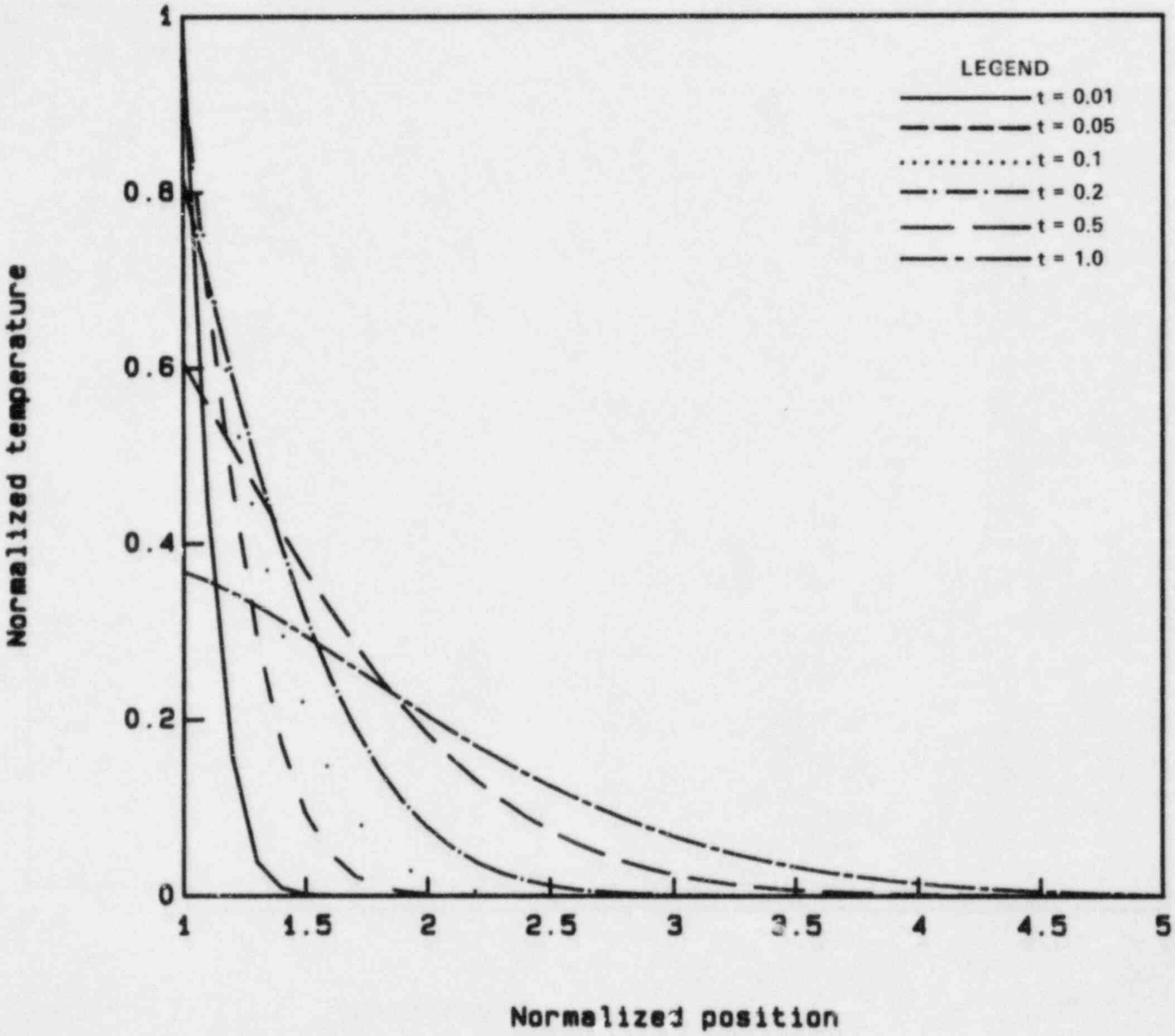

Figure 3.53. Temperature profiles near waste package, calculated with $\tau = 1.0$.

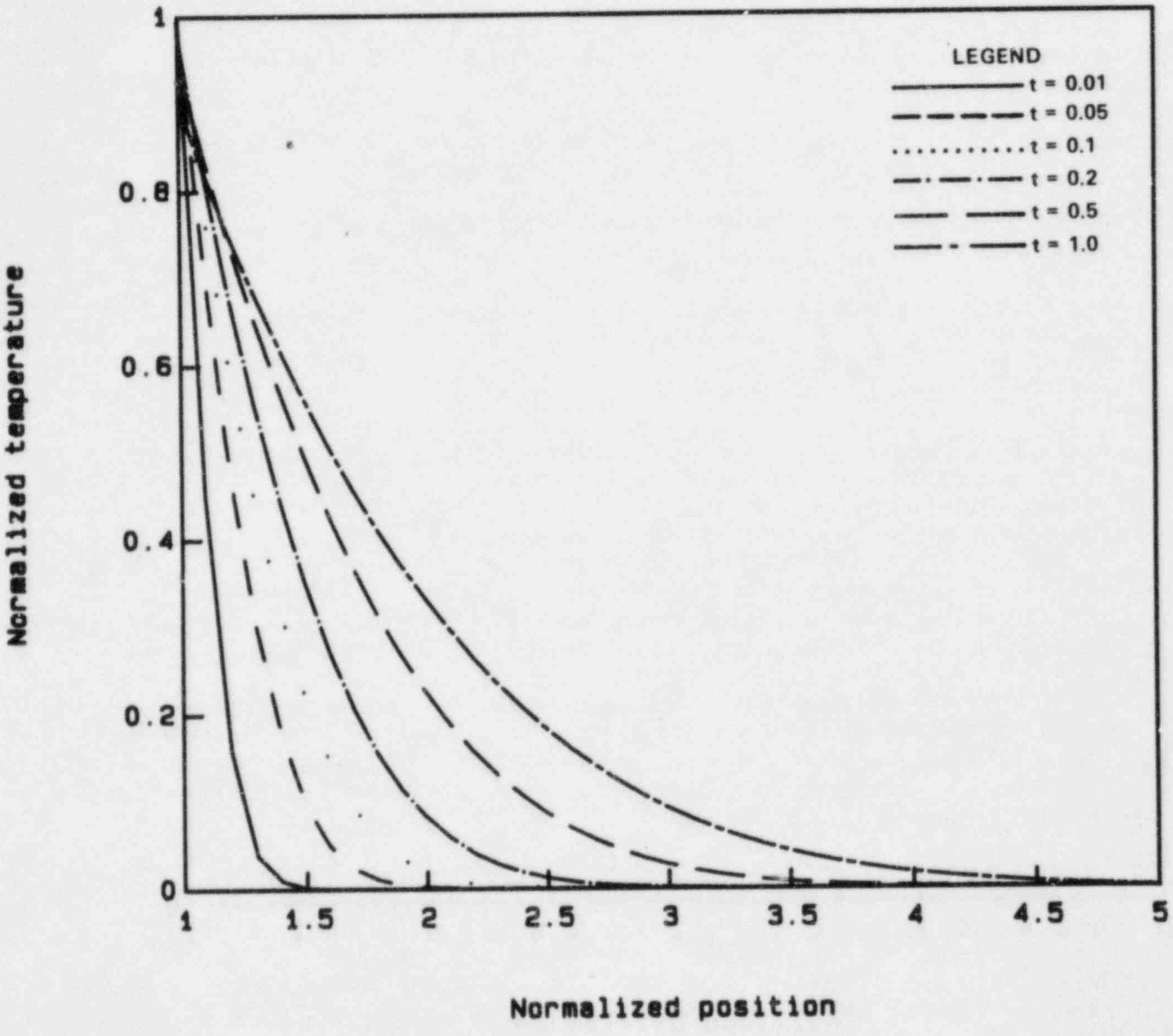

Figure 3.54. Temperature profiles near waste package, calculated with $\tau = 10$.

The intensity, I, of the gamma field was assumed to be

$$I\ (r,t) = \exp(-t)\ \exp\left[-\varepsilon(r-1)\right]/r$$

where ε is the linear absorption coefficient.

A single radiolytic species was considered, nominally O_2. The rate of production of O_2 was assumed to be I_g, where g is a dimensionless "g-value".

The diffusivity of O_2 was assumed to be 1. Tortuosity effects were eliminated by setting tortuosity to 1, independent of position.

The rate of recombination of O_2 with (unspecified) species was set to zero.

The initial and boundary conditions were set as follows:

$$c\ (r = 1,\ t > 0) = 0$$
$$c\ (1 < r < 5,\ t = 0) = c\ (r = 5,\ t > 0) = 1$$

where c is the concentration of O_2. These initial and boundary conditions were chosen because they are appropriate for a maximum-rate calculation. The concentration of O_2 on the outer boundary and the initial concentration of O_2 away from the waste package are set to the background concentration of O_2 in the groundwater. By setting the concentration of O_2 at the surface of the package to zero, one can calculate the maximum rate of oxidation of the container, limited by diffusivity rather than by growth kinetics of an oxide layer.

In Figure 3.55 we show the concentration profiles for O_2 at various times, calculated with $\varepsilon = 1$ and $g = 1$. For this choice of parameters, radiolytic production of O_2 is so small that the maximum concentration is just slightly above 1. The O_2 behavior is dominated by diffusion to the waste package.

To obtain the results shown in Figure 3.56, we left $\varepsilon = 1$ but increased the rate of radiolysis by setting $g = 10$. In this case, significant accumulation of O_2 results, reaching a maximum concentration of over 1.4. Definite maxima are seen in the concentration profiles; to the left of the maxima, O_2 diffuses toward the waste package, whereas to the right of the maxima, it diffuses toward the outer boundary. In this problem, both inner and outer boundaries are sinks for O_2. If the rate of radiolytic production is low, as in Figure 3.55, there may be no maximum in the concentration profile, and then the outer boundary will act as a source rather than a sink. In Figure 3.56, for times approaching 1, the outer boundary is beginning to affect the calculation. There is a noticeable slope at $r = 5$.

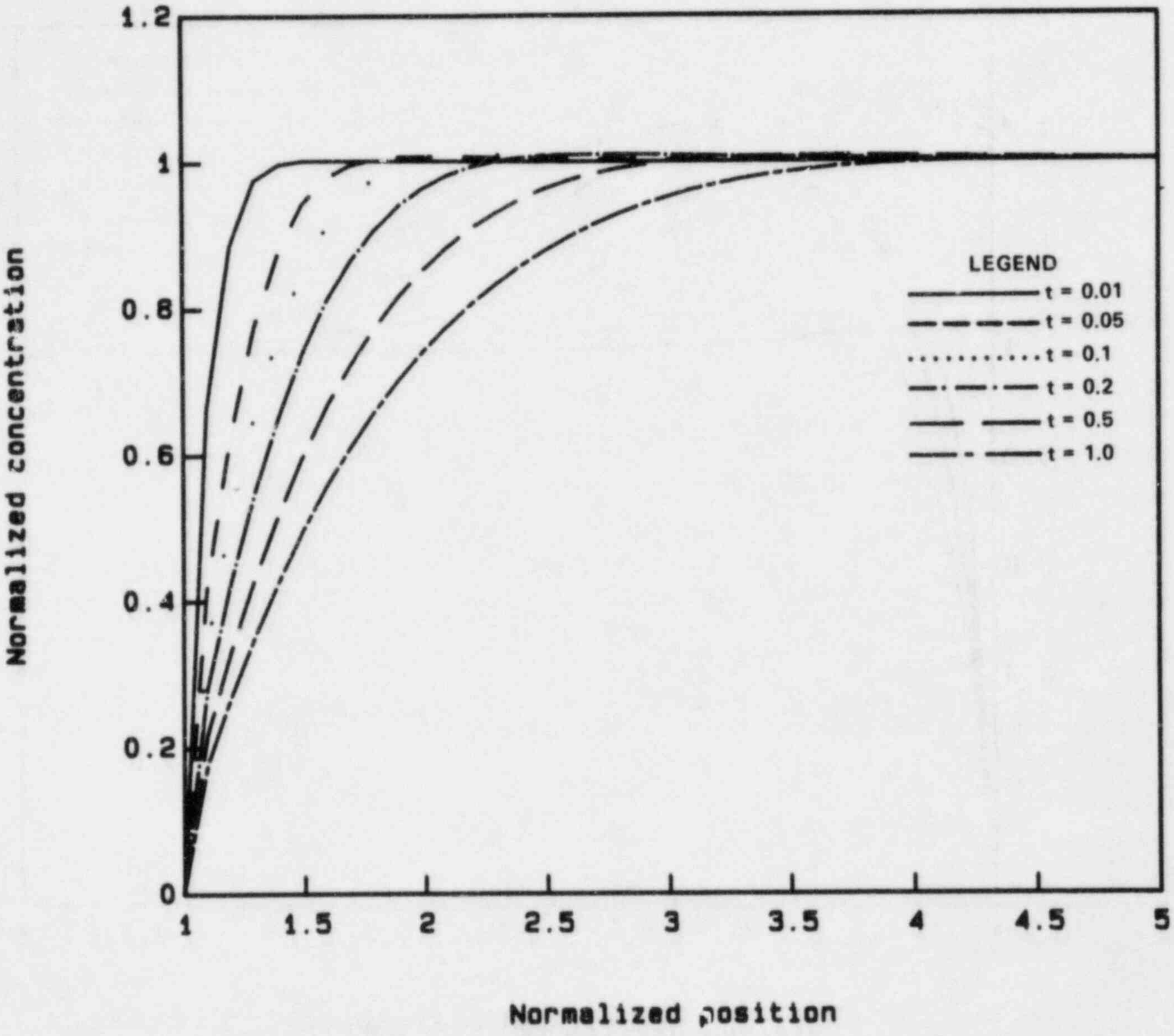

Figure 3.55. Concentration profile for a radiolytic species near waste package, calculated with $g = 1$ and $\varepsilon = 1$.

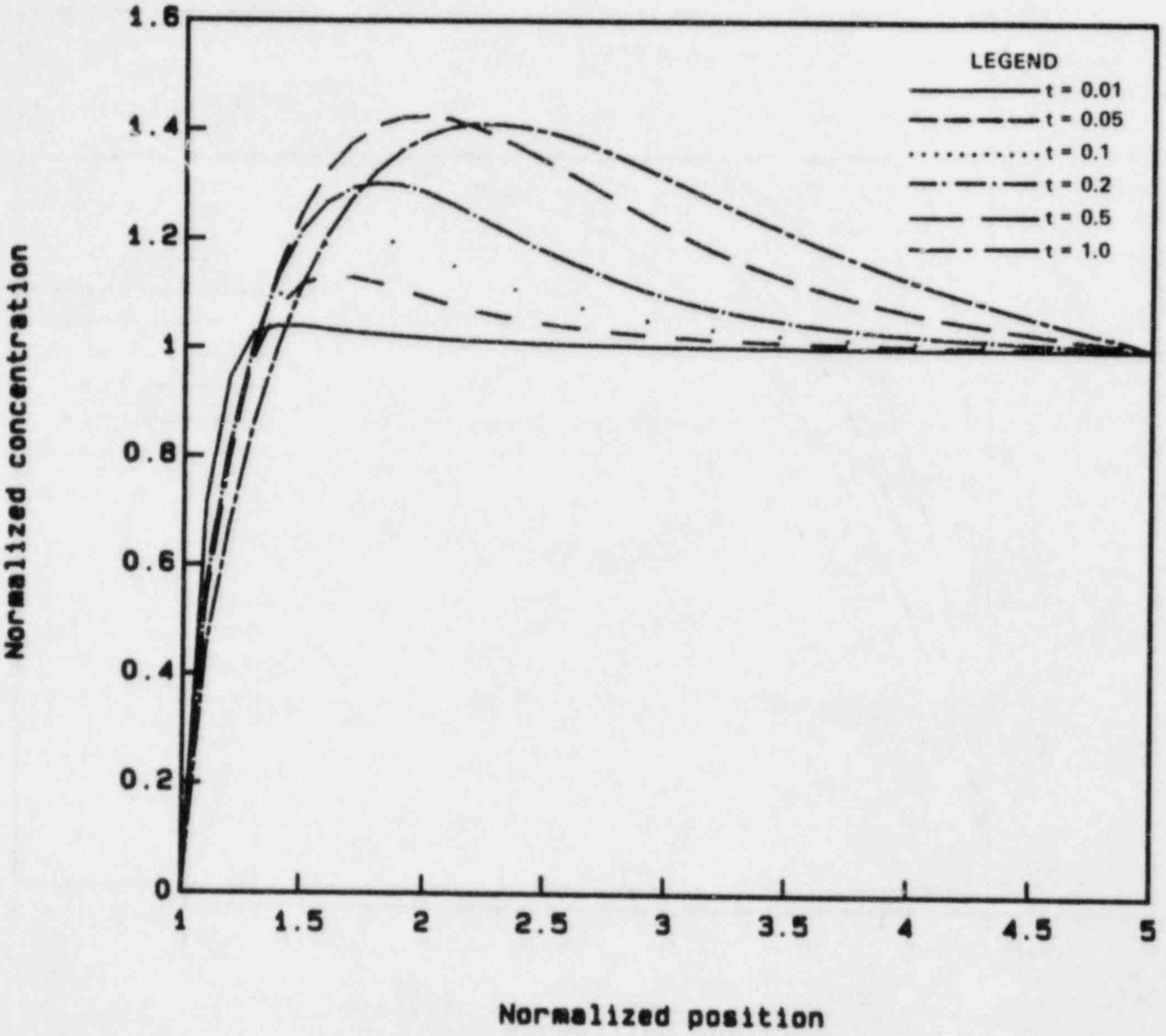

Figure 3.56. Concentration profiles for a radiolytic species near waste package, calculated with g = 10 and ε = 1.

Figure 3.57 was calculated for the same conditions as Figure 3.56 except that the linear absorption coefficient was increased to $\varepsilon = 2$. This has the effect of restricting radiolysis to a region closer to the waste package. Comparison of Figures 3.56 and 3.57 also shows that the maximum concentrations are reduced.

3.4.2 Pitting-Corrosion Correlation

The development of pits on a container surface is likely to be an important mechanism for the ultimate loss of container integrity. Considerations of pitting corrosion have, during the past year, been centered on three different aspects of the overall process: pit-initiation kinetics, pit-growth kinetics, and the evolution of the pit-depth distribution. Actually, the last aspect is just a combination of the first two; that is, if one knows the rate at which pits are generated on a container surface as well as the rate at which a pit, once generated, will grow, then the time-dependence of the pit-depth distribution follows directly. Of course, additional considerations such as the "deactivation" or cessation of growth of certain pits must also be considered. Nevertheless, it is possible to make some generalizations regarding the pit-depth distribution without having full knowledge regarding either pit generation or growth. Battelle's second-year efforts in these areas are summarized below.

3.4.2.1 Pit-Generation Kinetics

Battelle's analysis of pit-generation kinetics was limited, during this reporting period, to a review of existing studies. One shortcoming of these studies is that, in general, they do not represent conditions appropriate to a repository environment. Such effects as those resulting from the ambient gamma field, from heat transfer across the container surface, and from the presence of various chemical species unique to this environment are therefore not treated and must be the subject of future study.

In general, a theoretical model that is to be used to describe the kinetics of pit generation must account for the following observations:

(a) Pitting occurs when the redox potential of the environment exceeds some critical value, E_c.

(b) Pits nucleate only after some induction time has elapsed which depends upon the overpotential $\Delta E \equiv E_{redox} - E_c$.

(c) Pits usually are generated progressively across a surface; that is, new pits are formed throughout the exposure period. The number of pits generated per unit time is assumed to obey some well-defined distribution law.

(d) In extreme cases, individual pits may overlap and coalesce.

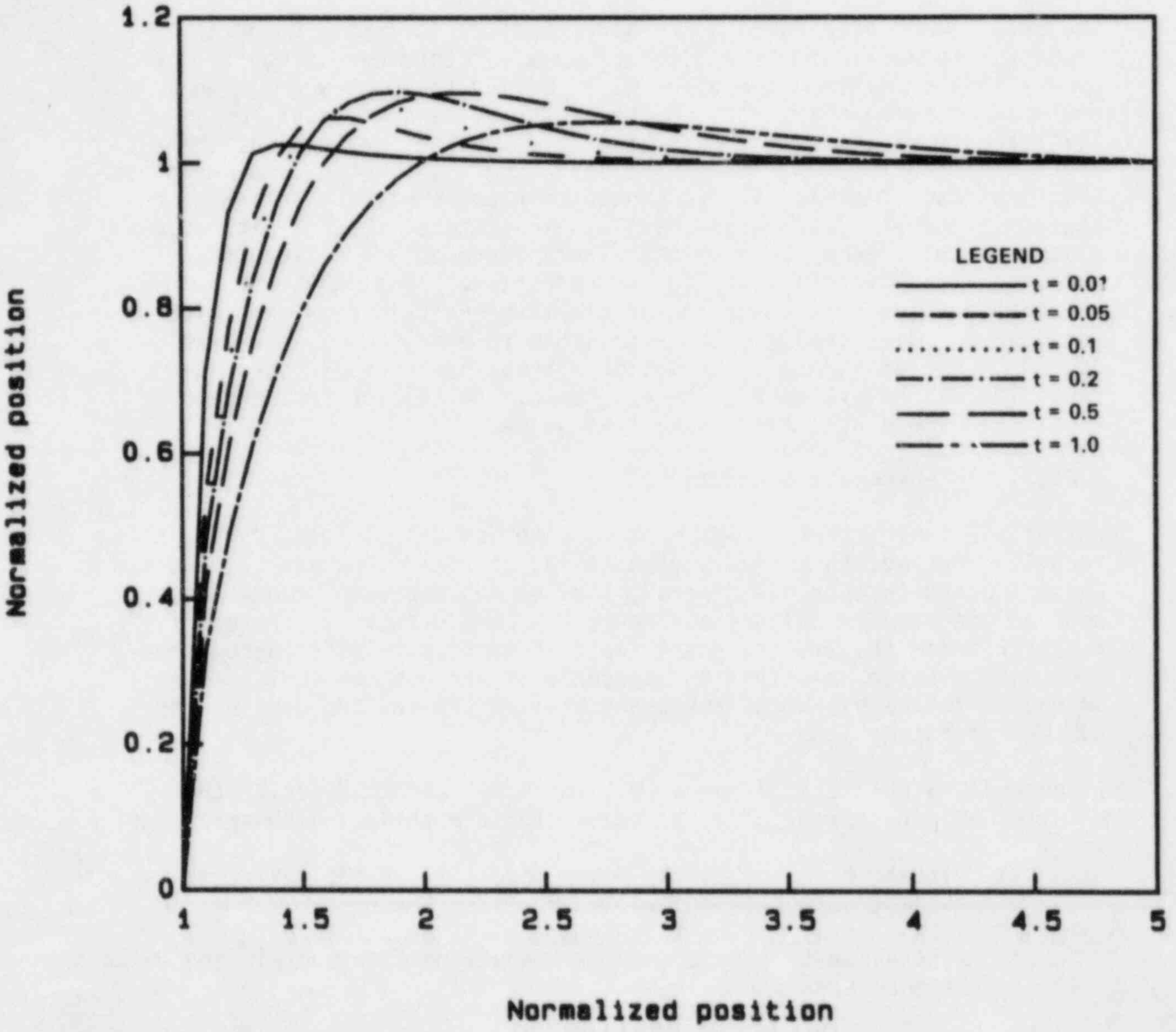

Figure 3.57. Concentration profiles for a radiolytic species near waste package, calculated with g = 10 and ε = 2.

As far as the induction time for localized attack is concerned, Heusler and Fischer(3.20) proposed the following empirical relationship between the generation time, t_N, and the overvoltage, ΔE:

$$t_N = t_o \exp (V_o/\Delta E)$$

where t_o and V_o are constants. This equation was found to account satisfactorily for the pitting characteristics of iron and borate buffer solution containing chloride ions for induction times ranging from a few seconds to more than 28 hours. On the other hand, Lin et al(3.21) derived the following theoretical expression for t_N from a point-defect model for passive-film growth:

$$t_N = \xi' \left[\exp \left(\frac{XF\alpha\Delta E}{2RT} \right) - 1 \right]^{-1} + \tau \qquad (3.5)$$

where τ is a relaxation time for the movement of cation vacancies within the film, X is the stoichiometry ($MO_{X/2}$), α is the fraction of the total voltage between the metal and the solution which appears across the film/solution interface (= 0.743 for iron at 25 C) and ξ' is given by

$$\xi' = \xi / \left[J^o u^{-X/2} \, (a_{Cl^-})^{X/2} \exp \left(\frac{XF\alpha E_c}{2RT} \right) \right] . \qquad (3.6)$$

The parameters ξ, J^o, and u are constants which depend upon the properties of the film, and a_{Cl^-} is the activity of chloride ion. In principle, all the parameters in Equations 3.5 and 3.6 are known for any given film; in practice, some of these are better determined empirically by fitting Equation 3.6 to experimental data. Nevertheless, Equation 3.5 was found to account for the data of Heusler and Fischer(3.22) in a reasonably precise manner. Accordingly, we propose to use Equation 3.5 to describe the generation of pits on waste-storage containers.

It is important to note that Equation 3.6 describes the generation of pits on a uniform, perfect surface. In reality, pits will be generated at different times even though a uniform (constant) overpotential exists across the interface. Theoretically, this distribution in t_N may be accounted for by variations in film properties across a real surface (see Equations 3.5 and 3.6) and by a distribution in E_c as given by the point-defect model,(3.21) i.e.,

$$E_c = \frac{4.606RT}{XF\alpha} \log_{10} \frac{J_m}{J^o u^{-X/2}} - \frac{2.303RT}{\alpha F} \log_{10} (a_{Cl^-}) \qquad (3.7)$$

where J_m is the rate at which metal holes submerge into the metal. However, a theoretical derivation of the distribution function does not appear to be possible at this time because insufficient data are available relative to the variation of the parameters in Equations 3.5 and 3.6 for real passive films. Instead, the most profitable approach appears, at this time, to be empirical, that is, to use Equations 3.6 and 3.7 to define the induction time for an "average" site and then to introduce the distribution in t_N using essentially empirical statistical techniques. Various distribution functions will be evaluated for this purpose.

A number of other investigators have considered the problem of pit-generation kinetics. For example, Sato et al,(3.23) in their studies of chloride pitting associated with a rotating stainless-steel electrode in acid solution, found the pit-generation rate to be approximately constant in time. On the other hand, Janik-Czachor and Ives(3.24) have suggested that the pit-generation rate for a metal in an aggressive solution is of a "peaked" type, which they interpreted as probably being representative of a statistical distribution of pitting susceptibilities existing on the metal surface, centered at a "mean" susceptibility which is represented by a characteristic time of incubation. For the alloys they studied, there was no evidence for a time-independent pit-generation rate. Interestingly, in their modeling studies of the evolution of the pit-depth distribution, they used a simple, $\sin^2 (0.2\ t)$ function to represent the "peaked" function describing the rate of pit nucleation.

3.4.2.2 Pit-Growth Kinetics

The rate at which a pit on a metal surface, once initiated, penetrates into the metal is a subject that has long been of interest. A general relationship that has been found to describe many types of pit growth is the following:

$$h = a(t - t_o)^b \tag{3.8}$$

where h is the depth, at time t, of a pit that had been generated at time $t_o \leq t$, and where a and b are parameters that characterize the particular pit-growth process. It has been found experimentally that, in a wide variety of cases, the parameter b lies within the range $0.3 \leq b \leq 1$.

A few examples can be cited. A relationship similar to Equation 3.8 was used many years ago(3.25) to describe the variation with time of the maximum pit depth for ferrous specimens in a soil environment. Somewhat more recently,(3.26) it was pointed out that the special case for which $b = 1/3$ has been found to apply to a number of situations, including the maximum pit depth in laboratory tests in almost 200 fresh waters, a 2000-foot industrial water-carrying pipeline for an interval of more than 13 years, and the pitting of aluminum in seawater. A time dependence for pit growth similar to that in Equation 3.8 has also been discussed by Sato and coworkers.(3.23) Finally, in an experimental study of the pitting corrosion of carbon steels to be used for nuclear-waste containment, preliminary results, reported by Marsh,(3.27) for the variation with time t, in years, of the maximum pit depth, h_{max}, in mm, indicated that

$$h_{max} = 3.2t^{0.49} \quad . \tag{3.9}$$

Clearly, the value of b in Equation 3.9 lies within the indicated range.

Of course, the exact nature of the parameters a and b is determined by a number of factors, such as the pit geometry and the mass-transport processes that contribute to pit growth. Also, since these factors, as well as the experimental conditions (e.g., temperature), in general, vary with time, the parameters a and b are likely themselves to be time-dependent, particularly when we consider the pitting kinetics as occurring over extended periods of time.

A few very simple examples serve to illustrate the validity of Equation 3.8 for various pit geometries and rate-controlling kinetic processes. Without presenting the details, one can show that:

- For dissolution-controlled growth of a hemispherical pit of radius h, with time-independent total current to the pit and with the current density across the pit surface being everywhere the same,

  $$h \sim (t - t_0)^{1/3} \ .$$

- For dissolution-controlled growth of a hemispherical pit, with time-independent and spatially-independent current density across the pit surface,

  $$h \sim (t - t_0)^1 \quad .$$

  The same relation holds for a cylindrical pit having constant cross-sectional area perpendicular to the growth direction and time-independent current supplied to its bottom, dissolving surface. Of course, the constant of proportionality is different for the two cases, and h represents pit depth for the case of a cylindrical pit.

- For a cylindrical pit of depth h, again having constant cross-sectional area perpendicular to the growth direction, but growing by diffusion-controlled migration of the metal-containing species from the pit bottom to the upper surface,

$$h \sim (t - t_0)^{1/2} \quad ,$$

assuming time-independent values for the concentration of that species in the solution at the upper and lower pit surfaces.

It is clear that, in each of the above cases, pit growth is indeed described by a specific form of Equation 3.8, despite the fact that the assumed pit geometries and rate-controlling processes do vary from one case to another. This may help explain why Equation 3.8, in some form, is so often found to describe pit-growth data.

3.4.2.2.1 Physically Based Pit-Growth Models: Background

It is, of course, desirable to place our understanding of pit-growth kinetics on a firm, quantitative basis in terms of physical models, particularly if one is to predict, with some degree of confidence, the long-term pitting behavior of a metal surface. Indeed, a number of models for pitting corrosion, based essentially on the application of mass-transport kinetics to simple pit geometries, have been developed over the years. Examples of these can be found in the reported studies of Engell and Stolica,(3.28) Vetter and Strehblew,(3.29) Pickering and Frankenthal,(3.30) Isaacs,(3.31) Sato et al,(3.23) Tester and Isaacs,(3.32) Galvele,(3.33) Nisancioglu and Holtan,(3.34) Alkire and Siitari(3.35) and Beck and Alkire.(3.36)

In addition, a number of detailed mathematical treatments of pitting corrosion have been reported, for example, by Newman,(3.37) Cherepanov,(3.38) and Kolotyrkin and coworkers.(3.39) A related area, in which a considerable amount of modeling has been carried out, is stress-corrosion cracking of metals; however, this particular field is not reviewed here.

3.4.2.2.2 Binary-Electrolyte Pit-Growth Model

As an initial step in developing a physically realistic model for pitting corrosion of a waste-package container, a model was developed during this reporting period based on the well-known transport theory characterizing a "binary electrolyte", which is a solution containing one type of cation and one type of anion. A detailed discussion of the general theory of binary electrolytes has been presented by Newman.(3.40) For our purposes, the cation represents the dissolving metal and the anion represents an "average" of all the anions that may exist within the solution inside the pit.

Assumptions included in the present model are as follows:

- The pit geometry is as illustrated in Figure 3.58, consisting of a cylindrical configuration.
- The pit grows only along its length, which is taken to be parallel to the x-axis, with growth occurring as a result of

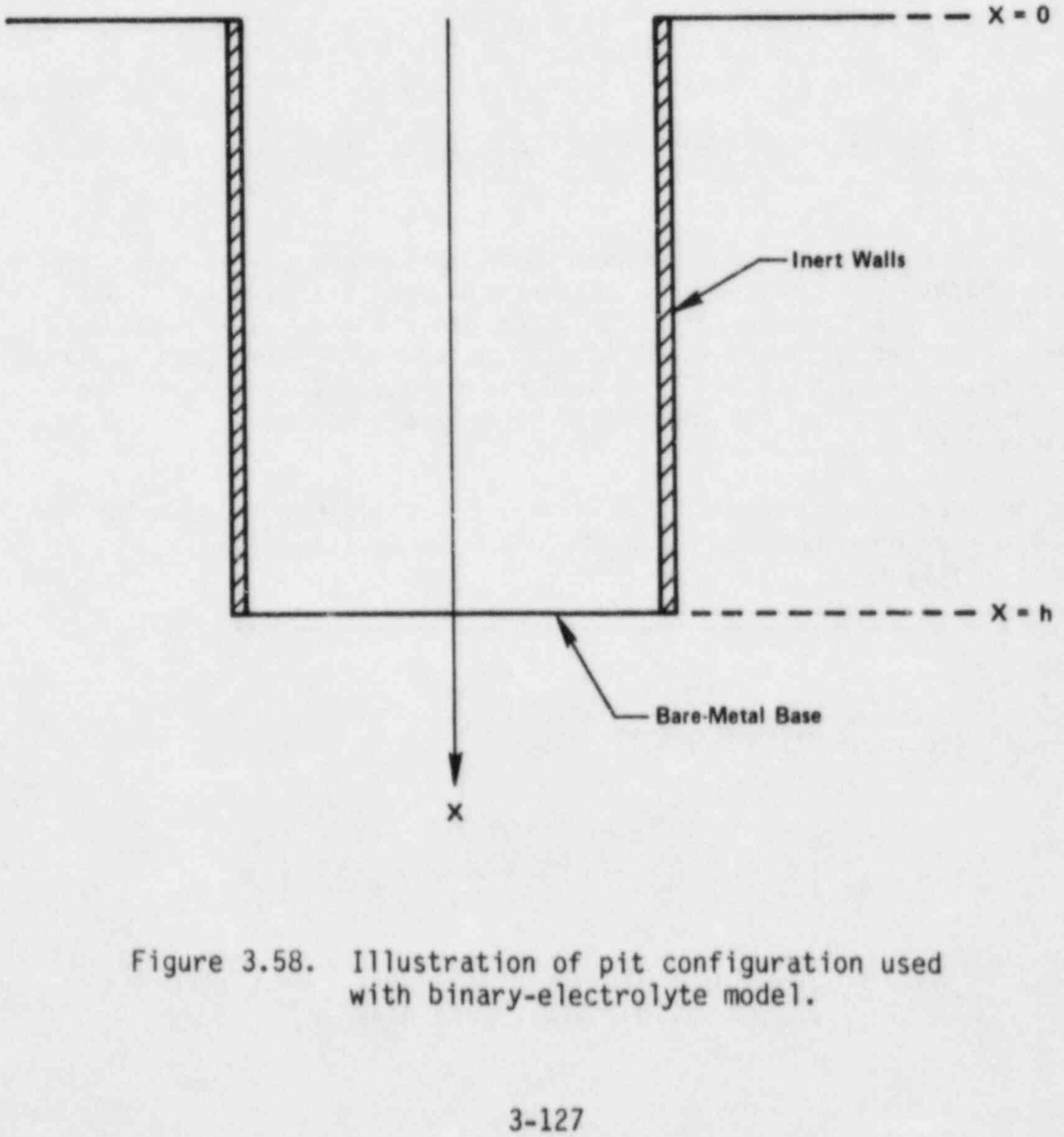

Figure 3.58. Illustration of pit configuration used with binary-electrolyte model.

anodic dissolution of the bare metal that is assumed to comprise the pit base located at x = h. The walls of the pit are taken to be inert, so that current flow within the pit is likewise one-dimensional.

- No chemical reactions occur within the solution.
- No convective flow of solution takes place.
- Mass transport occurs under steady-state conditions.
- The mobility of each of the ionic species is given by the Nernst-Einstein relation.(3.40)

Given these assumptions, one can show (using, for example, Equation 69-1 of Newman(3.40) that the flux, $N_+(x)$ and $N_-(x)$, of cations and anions, respectively, within the solution inside the pit, is given by

$$N_+(x) = -D_+ \left[\frac{F}{RT} z_+ c_+(x) \frac{d}{dx} \phi(x) + \frac{d}{dx} c_+(x)\right] \tag{3.10a}$$

$$N_-(x) = -D_- \left[\frac{F}{RT} z_- c_-(x) \frac{d}{dx} \phi(x) + \frac{d}{dx} c_-(x)\right] \tag{3.10b}$$

where $D_\pm$, $z_\pm$ and $c_\pm(x)$ are, respectively, the diffusivity, number of proton charges, and x-dependent concentration of the cation (+) and anion (-), F the Faraday constant, R the gas constant, T the absolute temperature, and $\phi(x)$ the electrostatic potential. Clearly, the first term within brackets in Equation 3.10 represents a contribution due to electromigration, whereas the second term is a contribution due to chemical diffusion.

Since no chemical reactions occur within the solution, expressions for cation and anion material balance become (see Equation (69-3) of Newman(3.40)).

$$\frac{d}{dx} N_\pm(x) = 0 \quad . \tag{3.11}$$

Combining Equations 3.10 and 3.11,

$$\frac{F}{RT} z_+ \frac{d}{dx} \left[c_+(x) \frac{d}{dx} \phi(x)\right] + \frac{d^2}{dx^2} c_+(x) = 0 \tag{3.12a}$$

$$\frac{F}{RT} z_- \frac{d}{dx} \left[c_-(x) \frac{d}{dx} \phi(x)\right] + \frac{d^2}{dx^2} c_-(x) = 0 \quad . \tag{3.12b}$$

Moreover, since the solution must be electrically neutral at all points,

$$z_+ \, c_+(x) + z_- \, c_-(x) = 0 \quad . \tag{3.13}$$

From Equation 3.13, we obtain

$$c_-(x) = -\frac{z_+}{z_-} c_+(x) \quad . \tag{3.14}$$

Equations 3.12a and 3.12b can be added, and Equation 3.13 applied to the resultant expression, to obtain

$$\frac{d^2}{dx^2}\left[c_+(x) + c_-(x)\right] = 0 \quad . \tag{3.15}$$

Using Equation 3.14 to eliminate $c_-(x)$ from Equation 3.15,

$$\left(1 - \frac{z_+}{z_-}\right)\frac{d^2}{dx^2} c_+(x) = 0 \quad . \tag{3.16}$$

Since the quantity in parentheses in Equation 3.16 is clearly non-zero, it follows that

$$\frac{d^2}{dx^2} c_+(x) = 0 \quad , \tag{3.17}$$

so that $c_+(x)$ satisfies the Laplace equation. The solution of Equation 3.17 can be expressed as

$$c_+(x) = c_+(0) + \left[c_+(h) - c_+(0)\right](x/h) \quad . \tag{3.18}$$

The functional form for the potential distribution, $\phi(x)$, can now be determined through comparison of Equations 3.12a and 3.17, from which we obtain

$$\frac{d}{dx}\left[c_+(x)\frac{d}{dx}\phi(x)\right] = 0 \quad . \tag{3.19}$$

Equation 3.19 can readily be solved to yield

$$\phi(x) = \phi(h) + \frac{\phi(0) - \phi(h)}{\ln\left[c_+(0)/c_+(h)\right]} \ln\left[\frac{c_+(x)}{c_+(h)}\right] \quad . \tag{3.20}$$

Next, consider the flux of anions. From Equations 3.14 and 3.18, we obtain

$$c_-(x) = -\frac{z_+}{z_-}\left\{c_+(0) + \left[c_+(h) - c_+(0)\right](x/h)\right\} \quad . \tag{3.21}$$

Combining Equations 3.18, 3.20, and 3.21 with 3.10b,

$$N_-(x) = -D_-\left\{\frac{F}{RT} z_- \frac{c_-(x)}{c_+(x)} \frac{\phi(0) - \phi(h)}{\ln\left[c_+(0)/c_+(h)\right]} - \frac{z_+}{z_-} \frac{c_+(h) - c_+(0)}{h}\right\} \quad . \tag{3.22}$$

Since the anions do not undergo reaction at the pit base, it follows that $N_-(x) = 0$, in which case we deduce from Equations 3.13 and 3.22, that

$$\phi(h) = \phi(0) + \frac{RT}{z_-F} \ln\left[\frac{c_+(0)}{c_+(h)}\right] \quad . \tag{3.23}$$

Finally, combining Equations 3.20 and 3.23,

$$\phi(x) = \phi(0) - \frac{RT}{z_-F} \ln\left[\frac{c_+(x)}{c_+(0)}\right] \quad . \tag{3.24}$$

Clearly, Equation 3.24 is a form of the Nernst equation.(3.40)

The cation flux is of particular interest, because it is this quantity that is directly related to the rate of pit growth. It is now a simple matter to calculate this flux simply by using Equations 3.18 and 3.24 in conjunction with 3.10a, from which we obtain

$$N_+ = D_+ \left(\frac{z_+}{z_-} - 1\right) \left[c_+(h) - c_+(0)\right] \left(\frac{1}{h}\right) \quad . \tag{3.25}$$

Clearly, the rate of pit growth is given by

$$\frac{dh}{dt} = - \frac{m}{\rho} N_+ \tag{3.26}$$

where m is the molar mass of the dissolving metal and ρ is its mass density. The minus sign on the right-hand side of Equation 3.26 is included because $N_+ < 0$ (i.e., cation flux in the direction of the crevice mouth) implies $dh/dt > 0$ (i.e., crevice growth). Combining Equations 3.25 and 3.26, and recalling that $z_+ > 0$ and $z_- < 0$, we obtain, taking $h = 0$ at $t = 0$,

$$h^2 = \frac{mD_+}{\rho} \left(\left| \frac{z_+}{z_-} \right| + 1 \right) \left[c_+(h) - c_+(0)\right] t \quad . \tag{3.27}$$

Hence, for this model the parameter b is exactly 0.5. Again, the first term inside parentheses on the right-hand side of Equation 3.27 is a contribution to pit growth due to electromigration, whereas the second term is a contribution due to chemical diffusion. Thus, for example, for $z_+ = +2$ and $z_- = -1$, electromigration contributes twice as much to pit growth as does chemical diffusion.

3.4.2.2.3 Comparison with G.P. Marsh Data

While being careful not to claim detailed physical validity of the pit-growth model just derived, it is nevertheless interesting to compare predictions obtained therefrom with preliminary results reported by Marsh,(3.27) as presented above in Equation 3.21. This is a particularly attractive comparison to make in view of the fact that Marsh reported a b-value of 0.49, which is very close to the 0.5 value obtained in our analysis.

Toward this end, let us take $z_+ = +2$, $z_- = -1$, $m = 55.847$ gm/mol (for iron), $\rho = 7.86$ gm/cm^3 (also for iron), and $D_+ = 1 \times 10^{-5}$ cm^2/sec. Then, taking Marsh's b-value to be 0.5, one can directly compare Equations 3.21 and 3.27 to obtain a value for the difference in cation concentration along the crevice length. One thus obtains

$$c_+(h) - c_+(0) = 7.6 \times 10^{-3} \text{ mol/l.}$$

This value is indeed within "reasonable" limits. For example, Ateya and Pickering(3.41) estimated the concentration of Fe^{2+} ions at the base of a crack-like slot to be < 0.1 M.

3.4.2.3 Evolution of the Pit-Depth Distribution

In Battelle's first Annual Report(3.42) for this program, an analysis of the evolution of the pit-depth distribution was developed for the special case b = 1, i.e., a linear variation of the depth of a given pit with time. Under this assumption, together with the additional assumption that the rate at which new pits are generated is an arbitrary function of time, G(t), an expression was derived for the time-dependent frequency distribution for the pit depth.

During the past year, this analysis was extended to account for a more general growth-rate expression, namely, that given by Equation 3.20. One can, for example, use either of the two methods discussed in Reference 3.42 and thereby obtain the following general expression for the pit-depth frequency distribution, assuming G(t) applies for time t > 0:

$$f(h,t) = \frac{1}{ab} \ \frac{h}{a}^{\frac{1-b}{b}} \ G\left(t - \left(\frac{h}{a}\right)^{\frac{1}{b}}\right) \quad \text{for } h < at^b \qquad (3.28a)$$

and

$$f(h,t) = 0 \quad \text{for } h > at^b \quad . \qquad (3.28b)$$

It was assumed, in the analysis leading to Equation 3.28, that the parameters a and b are independent of time. However, as previously noted, both are likely to vary with time as the temperature and other conditions vary.

An example of the application of Equation 3.28 is presented in Figure 3.59 for the special case b = 0.5. Here, the pit-generation rate is given by

$$G(t) = G_0 \left\{1 - \exp\left[- (\lambda t)^n\right]\right\} \qquad (3.29)$$

for $t \geq 0$, where G_0 and λ are constants, and G(t) = 0 for t < 0. For this particular form for G(t), the pit-generation rate is zero prior to time t = 0, after which it rises and gradually approaches the constant value G_0. (Whether or not this is a physically realistic form for G(t), even over a limited interval of time, is immaterial; it serves as a useful illustration.) Values of f(h,t) are shown in the figure for several times after the onset of pit generation. Two important features

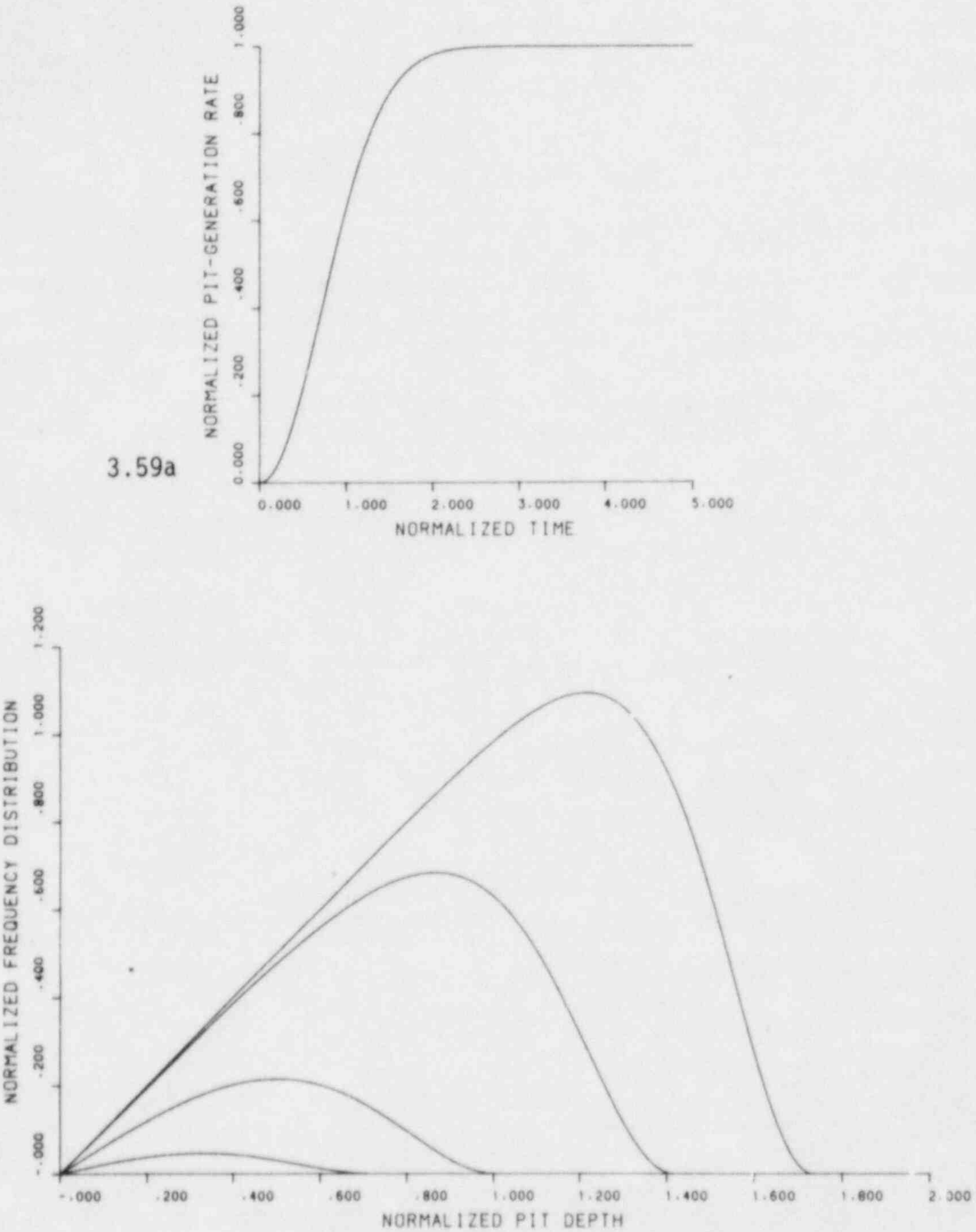

3.59a

3.59b

Figure 3.59. Variation of pit-depth distribution with time, shown in 3.58b (after Equation 3.28), for the pit-generation rate shown in 3.59a (after Equation 3.20) taking $b = 0.5$.

The abscissa and ordinate in 3.59a are λt and $G(t)/G_0$, respectively; the corresponding quantities in 3.59b are $\lambda^b h/a$ and $ab\,\lambda^{1-b}\, f(h,t)/G_0$, respectively.

relative to the change of f(h,t) with increasing time are: (1) as expected, the maximum pit depth increases with increasing time, which would ultimately lead to container penetration, and (2) the total number of pits, which is proportional to the "area" beneath the distribution function, is clearly increasing with time, as expected from the functional form assumed for G(t) in this calculation.

3.5 References for Section 3

(3.1) "Long-Term Performance of Materials Used for High-Level Waste Packaging", D. Stahl and N. E. Miller (compilers), NUREG/CR-3405, BMI-2105, Vol. 1 (July, 1983).

(3.2) T. E. Jones, "Reference Material Chemistry - Synthetic Groundwater Composition", RHO-BW-St-37 P (April, 1982).

(3.3) P. J. Bradley et al, "Nuclear Waste Package Materials Testing Report: Basaltic and Tuffaceous Environments", PNL-4452 (March, 1983).

(3.4) R. N. Parkins, "Environmental Aspects of Stress-Corrosion Cracking in Low Strength Ferritic Steels", Stress-Corrosion Cracking and Hydrogen Embrittlement of Iron Base Alloys, Ed. R. W. Staehle, et al, NACE, 1977, p. 601.

(3.5) R. N. Parkins, "Predictive Approaches to Stress Corrosion Cracking Failure", Corrosion Science, Vol. 20, No. 2, 1980, p. 147.

(3.6) G. H. Koch, N. G. Thompson, and J. L. Means, "Trace Elements in Flue Gas Desulfurization Environments and Their Effect on Corrosion of Alloys", EPRI Research Project RP1871-6, to be published December, 1984.

(3.7) F. P. Ford, "Stress Corrosion Cracking", Corrosion Processes, Ed. R. N. Parkins, Applied Science Publisher, 1982.

(3.8) T. Furuya, et al, "Study of ,-Ray Radiation Effects on Corrosion Resistance of Alloys for Storage of High-Level Waste Packages", JAERI-M 82-061, May, 1982.

(3.9) C. E. Sims, "Hydrogen Elimination by Aging", Transactions AIME, Journal of Metals, 188, 1321 (November, 1950). See also C. E. Sims, G. A. Moore, and D. W. Williams, "The Effect of Hydrogen on the Ductility of Cast Steels", Transactions AIME, 176, 283 (1948).

(3.10) "Waste Package Conceptual Designs for a Nuclear Repository in Basalt", Westinghouse Electric Company, AESD-TME-3142 (1982). See also S. Bashen, "Waste Package for Repository Located in Salt", Proceedings 1983 Civilian Radioactive Waste Management Information Meeting, Washington, D.C., Paper No. 831217, December, 1983.

(3.11) See, for example, R. Gerber, I. M. Bernstein, and A. W. Thompson, Scr. Metall. 10, 341 (1976); also H. Cialone and R. J. Agavo, Metall. Trans. A, 12A, 1373 (1981).

(3.12) P. C. Paris, H. Tada, A. Zahoor, and H. Ernst, "The Theory of Instability of the Tearing Mode of Elastic-Plastic Crack Growth", Elastic-Plastic Fracture, ASTM STP 668, J. D. Landes, J. A. Begley, and G. A. Clarke, eds., ASTM, Philadelphia (1975), p. 5.

(3.13) M. L. Hill and E. W. Johnson, "The Solubility of Hydrogen in Alpha Iron", Transactions, TMS-AIME, 221, 662-629 (1961).

(3.14) C. Y. Chao, L. F. Lin, and D. D. Macdonald, J. Electrochem. Soc., 128, 1981, p. 1187.

(3.15) D. D. MacDonald, A. C. Scott, and P. Wentrcek, J. Electrochem. Soc., 126, 1979, p. 1618.

(3.16) "Long-Term Performance of Materials Used for High-Level Waste Packaging", D. Stahl and N. E. Miller (compilers), NUREG/CR-3427, Volume 2 (December, 1983), pp 3-42 to 3-44.

(3.17) M. Golomb and M. Shanks, Elements of Ordinary Differential Equations, p. 20, McGraw-Hill, New York, 1965.

(3.18) J. Crank and P. Nicholson, Proc. Camb. Phil. Soc. 43, pp 50-67 (1947).

(3.19) G. Dahlquist and A. Bjorck, Numerical Methods, p. 347, Prentice-Hall, Englewood Cliffs, NJ, 1974.

(3.20) K. E. Heusler and L. Fischer, Werkst. Korros., 27, 1976, p. 551.

(3.21) L. F. Lin, C. Y. Chao, and D. D. Macdonald, J. Electrochem. Soc., 128, 1981, p. 1194.

(3.22) K. E. Heusler and L. Fischer, Werkst. Korros., 27, 1976, p 551.

(3.23) N. Sato, T. Nakagawa, K. Kudo, and M. Sakashita, in Localized Corrosion, R. W. Staehle, B. F. Brown, J. Kruger, and A. Agrawal (editors), NACE-3, Nat. Assoc. of Corrosion Engrs., Houston, TX (1974), p. 447.

(3.24) M. Janik-Czachor and M. B. Ives, in Passivity of Metals, R. P. Frankenthal and J. Kruger (editors), Electrochem. Soc., Princeton, NJ (1978), p. 369.

(3.25) M. Romanoff, Underground Corrosion, National Bureau of Standards Circular 579 (April, 1957), pp. 38, 47, 64, 72.

(3.26) H. P. Godard, W. B. Jepson, M. R. Bothwell, and R. L. Kane, The Corrosion of Light Metals, John Wiley & Sons, Inc. (New York, 1967), pp. 60, 61.

(3.27) G. P. Marsh, Trans. Am. Nucl. Soc., 45, 1983, p. 292.

(3.28) H. J. Engell and N. D. Stolica, Zeit. Physik-Chemie Neue Folge, 20, 1959, p. 113.

(3.29) K. J. Vetter and H. H. Strehblew, Ber. Bunsen. Gesell. Physik. Chemie, 74, 2970, p. 1024.

(3.30) H. W. Pickering and R. P. Frankenthal, J. Electrochem. Soc., 119, 1972, p. 1297.

(3.31) H. S. Isaacs, J. Electrochem. Soc., 120, 1973, p. 1456.

(3.32) J. W. Tester and H. S. Isaacs, J. Electrochem. Soc., 122, 1975, p. 1438.

(3.33) J. R. Galvele, J. Electrochem. Soc., 123, 1976, p. 464.

(3.34) K. Nisancioglu and H. Holtan, Electrochim. Acta, 23, 1978, p. 251.

(3.35) R. Alkire and D. Siitari, J. Electrochem. Soc., 126, 1979, p. 15.

(3.36) T. R. Beck and R. C. Alkire, J. Electrochem. Soc., 126, 1979, p. 1662.

(3.37) J. Newman, in Localized Corrosion, (Ref. 3.23), p. 45.

(3.38) G. P. Cherepanov, in Comprehensive Treatise of Electrochemistry, Vol. 4: Electrochemical Materials Science, J. O'M. Bockris, B. E. Conway, E. Yeager, and R. E. White (editors), Plenum Press (New York, 1981), p. 333.

(3.39) Ya. M. Kolotyrkin, Yu. A. Popov, and Yu. V. Alekseev, in *Advances in Physical Chemistry - Current Developments in Electrochemistry and Corrosion*, Ya. M. Kolotyrkin (editor), MIR Publishers (Moscow, 1982), p. 11.

(3.40) J. S. Newman, *Electrochemical Systems*, Prentice-Hall, Inc. (Englewood Cliffs, NJ, 1973), pp. 223 ff and elsewhere within volume.

(3.41) B. G. Ateya and H. W. Pickering, *J. Electrochem. Soc.*, *122*, 1975, p. 1018.

(3.42) Long-Term Performance of Materials Used for High-Level Waste Packaging", D. Stahl and N. E. Miller (compilers), NUREG/CR-3405, BMI-2105, Vol. 1 (July, 1983), pp. 6-18 to 6-21.

4. INTEGRATED SYSTEM PERFORMANCE

One objective of the Integrated System Performance task is to develop an improved understanding of phenomena that affect waste-package performance at the system level. This involves phenomena that arise from combined effects as well as processes which drive the evolution of the waste-package condition.

This year our efforts have been directed towards obtaining a better understanding of gamma-radiation effects on the waste-form environment. This involved performing energy deposition calculations for the gamma-radiation field in the vicinity of the waste package and studies of water radiolysis.

4.1 Considerations in Developing a General Description of Groundwater Radiolysis Near Waste Packages

Material-corrosion experiments have demonstrated that a radiation field can produce adverse effects. Furuya et al(4.1) have observed stress-corrosion cracking of Type 304L stainless steel in deionized water in a radiation field (1.1×10^5 R/hr) at 100 C but not in the absence of radiation, and Chikalla and Powell(4.2) have observed increases in corrosion rates of up to an order of magnitude in irradiated brines compared to nonirradiated brines for iron-based alloys. It is therefore necessary to account for effects of radiolysis in the corrosion theory which is described in Section 3.4.1, as well as in the corrosion research experiments discussed in Section 3.2.

One purpose of this work is to develop a general mathematical description for the gamma radiolysis of groundwater solutions. This description will then be used to perform a computer simulation of the radiolysis of groundwater in the vicinity of a waste package. This simulation will indicate the time-dependence of concentrations of the groundwater species present in the radiation field for a specified time-dose relationship and specified initial water chemistry. These results will be used to assess the suitability of the abbreviated description of water radiolysis that will be folded into the general-corrosion correlation. These results will also be evaluated to determine whether, and how, the water chemistry in the autoclave experiments should be changed to account for radiolysis.

4.1.1 Phenomenological Description of Water Radiolysis

When a gamma-ray photon passes through water, it may interact with a water molecule through Compton scattering, pair production, or photoelectric absorption. These processes cause energy from the gamma-ray photon to be transferred to the solution the photon travels through. One result of this energy transfer is the formation of secondary electrons of varying energies; these may interact with water molecules, causing excitation and ionization(4.3), which in turn cause the formation of radiolytic species in the solution along the path of the secondary electrons(4.4). If species are formed near each other, they may recombine or react with one another. Eventually, the radiolytic species and their reaction products will diffuse away from the region in which they were formed and become part of a homogeneous solution, where they will no longer have high local concentrations. Once distributed in solutions, they will interact with other aqueous species.

Two approaches are used to analyze the time-dependence of the concentrations of radiolytic species in solution. In one approach, energy deposition and species formation are modeled in detail as energy is transferred to the solution. The reactions and diffusion of these species are also modeled on a molecular level in this approach(4.4-4.17). The result of these calculations is the source rate of species which can participate in homogeneous chemical reactions in the host solution. Eventually, the detailed calculations along the tracks of the secondary electrons will be coupled to a description of the reactions occurring in the homogeneous host solution(4.18).

An alternative approach, which is being employed in this program, is to assume a source rate of species from regions where the primary species are formed to the homogeneous solution. This source rate is taken in the form of a G-value which indicates the source rate to solution for a given aqueous species. The homogeneous reactions and time-evolution of the species in solution are then analyzed using an appropriate chemical mechanism(4.19).

4.1.2 Kinetic Description of Water Radiolysis

The rate at which a complex chemical reaction proceeds can be established empirically either through an experimental determination, measuring reaction rates for specific conditions and concentrations, or through a more general approach of chemical kinetics, using empirical laws of kinetics and a mechanism. The difficulty with experimentally determining an overall reaction rate in a generalized application is that differences in experimental conditions and species concentrations can lead to significantly different results. The advantage of a kinetic description is that changes in the experimental conditions and the concentrations of species in the system can be accounted for appropriately within the description. The time-dependence of a chemical reaction can be described by chemical kinetics in three basic steps. First, it is necessary to establish a reaction mechanism through which a chemical reaction proceeds. The mechanism is a set of elementary reactions which comprise the overall reaction(s) of interest. The rates of each of the elementary reactions in the mechanism can then be expressed through the empirical laws of chemical kinetics as the product of the rate constant for the elementary reaction and the concentration of each of the reactant species in the elementary reaction raised to a power given by the species coefficient. The second step in describing the time-dependence of species in solution is to write out the differential equations describing the buildup and decay of each of the species involved in the mechanism. The third and final step in performing the kinetic analysis is to integrate the set of differential equations with respect to time(4.19). Solutions to these differential equations will be the concentrations of species stated in the mechanism as a function of time.

Several investigators have proposed reaction mechanisms for the radiolysis of aqueous systems. The mechanisms investigated in this program were chosen because they were judged to provide an adequate representation for their intended use. These radiolysis descriptions often use a subset of the reactions which have been identified for water-radiolysis species.

Bielski and Giebicki(4.20) have identified more than 228 elementary reactions between species in irradiated oxygenated aqueous solutions. Ninety-nine of these reactions, involving 27 species, have been identified for irradiated oxygenated water(4.18). The mechanisms of Boyd, et al,(4.21) Carver, et al,(4.22) Chatterjee, et al,(4.18) and Rosinger and Dixon(4.23) are for water which may contain dissolved hydrogen and/or oxygen. Burns' mechanism(4.24) is for granitic groundwater. This fluid may contain dissolved H_2 and/or O_2 as well as NO_3^- and Cl^-. The mechanism of Christensen and Bjergbakke(4.25) is for water containing dissolved H_2 and/or O_2 as well as dissolved iron. Simonson and Kuhn's mechanism(4.26) is for brine solutions. This description accounts for dissolved Cl^- as well as dissolved H_2 and/or O_2. This description also partitions the H_2 and O_2 between the aqueous and gas phases. The mechanisms of Schwarz(4.27) and of Kuppermann(4.28) are intended to apply only to the reactions taking place along the paths of secondary elections and radiolytic species. As such, they do not account for species and reactions which occur homogeneously in solution. These descriptions have been included in these studies because of their potential suitability for use in the corrosion correlation due to their abbreviated size.

4.2 Method for Developing a General Description of Groundwater Radiolysis Near Waste Packages

Work on the development of a general description for the radiolysis of groundwater will proceed in six steps:

(1) Determine energy-deposition rates from gamma radiation to groundwater near the waste package.

(2) Develop a general mechanism for groundwater radiolysis.

(3) Benchmark the general mechanism against experimental data available in the literature.

(4) Revise the general mechanism if necessary and use it to:
   (a) assess the simplified description of water radiolysis used in the corrosion correlations
   (b) estimate the concentrations of species in groundwater that is expected to contact the waste package.

(5) Perform benchmark experiments to:
    (a) fill data needs identified in Step 3
    (b) provide additional assurance that the groundwater-radiolysis mechanism provides credible results.

(6) Revise the description of groundwater radiolysis if necessary.

Efforts to date in the Integrated System Performance task have focused on Steps 1-3. Progress in these areas is described in Sections 4.2.1-4.2.3. In preparation for Step 4, the current status of the water-chemistry description used in the corrosion correlations is described in Section 4.2.4.

4.2.1 Gamma-Energy Deposition Calculations

A quantitative knowledge of the gamma-energy deposition rates to the aqueous system near the waste package is required for the gamma-radiolysis studies as well as for the general-corrosion correlation being developed. To quantify the gamma fluxes and energy-deposition rates in the waste-package environment, calculations were performed with the ANISN(4.29) code. Details of these calculations have been discussed in an earlier report(4.30).

Results are reported for the gamma-deposition rates to the commercial high-level glass waste form, and to the package materials and groundwater for commercial high-level waste packages and spent-fuel waste packages. These data are presented for three points in time for each type of waste package. For the commercial high-level waste package and environment, these are 0 years after reprocessing, 50 years after reprocessing, and 100 years after reprocessing. It is assumed that the fuel is reprocessed at 10 years after discharge from the reactor. Dose rates for the spent-fuel waste package and environment are presented for 0 years after discharge, 50 years after discharge, and 100 years after discharge.

Figure 4.1 shows the gamma-energy deposition rate to the commercial high-level glass waste form as a function of distance from the central axis of the solid cylinder. In this figure, the gamma-energy deposition rates decrease by ~10% as the outer surface of the waste form is approached. The contribution from alpha decay is not included in these data. Figure 4.2 shows the gamma-energy deposition rates to the packing material and basalt rock surrounding a commercial high-level waste package. Figure 4.3 shows the corresponding gamma-energy deposition rate to water if it were to occupy voids in the packing material and basalt rock. These calculations do not account for energy-transfer effects which might occur as secondary electrons escape from one material and provide a dose to another in the packing material. Experiments by Christensen and Bjergbakke(4.31) imply that this effect might increase the dose rate to the water by 30 percent. Figure 4.4 shows the gamma-energy deposition rates to the packing material and basalt rock surrounding a spent-fuel waste package, and Figure 4.5 shows

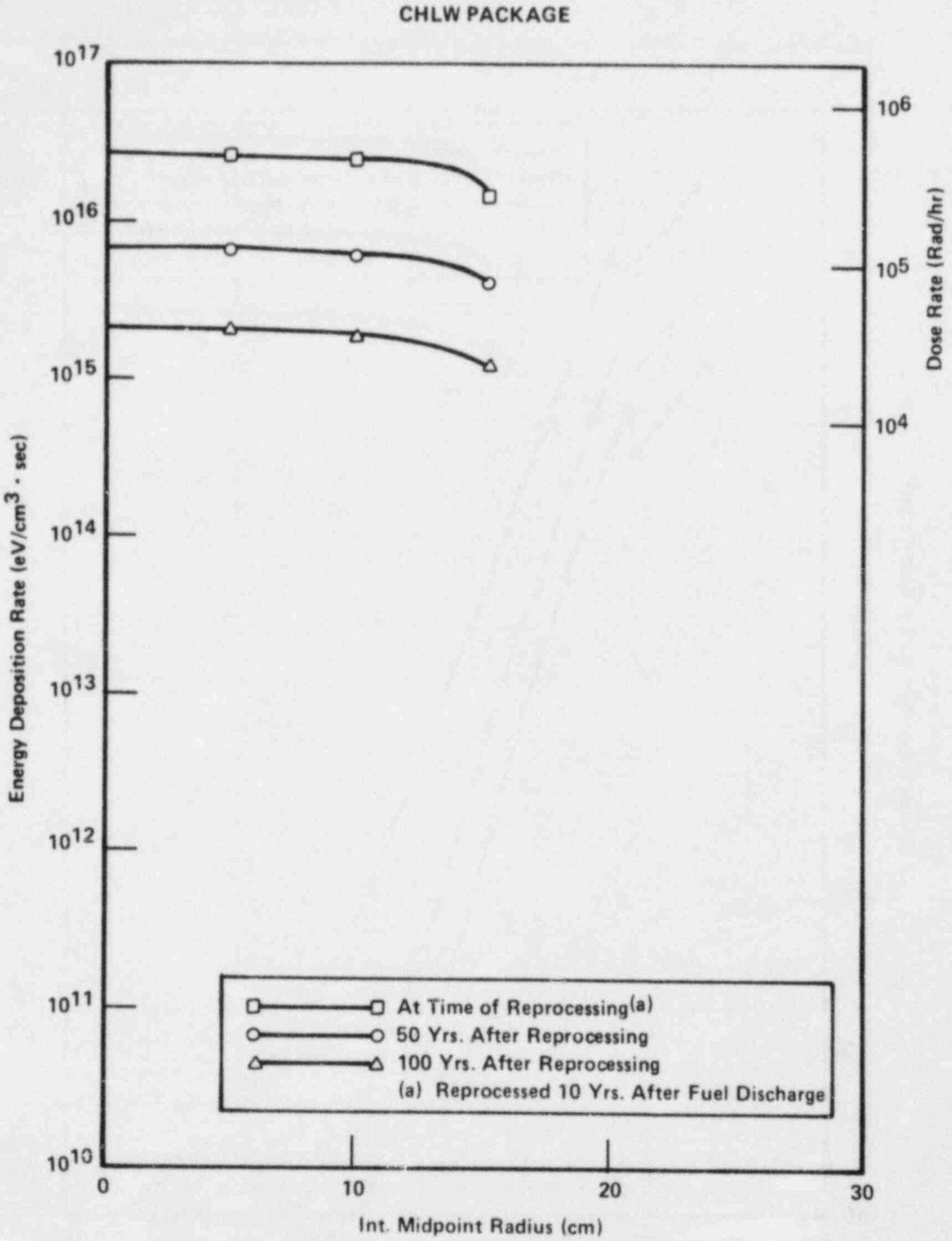

Figure 4.1 Gamma energy deposition rate to a commercial high level waste glass waste form at 0, 50, and 100 years after reprocessing.

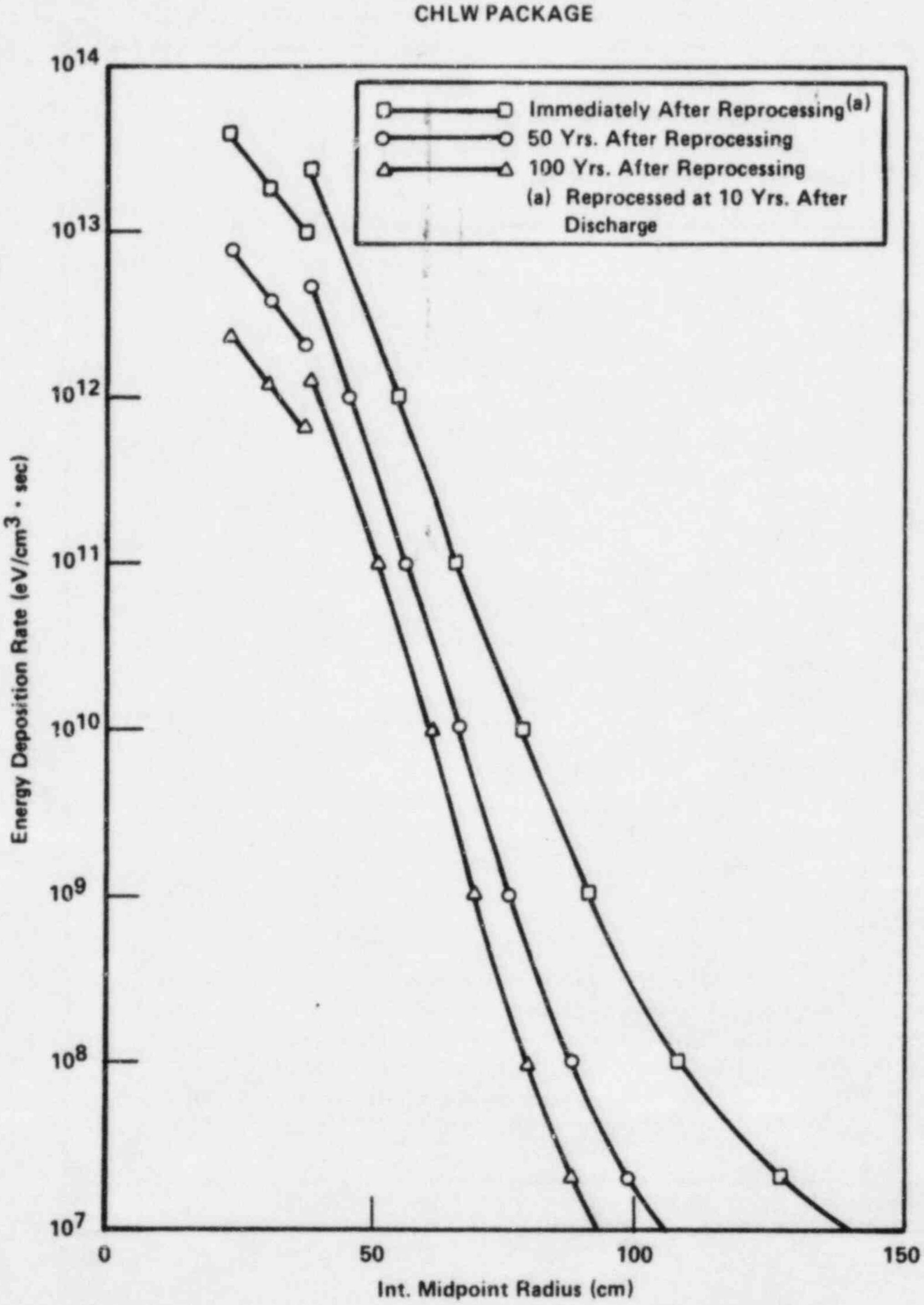

Figure 4.2 Gamma energy deposition rates to the packing material and basalt rock surrounding a CHLW waste package.

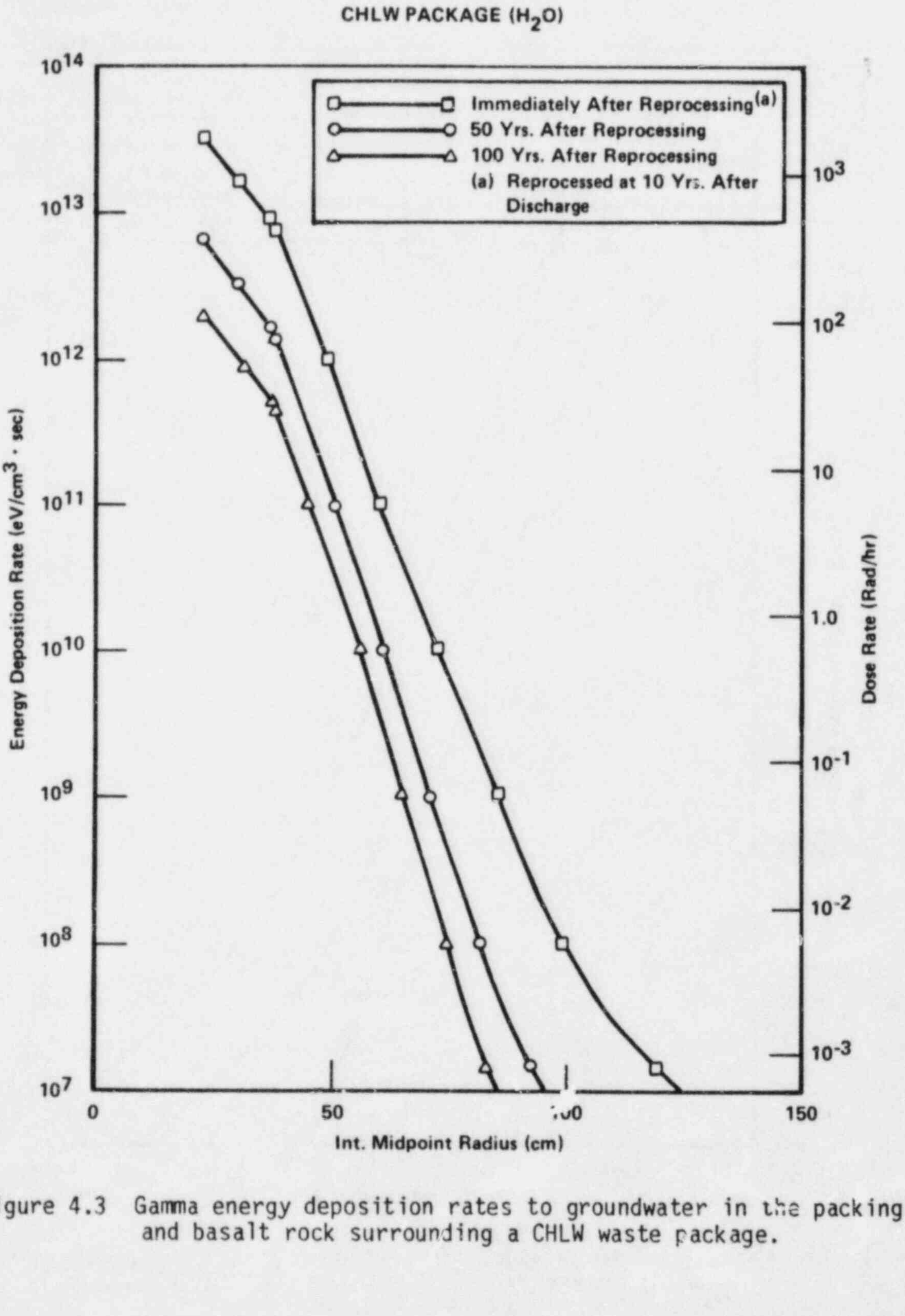

Figure 4.3 Gamma energy deposition rates to groundwater in the packing and basalt rock surrounding a CHLW waste package.

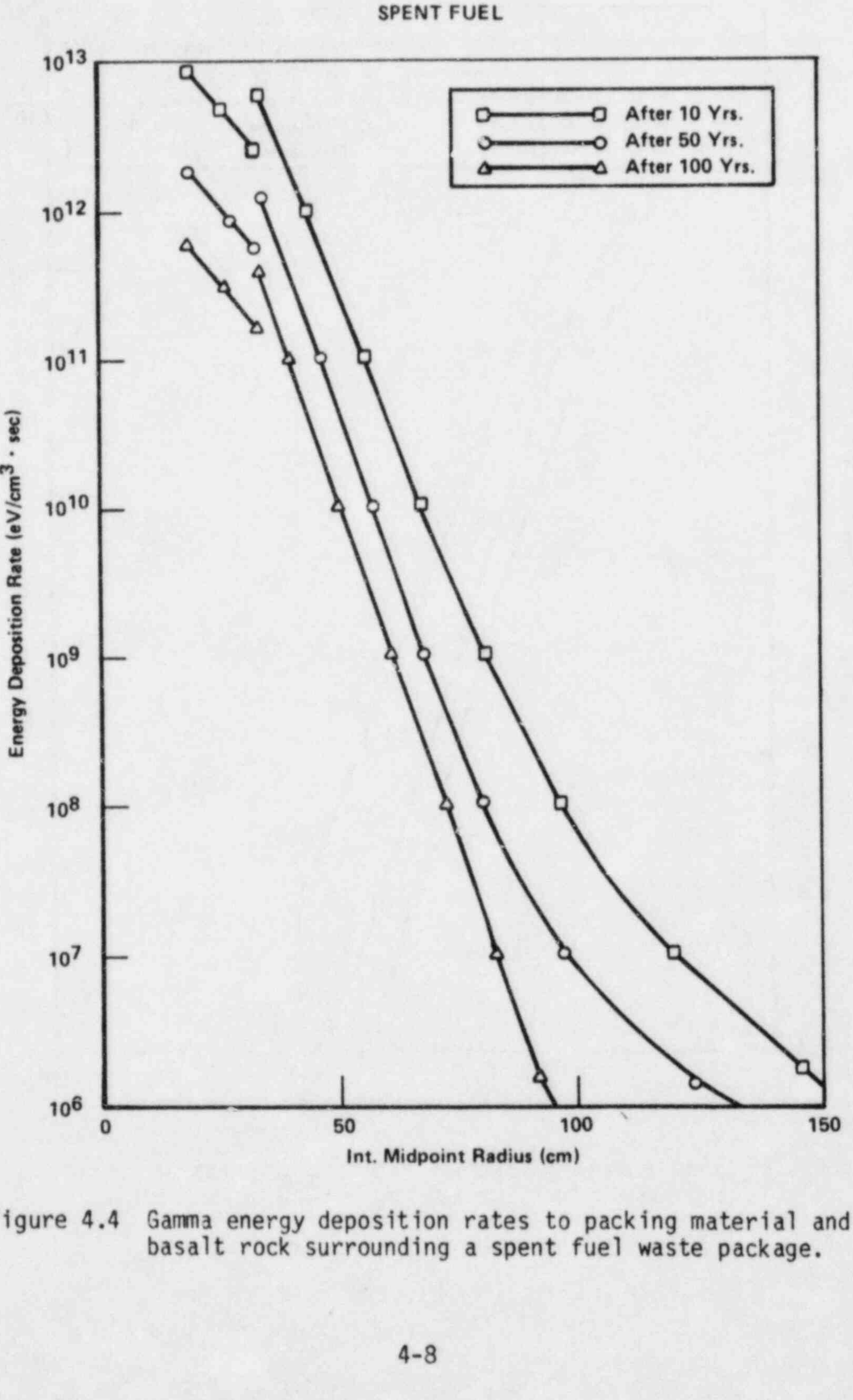

Figure 4.4 Gamma energy deposition rates to packing material and basalt rock surrounding a spent fuel waste package.

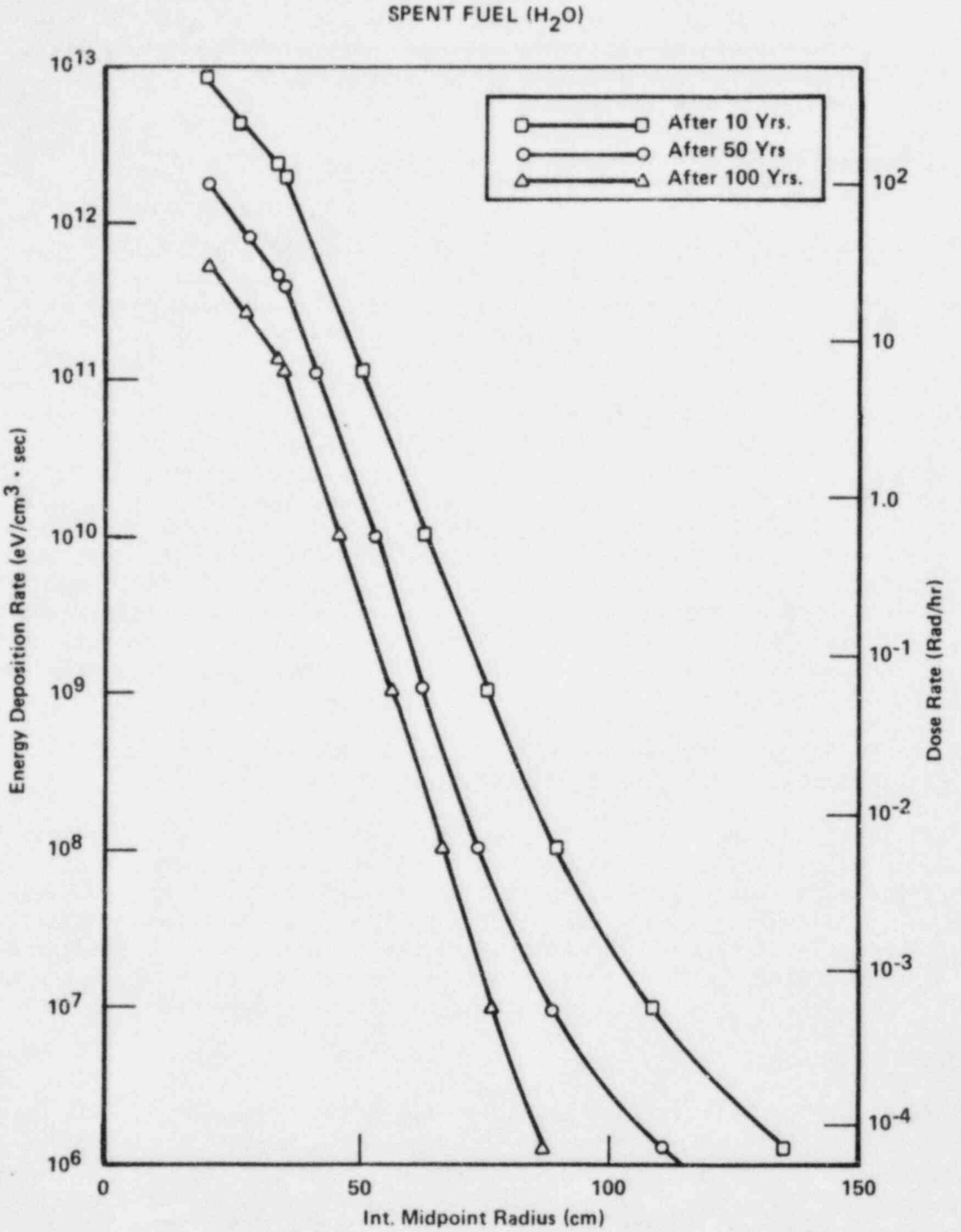

Figure 4.5 Gamma energy deposition rates to groundwater surrounding a spent fuel waste package.

the gamma-energy deposition rates to groundwater which might occupy voids in the packing material and basalt rock. Figure 4.2 shows the gamma energy deposition rates to the packaging material and basalt rock surrounding a CHLW waste package. The discontinuity in Figures 4.2 and 4.4 arises from differing gamma photon absorbance properties of the packaging material and basalt rock.

4.2.2 Development of a General Description for the Radiolysis of Groundwaters

The development of a general description for the radiolysis of water will proceed in several phases. First, a mechanism for the radiolysis of water containing dissolved H_2 and/or O_2 will be chosen from those cited in Section 4.1.2 to give suitable agreement with experimental data in the literature(4.21,4.32,4.33,4.34). This basic mechanism will then be extended by including elementary reactions and rate constants described in the literature to account for the presence of other dissolved species in groundwaters. In this work, the MAKSIMA-CHEMIST(4.22) code will be used to set up and integrate the differential equations for each mechanism under study. The MAKSIMA-CHEMIST code uses an improved version(4.21) of the Gear algorithm(4.35) for solving a stiff set of differential equations. When using MAKSIMA-CHEMIST, the user is required to input the reaction mechanism, the G-values for the production of primary radiolytic species, the initial concentrations of species in solution, the dose-rate history, and the points in time at which solutions to the set of differential equations are requested, as well as other ancillary data associated with the running of the code.

4.2.3 Comparisons of Experimental Data with Computed Predictions Using Water-Radiolysis Descriptions

Calculations were performed with MAKSIMA-CHEMIST using several descriptions of water radiolysis in order to choose or develop a mechanism upon which to build a generalized description of the radiolysis of groundwater. Identical calculations were performed for seven different descriptions for the radiolysis of water. The input parameters (dose rates, initial concentrations, etc.) used in these calculations were chosen so that comparisons of computed results with experimental data could be made.

4.2.3.1 Calculations

The first set of calculations was performed using a number of different mechanisms to see how well they could simulate three sets of data reported by Hochanadel(4.33). The conditions for these three cases are shown in Table 4.1. A sample of the graphical results of such calculations is given in Figures 4.6-4.8 for H_2, O_2, H_2O_2, H^+, and OH^-, as calculated using the Rosinger and Dixon mechanism(4.23). The calculated values of the H_2O_2 concentration at 1000 and 3×10^7 seconds are shown in Table 4.2, along with an interpolation of Hochanadel's measurements which were reported for other points in time. The interpolations were actually obtained from a graph of a fit of these data shown in Reference 4.21.

Table 4.1 Conditions for Hochanadel data(4.33).

Case A: H_2 = 0 mole/liter $O_2 = 4.52 \times 10^{-4}$ mole/liter

Case B: $H_2 = 7.33 \times 10^{-4}$ mole/liter $O_2 = 7.6 \times 10^{-5}$ mole/liter

Case C: $H_2 = 4.42 \times 10^{-4}$ mole/liter $O_2 = 5.48 \times 10^{-4}$ mole/liter

Dose Rate: 9.22×10^{15} eV/cm^3-sec

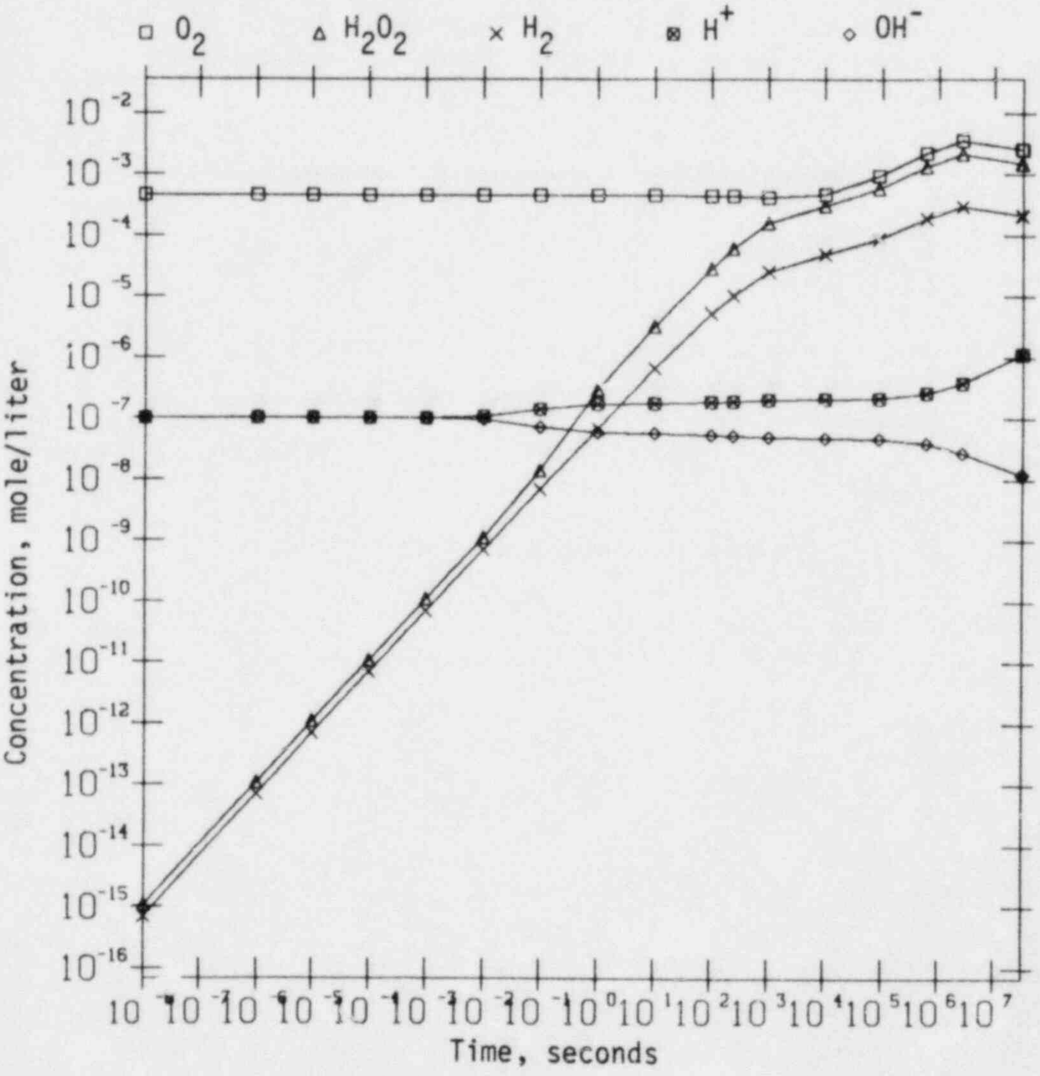

Figure 4.6 Simulation of water radiolysis for Case A using the mechanism of Rosinger and Dixon(4.23).

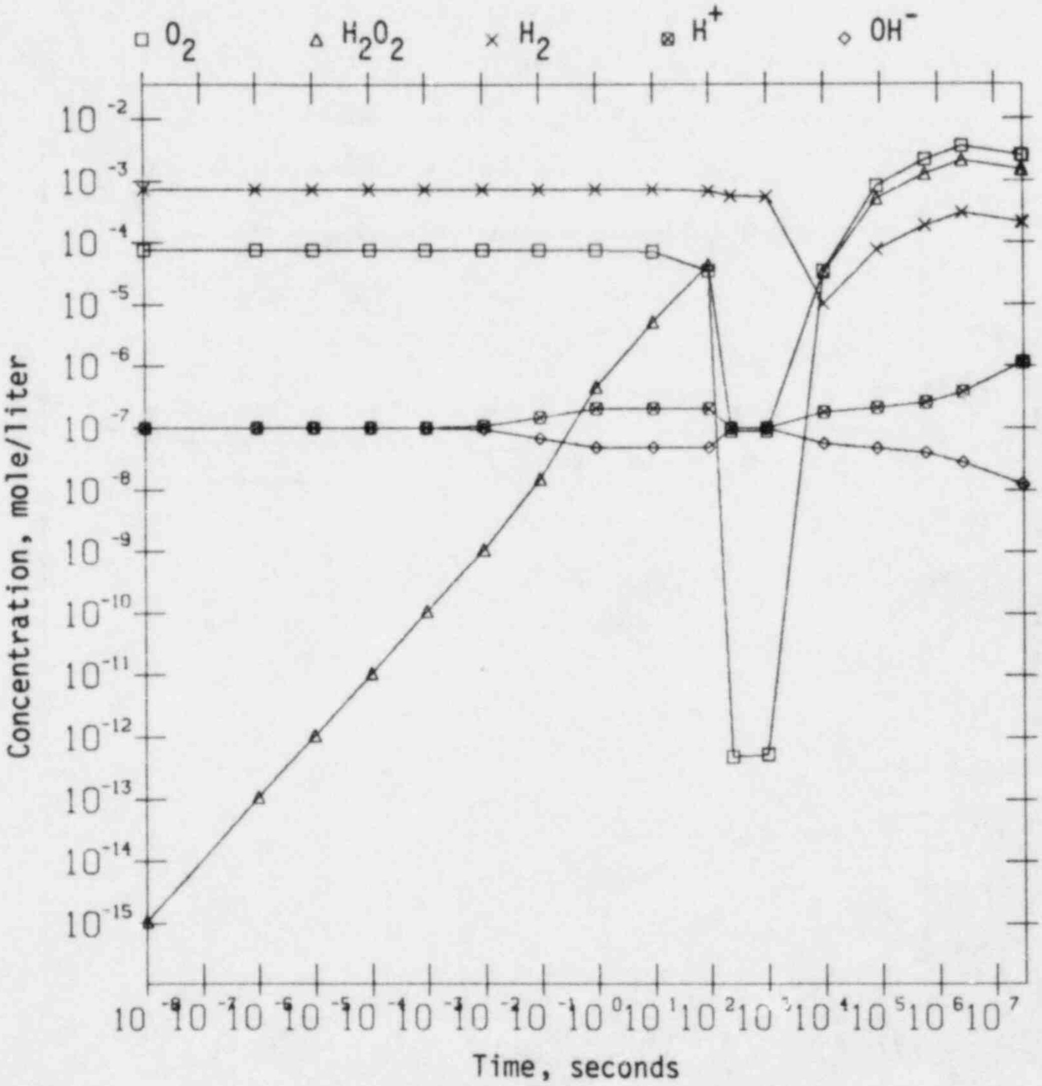

Figure 4.7 Simulation of water radiolysis for Case B using the mechanism of Rosinger and Dixon(4.23).

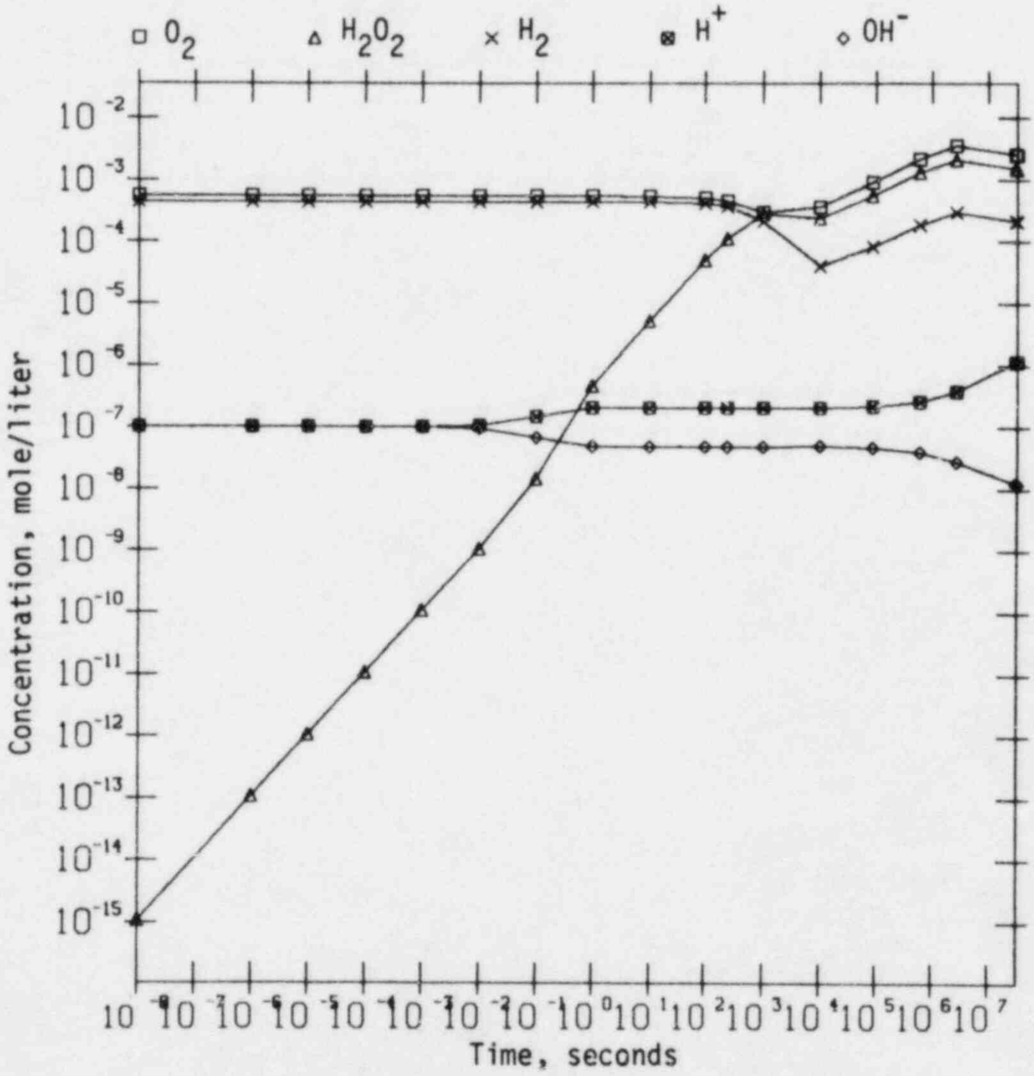

Figure 4.8 Simulation of water radiolysis for Case C using the mechanism of Rosinger and Dixon(4.23).

Table 4.2 Calculated values of H_2O_2 concentrations for Hochanadel's Experiments(4.33)

Mechanism	Case*	H_2O_2 mole/liter at 1000 sec	Literature H_2O_2 mole/liter at 1000 sec	H_2O_2 mole/liter 3×10^7 sec
Boyd, et al	A	1.2×10^{-4}	9.5×10^{-5}	1.8×10^{-7}
	B	1.6×10^{-7}	2.1×10^{-4}	1.7×10^{-7}
	C	2.7×10^{-4}	3.1×10^{-4}	1.8×10^{-8}
Carver, et al	A	1.2×10^{-4}	9.5×10^{-5}	3.8×10^{-8}
	B	3.5×10^{-8}	2.1×10^{-4}	3.8×10^{-8}
	C	2.3×10^{-4}	3.1×10^{-5}	3.8×10^{-8}
Chatterjee, et al	A	1.1×10^{-4}	9.5×10^{-5}	3.8×10^{-9}
	B	3.9×10^{-9}	2.1×10^{-4}	3.8×10^{-9}
	C	2.5×10^{-4}	3.1×10^{-4}	3.8×10^{-9}
Kuppermann	A	6.3×10^{-5}	9.5×10^{-5}	1.9
	B	6.3×10^{-5}	2.1×10^{-4}	1.9
	C	6.3×10^{-5}	3.1×10^{-4}	1.9
Rosinger and Dixon	A	1.6×10^{-4}	9.5×10^{-5}	1.5×10^{-3}
	B	9.0×10^{-8}	2.1×10^{-4}	1.5×10^{-3}
	C	2.8×10^{-4}	3.1×10^{-4}	1.5×10^{-3}
Schwarz	A	6.3×10^{-5}	9.5×10^{-5}	1.9
	B	6.3×10^{-5}	2.1×10^{-4}	1.9
	C	6.3×10^{-5}	3.1×10^{-4}	1.9
Simonson	A	1.2×10^{-6}	9.5×10^{-5}	1.2×10^{-6}
	B	1.2×10^{-6}	2.1×10^{-4}	1.2×10^{-6}
	C	1.2×10^{-6}	3.1×10^{-4}	1.2×10^{-6}

* Cases A, B, and C are described in Table 4.1.

As can be seen in Table 4.2, several of the descriptions give reasonable agreement with the experimental data for cases A and C. For case B, the Kuppermann(4.28), Schwarz(4.27), and Rosinger and Dixon(4.23) mechanisms give agreement at later times. As a test of the chemical sense of some of the results, the ion product of water was calculated for the calculated H^+ and OH^- concentrations at 1000 and 3×10^7 seconds. Results of these calculations are shown in Table 4.3. The ion product (K_w) of water should be very nearly 1×10^{-14}. As can be seen in Table 4.3, the Simonson and Kuhn(4.26), Carver, et al(4.22), Boyd, et al(4.21), and Rosinger and Dixon(4.23) descriptions give good agreement at 1000 and 3×10^7 seconds.

In the second set of calculations, the initial concentrations and dose rates were chosen to model experiments performed by Schwarz(4.32). In these experiments, H_2O_2 steady-state concentrations were measured for several different dose rates. Since the total doses reported in that work range from 10^{19} - 10^{20} eV/cc, the comparison data were chosen for calculated concentrations at one second after the initiation of constant irradiation at the prescribed dose rate. These data are shown in Table 4.4. As can be seen in Table 4.4, most of the calculated results are within an order of magnitude of the experimental observations. The data calculated using the Rosinger and Dixon mechanism are within a factor of three of the experimental data for each of the dose rates shown.

4.2.3.2 Results and Conclusions

The mechanism of Rosinger and Dixon(4.23) contains 55 reactions and is the most complete of the mechanistic descriptions of water radiolysis examined here. Rosinger and Dixon's mechanism was in fair agreement with the experimental data, using the rate constants reported by Rosinger and Dixon and the G-values shown in Table 4.5. Also, H^+ and OH^- concentrations calculated using this mechanism were in good agreement with the ion product for water. This mechanism therefore appears to be a reasonable base upon which to build a generalized description for groundwater radiolysis.

4.2.4 Water-Chemistry Description Used in Corrosion Correlations

Effects of water chemistry pertain to all the various degradation processes that result from the presence of groundwater, including waste-form dissolution and the general and localized corrosion of container materials. For this reason, a method for water-chemistry analysis has been developed that can be utilized in various other studies of the performance of the waste package.

Table 4.3 Ion product of water determined from calculated H^+ and OH^- concentrations.

Mechanism	Case*	K_w at 1000 sec	K_w at 3×10^7 sec
Boyd, et al	A	1.01×10^{-14}	1.36×10^{-14}
	B	1.01×10^{-14}	1.37×10^{-14}
	C	1.01×10^{-14}	1.37×10^{-14}
Carver, et al	A	1.03×10^{-14}	1.40×10^{-14}
	B	1.03×10^{-14}	1.40×10^{-14}
	C	1.02×10^{-14}	1.40×10^{-14}
Chatterjee, et al	A	2.65×10^{-18}	1.48×10^{-17}
	B	1.44×10^{-17}	1.48×10^{-17}
	C	5.60×10^{-18}	1.48×10^{-17}
Kuppermann	A	3.17×10^{-18}	3.17×10^{-18}
	B	3.17×10^{-18}	3.17×10^{-18}
	C	3.17×10^{-18}	3.17×10^{-18}
Rosinger and Dixon	A	1.01×10^{-14}	1.37×10^{-14}
	B	1.01×10^{-14}	1.38×10^{-14}
	C	1.01×10^{-14}	1.37×10^{-14}
Schwarz	A	3.25×10^{-18}	3.25×10^{-18}
	B	3.25×10^{-18}	3.25×10^{-18}
	C	3.25×10^{-18}	3.25×10^{-18}
Simonson	A	1.00×10^{-14}	1.20×10^{-14}
	B	1.00×10^{-14}	1.20×10^{-14}
	C	1.00×10^{-14}	1.20×10^{-14}

* Cases A, B, and C are described in Table 4.1.

Table 4.4 Calculated H_2O_2 concentrations after one second of irradiation and observed steady-state experimental data.

Mechanism	(Dose Rate)(eV/liter-sec)			
	(2.9×10^{21})	(1.2×10^{22})	(3.8×10^{22})	(8.0×10^{22})
Boyd, et al	3.0×10^{-6}	6.4×10^{-6}	1.1×10^{-5}	1.4×10^{-5}
Carver, et al	3.2×10^{-6}	7.5×10^{-6}	1.5×10^{-5}	2.1×10^{-5}
Chatterjee, et al	1.5×10^{-6}	3.2×10^{-6}	4.9×10^{-6}	4.9×10^{-6}
Kuppermann	2.0×10^{-5}	8.0×10^{-5}	2.6×10^{-4}	5.5×10^{-4}
Rosinger and Dixon	7.0×10^{-6}	1.5×10^{-5}	2.9×10^{-5}	4.4×10^{-5}
Schwarz	2.2×10^{-5}	8.5×10^{-5}	2.7×10^{-4}	5.7×10^{-4}
Simonson	1.8×10^{-5}	4.0×10^{-5}	7.5×10^{-5}	1.1×10^{-4}
Experimental Data*	4.2×10^{-6}	7.6×10^{-6}	1.3×10^{-5}	1.9×10^{-5}

* From Reference 4.32.

Table 4.5 G-Values used in the comparison calculations.

Species	G-Value
e^-_{aq}	2.80
H^+	2.90
OH^-	0.10
OH	2.7
H	0.48
H_2	0.45
H_2O_2	0.70
HO_2^-	0.0
HO_2	0.02
O_2^-	0.0
O_2	0.0
H_2O	0.0
$O_2^=$	0.0
O^-	0.0
O_3^-	0.0

4.2.4.1 Testing of the Water-Chemistry Description

In view of the importance of water chemistry, it is important to consider the various assumptions which are implicit in our description. One potential shortcoming of the water-chemistry analysis, in its current form, is the limited number of species that are included. As a test, we have compared calculations and experimental results for natural and synthetic groundwaters. As part of the Basalt Waste Isolation Project, chemical analyses have been carried out on Grande Ronde basalt groundwater. According to Jones,(4.36) this groundwater "would be the most likely to migrate into either of the two candidate repository horizons within the Grande Ronde Basalt (i.e., the Umtanum and Middle Sentinel Bluffs flows)." For experimental convenience, Rockwell Hanford developed a synthetic groundwater which closely reproduces the actual groundwater. The composition of this solution was given in Table 3.8.

As a measure of the accuracy of the water-chemistry analysis, we have selected the value of the calculated pH. At a given temperature, pH is the most important single variable in determining the solubility and rate of dissolution of a silicate glass. Accordingly, the accuracy of the predictions of any system model are heavily dependent on the accuracy with which pH may be calculated.

Three values for the pH of the synthetic groundwater have been obtained, two theoretical and one experimental. All of these values are for a temperature of 25 C. The first theoretical value was determined in the water-chemistry analysis that has been included in the system description. Because of the small number of species included, it was necessary to lump sodium and potassium as sodium, and chlorine and fluorine as chlorine. This method, which handles 16 solute species, yielded a calculated pH of 9.90. The second theoretical value was calculated using the program WATEQ of Truesdell and Jones(4.37). This program considers 109 solute species, and it was not necessary to lump any of the measured concentrations. However, WATEQ does not normally require that the electroneutrality condition be satisfied, so it was necessary to run the program repeatedly until a pH was found which made the solution electrically neutral. This pH is 9.88. By comparison, the experimental value of the pH of the synthetic groundwater as reported by Jones is 9.74 ± 0.10.

Some of the assumptions that were made in analyzing the water chemistry seem to be severe: many solute species were ignored, and the alkali metals were lumped together, as were the halogens. However, these assumptions may in fact be less important than they appear, since the neglected species generally have very low concentrations, and since the alkali metals are chemically similar, as are the halogens.

With regard to glass dissolution in basalt groundwaters, it is clear that there is little to be gained by including additional species. Increasing the number of solute species from 16 to 109 reduced the error in pH from 0.16 to 0.14. It should be noted, too, that Jones's procedure for preparing synthetic groundwater includes the addition of NaOH or HCl solutions to achieve the correct pH.

Both our current methods for water-chemistry analysis and the WATEQ code yield acceptable values for the pH of synthetic basalt groundwater. On this basis, it is reasonable to conclude that the current water-chemistry analysis is sufficiently detailed for use in describing the chemistry of a basalt groundwater. Additional species may still be necessary, however, to describe more concentrated groundwaters or the effects of the repository on the groundwater composition.

4.2.4.2 Software Maintenance

During the past year, a new, more accessible computer became available for work on this project. It was determined that the best long-term strategy would be to make a one-time effort to move our computer software to this computer. This work is now finished, and we are proceeding to develop more realistic analyses of the process of glass dissolution and its dependency on water chemistry.

Most of our computations to date have used two programs: the general-purpose water-chemistry code WATEQ, and our own program for coupled water-chemistry and glass-dissolution calculations. These programs have been moved to the new computer for more convenient access. No significant obstacles were encountered in transporting our own water-chemistry-plus-glass-dissolution program. The program appears to be functioning correctly on the new computer. It is believed that the current form of this program will be relatively easy to transport to other computer systems should the need arise.

Moving WATEQ was not quite so straightforward. The version of the code which we received contained certain machine dependencies, primarily in input/output and in the treatment of character data. These dependencies have been eliminated. In addition, there was a limitation in the Fortran compiler which made it impossible to compile the program. The vendor has provided a "fix" for the compiler, and the program has been compiled successfully. Results obtained from WATEQ in its current state appear to be correct.

4.3 Future Work

In the coming year, efforts in the Integrated System Performance task will focus on studies of groundwater radiolysis, homogeneous kinetics, and water chemistry. Work will be initiated on uncertainty analysis, and an experimental apparatus for high-level waste package integral studies will be constructed.

4.3.1 Groundwater Radiolysis Studies

In the near term, the Rosinger and Dixon(4.23) mechanism for water radiolysis will be extended to account for other species which may be present in groundwater. It is anticipated that elementary reactions for aqueous iron species will be added and the mechanism will be evaluated against available experimental data. Additional elementary reactions for water species reported by Bielski and Gebicki(4.20) will also be considered for inclusion in the mechanism.

4.3.2 Homogeneous Kinetic Studies

In the third year of the program, work in homogeneous kinetic studies will begin. This work will provide information on the kinetics of aqueous reactions relevant to the water chemistry near the waste package. This information will help to evaluate the limitations of the equilibrium water-chemistry descriptions. This information will also support the extension of the water-chemistry description to account for the time-dependence of reactions which are slow on the timescale of processes relevant to waste-package performance.

This work will be performed with the aid of the MAKSIMA-CHEMIST code which is currently used for groundwater radiolysis studies. First, mechanisms for relevant reactions will be developed and benchmarked with literature data. Once the mechanisms are established, the reactions for groundwater radiolysis will be folded in, along with reactions between species of interest and groundwater radiolysis species.

4.3.3 Water Chemistry Studies

Studies of water chemistry will be aimed at improving the realism of the description of the groundwater and the reactions taking place in it. Species will be added to the description to account for the repository environment, which includes the host rock and the packing material. Currently, the emphasis is on the steel - basalt system. Much of the work in the coming year will be closely coupled with the efforts of the radiolysis task. The water-chemistry model is also closely tied to the determination of corrosion of the overpack and, as modified by corrosion products, to the dissolution of the waste form. The water chemistry at the overpack-packing interface is also affected by the rate of flow of groundwater. This effect will be added to the description, as well as the kinetics of aqueous reactions (e.g., silicates).

Since the water-chemistry model involves several species, phases, and processes, it is not practical to model all relevant aspects in detail. More detailed concurrent studies in water radiolysis and homogeneous kinetics will provide the information necessary to enable the water chemistry model to account for these processes.

4.3.4 Uncertainty Analysis

In the third year of the program, work will be initiated on uncertainty analysis. The purpose of this work is to increase the understanding of the suitability of various uncertainty-analysis methods for analyzing nuclear-waste packages so that specific methods can be selected on a quantitative basis. This study will provide a scoping analysis for a selected model.

4.3.5 High-Level Waste Package Integral Experiments

In the third year of the program, we plan to initiate work on the construction of an apparatus for high-level waste package integral experiments. The motivation for these experiments is a product of work performed in the first year of the program in the system-performance task. These experiments will address technical issues which were raised while developing the first-cut version of the system description$^{(4.38)}$.

4.4 References for Section 4

(4.1) Takashi Furuya, et al, "Study on γ-ray Irradiation Effects on Corrosion Resistance of Alloys for Storage of High-Level Waste Packages", JAERI-M 82-061 (1982).

(4.2) T. D. Chikalla and J. A. Powell, "Nuclear Waste Management Semi-Annual Progress Report", (October 1982-March 1983), PNL-4250-3 (1983).

(4.3) R. S. Glass, "Effects of Radiation on the Chemical Environment of Waste Canisters in Proposed Repository Sites and Possible Effects on the Corrosion Process", SAND81/1677 (1981).

(4.4) A. Mozumder and J. L. Magee, "Model of Tracks of Ionizing Radiations for Radical Reaction Mechanisms", Radiation Research, 28, 203-14 (1966).

(4.5) A. Mozumder and J. L. Magee, "A Simplified Approach to Diffusion Controlled Radical Reactors in the Tracks of Ionizing Radiations", Radiation Research, 28, 215-31 (1966).

(4.6) Ivan G. Draganic and Zorica D. Draganic, The Radiation Chemistry of Water, Academic Press, New York (1971).

(4.7) Harold A. Schwarz, "Applications of the Spur Diffusion Model to the Radiation Chemistry of Aqueous Solutions", J. Phys. Chem., 73, 1928-1937 (1969).

(4.8) A. K. Ganguly and J. L. Magee, "Theory of Radiation Chemistry. III. Radical Reaction Mechanism in the Tracks of Ionizing Radiations", J. Chem. Phys., 25, 129-34 (1956).

(4.9) A. Mozumder and J. L. Magee, "Theory of Radiation Chemistry. VII. Structure and Reactions in Low LET Tracks", J. Chem. Phys., 45, 3332-41 (1966).

(4.10) J. L. Magee and A. Chatterjee, "Theory of the Chemical Effects of High Energy Electrons", J. Phys. Chem., 82, 2219-26 (1978).

(4.11) Conrad N. Trumbore, et al, "Effects of Pulse Dose on Hydrated Electron Decay Kinetics in the Pulse Radiolysis of Water. A Computer Modeling Study", J. Phys. Chem., 82, 2762-2767 (1978).

(4.12) David R. Short, Conrad N. Trumbore, and Jon H. Olson, "Extension of a Spur Overlap Model for the Radiolysis of Water to Include High Linear Energy Transfer Regions", J. Phys. Chem., 85, 2328-35 (1981).

(4.13) J. L. Magee and A. Chatterjee, "A Spur Unfolding Model for the Radiolysis of Water", Radiat. Phys. Chem., 15, 125-32 (1980).

(4.14) Gordon R. Freeman, "Several Interfaces Between Radiation Physics and Chemistry that Could Pleasure Each Other More", Proceedings of the Workshop on the Interface Between Radiation Chemistry and Radiation Physics, ANL-82-88, pp 9-30 (1983).

(4.15) J. H. Miller and W. E. Wilson, "Modeling Early Events in the Radiation Chemistry of Dilute Aqueous Solutions", Proceedings of the Workshop on the Interface Between Radiation Chemistry and Radiation Physics, ANL-82-88, pp 73-81, (1983).

(4.16) Conrad N. Trumbore and Walter Youngblade, "Recent Calculations Modeling Data from the Pulse Radiolysis and Gamma Radiolysis of Water and Aqueous Solutions", Proceedings of the Workshop on the Interface Between Radiation Chemistry and Radiation Physics, ANL-82-88, pp 82-90 (1983).

(4.17) H. A. Wright, J. E. Turner, R. N. Hamm, R. H. Ritchie, J. L. Magee, and A. Chatterjee, "Early Physical and Chemical Events in Electron Tracks in Liquid Water", Proceedings of the Workshop on the Interface Between Radiation Chemistry and Radiation Physics, ANL-82-88, pp 106-112 (1983).

(4.18) A. Chatterjee, J. L. Magee, and S. K. Dey, "The Role of Homogeneous Reactions in the Radiolysis of Water", Radiation Research, 96, 1-19 (1983).

(4.19) D. Edelson, "Computer Simulation in Chemical Kinetics", Science, 214, 981-86 (1981).

(4.20) Benon H. J. Bielski and Janusz M. Gebicki, "Species in Irradiated Oxygenated Water", Advances in Radiation Chemistry, ed. M. Burton and J. L. Magee, V.2, Wiley-Interscience (1970).

(4.21) A. W. Boyd, M. B. Carver, and R. S. Dixon, "Computed and Experimental Product Concentrations in the Radiolysis of Water", Rad. Phys. Chem., 15, 177-85 (1980).

(4.22) M. B. Carver, D. V. Hanley, and K. R. Chaplin, "MAKSIMA-CHEMIST: A Program for Mass Action Kinetics Simulation by Automatic Chemical Equation Manipulation and Integration Using Stiff Techniques", AECL-6413 (1979).

(4.23) E. L. J. Rosinger and R. S. Dixon, "Mathematical Modeling of Water Radiolysis: A Discussion of Various Methods", AECL-5958 (1977).

(4.24) W. G. Burns, et al, "Effects of Radiation on the Leach Rates of Vitrified Radioactive Waste", J. Nucl. Mat., 107, 145-70 (1982).

(4.25) H. Christensen and E. Bjergbakke, "Radiolysis of Groundwater from HLW Stored in Copper Canisters", SKBF-KBS-TR-82-02 (1982).

(4.26) S. A. Simonson and W. L. Kuhn, "Predicting Amounts of Radiolytically Produced Species in Brine Solutions", PNL-SA-11426, Presented at the Materials Research Society 1983 Annual Meeting, Boston MA, November 14-17, 1983.

(4.27) Harold A. Schwarz, "Applications of the Spur Diffusion Model to the Radiation Chemistry of Aqueous Solutions", J. Phys. Chem., 73, 1928-37 (1969).

(4.28) A. Kuppermann, "Diffusion Model of the Radiation Chemistry of Aqueous Solutions", Radiation Research, 1966, ed. G. Silini, North-Holland Publishers, Amsterdam (1967), p. 212; cited in Ivan Draganic and Zorica D. Draganic, The Radiation Chemistry of Water, Academic Press, New York (1971), pp. 181-8.

(4.29) W. W. Engle, Jr., "A User's Manual for ANISN, A One-Dimensional Discrete Ordinates Transport Code with Anisotropic Scattering", K-1693, Oak Ridge Gaseous Diffusion Plant, Oak Ridge, TN (March 1967).

(4.30) "Long Term Performance of Materials Used for High Level Waste Packaging", D. Stahl and N. E. Miller (compilers), NUREG/CR-3427, V.1 (August 1983).

(4.31) H. Christensen and E. Bjergbakke, "Radiolysis of Groundwater from HLW Stored in Copper Canisters", Materials Research Society Symposium Proceedings, V.15, Scientific Basis for Nuclear Waste Management VI, pp 429-36 (November 1982).

(4.32) Harold A. Schwarz, "A Determination of Some Rate Constants for the Radical Processes in the Radiation Chemistry of Water", J. Phys. Chem., 66, 255-62 (1962).

(4.33) C. J. Hochanadel, "The Radiation-Induced Reaction of Hydrogen and Oxygen in Water at 25 to 250 C", Proc. Intl. Conf. Peaceful Uses of Atomic Energy, United Nations (1955), 7, pp 521-25.

(4.34) C. J. Hochanadel, "Effects of Cobalt γ-Radiation on Water and Aqueous Solutions", J. Phys. Chem., 56, 587-94 (1952).

(4.35) Steven E. Gallun and Charles D. Holland, "Gear's Procedure for the Simultaneous Solution of Differential and Algebraic Equations with Application to Unsteady State Distillation Problems", Computers and Chemical Engineering, 6, 231-44 (1982).

(4.36) T. E. Jones, "Reference Material Chemistry - Synthetic Groundwater Composition", RHO-BW-ST-37P, April, 1982.

(4.37) A. H. Truesdell and B. F. Jones, "WATEQ, A Computer Program for Calculating Chemical Equilibria of Natural Waters", U.S. Geol. Surv. J. Res. 2, 223, 1974.

(4.38) "Long Term Performance of Materials Used for High Level Waste Packaging", D. Stahl and N. E. Miller (compilers) NUREG/CR-3405, V.1 (July 1983).

5. QUALITY ASSURANCE

Quality assurance surveillance activities for the High Level Waste Packaging Program were continued during the second year with review of program experimental data sheets and associated Battelle Laboratory Record Books. An ongoing program audit showed no areas of non-compliance as of January 1984.

Activities associated with preparation and approval of quality assurance program procedures were also continued. During the year, approximately 30 program procedures were prepared by program personnel, reviewed, and approved for use in conducting the various tasks of the experimental work. Three procedures were revised to reflect changes in testing requirements. These are: WF-PP-27, WF-PP-28, and WF-PP-35.

A summary of the program procedures which are being used to conduct the experimental program is given in Table 5.1. Included is the procedure number, the current revision number, the title, and the status.

Quality assurance surveillance activities will continue during the third year of the contract. Procedures will be revised and new ones prepared as necessary to meet program requirements.

Table 5.1. Status of NRC waste packaging program QA procedures.

Procedure No.	Title	Status
WF-PP-1 Revision 0	Procedures for Record Keeping and Documentation for NRC Waste Form System Model Development	Approved
WF-PP-5 Revision 0	Procedures for Record Keeping and Documentation for Separate Effects Model Development	Approved
WF-PP-10 Revision 0	Laboratory Procedure for Preparation of Glasses for NRC Waste Form Project	Approved
WF-PP-11 Revision 0	Laboratory Procedures for Preparation of Teflon-Leach Containers	Approved
WF-PP-14 Revision 0	Laboratory Procedure for Leaching Glass Samples	Approved
WF-PP-16 Revision 0	Laboratory Procedure for Operating the Orton Dilatometer	Approved
WF-PP-20 Revision 0	Procedure for Determining the Corrosion Rates of Alloys at High Temperatures	Approved
WF-PP-25 Revision 0	Procedure for Preparation of Carbon-Steel Casting	Approved
WF-PP-26 Revision 0	Procedure for Preparation of Steel Hydrogen-Embrittlement-Test Specimens	Approved
WF-PP-27 Revision 2	Procedure for J-Testing Compact Tension Specimens	Approved

Table 5.1. Continued.

Procedure No.	Title	Status
WF-PP-28 Revision 1	Procedure for Performing Tension Tests of Steel Specimens	Approved
WF-PP-29 Revision 0	Procedure for Conducting Hydrogen-Absorption Experiments	Approved
WF-PP-30 Revision 0	Laboratory Procedure for Preparation, Cleaning, and Evaluation of Titanium Grade-12 Specimens for Corrosion Studies of the Overpack Performance for the NRC Waste Packaging Program	Approved
WF-PP-31 Revision 0	Laboratory Procedure for Preparation, Cleaning, and Evaluation of Cast and Wrought Carbon Steel Specimens for Corrosion Studies of the Overpack Performance for the NRC Waste Packaging Program	Approved
WF-PP-32 Revision 0	Procedure for Preparation of Brine A for Corrosion Testing Under Simulated Repository Conditions	Approved
WF-PP-33 Revision 0	Procedure for Preparation of Simulated Basalt Groundwater Solution	Approved
WF-PP-33.1 Revision 0	Procedure for Preparation of Basalt Rock for Use in Corrosion Studies for the NRC Waste Packaging Program	Approved
WF-PP-34 Revision 0	Procedure for Preparation of Simulated Tuff Groundwater Solutions	To be Written

Table 5.1. Continued.

Procedure No.	Title	Status
WF-PP-35 Revision 1	Procedure for Performing Autoclave Exposures for Corrosion Tests in Simulated Brines	Approved
WF-PP-35.1 Revision 0	Procedure for Performing Autoclave Exposures for Corrosion Tests in Simulated Brines Using Sealed Internal Canister	Approved
WF-PP-36 Revision 0	Procedure for Performing Stagnant Autoclave Exposures for Corrosion Tests in Simulated Basalt or Tuff Groundwaters	Approved
WF-PP-37 Revision 0	Laboratory Procedure for Preparing Polarization Resistance Specimens, Performing Polarization Resistance Measurements and Evaluating Polarization Resistance Data	Approved
WF-PP-37.1 Revision 0	Laboratory Procedure for Performing Eh and Corrosion Potential Measurements in Autoclave Exposures in Simulated Basalt and Tuff Groundwater	Approved
WF-PP-37.2 Revision 0	Laboratory Procedure for Determination of the Polarization Behavior of Metal Specimens at Ambient Pressure	Approved
WF-PP-38 Revision 0	Procedure for Preparing and Evaluation of U-Bend Specimens for Stress Corrosion Studies of Overpack Materials for the NRC Waste Packaging Project	Approved
WF-PP-38.1 Revision 0	Procedure for Performing and Evaluating 3 Point Bend Beam Specimens for Stress Corrosion Studies of Overpack Materials for NRC Waste Package Program	Approved

Table 5.1. Continued.

Procedure No.	Title	Status
WF-PP-39 Revision 0	Procedure for Preparing, Testing and Evaluating Crevice Corrosion Specimens of Titanium Grade-12 and Cast Steel	Approved
WF-PP-40 Revision 0	Laboratory Procedures for Preparation, Cleaning, and Evaluation of Thermogalvanic and Heat-Transfer Specimens	Approved
WF-PP-41 Revision 0	Laboratory Procedures for Determination of Corrosion Rates Under Heat-Transfer Conditions	Approved
WF-PP-42 Revision 0	Laboratory Procedure for Determination of Thermogalvanic Corrosion Rates	Approved
WF-PP-43 Revision 0	Procedure for Welding Titanium Grade-12 Plate for Use in Corrosion Studies of Overpack Materials for NRC Waste Isolation Project	Approved
WF-PP-44 Revision 0	Procedure for Welding Cast and Wrought Steel Specimens	To be Written
WF-PP-45 Revision 0	Laboratory Procedure for Preparing and Evaluating Slow Strain-Rate Specimens and for Performing Slow Strain-Rate Tests	Approved
WF-PP-45.1 Revision 0	Laboratory Procedures for Performing Slow Strain-Rate Tests Under Potentiostated Conditions	Approved
WF-PP-46 Revision 0	Procedure for Preparation of Titanium Grade-12 Corrosion Specimens with Metallic Iron Embedded in the Surface	Approved

DISTRIBUTION LIST

Office of Regulatory Research
Division of Radiation Programs and Earth Sciences
Mail Stop 1130 SS
U.S. Nuclear Regulatory Commission, Washington, D.C. 20555

Attn: Division Director/Deputy Director
E. F. Conti, Chief, Waste Management Branch
F. A. Costanzi
J. R. Randall
M. B. McNeil
K. S. Kim, Project Manager (15)

Division of Waste Management, NMSS
Mail Stop 623 SS
U.S. Nuclear Regulatory Commission, Washington, D.C. 20555

Attn: Division Director/Deupty Director
Chief, Engineering Branch
E. A. Wick
M. Tokar
K. C. Chang
Document Control Center

Advisory Committee on Reactor Safeguards
Mail Stop H-1016
U.S. Nuclear Regulatory Commission, Washington, D.C. 20555

Attn: Waste Management Subcommittee
R. C. Tang

Battelle's Columbus Laboratories
505 King Avenue
Columbus, Ohio 43201-2693

Attn: D. Stahl, Program Manager (50)

DISTRIBUTION LIST (Continued)

Martin Seitz
Argonne National Lab.
Argonne, IL 60439

Martin J. Steindler
Argonne National Lab.
Argonne, IL 60439

Donald G. Schweitzer
Brookhaven National Lab.
Upton, NY 11973

Peter Soo
Brookhaven National Lab.
Upton, NY 11973

David Martin
Iowa State University
Ames, IA 50011

Harold Wollenberg
Lawrence Berkeley Lab.
Berkeley, CA 94720

Nestor Ortiz
Sandia National Lab.
Albuquerque, NM 87185

Pedro B. Macedo
Catholic University of America
Washington, D.C. 20064

Robert Williams
Electric Power Research Institute
P.O. Box 10412
Palo Alto, CA 94301

William P. Reed
U.S. Department of Commerce
National Bureau of Standards
Washington, D.C. 20234

Ray Walton
U.S. Department of Energy
Washington, D.C. 20545

John E. Mendel
Materials Characterization Center
Pacific Northwest Lab.
Richland, WA 99352

John Crandall
Savannah River Lab.
Aiken, SC 29808

Edward J. Hennelly
Savannah River Lab.
Aiken, SC 29808

Arthur A. Bauer
Office of Nuclear Waste Isolation
Battelle Memorial Institute
505 King Avenue
Columbus, OH 43201

Michael Smith
Basalt Waste Isolation Projects
Rockwell Hanford Operation
Richland, WA 99352

Kenneth Russell
Department of Materials Science
and Engineering
Massachusetts Institute of
Technology
Cambridge, MA 02139

Robert H. Doremus
Materials Engineering Department
Rensselaer Polytechnic Institute
Troy, NY 12181

David C. Kocher
Oak Ridge National Lab.
P.O. Box X
Oak Ridge, TN 37830

Stanley Wolf
DOE/BES
Washington, D.C. 20585

Neville Moody
Sandia Livermore Lab.
Livermore, CA 94550

Donald E. Clark
ONWI
Battelle Memorial Institute
505 King Avenue
Columbus, OH 43201

DISTRIBUTION LIST (Continued)

Martin A. Molecke
Sandia National Lab.
Albuquerque, NM 87185

Neville Pugh
National Bureau of Standards
Washington, D.C. 20234

Nicholas Grant
Department of Metallurgy
Massachusetts Institute
of Technology
Cambridge, MA 02139

Jerome Kruger
Corrosion Section
National Bureau of Standards
Washington, D.C. 20234

Tae-Moon Ann
Brookhaven National Lab.
Upton, NY 11973

Don J. Bradley
Waste Package Programs
Battelle Pacific Northwest Labs
Richland, WA 99352

Allen G. Goff
Oak Ridge National Laboratory
P.O. Box X
Oak Ridge, TN 37830

Lynn Hobbs
Department of Materials Science
Massachusetts Institute of
Technology
77 Massachusetts Avenue
Cambridge, MA 02139

Richard E. Westerman
Pacific Northwest Lab.
P.O. Box 999
Richland, WA 99352

Thomas D. Chikalla
Pacific Northwest Lab.
P.O. Box 999
Richland, WA 99352

Larry Hench
University of Florida
Gainesville, FL 32611

Davis E. Clark
University of Florida
Gainesville, FL 32611

Joseph Mascara
MS 5650 NL
U.S. Nuclear Reg. Comm.
Washington, DC 20555

Ken W. Stephens
The Aerospace Corp., Suite 400
955 L'Enfant Plaza, S.W.
Washington, DC 20024

Robert S. Dyer
Office of Radiation Programs (ANR-461)
U.S. Environmental Protection Agency
401 M Street, S.W.
Washington, DC 20460

Lorenzo Ricks
Office of Energy Research
U.S. Department of Energy
Washington, D.C. 20545

Larry Evans
Armco Research Center
703 Curtis Avenue
Middletown, OH 45043

Woody Swope
Armco Stainless Steel Division
P.O. Box 1697
Baltimore, MD 21203

M. John Plodinec
Savannah River Laboratory
Aiken, SC 29808

☆ U.S. GOVERNMENT PRINTING OFFICE: 1984-421-297:4020

NRC FORM 335
(11-81)

U.S. NUCLEAR REGULATORY COMMISSION

BIBLIOGRAPHIC DATA SHEET

1. REPORT NUMBER (*Assigned by DDC*)
NUREG/CR-3427, Vol. 4
BMI-2113

4. TITLE AND SUBTITLE (*Add Volume No., if appropriate*)
Long-Term Performance of Materials Used for High-Level Waste Packaging
Annual Report - April 1983-April 1984

2. (*Leave blank*)

3. RECIPIENT'S ACCESSION NO.

7. AUTHOR(S)
Compiled by D. Stahl and N. E. Miller

5. DATE REPORT COMPLETED

MONTH	YEAR
May	1984

9. PERFORMING ORGANIZATION NAME AND MAILING ADDRESS (*Include Zip Code*)
Battelle's Columbus Laboratories
505 King Avenue
Columbus, Ohio 43201-2693

DATE REPORT ISSUED

MONTH	YEAR
June	1984

6. (*Leave blank*)

8. (*Leave blank*)

12. SPONSORING ORGANIZATION NAME AND MAILING ADDRESS (*Include Zip Code*)
Division of Radiation Programs and Earth Sciences
Office of Nuclear Regulatory Research
U.S. Nuclear Regulatory Commission
Washington, D.C. 20555

10. PROJECT/TASK/WORK UNIT NO.

11. FIN NO.
B6764

13. TYPE OF REPORT
Annual

PERIOD COVERED (*Inclusive dates*)
April 1983-April 1984

15. SUPPLEMENTARY NOTES

14. (*Leave blank*)

16. ABSTRACT (*200 words or less*)

The effects on glass waste-form dissolution of temperature, pressure, solution chemistry, and ratio of glass surface area to solution volume have been studied. The glass-dissolution correlation is ready to be evaluated by comparison with experiments. The devitrification correlation has been completed. In canister-corrosion studies, CF8 alloy was found less susceptible to glass attack than Type 304L stainless steel. Limited experiments revealed no corrosion mechanism which would indicate that cast steel could not be used as a container material; additional tests with cracking agents are planned. In hydrogen-uptake studies, cast steel was found to absorb more hydrogen than wrought steel. Parts of the general-corrosion correlation have been tested, and work continues on obtaining realistic experimental data as input for it. Gamma fluxes and dose rates in and near the waste package were calculated for CHLW and spent-fuel waste forms. The current water-radiolysis model was found adequate when tested against existing data, and preliminary calculations were performed with the current water-chemistry model; in both cases, additional chemical species are being incorporated.

17. KEY WORDS AND DOCUMENT ANALYSIS

17a. DESCRIPTORS

High-level waste
Waste package
Waste form/container/overpack

17b. IDENTIFIERS/OPEN-ENDED TERMS

18. AVAILABILITY STATEMENT
Unlimited

19. SECURITY CLASS (*This report*)
Unclassified

20. SECURITY CLASS (*This page*)
Unclassified

21. NO. OF PAGES

22. PRICE
$

NRC FORM 335 (11-81)

UNITED STATES
NUCLEAR REGULATORY COMMISSION
WASHINGTON, D.C. 20555

OFFICIAL BUSINESS
PENALTY FOR PRIVATE USE, $300

120555078877 1 IANICH
US NRC
ADM-DIV OF TIDC
POLICY & PUB MGT BR-PDR NUREG
W-501
WASHINGTON DC 20555